STRUCTURAL BEHAVIOUR OF SANDWICH STRUCTURES CONSTRUCTED OF BIO-BASED MATERIALS UNDER MONOTONIC AND IMPACT LOADING

by

Dillon Betts

Submitted in partial fulfilment of the requirements
for the degree of Doctor of Philosophy

at

Dalhousie University
Halifax, Nova Scotia
March 2021

Dedicated to my wife, Courtney

TABLE OF CONTENTS

LIST OF TABLES

LIST OF FIGURES

ABSTRACT

As a part of this thesis project, 69 sandwich specimens with flax fibre-reinforced polymer (FFRP) faces were manufactured, tested and analysed, specifically 57 one-way sandwich beams (1200 mm long x 150 mm wide x 80 mm thick) and 12 two-way sandwich panels (1200 mm x 1200 mm x 80 mm thick). The cores were made of either polyisocyanurate (PIR) foam or corrugated cardboard. A total of 1192 tests were performed as a part of this thesis research, including quasi-static three-point bending tests of one-way beams, quasi-static concentrated loading of two-way panels, impact loading of one-way beams, impact loading of two-way panels, and post-impact flexural testing. The testing program showed that sandwich structures with FFRP faces are viable alternatives to sandwich structures constructed with synthetic FRP faces. They exhibit high relative strength and resiliency.

The structures were modelled analytically and numerically. For the one-way behaviour of the sandwich structures, a design-oriented analysis procedure was developed which can be feasibly used by practicing engineers. Additionally, a nonlinear energy balance model to predict the deflection of FFRP-foam sandwich beams under impact was developed. For the two-way behaviour of the FFRP-foam sandwich structures, the Mindlin Plate Theory was used to create a nonlinear model to predict the flexural load-deflection and load-strain responses. However, the model was not able to predict the localized deformation and failure present in thick-faced sandwich panels. Therefore, a finite element (FE) model was created to predict the quasi-static and impact behaviour of the panels and was verified using the test data. Based on the FE model, a parametric study was performed to observe the effect of core density, core thickness, face thickness and loading size. Panels with low-density cores were more susceptible to face wrinkling failure and panels with high-density cores were susceptible to both tensile rupture and core shear failure. It was also shown that the impulse duration and maximum displacement experienced under low energy impacts increased with a decrease in core thickness, face thickness and core density.

LIST OF ABBREVIATIONS AND SYMBOLS USED

A = area, mm^2

= geometric property used in shear deflection calculation = bd^2 / c

= used in failure equations by Triantafillou and Gibson (1987) as a constant term

AVE = average

B = used in failure equations by Triantafillou and Gibson (1987) as a constant term

b = one-way sandwich specimen width, mm

$C_\#$ = general representation of constants

CAI = compression-after-impact

CC = compression crushing failure

CL = concentrated load

CS = core shear failure

CW = compression face wrinkling failure

c = sandwich specimen core thickness, mm

D = flexural rigidity = EI

D = moment arm of sandwich panel cross-section (ie. distance between centroid of top and bottom faces

E_b = impact energy absorbed through flexural deflection

E_c = Young's modulus of core, MPa

E_{fc} = compressive Young's modulus of face material, MPa

E_{fo} = initial Young's modulus for nonlinear face material, MPa

E_{ft} = tensile Young's modulus of face material, MPa

E_{fu} = ultimate secant Young's modulus for nonlinear face material (passes through 0,0 and ϵ_{fu}, σ_{fu}), MPa

E_i = impact energy absorbed through contact / indentation

E_s = Young's modulus of unfoamed core material

E_T = total energy due to drop weight impact

E_v = impact energy absorbed through shear deformation

FEM = finite element method

FRP = fibre-reinforced polymer
FFRP = flax fibre-reinforced polymer
f_{fo} = stress in sandwich panel face corresponding to point of transition, MPa
f_{fu} = ultimate stress in sandwich panel face, MPa
G_c = shear modulus of core material, MPa
G_{co} = initial shear modulus of nonlinear core material, MPa
GFRP = glass fibre-reinforced polymer
g = acceleration due to gravity, 9.8 m/s^2
h = total thickness of sandwich panel, mm
h_d = drop height of impact test, mm
K = stiffness, N/mm
L = span length, mm
M_u = ultimate moment, N-mm
m = mass, kg
= sometimes used as mass per unit length, kg/mm
NIIM = nonlinear incremental iterative model
P_{CS} = load causing core shear failure, N
P_{CW} = load causing compression face crushing, N
P_{TR} = load causing tensile face rupture, N
P_u = ultimate load, N
PC = plain cardboard core
PIR = polyisocyanurate (foam type)
POT = point of transition
SD = standard deviation
T_d = damped period, s
TPB = three-point bending
TR = tensile rupture failure
t = sandwich panel face thickness, mm
= time, s
WC = waxed cardboard core
γ_c = shear strain in sandwich panel core, mm/mm
γ_{cu} = ultimate shear strain of the core, mm/mm

Δ = overall deflection of sandwich panel, mm

Δ_b = flexural deflection of sandwich panel, mm

Δ_v = shear deflection of sandwich panel, mm

δ_u = deflection corresponding to ultimate load capacity, mm

ϵ_{bott} = recorded strain in bottom sandwich panel face, mm/mm

ϵ_f = model strain in sandwich panel face, mm/mm

ϵ_{fc} = compressive strain in sandwich panel face, mm/mm

ϵ_{fo} = strain in sandwich panel face corresponding to point of transition, mm/mm

ϵ_{ft} = tensile strain in sandwich panel face, mm/mm

ϵ_{fu} = ultimate strain of sandwich panel face, mm/mm

ϵ_{top} = recorded strain in top sandwich panel face, mm/mm

ξ = damping ratio of sandwich panel

ν_c = Poisson's ratio of the core material

ρ_c = density of core material, kg/mm^3

ρ_s = density of unfoamed core material, kg/mm^3

σ_{cr} = critical compressive stress in sandwich panel face causing wrinkling, MPa

σ_f = stress in sandwich panel face, MPa

σ_{fu} = ultimate stress in sandwich panel face (sometimes shown as f_{fu}), MPa

σ_{ys} = yield stress of unfoamed core material, MPa

τ_c = shear stress in the core, MPa

τ_{cu} = ultimate shear stress of core material, MPa

τ_s = ultimate shear stress of unfoamed core material, MPa

ψ = curvature of sandwich specimens, 1/mm

ω_d = damped angular frequency, radians/s

ω_n = natural angular frequency, radians/s

ACKNOWLEDGEMENTS

Firstly, I would like to acknowledge my supervisors, Dr. Pedram Sadeghian and Dr. Amir Fam. They helped and encouraged me throughout my PhD program. They helped me grow into a better researcher, writer, and leader. I would also like to thank my supervisory committee members, Dr. Farid Taheri and Dr. Yi Liu for their support and their constructive criticism which improved the quality of this thesis. Thank you to Dr. Khaled Sennah for acting as my external examiner for his time, effort and for his feedback.

The experimental portion of my research would not have been possible without the help of the excellent technicians in our department, Brian Kennedy, Jordan Maerz, Blair Nickerson, Brian Liekens and Jesse Keane. They were always willing to help design and set up tests, prepare data acquisition programs, fabricate parts, and brainstorm ideas. I would also like to thank the administration team at the department, specifically June Ferguson and Shelley Parker. They always made sure that I was aware of the deadlines that I probably (definitely) would have otherwise missed.

Thank you to the Natural Sciences and Engineering Research Council of Canada (NSERC) for funding my PhD research. I would like to like to acknowledge and thank Bioindustrial Innovation Canada (BIC), Queen's University, and Dalhousie University for their in-kind and financial support. Additionally, I would like to acknowledge the suppliers of the materials used for this thesis: Entropy Resins (bio-based epoxy), Composites Evolution (flax fabric), Elliott Company (PIR foams) and Maritime Paper (cardboard).

Thank you to all my colleagues at Dalhousie during my PhD program, and specifically those in my lab group who assisted me along the way. Thank you to all my friends for the coffee breaks and the late-night chats. Also, thanks for getting me out of the office and onto a river every once and a while.

Thank you to my parents, Elaine and Allan Betts, for always encouraging me and for being there when I needed someone to talk to. Finally, thank you to my wife, Courtney, who makes me smile every day. Thank you for supporting me in pursuing my dream. I could not have done this without you.

CHAPTER 1: INTRODUCTION

1.1. BACKGROUND

Interest in sustainable materials is increasing around the world. One material that is gaining attention in the field of sustainable infrastructure is natural fibre-reinforced polymers (FRPs). Natural fibres have been used as reinforcing for modern FRPs since the early 1900s (Sparnins 2006). They can be classified as one of the three main types: plant, animal or mineral. Due to their mechanical properties, one of the most popular choices of natural fibres for use in FRPs is the plant fibre, flax. Plant fibres can come from several parts of the plant, such as (Ramesh et al. 2017): the leaves, the stem (bast fibres), the fruit, or the reed. The flax fibre is an example of a bast-type fibre, which are characterised as long fibres with relatively high mechanical properties (when compared to other natural fibres) (Ramesh et al. 2017).

Flax fibres are comprised of 72.5% cellulose, 14.5% hemicellulose, 2.5% lignin and 0.9% pectin (Ramesh et al. 2017). They have a reported strength and stiffness of approximately 500 – 900 MPa and 50 – 70 GPa, respectively (Sparnins 2006). In Canada, the use of the flax fibres is often over-looked and the fibres are mainly considered a waste product of the flax seed industry. At approximately a third of the strength of E-glass fibres, flax has the potential to replace glass in some applications. For instance, the main objective of the current research is to show their use in the faces of structural sandwich panels.

Sandwich panels are often used in applications where light weight and/or insulation efficiency are requirements. They are comprised of two strong faces separated by a weaker lightweight core, often made of a foam material. The separation of the faces by the core provides a large moment of inertia to resist bending (Allen 1969). Recently, synthetic fibre-reinforced polymers (FRPs), such as carbon FRPs or glass FRPs, have been a popular choice for sandwich panel faces due to their relatively high specific strengths. Because the core materials typically have much lower strength, they often govern the failure of sandwich structures and the FRP facings rarely reach their full tensile strength. Therefore, the high strength of the synthetic FRP facings is often not fully utilized (Fam et al., 2016; Sadeghian et al., 2016). This presents an opportunity to use lower strength, but more environmentally friendly, materials as alternatives to synthetic FRPs. Flax FRPs (FFRPs) represent a sustainable option with a lower embodied energy then traditional fibres such as a glass or carbon (Mak and Fam, 2016). The use of natural fibres and bio-based resins for facings of sandwich panels in civil applications has been studied in the recent past under flexural (Mak et al., 2015; Sadeghian et al., 2016) and axial loads (Codyre et al., 2016). However, the studies were only experimental and focused only on the one-way behaviour of the sandwich panels.

Sandwich panels are also regularly used as a part of building envelopes. As these structures can be subjected to impacts from flying debris during high wind events, it is important to understand their behaviour under low velocity impact loading. The impact behaviour of sandwich panels with synthetic faces has been investigated under low velocity impacts (Abrate 1997; Hazizan and Cantwell 2002; Anderson and Madenci 2000; Atas and Potoglu 2016; Plagianakos et al. 2016; Schubel et al. 2005; Torre and Kenny 2000). Some studies have been performed on natural fibre sandwich panels under impact (Ude et al. 2013), however, there is still a gap in the field concerning the impact and post-impact behaviour of sandwich panels with natural fibre faces such as FFRPs. A more detailed review of the current literature is provided in the introduction of each subsequent chapter.

1.2. PROBLEM STATEMENT

There is currently a gap in the literature with regards to the impact and post-impact behaviour of sandwich beams with flax fibre-reinforced polymer (FFRP) faces. Additionally, there are no available studies on the two-way behaviour of large-scale sandwich panels with FFRP faces and foam cores under quasi-static or impact loads. Therefore, the aim of the research presented in this thesis is to provide an in-depth understanding of the flexural behaviour of sandwich beams and panels with natural FFRP faces under both quasi-static and impact loads. The research presented in this thesis shows the viability of using sandwich structures with FFRP faces in infrastructure and architectural applications, such as for building cladding materials or wall panels.

1.3. OBJECTIVES

The goal to be achieved by this research is to provide a deeper insight into the structural behaviour of sandwich structures with FFRP faces and foam for use in sustainable infrastructure applications. This goal will be obtained by completing the following objectives:

- Investigate the monotonic and impact behaviour of one-way FFRP-foam and FFRP-cardboard sandwich beams
- Explore the post-impact residual behaviour of one-way FFRP-foam sandwich beams.
- Provide a deeper understanding the behaviour of two-way FFRP-foam sandwich panels under monotonic and dynamic loading.
- Develop design-oriented models for one-way and two-way FFRP sandwich structures, such that the model can be feasibly used by practicing engineers.
- Create a Finite Element Model (FEM) to predict the behaviour of two-way FFRP-foam sandwich panels and perform a parametric study using this model.

1.4. THESIS STRUCTURE

In this thesis, the flexural behaviour of sandwich panels with flax FRP faces is explored both experimentally and theoretically. As a part of this research, 57 sandwich beams (1200 mm long x 80 mm thick x 150 or 75 mm wide) were fabricated and tested under various loading conditions. Additionally, 12 large scale sandwich panels (1200 mm x 1200 mm x 80 mm thick) were fabricated and tested under quasi-static and impact loading. An overall test matrix for the entire thesis is presented in Table 1-1.

Table 1-1. Overall test matrix

Chapter	Face Layers	Core Types	Specimen Sizes	Test Types	Number of Specimens	Number of Tests
2	1, 2, 3	PIR foam (32 kg/m^3, 64 kg/m^3, 96 kg/m^3)	1200 mm x 150 mm x 80 mm	quasi-static TPB	9	9
3	1, 2, 3	PIR foam (32 kg/m^3, 64 kg/m^3, 96 kg/m^3)	1200 mm x 150 mm x 80 mm	ramped impact TPB	9	92
4	1, 2, 3	PIR foam (32 kg/m^3, 64 kg/m^3, 96 kg/m^3)	1200 mm x 75 mm x 80 mm	impact and post-impact TPB	27	660
5	1, 2, 3	cardboard (plain and waxed)	1200 mm x 150 mm x 80 mm	impact and post-impact TPB	12	16
6	1, 2, 3	PIR foam (96 kg/m^3)	1200 mm x 1200 mm x 80 mm	quasi-static CL and impact CL	12	415
Total	-	-	-	-	69	1192

TPB = Three Point Bending; CL = Concentrated Load

The research was separated into two major phases and further broken down into subcategories, as follows:

- Phase 1: Testing and Analysis of One-Way Sandwich Beams
    - Chapter 2: Behaviour of FFRP-Foam Sandwich Beams Under Monotonic Loads
    - Chapter 3: Behaviour of FFRP-Foam Sandwich Beams Under Low Velocity Impact Loads
    - Chapter 4: Post-Impact Residual Behaviour of FFRP-Foam Sandwich Beams
    - Chapter 5: Behaviour of FFRP-Cardboard Sandwich Beams

- Phase 2: Testing and Analysis of Two-Way Sandwich Panels
    - Chapter 6: Experimental Behaviour of Two-way FFRP-Foam Sandwich Panels

- Chapter 7: Analytical Modelling of Two-way FFRP-Foam Sandwich Panels
- Chapter 8: Finite Element Modelling of Two-way Foam-FFRP Sandwich Panels

In Chapter 2, nine sandwich beams were tested under three-point bending. The main test parameter was face thickness and foam core density. A design-oriented model to predict the load-deflection and moment-curvature behaviour of the beams was developed and is presented. In Chapter 3, nine beam specimens (identical to those in Chapter 2) were tested under increasing impact loads until failure. A nonlinear model based on the energy balance method to predict the deflection and face strains of a given impact energy was developed and is presented. In Chapter 4, 27 beam specimens were tested under multiple impacts at a set impact energy level (100% failure energy, 75% failure energy or 50% failure energy) and subsequently tested under post-impact flexural loads. These tests showed that sandwich panels that survived the impact events showed remarkable resilience. In Chapter 5, 12 sandwich beams with cardboard cores and FFRP faces were fabricated and tested under static, impact, and post-impact flexural loads. Again, these tests showed that sandwich panel that survived the impact event showed remarkable resilience. However, these tests showed high variability in ultimate strength due to the connection between the cardboard cores and the faces.

In Chapter 6, 12 large scale two-way sandwich panels were tested under both quasi-static concentrated load tests and low velocity impact loads. The main test parameter was the face thickness and the impact energy level. Based on the tests, it was determined that the two-way sandwich panels were susceptible to hidden damage within the core before and signs of obvious failure. In Chapter 7, a nonlinear model based on the Mindlin Plate Theory was developed and used to predict the load-deflection behaviour of sandwich panels under a concentrated load. In this chapter, it was discovered that this analytical modelling was unable to account for the development of localized deformation in the sandwich panels. Therefore, it was necessary to develop a finite element model (FEM) which is presented in Chapter 8. FEM models were created to predict both the quasi-static and impact behaviour of the sandwich panels. The models were used to perform a parametric study.

CHAPTER 2: BEHAVIOUR OF FFRP-FOAM SANDWICH BEAMS UNDER MONOTONIC LOADS [1]

2.1. INTRODUCTION

Sandwich panels are often used in applications where light weight and/or insulation efficiency are required. They have high flexural strength as the lightweight core separates the strong facings apart, thereby providing a large moment of inertia to resist bending (Allen 1969). As fibre-reinforced polymer (FRP) composites have relatively high specific strengths, they are a popular choice for facing materials. However, due to the relatively low strength of typical core materials, the core often governs the failure mechanism and the FRP facings rarely reach their full tensile strength. As such, the high strength of the FRP facings is often not utilized (Fam et al., 2016; Sadeghian et al., 2016). This phenomenon presents an opportunity to use natural fibres (e.g. flax) with lower strength, which are more environmentally friendly, as alternatives to synthetic fibres. Moreover, thermoset resins with high bio-content can be used to make the FRP facings more environmentally friendly. Flax FRP (FFRP) composites represent a sustainable option with a lower embodied energy than traditional fibres such as glass or carbon (Mak and Fam, 2016).

Behaviour of sandwich structures, in general, has been studied extensively since the mid-20th century. Allen (1969) presented fundamental approaches for the analysis of sandwich panels using the ordinary beam theory. For ease of calculation, Allen's text provides a simplified analysis which produces moderately accurate results. In the early 1990s, researchers began to use high-order analyses to model the behaviour of sandwich panels, in order to achieve more accurate results (Frostig et al., 1992; Frostig and Baruch, 1996; Thomsen and Rits, 1998). The high-order theory presented by Frostig et al. (1992) improves upon the method presented by Allen (1969) by accounting for the nonlinearity of the transverse and longitudinal deflections of the

---

[1] **This chapter has been published in the ASCE *Journal of Composites for Construction:***

Betts, D., Sadeghian, P., and Fam, A. (2018). "Experimental Behaviour and Design-Oriented Analysis of Sandwich Beams with Bio-Based Composite Facings and Foam Cores." *Journal of Composites for Construction*, 22(4), 1–12.

core material. Finite element modelling of sandwich panels has also been used. Sharaf and Fam (2012) developed a finite element model for the analysis of sandwich panels with soft cores and glass FRP (GRFP) facings. The model is able to predict flexural behaviour and failure modes. Fam et al. (2016) developed a semi-analytical model to predict behaviour of sandwich panels constructed of polyurethane foam cores and GFRP facings under flexural loading. This model accounts for nonlinear properties of the foam cores and the GFRP facing properties and was validated with experimental testing.

The use of natural fibres and bio-based resins for facings of sandwich panels in civil applications has been studied in the recent past under flexural (Mak et al., 2015; Sadeghian et al., 2016) and axial loads (Codyre et al., 2016). However, the studies were only experimental and used unidirectional FFRP sheets for the facings. The experimental database for bio-based sandwich panels remains extremely limited. There is a gap regarding bidirectional FFRPs providing two-way behaviour as expected for many wall and roof panels. Additionally, because of the complex behaviour of sandwich panels in combined flexural and shear loading and the wide variety of failure modes, the currently available analytical models are quite sophisticated and require very advanced knowledge in mathematics and computer programming. No simple design-oriented models are available for structural engineering applications of sandwich panels. This paper aims to fill the several gaps stated above using an experimental program and a design-oriented analytical modeling.

2.2. EXPERIMENTAL PROGRAM

2.2.1. Test Matrix

Nine sandwich beam specimens were fabricated and tested under three-point bending. The specimens were comprised of FFRP facings and closed cell polyisocyanurate foam cores with a thickness of 75 mm. The test parameters were facing thickness and foam core density. Three facing thicknesses of approximately 1.25 mm, 2.5 mm and 3.75 mm thick (1, 2 and 3 layers of flax fabric) and three core densities (32, 64, and 96 kg/m^3) were compared. The parameters were chosen such that different failure modes could be examined. The test matrix is shown in Table 2-1. The specimens were identified according to the core type and number of flax layers as per the following convention: XFL-CY, where X is the number of flax layers (i.e. 1, 2, or 3) and Y is the nominal core density in kg/m^3 (i.e. 32, 64, or 96). For example, 2FL-C64 indicates a sandwich specimen with 2 flax layers at either side of a core with a density of 64 kg/m^3.

Table 2-1. Test matrix for quasi-static tests of one-way sandwich beams

No.	Specimen I.D.	Number of FFRP layers in each facing	Nominal core density (kg/m^3)
1	1FL-C32	1	32
2	2FL-C32	2	32
3	3FL-C32	3	32
4	1FL-C64	1	64
5	2FL-C64	2	64
6	3FL-C64	3	64
7	1FL-C96	1	96
8	2FL-C96	2	96
9	3FL-C96	3	96

2.2.2. Materials

For the facings, a balanced bidirectional flax fibre fabric (2x2 twill) was used with a bio-based epoxy resin. The fabric had a reported nominal areal mass of 400 g/m^2 (gsm) which was measured to be 410 gsm. For the resin, a bio-based epoxy was used. This resin is typically used with a fast setting hardener, however, for this experiment a longer pot life was required, and a different hardener was used. The reported technical data from the manufacturer is approximate as it assumes the use of the fast setting hardener. When mixed with the fast setting hardener, the resin has a reported tensile strength, modulus and elongation of 53.2 MPa, 2.65 GPa, and 6%, respectively. It has an approximate bio-based carbon content of 30% after mixing. In order to determine the properties of the epoxy, five identical dumbbell-shape coupon specimens were fabricated and tested in accordance with ASTM D638 (ASTM 2013). The tests showed that the average and standard deviation (SD) of the tensile strength, Young's modulus and ultimate strain were 57.9 ± 0.4 MPa, 3.20 ± 0.13 GPa, and 0.0287 ± 0.0018 mm/mm, respectively.

The mechanical properties of the facing FFRP were determined through compression and tension coupon testing. A uniaxial tension test was performed on five identical FFRP specimens fabricated using the materials cited above as per ASTM D3039 (ASTM 2014). The specimens were 250 mm long, 25 mm wide, and two plies thick (approximately 2.5 mm thick). The specimens had 62.5 mm long FFRP tabs on each end, which were adhered to the specimen using the bio-based resin. The specimens were tested in uniaxial tension at a rate of 2 mm/min. The results (average ± SD) of these tests show that the facing composites have a tensile strength, initial tensile modulus, and ultimate strain of 45.4 ± 1.8 MPa, 7.51 ± 0.69 GPa and 0.0083 ± 0.0009 mm/mm, respectively. The stress-strain plot of each test specimen is shown in Figure 2-1.

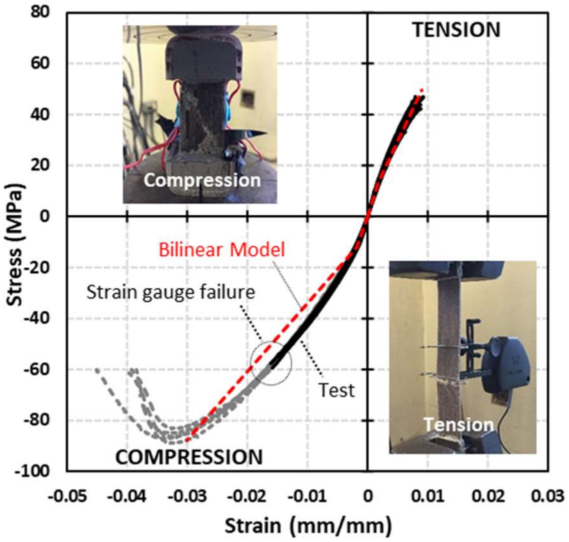

Figure 2-1. Stress-strain curves of facing materials in tension and compression: coupon tests and proposed bilinear model.

Five identical compression coupon specimens were also tested. Due to the unavailability of the testing apparatus with hydraulic grips for standard test method in compression, an alternative test was developed to evaluate the FFRP strength. Compression specimens were manufactured by laminating eight two-ply composite strips together using the same bio-epoxy. The ends were fixed into a square aluminum cap (38 mm wide and 18 mm deep) using a fast curing adhesive. The specimens were 70 mm long, 25 mm wide and 25 mm thick. Strain gauges were applied at the center of both sides in the longitudinal direction. The specimens were tested in uniaxial compression at a rate of 0.5 mm/min. The results (average ± SD) show that the facing composites have an initial compressive modulus of 6.73 ± 1.59 GPa and a compressive strength and corresponding strain of 86.4 ± 2.2 MPa and 0.0327 ± 0.0010 mm/mm, respectively. The stress-strain plots and typical test specimens are shown in Figure 2-1. During the tests, the strain in the specimens exceeded the capacity of the strain gauges. Therefore, to show the rest of the stress-strain curve, the stroke was converted to strain and calibrated using the available strain gauge data. This portion of the plot is shown in Figure 2-1 as a dashed grey line.

As shown in Figure 2-1, the coupons made of bidirectional flax fabric exhibit a nonlinear behaviour. The nonlinearity of composites made of natural fibres have been reported, previously (Christian and Billington, 2011; Yan et al., 2012; Mak et al., 2014; Mathura and Cree, 2016; and Hristozov et al., 2016). In this study, the stress-strain behaviour of the FFRPs is modelled as a bilinear plot with a point of transition (POT) at a strain of 0.0018 mm/mm. The primary modulus was determined by finding the slope of the stress-strain diagram between strains of zero and 0.0018 mm/mm. The secondary modulus was defined as the slope of a chord passing through a strain of 0.0018 mm/mm and the ultimate strain. From the compression and tension tests, the secondary tensile modulus and secondary compression modulus were found to be 4.59 ± 0.37 GPa and 2.36 ± 0.19 GPa, respectively.

Each specimen had a core made of a closed cell polyisocyanurate foam. Three different densities were used: 32 kg/m^3, 64 kg/m^3 and 96 kg/m^3. The actual densities have been measured as 31.2 kg/m^3, 62.4 kg/m^3 and 91.7 kg/m^3, respectively (Codyre et al., 2016). Each foam type was received in sheets, 1200 mm wide, 2400 mm long and 75 mm thick. The moduli and strengths of each foam as given by the manufacturer are shown in Table 2-2.

Table 2-2. Mechanical properties of foam cores

Foam	Parallel to rise						Perpendicular to rise					
type	E_c	E_t	G	f_{cu}	f_{tu}	τ_u	E_c	E_t	G	f_{cu}	f_{tu}	τ_u
C32	4 823	8 268	2 067	186	248	172	2 302	3 190	1 515	124	179	124
C64	14 469	18 603	5 856	585	551	379	9 646	10 748	5 167	427	406	344
C96	32 865	27 146	7 234	978	930	585	21 290	15 709	6 063	834	792	489

Note 1. *Data is presented in kPa.*

Note 2. *E_c = compressive modulus, E_t = tensile modulus, G = shear modulus, f_{cu} = compressive strength, f_{tu} = tensile strength, and τ_u = shear strength.*

2.2.3. Specimen Fabrication

The fabrication process is shown in Figure 2-2. A 600 mm x 1200 mm section of the foam was cut from a 1200 mm x 2400 mm foam board. The foam surface was then cleaned of all dust and debris. Once the epoxy and hardener were mixed, a layer of resin was applied to the top surface of the foam. A section of flax fibre fabric 600 mm wide and 1200 mm long was then placed on the foam with its warp direction fibres oriented parallel to the longitudinal axis of the specimen. Additional resin was applied on the fabric. This was repeated as required depending on the specimen's facing thickness. To create a clean finish, parchment paper was placed on the top surface and a steel roller was used to remove air and excess resin. A weighted flat board was then placed on the section and the resin was allowed to cure for a minimum of seven days. This process was repeated on the other side of the panel to complete the opposite facing. After both sides of a section were cured, the specimens were cut to their final size of 150 mm wide and 1200 mm long using a band saw and stored in a dry environment until testing.

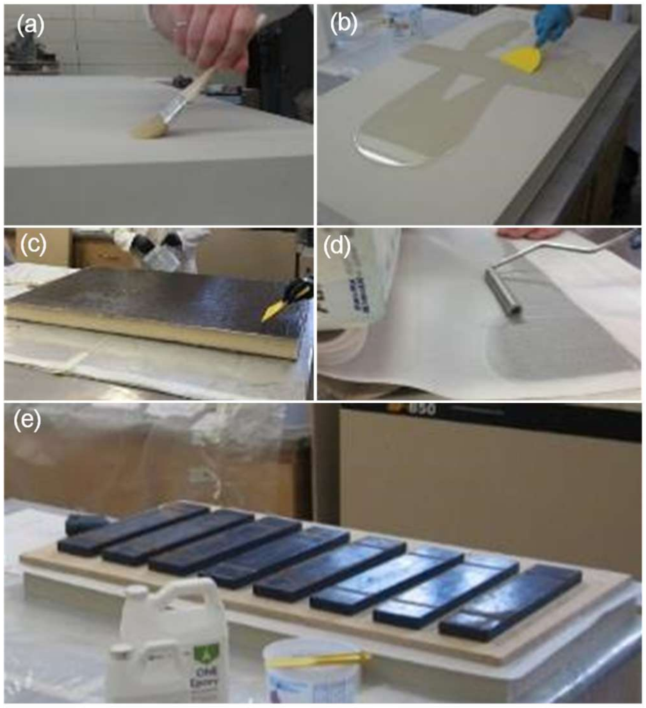

Figure 2-2. Specimen fabrication: (a) dust removal; (b) resin application on foam; (c) resin application on flax fabric layer; (d) consolidation; and (e) curing.

2.2.4. Test Setup and Instrumentation

Each specimen was tested under three-point bending using a 1 MN actuator that applied the load to the specimen at a rate of 8 mm/min through a 150x150x225 mm Hollow Structural Section (HSS) as shown in Figure 2-3. The HSS was used to avoid local failure and to ensure an even distribution of the load. A 25-mm diameter hole was cut into the bottom face of the HSS such that a strain gauge with a 6 mm gauge length could be installed at the center of the top FFRP facing. Another strain gauge was also installed at the center of the bottom facing. Both strain gauges were installed to measure longitudinal strains. Two displacement transducers were placed at mid-span, 10 mm from each edge, to measure deflection. As shown in the test set-up schematic in Figure 2-3, one support was a roller, while the other was a hinge. A data acquisition system recorded the force, stroke, displacement and strains at a rate of six samples per second.

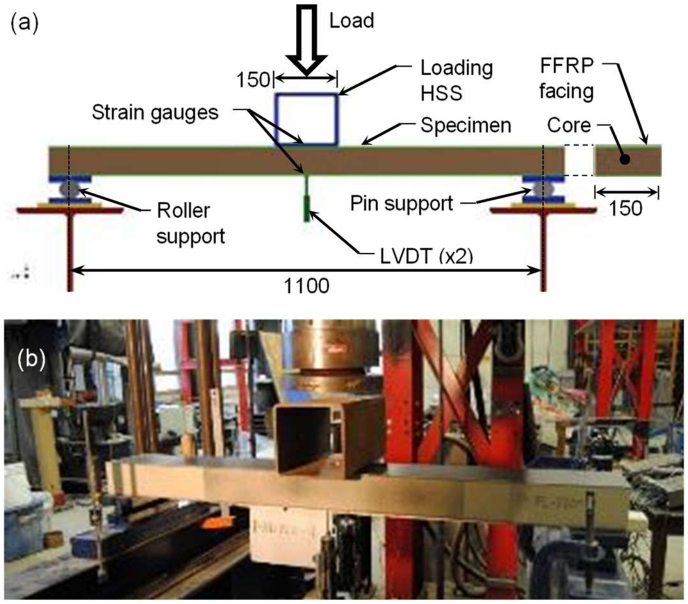

Figure 2-3. Test set-up and instrumentation: (a) schematic drawing; and (b) photo (dimensions in mm).

2.3. EXPERIMENTAL RESULTS AND DISCUSSIONS

The main test results are load-deflection, and load-facings strain, and moment-curvature responses of the sandwich beam specimens. Table 2-3 presents the test results of each specimen, including: the peak load (P_u) and corresponding deflection (δ_u), the peak moment (M_u), the initial stiffness (K), the initial flexural rigidity (EI), and the failure mode. The initial stiffness was taken as the first linear slope of the load-deflection plot and the initial flexural rigidity was determined likewise using the moment-curvature plot. The following sections present the various observations and test results, including failure modes and the effect of facing thickness and core density on the moment-curvature and load-deflection diagrams.

2.3.1. Failure Modes

Sandwich panels are susceptible to several types of failure. In this study, four failure modes were observed: compression face wrinkling (CW), compression face crushing (CC), tensile face rupture (TR), and core shear failure (CS). The failure mode for each specimen is presented in Table 2-3 and a photo of each failure mode is also shown in Figure 2-4. For the specimens with facings containing only one layer of flax fabric, the compression facing governed failure in both 1FL-C32 and 1FL-C64, whereas the tension face of 1FL-C96 controlled failure. As compression face wrinkling is dependent on the core strength (Allen 1969), the two weaker core specimens exhibit face wrinkling, whereas the strongest core result in a tensile facing failure.

Specimens 2FL-C32 and 2FL-C64 with two-layer facings show compression wrinkling and shear type failure mechanisms. As the facing strength is approximately double that of the 1FL specimens, it is not surprising that failure mode would shift to a core type failure. On the other hand, the 2FL-C96 specimen failed in tensile rupture due to the higher shear strength of the core. Looking at the failure of the 3FL-C32 and 3FL-C64 specimens with three-layer facings, it is clear that the core material-controlled failure, as in both cases the failure was in pure shear, completely independent of the facing materials. Specimen 3FL-C96 failed simultaneously by facing tensile rupture and core shear, referred to herein as a balanced condition. Generally, as the foam core density and facing thickness increase, the peak loads and the corresponding deflections also increase. Typically, the lower density foams (C32 and C64) govern the failure mode, while the FFRP facings govern the failure mode for the C96 specimens.

Table 2-3. Summary of experimental and numerical results

		Peak load (kN)			Deflection at peak load (mm)			Initial stiffness (N/mm)			Peak moment (kN-m)			Initial rigidity, EI (kN-m^2)			Failure mode	
No	Specimen	Test	Model	Err.	Test	Model	Err.	Test	Model	Err.	Test	Model	%	Test	Model	Err.	Test	Model
1	1FL-C32	1.31	1.31	0%	29.49	30.43	3%	54.00	49.58	-8%	0.36	0.37	0%	5.09	4.16	-18%	CC/CW	CW
2	2FL-C32	2.34	2.62	12%	37.39	46.04	23%	73.40	61.98	-16%	0.65	0.73	12%	10.98	8.60	-22%	CS	CW
3	3FL-C32	3.07	3.27	7%	50.09	49.85	0%	87.70	68.85	-21%	0.86	0.91	7%	13.90	13.32	-4%	CS	CS
4	1FL-C64	2.37	2.42	2%	29.77	38.56	30%	100.80	88.74	-12%	0.66	0.67	2%	6.27	4.16	-34%	CC/CW	TR
5	2FL-C64	3.26	4.83	48%	38.37	47.24	23%	114.50	132.94	16%	0.91	1.35	48%	7.17	8.60	20%	CW	TR
6	3FL-C64	4.62	7.25	57%	35.55	55.34	56%	161.10	161.53	0%	1.29	2.02	57%	15.00	13.32	-11%	CS	TR/CS
7	1FL-C96	3.07	2.42	-21%	35.21	36.79	5%	121.30	94.92	-22%	0.83	0.67	-19%	5.69	4.16	-27%	TR	TR
8	2FL-C96	6.71	4.83	-28%	45.21	43.82	-3%	206.50	146.77	-29%	1.87	1.35	-28%	11.19	8.60	-23%	TR	TR
9	3FL-C96	9.07	7.25	-20%	52.02	50.37	-3%	248.80	181.66	-27%	2.29	2.02	-12%	15.85	13.32	-16%	TR/CS	TR
	Average			6%			15%			-13%			7%			-15%		

Note: Err. = Error (Model vs. Test), CC = Compression Face Crushing, CW = Compression Face Wrinkling, CS = Core Shear, TR = Tension Face Rupture, positive strain = tension, negative strain = compression.

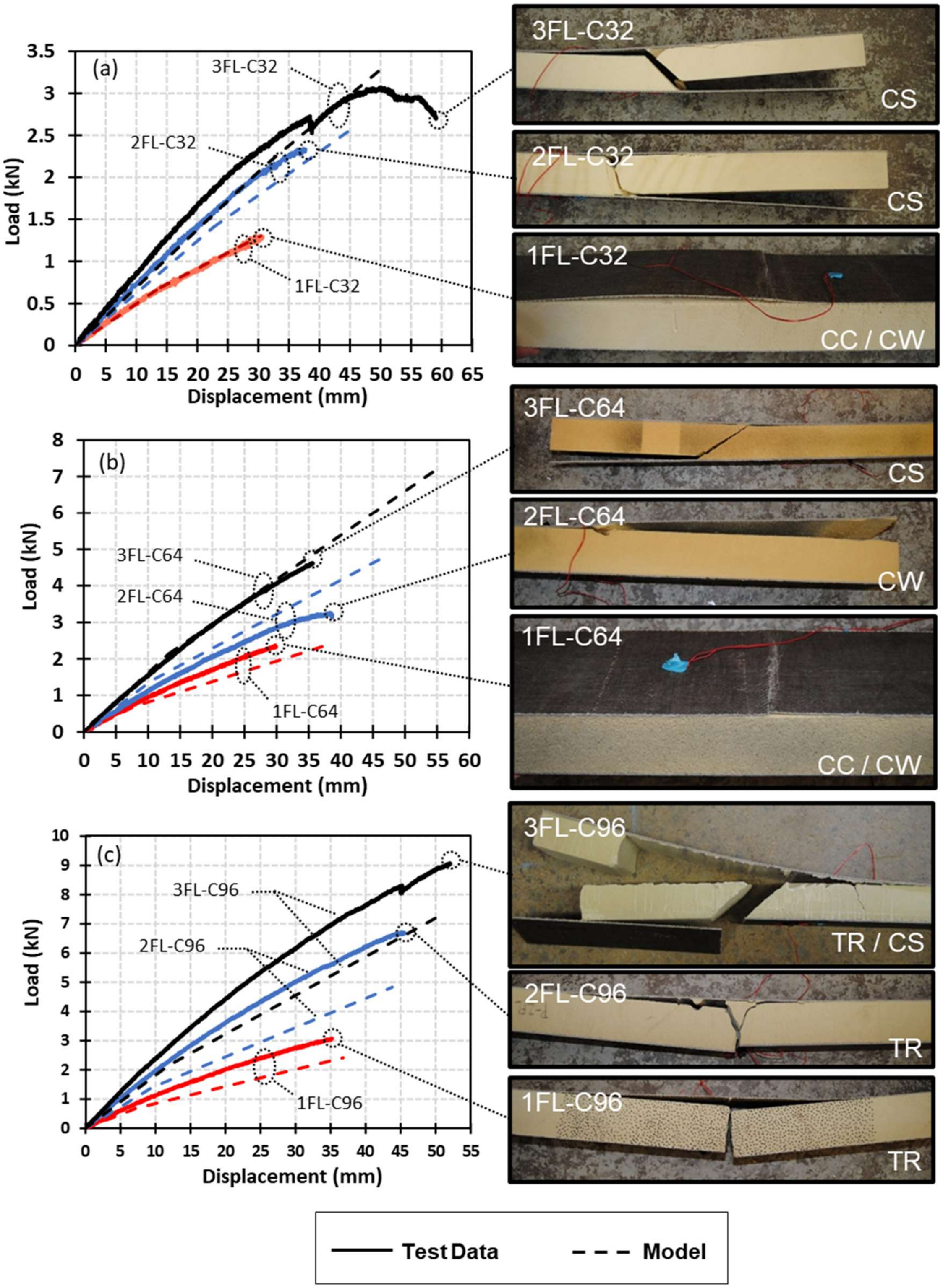

Figure 2-4: Effect of facing thickness on load-deflection diagrams for different core densities: (a) 32 kg/m^3; (b) 64 kg/m^3; and (c) 96 kg/m^3

2.3.2. Effect of Facing Thickness

Figure 2-4 shows the effect of facing thicknesses on the load-deflection diagrams for the different core densities. The deflection used to make these plots was taken as the average from the two displacement transducers. For each foam density, the peak load and initial stiffness increase with facing thickness. For example, by looking at the 32 kg/m^3 foam cores, when the facing thickness increases from one to two layers of flax (i.e. from 1FL-C32 to 2FL-C32), the peak load and initial stiffness increase by 79% and 36%, respectively. Looking at the failure modes (in the same figure), it can be seen that the failure mode progresses from facing-controlled failure (compression crushing/wrinkling) to a core-controlled failure (wrinkling/shear).

Figure 2-5 shows the effect of facing thickness on the moment-curvature and load-strain diagrams for each foam density. The measured curvature, ψ, is based on the top face strain, ϵ_{top}, the bottom face strain, ϵ_{bott}, and the specimen height, h, and was calculated using Eq. 2-1. As expected, the peak moment and initial rigidity increased with facing thickness. For example, moving from 1FL-C32 to 2FL-C32, the increases in moment and rigidity (i.e. the initial slope of the moment-curvature diagram) were 79% and 116%, respectively.

$$\Psi = \frac{\epsilon_{top} + \epsilon_{bott}}{h} \tag{2-1}$$

2.3.3. Effect of Core Density

The core density has a major impact on the failure mode of these sandwich panels. The beam stiffness is greatly affected by the core density whereas it has little effect on the initial flexural rigidity as the facings provide the bending stiffness of the member. For example, looking at the difference between 1FL-C32 and 1FL-C64, the initial stiffness is increased by 87%, whereas the initial flexural rigidity is only increased by 23%. This difference could be explained by the fact that shear deformation influences the load-deflection behaviour of the specimens but does not affect the moment-curvature behaviour. This is also accounted for in the design-oriented model as discussed in a subsequent section. The change in core density had a major impact on the ultimate moment at the peak load observed, but little effect on the rigidity as indicated before. For example, looking again at the difference between 1FL-C32 and 1FL-C64, the increase in peak moment is 81%, whereas the increase in rigidity is only 23%.

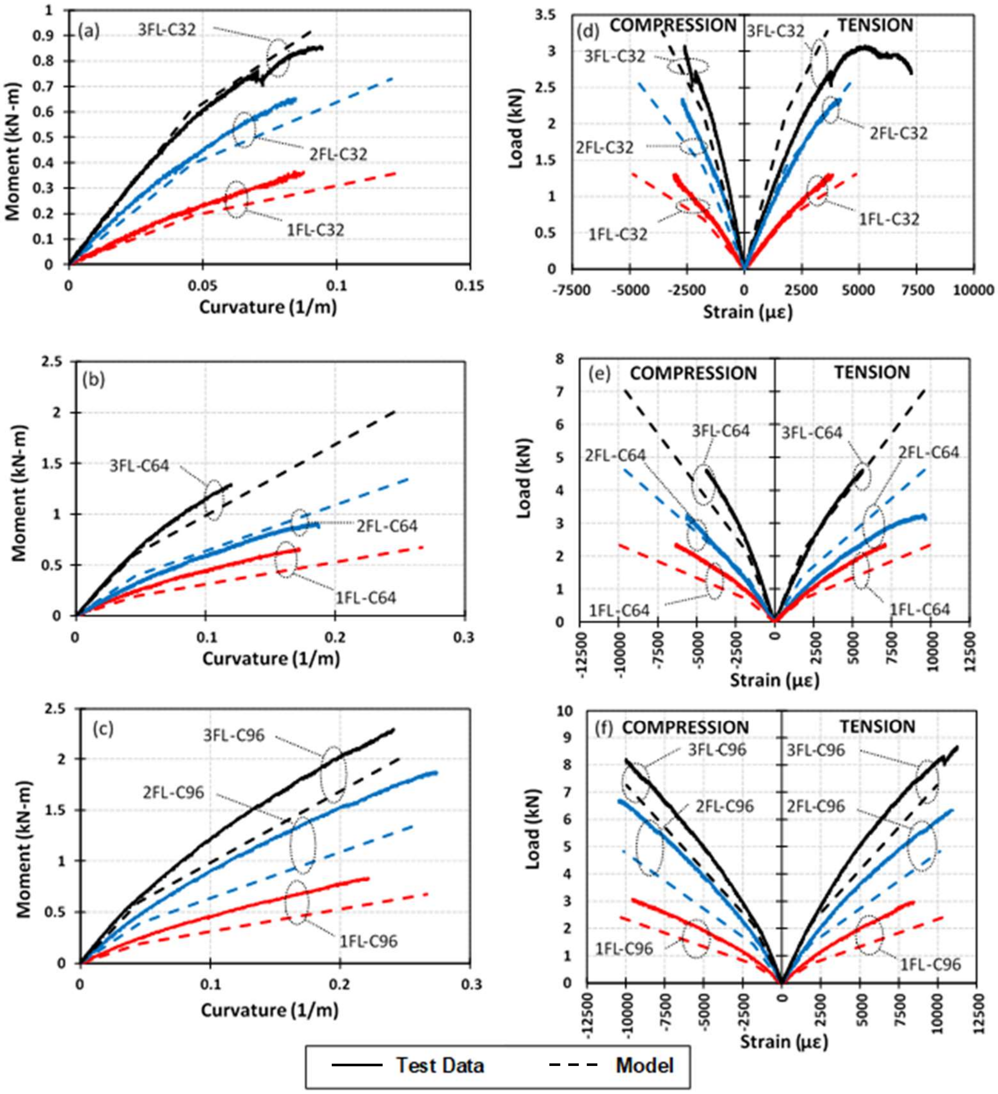

Figure 2-5. Effect of facing thickness on moment-curvature diagrams for (a) C32; (b) C64; and (c) C96 and load-strain diagrams for (d) C32; (e) C64; and (f) C96

2.4. ANALYTICAL STUDY

Simplified models were developed for the calculation of the moment-curvature and load-deflection behaviour of sandwich panels constructed of foam cores and FFRP facings. The models were verified with the data presented in this study as well as data presented by Mak et al. (2015) and were then expanded to develop a simple design procedure which could be used by designers.

2.4.1. Moment-Curvature Behaviour

As noted by numerous researchers, FFRPs display a bilinear stress-strain behaviour (Bensadoun et al., 2016; Mak et al., 2015; Sadeghian et al., 2016; Hristozov et al., 2016). This is also evident when examining the stress-strain curves shown in Figure 2-1. As a result, the moment-curvature behaviour of the sandwich panels could also be approximated as bilinear. Figure 2-6a shows the cross-section of a panel and Figure 2-6b shows the bilinear models used in developing the analytical model.

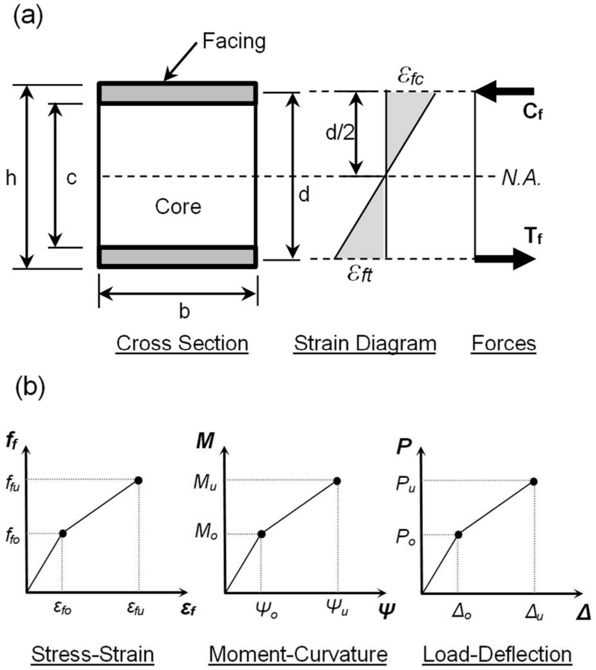

Figure 2-6. Simplified model: (a) cross-sectional analysis of sandwich panel with FFRP facings; and (b) bilinear stress-strain, moment-curvature, and load-deflection models

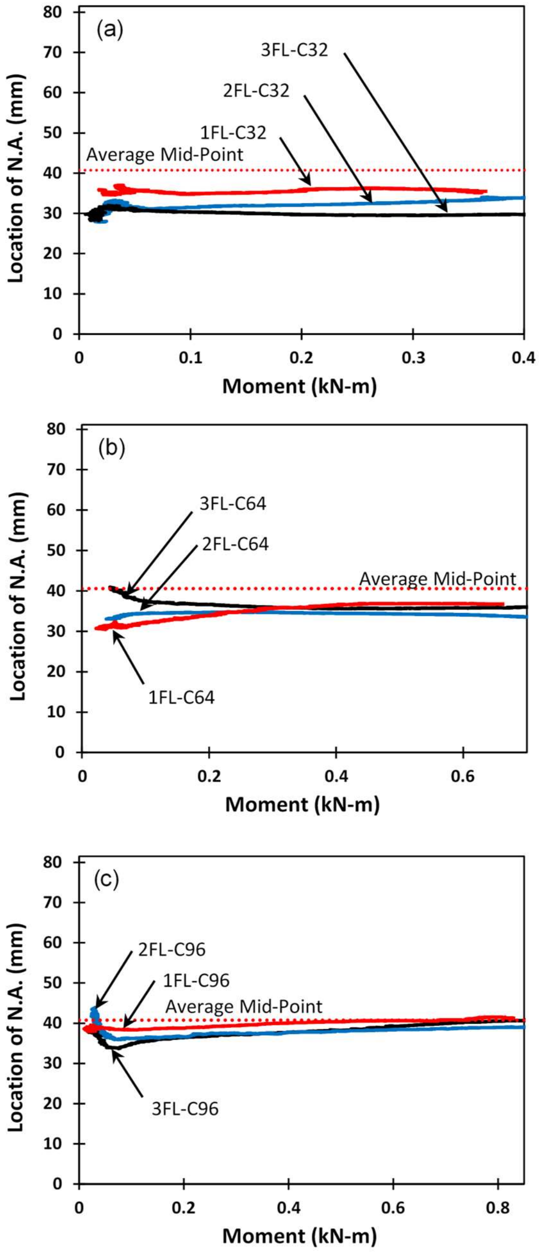

Figure 2-7. Location of neutral axis vs. moment: (a) C32; (b) C64; and (c) C96

2.4.1.1. Assumptions

The following assumptions were made to develop the simplified moment-curvature model:

a) The moment resistance provided by the foam is negligible when compared to the resistance of the FFRP facings. This assumption is based on the extremely small values of Young's modulus of the core (shown in Table 2-2), compared to the facings.

b) The secondary tensile modulus is approximately two thirds of the initial tensile modulus (Wroblewski et al., 2016) and the secondary compression modulus is approximately two fifths of the initial compression modulus. These assumptions are established based on the measured stress-strain curves in Figure 2-1. Conservatively, the modulus used in the failure mode equations, presented later, is based on these secondary moduli, as shown in Equation 2-3.

c) The neutral axis is located at the center of the cross section. Figure 2-7 shows a diagram of the neutral axis (established from top and bottom longitudinal strain measurements) versus moment, which justifies this assumption. This means that the moduli used in the moment-curvature model can be approximated as the average of the compression and tensile moduli, which were determined through testing. Therefore, the moduli are taken as shown in Equations 2-2 and 2-3, where E_{ft} and E_{fc} are the primary tensile modulus and the primary compression modulus, respectively.

$$E_{f_1} = \frac{1}{2}(E_{f_t} + E_{f_c}) \tag{2-2}$$

$$E_{f_2} = \frac{1}{2}(\frac{2}{3}E_{f_t} + \frac{2}{5}E_{f_c}) = \frac{1}{3}E_{f_t} + \frac{1}{5}E_{f_c} \tag{2-3}$$

2.4.1.2. Analysis Procedure

The bilinear model requires the calculation of the coordinates of two points in terms of moment and curvature: the point of transition (POT) at the end of the first slope (M_o, Ψ_o), and a 'hypothetical' ultimate point at the end of the second slope (M_u, Ψ_u). The reason for referring to the ultimate point as 'hypothetical' is because it is based on the ultimate failure strain of the facing which may never be reached (for example due to core shear or wrinkling, which will be considered later). The calculations are based on the strain developed in the facings. The POT strain, ϵ_{fo}, is a material property that can be determined from the stress-strain plots of the facing material. As shown in Figure 2-6(b), the ultimate strain of the facing material, ϵ_{fu}, is based on the ultimate tensile strength of the facing material, f_{fu}, the stress at the material POT, f_{fo}, and the secondary modulus of the material, E_{f2} and is determined by Equation 2-4.

$$\epsilon_{f_u} = \epsilon_{f_o} + \frac{f_{fu} - f_{fo}}{E_{f2}} \tag{2-4}$$

The calculation of both the POT moment and the 'hypothetical' ultimate moment are based on the geometrical and material properties of the specimens, as given by:

$$M_0 = tbdE_{f_1}\epsilon_{f_0} \tag{2-5}$$

$$M_u = tbd[E_{f_1}\epsilon_{f_0} + E_{f_2}(\epsilon_{f_u} - \epsilon_{f_0})] \tag{2-6}$$

where t is the facing thickness, b is the specimen width, and d is the distance between the centroids of the top and bottom facings. The curvatures at the POT and ultimate points are calculated using Equations 2-7 and 2-8.

$$\Psi_0 = \frac{2}{d}\epsilon_{f_0} \tag{2-7}$$

$$\Psi_u = \frac{2}{d}\epsilon_{f_u} \tag{2-8}$$

As shown in Figure 2-6b, the bilinear response established up to the 'hypothetical' ultimate moment M_u may be terminated at a lower load level based on the various failure criteria. The model prediction for each test specimen is shown in Figure 2-5, after implementing the proper failure criteria predicted for each case (discussed later). These moment-curvature diagrams will be used to determine the load-deflection diagrams required to complete the analysis.

2.4.2. Load-Deflection Behaviour

The load-deflection model was developed by superimposing both bending and shear deformations of three-point loading as shown in Figure 2-8a. The bending deformation (Δ_B) was derived by integration of curvature over the length of the beam using the moment-area method (Δ_B=$\Sigma A_i X_i$), where A_i is the area of each segment under curvature diagram over the half length of the beam and X_i is the distance from the centroid of each segment to the end of the beam as shown in Figure 2-8a. The major assumption in the load-deflection model is a bilinear behaviour that follows the bilinear behaviour of the moment-curvature diagrams. The primary and secondary slopes are based on the loads corresponding to the POT moment, M_0, and the ultimate moment, M_u, and are determined by Equations 2-9 and 2-10.

$$P_0 = \frac{4}{L} M_0 \tag{2-9}$$

$$P_u = \frac{4}{L} M_u \tag{2-10}$$

The equations for the deflections at the POT and ultimate load were developed based on curvatures as shown in Figure 2-8. Then, the equations were modified to include the contribution of core shear deflection ($\Delta_V = VL_a/G_cA_v$), where V is the shear force over the shear span L_a, G_c is the core shear modulus, and A_v is the shear area. The equations for the POT and ultimate deflections are given in Equations 2-11 and 2-12, respectively.

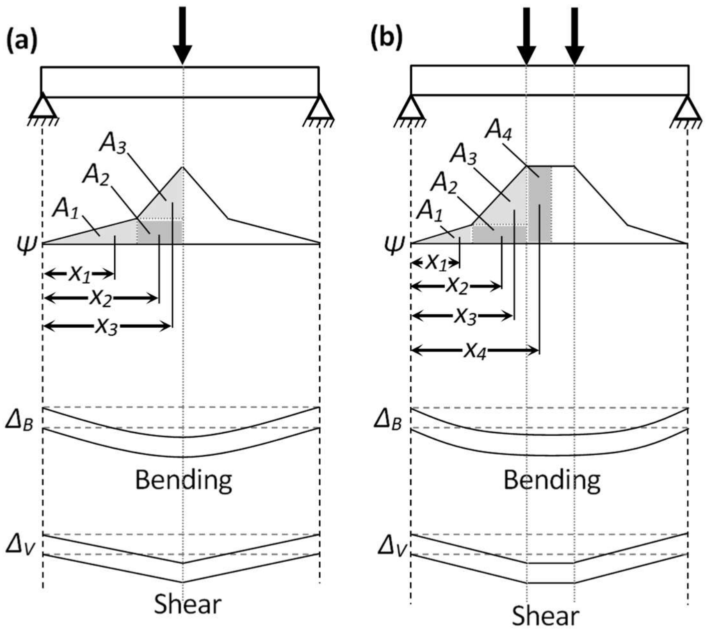

Figure 2-8: Determinations of deflection through superposition of bending and shear deflections: (a) 3-point bending; and (b) 4-point bending

$$\Delta_0 = \frac{L^2}{6d}\epsilon_{f_o} + \frac{P_0 L}{4G_c(\frac{bd^2}{c})} \tag{2-11}$$

$$\Delta_U = \frac{L^2}{12d}\left[(1+\lambda)\epsilon_{f_0} + (2-\lambda-\lambda^2)\epsilon_{f_u}\right] + \frac{P_U L}{4G_c(\frac{bd^2}{c})} \tag{2-12}$$

$$\lambda = \frac{1}{2 + 2\frac{E_{f_2}}{E_{f_1}}\left(\frac{\epsilon_{f_u}}{\epsilon_{f_0}} - 1\right)} \tag{2-13}$$

After determining the ultimate deflection due to shear and moment, the curve is truncated by implementing the failure criteria as presented in the next section. It should be highlighted that Equations 2-11 and 2-12 were derived for three-point bending loading. The equations can be easily modified for the case of four-point bending as presented in Figure 2-8b and other loading conditions.

2.4.3. Ultimate Conditions Prediction

The moment-curvature and load-deflection models presented are based on the ultimate strength of the facings. Therefore, the models as they are would be adequate for predicting the ultimate load capacity for the cases of compression face crushing or tensile face rupture failure modes. However, as previously discussed, sandwich panels are susceptible to several failure modes, and as such, additional failure criteria are required.

2.4.3.1. Failure Criteria

The range possible failure modes are: (i) compression face wrinkling, (ii) tension face rupture, (iii) core shear failure and (iv) compression face crushing. The failure loads for failure modes (i), (ii) and (iii) can be determined by the equations developed by Triantafillou and Gibson (1987), which are presented as Equations 2-14, 2-15 and 2-16, respectively:

$$P_{CW} = 0.57\, C_1 C_3^{2/3} E_f^{1/3} E_s^{2/3}\, (\rho_c/\rho_s)^{2A/3}\, bc\frac{t}{L} \tag{2-14}$$

$$P_{TR} = C_1 \sigma_{ft} bc \frac{t}{L} \tag{2-15}$$

$$P_{CS} = \frac{C_4 (\rho_c/\rho_s)^B \sigma_{ys} bc}{\sqrt{\left(\frac{C_3 (\rho_c/\rho_s)^A E_s}{2C_1 \frac{t}{L} E_f}\right)^2 + \left(\frac{1}{C_2}\right)^2}} \tag{2-16}$$

where P_{CW}, P_{TR}, and P_{CS} are the failure loads for compression face wrinkling, tensile face rupture, and core shear failure, respectively. C_1 and C_2 are constants depending on the loading arrangement; for three-point bending they are taken as 4 and 2, respectively. A, B, C_3, and C_4 are constants depending on the relative core density, the relative core modulus, and the relative core strength (Triantafillou and Gibson, 1987). These values are determined by relating the density, modulus and strength of each core to the values of the material from which the core was foamed. That is, the relative core density, relative core modulus and relative core strength are represented as (ρ_c/ρ_s), (E_c/E_s) and (τ_{cu}/τ_s), respectively. A, B, C_3, and C_4 were found to be 1.52, 1.24, 0.75 and 0.10, respectively by plotting (ρ_c/ρ_s) *vs.* (E_c/E_s) and (ρ_c/ρ_s) *vs.*(τ_{cu}/τ_s) and using Equations 2-17 and 2-18.

$$\left(\frac{E_c}{E_s}\right) = C_3 \left(\frac{\rho_c}{\rho_s}\right)^A \tag{2-17}$$

$$\left(\frac{\tau_{cu}}{\tau_s}\right) = C_4 \left(\frac{\rho_c}{\rho_s}\right)^B \tag{2-18}$$

As was proposed by Triantafillou and Gibson (1987), the failure mode map developed in this study is based on the interface between these three failure modes and therefore does not account for compression crushing (iv). Since the ultimate compressive strength of FFRP skin is double that of its tensile strength (Figure 2-1), facing crushing without (iv) wrinkling will not govern. In this study, failure models developed by Triantafillou and Gibson (1987) will be used.

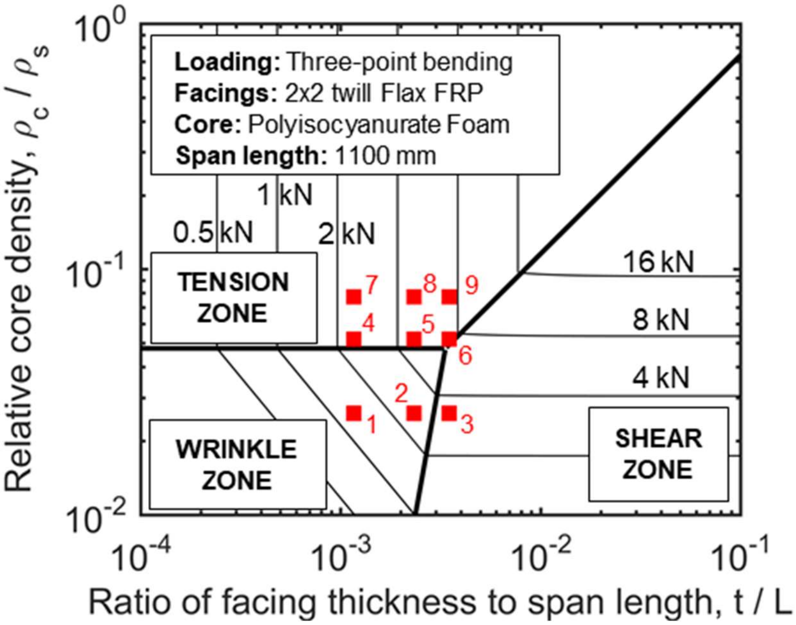

Figure 2-9: Failure mode map of FFRP-foam sandwich panel

2.4.3.2. *Failure Mode Maps*

To predict the failure mode of the sandwich panels, a failure mode map was developed in the Matlab programming language based on the equations presented by Triantafillou and Gibson (1987) and is shown in Figure 2-9 for the loading case discussed in this paper. The failure mode maps will be beneficial for the design of these sandwich panels as they can be used to ensure a desired failure mode or provide the minimum design parameters for a design load. Also shown on this map are specimens 1 to 9 based on their geometric and relative density properties represented by the horizontal and vertical axes. It can be seen that the specimens land in various regions representing the three predicted primary failure modes. It can also be seen that specimen 6 lies on the border line between two regions.

2.4.4. Verification

Table 2-3 shows the properties of the test specimens and the results of the model. Figure 2-4 and Figure 2-5 show the verification of the load-deflection and moment-curvature models. These figures show the comparison of the models for different facing thicknesses for each foam type. In specimen 2FL-C64, the ultimate moment and peak load were both overestimated by 48%. This error is introduced through the failure equations used to predict these ultimate capacities. For the same specimen, the new models predicted the initial stiffness and initial rigidity to within 16% and 20%, respectively. This was the only specimen for which these values were overestimated, for all other specimens, the models predicted under the actual values. This could be due to the fact, that due to an error in the test set-up for the 2FL-C64 specimen, both supports were hinge type supports. There is the potential that this caused an axial compression load in the specimen which could have caused premature failure. The average differences of the initial stiffness and rigidity between the model and the test results were -13% and -15%, respectively.

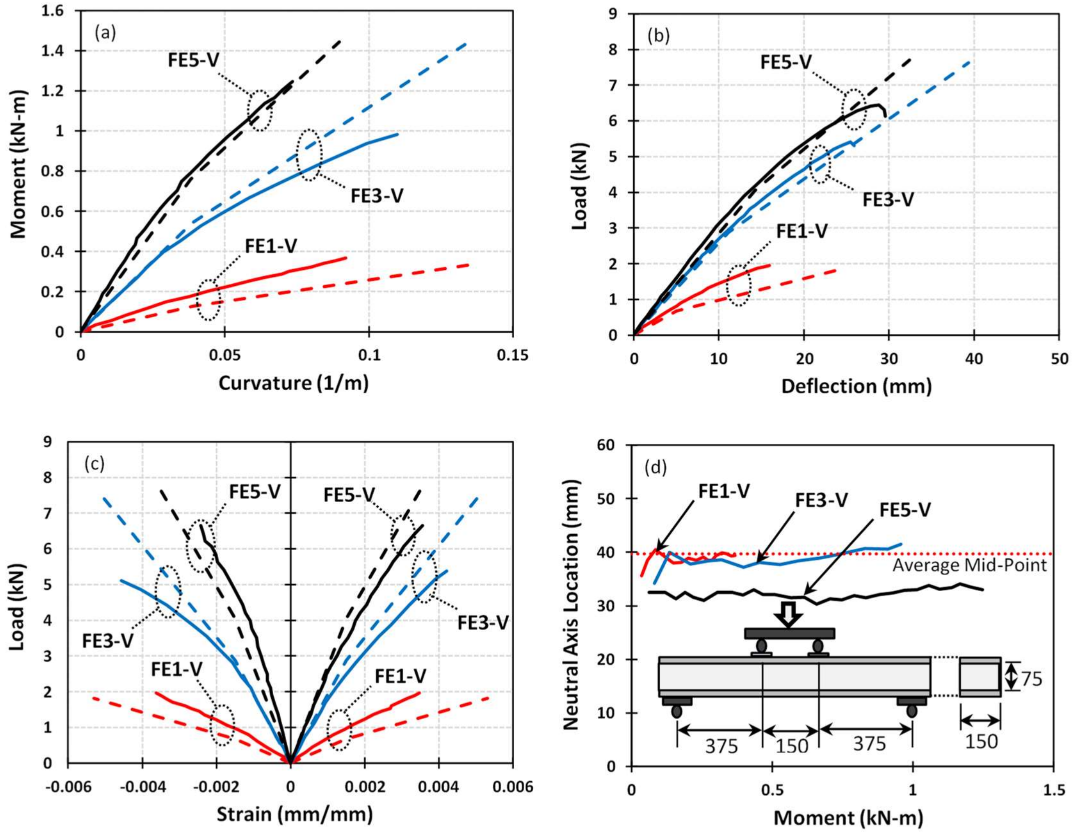

Figure 2-10. Model verification using test data from Mak et al. (2015):(a) moment-curvature; (b) load-deflection; (c) load-strain; and (d) neutral axis location and test set-up (dimensions in mm).

The model has also been verified using data of specimens tested by Mak et al. (2015) as shown in Figure 2-10. In the study by Mak et al. (2015) a number of different specimens were tested. The FE-V type specimens were chosen for verification as they were fabricated using unidirectional FFRP faces which were made by using vacuum bags which differs from the wet lay-up method used in the current study. Because the study by Mak et al. (2015) was four-point bending, the model had to be adjusted to accommodate this difference. This adjustment is shown alongside the original model development in Figure 2-8. The results imply that the proposed bilinear models are applicable for predicting behaviour of sandwich beams with foam cores and FRP facing made of both unidirectional and bidirectional flax fabrics.

2.4.5. Design Procedure and Example

Based on the failure mode maps, the load-deflection and moment-curvature models, a simple design procedure was developed for sandwich panels with FFRP facings and soft foam cores. The design procedure is shown in the form of a flow chart in Figure 2-11. Given a factored design load, the preliminary design variables (i.e. the FFRP facing thickness and core density) can be obtained using the failure mode map. This can be used to dictate the failure mode or to determine the minimum allowance for the design variables. With the known facing thickness and core density, the designer can develop the load-deflection and moment-curvature plots, as well as the exact failure load as the minimum calculated from Equations 2-14, 2-15 and 2-16. The deflection limit criteria for serviceability can then be checked, and if necessary, the design can be updated (for example by increasing core thickness or density or facing thickness) to satisfy the required deflection limits. It should be noted that as this design procedure has been developed with limited test data, more research is required in this area. This research should include tests on panels with different core densities, different face thicknesses, different polymer types and different fabric configurations. As the proposed models used in this design procedure have already been shown as applicable for use with data from an independent study (Mak et al. 2015), this procedure warrants further investigation.

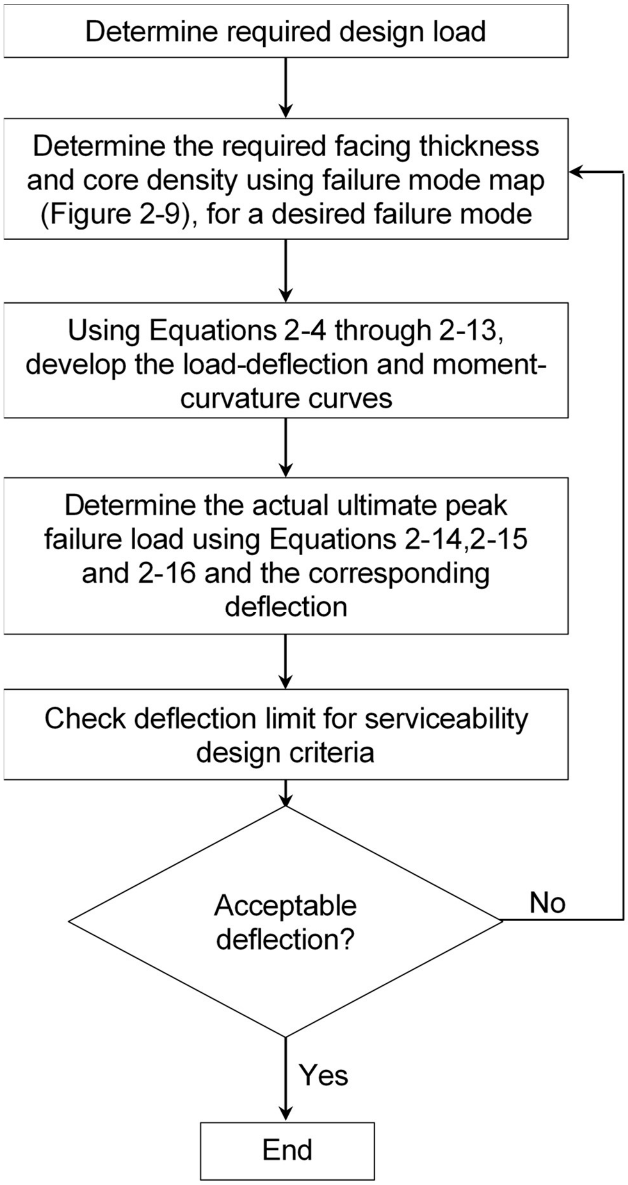

Figure 2-11. Flow chart for the design of FFRP-foam sandwich beams

As an example of how to use the proposed design procedure, let us assume that a sandwich panel constructed of FFRP facings and foam core needs to be designed for a span length of 1100 mm and is required to support a factored concentrated load of 6 kN applied at its mid-span. Referring to Figure 2-9, it can be seen that to resist 6 kN, the minimum values of t/L of 0.003 and ρ_c/ρ_s of 0.05 would be required. Knowing the span length of 1100 mm and the density and elastic modulus of the unfoamed core material of 1200 kg/m^3 and 1600 MPa, respectively, we can determine that the minimum required facing thickness and foamed core density would be 3.3 mm and 60 kg/m^3, respectively. This point happens to be in the Tension failure region of the failure mode map, however, each failure load (Equations 2-14 to 2-16) should be calculated and the minimum value should be considered to govern. Taking E_f as E_{f2}, we can determine the failure loads P_{cw}=6.54 kN, P_{TR}=6.23 kN, and P_{CS}=7.10 kN using Equations 2-14, 2-15 and 2-16, respectively. As expected, the tensile rupture failure load, P_{TR}, governs, which agrees with the failure map observation. To ensure that this failure load is reached, a relative core density equal to or exceeding 0.05 (therefore, for a material with an unfoamed density of 1200 kg/m^3, a foam density of 60 kg/m^3) must be selected along with a facing thickness equal to or exceeding 3.3 mm. Therefore, three layers of FFRP and the C64 type foam are required.

At this point, the load-deflection and moment-curvature model would need to be developed using the procedure outlined earlier. For this example, the models are shown in Figure 2-4 and Figure 2-5. Assuming that the load was factored using a factor of 1.4, the service load in this problem would be approximately 4.3 kN. Looking at the load-deflection model, a 3FL-C64 sandwich panel has a deflection of approximately 32 mm at a load 4.3 kN. Based on the simplicity of this example and assuming that the failure mode maps for these types of sandwich panels were readily available to practicing engineers, this design procedure could be economically feasible for use in industry. Alternatively, designers could develop the failure maps using Equations 4-14, 4-15 and 4-16, relatively easily.

2.5. SUMMARY

In this chapter, sandwich beams made of bio-based fibre-reinforced polymer (FRP) composite facings and foam cores were studied. The FRP facings consisted of a plant-based bidirectional flax fibre fabric (400 g/m^2) and a bio-based epoxy resin (30% bio content) and the foam cores were made of 75 mm thick closed cell polyisocyanurate. A total of nine sandwich beam specimens (1200 mm long and 150 mm wide) were prepared and tested under three-point bending. The parameters of the study were core density (32, 64, and 96 kg/m^3) and facing thickness (one, two, and three layers of flax fabric). Three failure mechanisms were observed during testing, including: top face wrinkling/crushing, core shear, tensile rupture of bottom face. It was shown that the foam with the density of 96 kg/m^3 is stiff and strong enough to achieve the tensile rupture of the flax FRP (FFRP) facing. Also, a nonlinear behaviour was observed for the sandwich beams. A bilinear stress-strain model for FFRP facing was proposed and, based on that, closed-form moment-curvature and load-deflection equations of the sandwich beams were derived for design applications. The proposed design-oriented model was verified against the test data of this study and an independent study capturing the stiffness, strength, and nonlinearity of the test specimens.

CHAPTER 3: BEHAVIOUR OF FFRP-FOAM SANDWICH BEAMS UNDER LOW VELOCITY IMPACT LOADS [2]

3.1. INTRODUCTION

As the need for environmental consciousness increases, it is necessary to have sustainable building material options to replace or supplement conventional building materials. One method of making infrastructure more sustainable is the use of natural materials, such as plant fibres in fibre-reinforced polymer (FRP) composites. Numerous types of plant fibres have been researched for this purpose and one notable fibre is flax. Flax is readily available and has been shown to exhibit relatively high strength and stiffness when compared to other types of natural fibres (Ramesh et al. 2017).

A structural element for which natural FRPs can be used is the sandwich panel. Sandwich panels are often employed when a light weight and/or insulated structure is required. These panels are made up of strong thin faces separated by a weaker, lightweight core which increases the moment of inertia and improves the flexural rigidity of the structure (Allen 1969). Sandwich panel faces are often made of synthetic FRPs, such as glass or carbon FRPs, due to their relatively high strength and stiffness. Though weaker than traditional synthetic FRPs, flax FRPs (FFRPs) have been shown to have a lower embodied energy (Cicala et al. 2010) and are therefore considered to be a more environmentally friendly. As the weak core material often dictates failure in sandwich panels, high performance FRPs are typically underutilized and FFRPs can be efficiently used as a sustainable replacement for synthetic FRPs for these structures (Fam et al. 2016; Mak et al. 2015; Sadeghian et al. 2018). Sandwich panels made with foam cores and FFRP faces have recently been studied under axial (CoDyre et al. 2018) and flexural loading (Betts et al. 2018a; Mak et al. 2015).

Sandwich panels are regularly used as a part of building envelopes. As these structures can be subjected to impacts from flying debris during high wind events, it

---

[2] **This chapter is published in the *Journal of Sandwich Structures and Materials*:**

Betts D, Sadeghian P, Fam A. Experiments and Nonlinear Analysis of the Impact Behaviour of Sandwich Panels Constructed with Flax Fiber-Reinforced Polymer Faces and Foam Cores. *Journal of Sandwich Structures and Materials*. 2020; 0(0):1-25.

is important to understand their behaviour under low velocity impact loading. The low-velocity impact behaviour of composite plates (Tuo et al. 2019; Xiao et al. 2019; Zhang et al. 2019) and sandwich panels with synthetic faces (Abrate 1997; Akil Hazizan and Cantwell 2002; Anderson and Madenci 2000; Atas and Potoglu 2016; Plagianakos et al. 2016; Schubel et al. 2005; Torre and Kenny 2000) has been investigated. Abrate (1998) and others (Christoforou and Yigit 2009; Icardi and Ferrero 2009; Malekzadeh et al. 2006) have presented a number of techniques for modelling synthetic FRP sandwich structures. Failure mode maps have been developed to predict the failure of these panels under dynamic loading (Andrews and Moussa 2009; Zhu and Chai 2013). A sophisticated method of optimising properties of synthetic FRP sandwich panels for impact loading based on a genetic algorithm has also been developed (Kalantari et al. 2010). Additionally, numerous studies have been completed on the modelling of sandwich structures under impact loads using the finite element method (Besant et al. 2001; De Cicco and Taheri 2018a; b; Feng and Aymerich 2013; Meo et al. 2005; Nguyen et al. 2005; Zhang et al. 2016; Zhou et al. 2012). Some studies have also been performed on natural fibre sandwich panels under impact (Boria et al. 2018; Ude et al. 2013), however, there is still a gap in the field concerning the impact behaviour of sandwich panels with natural fibre faces such as FFRPs.

The existing modelling techniques for impact on composite sandwich panels typically assume that the face acts in a linear behaviour (Akil Hazizan and Cantwell 2002) as is typical for panels with synthetic FRP faces. However, numerous authors have shown that FFRPs exhibit a nonlinear stress-strain response under tensile (Betts et al. 2018a; Christian and Billington 2011; Hristozov et al. 2016; Mak et al. 2015; Mathura and Cree 2016; Yan et al. 2016) and compressive loads (Betts et al. 2018a). Additionally, it is known that foam materials behave in a nonlinear manner under shear loading (Fam and Sharaf 2010). Therefore, to more accurately model the behaviour of sandwich panels with FFRP faces, the analysis must account for the nonlinear behaviour of the face and foam materials. There are currently no models available for sandwich panels with FFRP faces with nonlinear mechanical behaviour under impact loading in the literature.

This paper fills gaps in the field of study by providing test data on sustainable sandwich panels constructed with bio-based materials as well as presenting an accurate analytical procedure for predicting their behaviour under impact loads. In this study, the effect of low velocity impact of a large mass on one-way sandwich panels is investigated. The sandwich panels were constructed using foam cores and natural FFRP faces and were tested under a drop weight impact multiple times with increasing energy until ultimate failure. An analytical model has been developed to predict their behaviour under these loading conditions. The model is based on the energy balance method and includes the effect of the nonlinear mechanical behaviour of the FFRP faces and the foam core.

3.2. EXPERIMENTAL PROGRAM

3.2.1. Test Matrix

Nine sandwich panels were fabricated with foam cores and FFRP faces for drop weight impact tests. The main parameters of the study were the effect of facing thickness and core density on the impact behaviour of these panels. The test matrix is presented in Table 3-1. The naming convention is as follows: XFL-CYY, where X is the number of flax layers (1, 2 or 3) and YY is the nominal core density in kg/m^3 (32, 64 or 96). For example, a specimen with faces comprised of a one-ply FFRP and a foam core density of 96 kg/m^3 is referred to as 1FL-C96. The one, two and three layers of FFRP correspond to nominal face thicknesses of 1.5, 2.5 and 3.5 mm.

Table 3-1. Test matrix for ramped impact tests of one-way sandwich beams

No.	Specimen I.D.	Number of FFRP layers in each facing	Nominal core density (kg/m^3)	Number of Impacts
1	1FL-C32	1	32	2
2	2FL-C32	2	32	4
3	3FL-C32	3	32	7
4	1FL-C64	1	64	4
5	2FL-C64	2	64	5 *
6	3FL-C64	3	64	17
7	1FL-C96	1	96	10
8	2FL-C96	2	96	18
9	3FL-C96	3	96	25

* *This specimen was tested at drop height increments of 300 mm*

3.2.2. Materials

For the specimen cores, three different closed cell polyisocyanurate foams were used. The nominal core densities were 32 kg/m^3, 64 kg/m^3 and 96 kg/m^3 and were measured to be 31.2 kg/m^3, 62.4 kg/m^3 and 91.7 kg/m^3, respectively, by Codyre et al. (CoDyre et al. 2018). The FFRP faces were fabricated with a balanced bidirectional flax fabric with a measured areal density of 410 g/m^2 and epoxy with a bio-content of 30% after mixing. The properties of these FFRPs were measured in a previous study by testing five identical two-ply bidirectional FFRP tensile tension coupons (average thickness of 3.0 mm) and five identical eight-ply bidirectional FFRP compression coupons (average thickness of 24 mm) (Betts et al. 2018a). The measured tensile strength, the initial Young's modulus and the ultimate strain were 45.4 ± 1.8 MPa, 7.51 ± 0.69 GPa and 0.0083 ± 0.0009 mm/mm, respectively. The measured initial compressive Young's modulus was 6.73 ± 1.59 GPa and the compressive strength and corresponding strain were 86.4 ± 2.2 MPa and 0.0327 ± 0.0010 mm/mm, respectively.

3.2.3. Specimen Fabrication

The specimen fabrication process is shown in Figure 3-1. The foams were supplied in 1200 mm x 2400 mm sections and were cut down to a size of 1200 mm x 600 mm for fabrication. To fabricate the specimens, the top face of the foam was first cleaned of all debris and then coated with epoxy. A layer of dry fabric was placed on the face (with its warp direction parallel to the longitudinal direction of the specimens) and coated with epoxy. This procedure was repeated as required for each facing thickness. After placing the last layer of fabric and epoxy, a layer of parchment paper was applied to the face and all excess resin and air were removed using an aluminum roller. The specimen was then covered with a weighted flat board and allowed to cure for seven days, after which the other face was completed following the same procedure. Once both faces were completed, four identical 150 mm wide specimens were cut from the 600 mm wide section using a band saw.

Figure 3-1. Specimen fabrication: (a) mixing epoxy and section of cleaned foam; (b) application of epoxy; (c) specimen curing with weighted board; and (d) finished specimens

3.2.4. Test Setup and Instrumentation

The drop-weight test set-up is presented in Figure 3-2. Strain gauges were installed at the centre of the top and bottom faces at mid-span. A fast-action string potentiometer was connected to the bottom face of the specimen and an accelerometer was attached to the drop weight. The data was sampled at a rate of 25 kHz. Additionally, a video of each test was recorded by a camera with a frame rate of 500 fps. The bottom of the drop weight impact was fitted with a 9.5 mm thick section of a steel hollow structural section (HSS) impact surface 150 mm wide as shown in Figure 3-2. This impact surface was used to limit the potential for local indentation. To avoid damaging the strain gauge on the top face, a 25 mm diameter hole was cut into the center of the HSS impact surface. The mass of the drop weight was 10.413 kg. Each specimen was tested multiple times until failure starting at a drop height of 100 mm and increased by increments of 100 mm. This test procedure meant that each specimen was tested a different number of times depending on the maximum drop height that was resisted. Note that specimen 2FL-C64 was tested first and started at a height of 300 mm and incremented likewise. After testing this specimen, it was decided that this increment did not yield enough data and therefore the starting height and increment were decreased to the 100 mm used for the remaining specimens. For specimen 3FL-C96, the maximum possible drop height of the test frame (2100 mm) was achieved before ultimate failure. Therefore, the drop weight mass was increased by 6.015 kg and the tests were restarted at a height of 1395 mm, such that the energy was equivalent to the original mass dropped from a height of 2200 mm. It is recognized that, while the energy level increment was maintained, the impact velocity increment was affected by this procedure. However, as the maximum possible drop height was reached, this was the only available option to maintain the energy level increments for testing. The height increment was also reduced to 63 mm such that the increase in impact energy remained constant between tests.

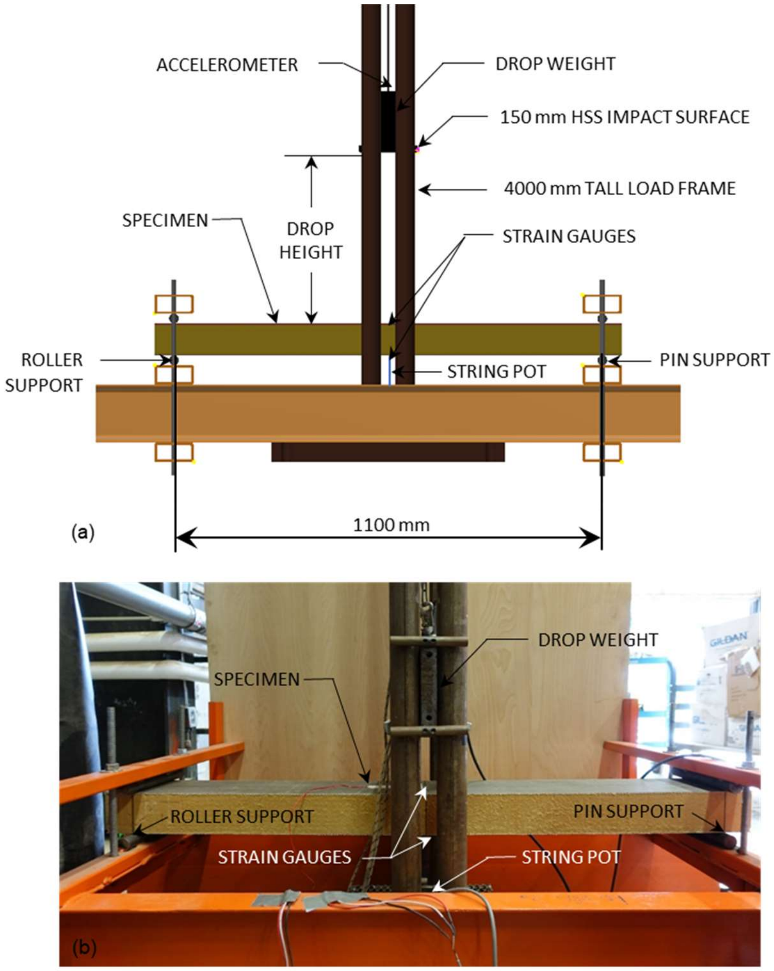

Figure 3-2. Test set-up (a) schematic and (b) photo

3.3. EXPERIMENTAL RESULTS AND DISCUSSIONS

The main results obtained through these tests were the ultimate impact resistance (*E*), maximum deflection (*Δ*), and the maximum strain in each face (ϵ_t and ϵ_c). Note that for this discussion the ultimate energy resistance is the maximum impact energy at which specimen did not experience failure and the energy failure is the impact energy at which the specimen experienced ultimate failure. Additionally, the specimen stiffness (*K*) and damping ratio (ξ) were calculated based on the deflection measurements. The data in this study was processed using both Matlab and the scientific Python package, Anaconda. Due to electrical noise in the deflection readings, the data was filtered using a moving average filter. Though this filter affected the amplitude of the measurements, upon inspection it was determined that the data remained accurate to within 0.1 mm (< 0.5%) after filtering. The strain gauge data was unaffected by this noise.

3.3.1. Energy Resistance and Failure Modes

Figure 3-3 presents a bar chart showing the maximum energy resisted by each panel type and compares the energies to those resisted by the panels tested under quasi-static load by Betts et al. (2018a). There was a large variation in energy capacity between the different panels; the strongest panel (3FL-C96) resisted a maximum impact energy of 245 J before ultimate failure whereas the weakest panel (1FL-C32) resisted only 10.2 J. The figure shows that the capacity increased with core density. For instance, specimen 3FL-C32 resisted a maximum of energy of 91.9 J whereas specimen 3FL-C64 resisted a maximum energy of 173.7 J, an increase of 89%. Again, going from specimen 3FL-C64 to specimen 3FL-C96 there was an increase in capacity of 41%. Panel capacity also increased with facing thickness. Specimen 1FL-C96 resisted a maximum energy of 61.3 J whereas, increasing the face thickness by one layer of flax fabric, 2FL-C96 resisted an energy of 163.4 J, an increase of 167%. Similarly, increasing the facing thickness by one more layer of flax fabric yielded another increase in capacity of 41%.

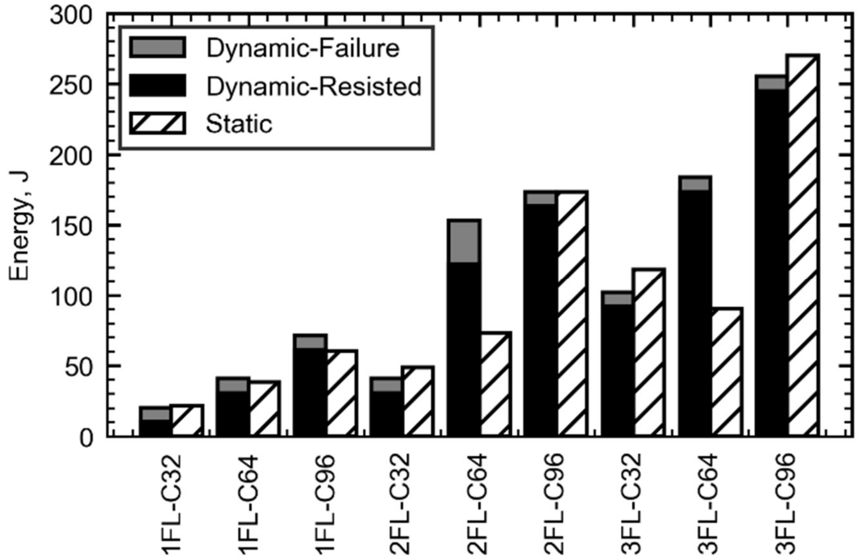

Figure 3-3. Comparison of energy resistance between dynamic and static tests

The dynamic and static energies are similar for most specimens, however, specimens 2FL-C64 and 3FL-C64 exhibited less energy resistance under static loading. In the study by Betts et al. (2018a) it was noted that specimen 2FL-C64 was tested with two pinned supports which may have reduced its ultimate capacity. Also, upon examination of the test results of their study, the deflection of specimen 3FL-C64 was overpredicted by the model by 56% whereas the next highest overprediction was only 30%. This indicates that the static specimen potentially experienced premature failure and would therefore account for the difference between the static and dynamic capacities.

Figure 3-4 presents a comparison of the failure modes exhibited during the static and dynamic tests. It shows that all the specimens save one failed in the same manner in the static and dynamic tests. The exception is specimen 2FL-C64. However, as mentioned previously, this specimen was tested at drop height increments of 300 mm. Therefore, there is the potential that the impact causing failure was well above the actual ultimate capacity of the specimen and caused it to fail in a different manner than it would have had it been impacted by an energy closer to its actual capacity. The fact that the energy levels and failure modes are comparable between the static and dynamic tests indicates that there is the potential to use the failure mode maps presented by Betts et al. (2018a) to predict the failure mode of these panels under impact loading. It also indicates that it may be viable to determine impact properties of similar foam-core FFRP sandwich panels using only quasi-static testing.

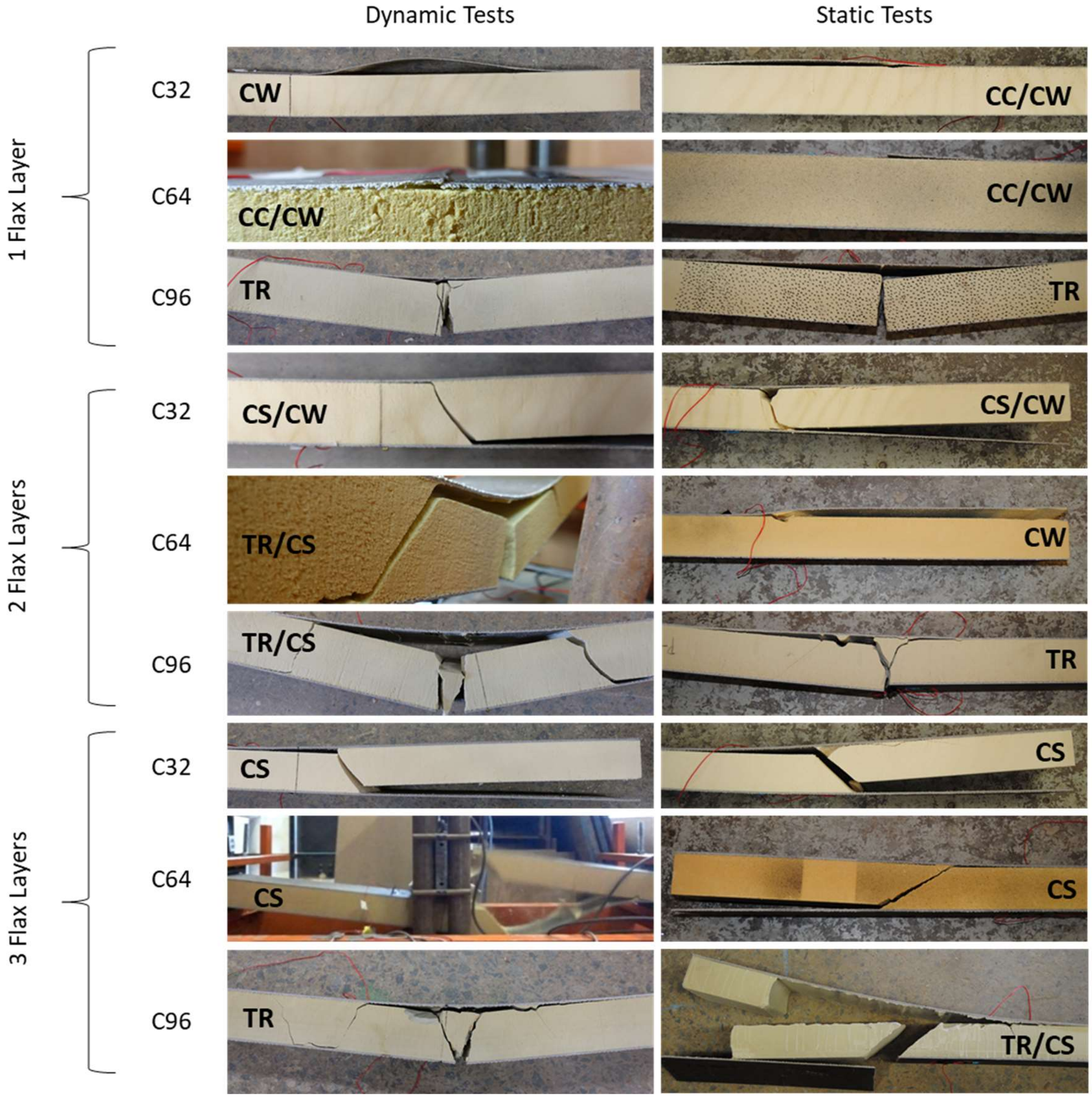

Figure 3-4. Comparison of static and dynamic failure modes (Note: CC = Compression Crushing; CW = Compression Wrinkling; CS = Core Shear; and TR = Tensile Rupture)

3.3.2. Specimen Deflections and Face Strains

Figure 3-5 shows the effect of face thickness on the maximum deflection. For specimens with higher core densities the deflection decreased with facing thickness. For example, at an energy level of 51.1 J, the deflection of specimen 1FL-C96 is 26.9

mm which is a 27% increase from the 21.1 mm deflection of 2FL-C96 and a 60% increase from the 16.8 mm deflection of specimen 3FL-C96. Interestingly, from Figure 3-5a (specimens with a core density of 32 kg/m^3), the face thickness had less influence on the deflection at each energy level than it did for the higher density foam-cored specimens. This is indicative that the shear deflection in specimens with weaker cores is more prominent than in specimens with higher density cores. This behaviour is discussed further in the modelling section of this paper.

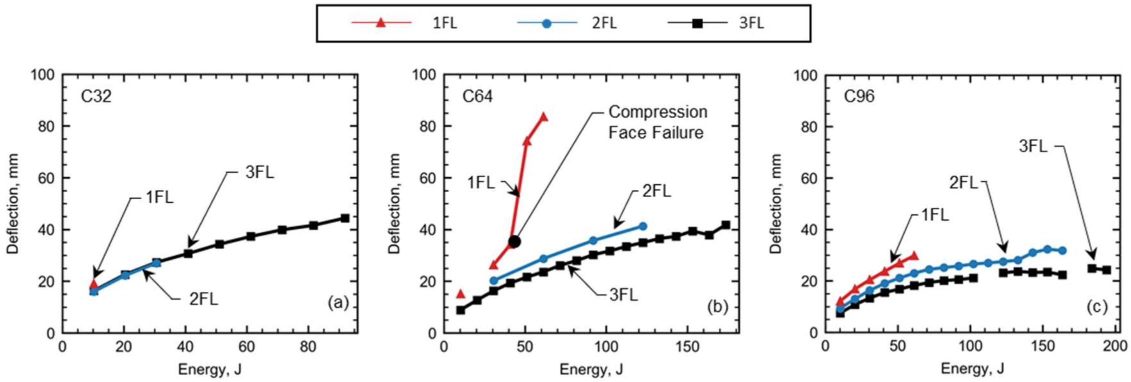

Figure 3-5. Measured maximum deflection at mid-span during each impact event: (a) C32; (b) C64; and (c) C96

Figure 3-6 presents the effect of face thickness on the strain in each face at mid span. Note that compressive strain is represented as negative and tensile strain is represented as positive. Looking at Figure 3-6a, specimens 2FL-C32 and 3FL-C32 exhibited similar face strains whereas the face strains of specimen 1FL-C32 were greatly increased when compared to specimen 2FL-C32, especially on the bottom face. This indicates that the bending deflection was more prevalent in this specimen, whereas shear deflection may have governed the deflection behaviour of the specimens with thicker faces. This trend is also evident to a lesser degree in Figure 3-6b and Figure 3-6c. For all core types, face strain increased with a decrease in face thickness and the largest increase in face strain is observed when moving from a face with two layers of flax to a face with one layer of flax.

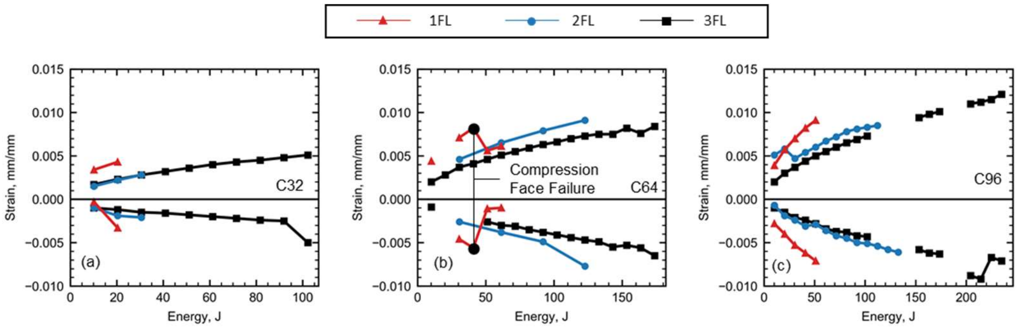

Figure 3-6. Measured maximum face strains at midspan during each impact event: (a) C32; (b) C64; and (c) C96 (Note: top face strains are negative; bottom face strains are positive)

3.3.3. Calculation of Specimen Stiffness

The damped period of the structure was determined based on the first natural frequency by calculating the average time between the peaks and troughs of the deflection data. The damped angular frequency could then be calculated by:

$$\omega_d = \frac{2\pi}{T_d} \tag{3-1}$$

where ω_d is the damped angular frequency and T_d is the damped period of the sandwich panel, the average values of which are presented in Table 3-2. The natural angular frequency and damping ratio could then be determined using the relationship between the damped and natural angular frequencies (Eq. 3-2) and the logarithmic fit of the damping behaviour of the beams (Eq. 3-4). To determine the natural angular frequency and the damping ratio, these two equations were iterated until the value of the natural angular frequency converged to within less than 1%.

$$\omega_n = \frac{\omega_d}{\sqrt{1-\xi^2}} \tag{3-2}$$

$$f(t) = Ce^{\xi\omega_n t} \tag{3-3}$$

where C is a constant, ξ is the damping ratio based on the first natural frequency, ω_n is the natural angular frequency, and t is time. Eq. 3-3 was fit to the peak values of the free vibration portion of deflection versus time plot. An example of the fit of Eq. 3-

3 is shown for specimen 2FL-C64 impacted using a drop height of 1200 mm in Figure 3-7c. The specimen stiffness was calculated by:

$$K = \frac{{\omega_n}^2\, mL}{2} \qquad (3\text{-}4)$$

where m is the specimen mass per unit length, and L is the span length.

Table 3-2. Summary of impact test results and comparison with static tests

Specimen I.D.	Impact Energy Resisted (N·m)	Specific Absorbed Energy (N·m/kg)	Damped Period (s)		Impact Test Stiffness (N/mm)		Static Test Stiffness (N/mm)	Ratio of Impact to Static Stiffness
			AVE	SD	AVE	SD		
1FL-C32	10.2	10.4	0.0175	N/A	63.2	N/A	54.0	1.17
2FL-C32	30.6	20.0	0.018	0.0003	94.8	3.1	73.4	1.29
3FL-C32	91.9	46.0	0.0196	0.0012	97.5	10.6	87.7	1.11
1FL-C64	30.6	19.6	0.019	0.0001	84.2	0.7	100.8	0.84
2FL-C64	122.6	60.6	0.0173	0.0004	133.0	6.6	114.5	1.16
3FL-C64	173.7	69.7	0.0167	0.0006	172.4	11.4	161.1	1.07
1FL-C96	61.3	31.6	0.0174	0.0003	124.7	4.7	121.3	1.03
2FL-C96	163.4	66.3	0.0159	0.0006	192.1	14.7	206.5	0.93
3FL-C96	245.1	84.5	0.0147	0.0012	261.3	33.2	248.8	1.05
AVE								1.07
SD								0.14

Note: AVE = average and SD = standard deviation.

Figure 3-8 shows the effect of the facing thickness on the specimen stiffness. The stiffness does not change significantly after multiple tests of each specimen which supports the observation during the tests that there was no significant observable damage before ultimate failure. While it is possible that unobservable microscopic damage could be caused by an impact event, this would be evidenced by a reduction in specimen stiffness. Therefore, the test results do not support the presence of microscopic damage due to the repeated impact events throughout testing. This also means that the specimen stiffness can be taken as the average stiffness calculated from the data of each test, which is presented in Table 3-2. From Figure 3-8, it is evident that stiffness increased with facing thickness. For specimens with weak cores (32 kg/m^3), the effect of face thickness is less significant. This is because these specimens are more affected by shear deflection that the specimens with stronger cores. Table 3-2 shows there is a 54% increase in average stiffness from specimen 1FL-C96 to specimen 2FL-C96 and a 36% increase from specimen 2FL-C96 to specimen 3FL-C96. It is also evident that stiffness increased with core density. For example, specimen 2FL-C32 exhibited a stiffness of 94.8 N/mm, whereas specimen 2FL-C64 exhibited a stiffness of 133.0 N/mm, which is an increase of 40%. The stiffness of specimen 2FL-C96 was found to be 192.1 N/mm, an increase of 44% from specimen 2FL-C64.

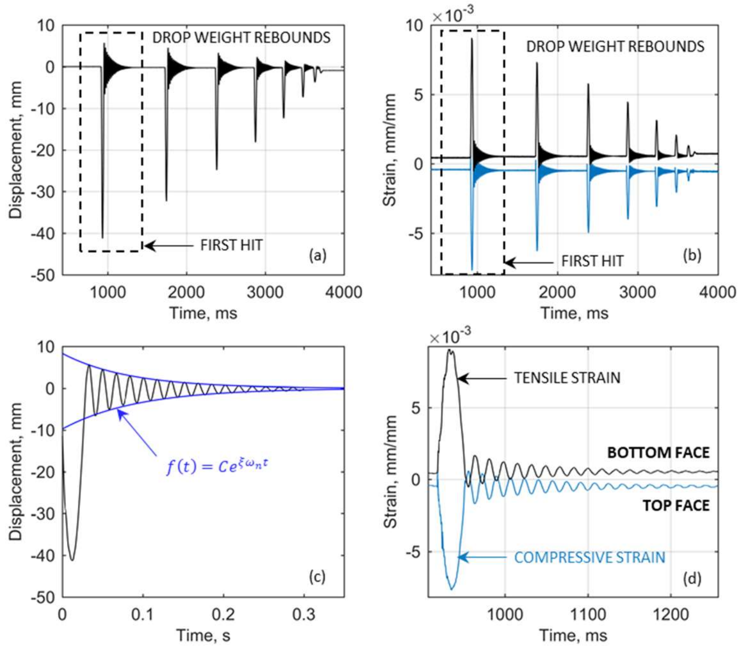

Figure 3-7. Measured data for a drop height of 1200 mm on specimen 2FL-C64: (a) midspan displacement during test; (b) midspan face strain during test; (c) displacement due to first hit; and (d) face strains due to first hit

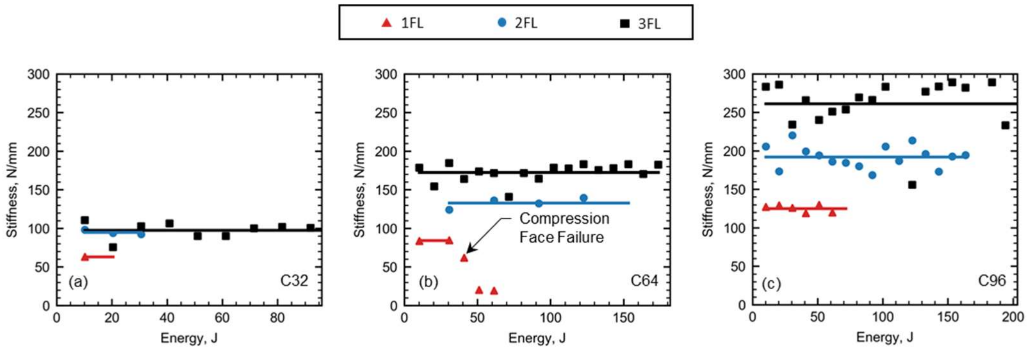

Figure 3-8. Calculated stiffness during each impact event: (a) C32; (b) C64; and (c) C96 (Note: lines represent the average calculated stiffness)

3.4. ANALYTICAL STUDY

As a part of this study, a nonlinear incremental iterative model (NIIM) was developed to predict deflection and face strain during an impact event based on the conservation of energy. The NIIM assumes that the potential energy of the drop is completely absorbed by the shear and flexural bending induced in the sandwich panel due to the impact. This section presents the development and the verification of the deflection and face strain models.

3.4.1. Nonlinear Behaviour of Constituents

As found by numerous authors, FFRPs typically exhibit nonlinear mechanical behaviour (Betts et al. 2018a; Christian and Billington 2011; Hristozov et al. 2016; Mak et al. 2015; Mathura and Cree 2016; Yan et al. 2016). It is also known that core foams typically exhibit a nonlinear shear stress-strain response (Fam and Sharaf 2010). Therefore, to accurately predict the behaviour of sandwich panels with FFRP faces and foam cores, it is important to consider the nonlinearity of the constituent materials.

3.4.1.1. Behaviour of FFRP Faces

The behaviour of the FFRP faces was modelled using a parabolic equation, presented in Eq. 3-5. A verification of the model is provided in Figure 3-9. Previously, the authors used a simple bi-linear model to predict the behaviour of FFRP faces for sandwich panels tested under static loading (Betts et al. 2018a). However, this bi-linear model was intended to simplify the analysis for use in a design-oriented model. To improve the NIIM accuracy a parabolic model was chosen for the current study. The parabolic model was developed based on the assumptions that the initial slope was E_{fo}, the initial FFRP modulus determined through testing, and the ultimate stress-strain point was defined by σ_{fu}, the ultimate FFRP stress and ϵ_{fu}, the ultimate FFRP strain, both determined through testing.

$$\epsilon_f = \frac{\sigma_f^2}{\sigma_{fu}^2}\left(\epsilon_{fu} - \frac{\sigma_{fu}}{E_{fo}}\right) + \frac{\sigma_f}{E_{fo}} \tag{3-5}$$

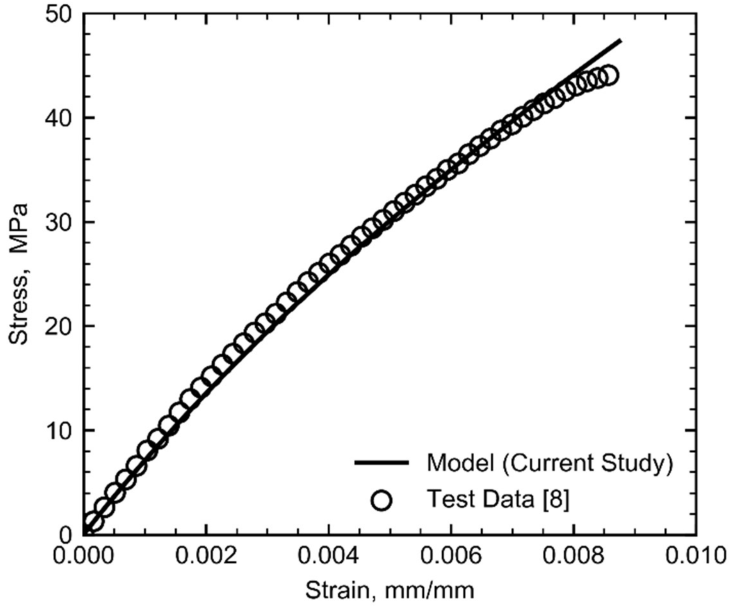

Figure 3-9. Verification of FFRP face parabolic model against test data from an independent study (Betts et al. 2018a)

3.4.1.2. Behaviour of Foam Cores

To model the shear stress-strain behaviour of the cores, a cubic model was developed and is presented in Eq. 3-6. A model verification using data from an independent study (Sharaf and Fam 2012) is shown in Figure 3-10a and the results and the shear stress-strain behaviour of the core foams used in the current study are shown in Figure 3-10b.

$$\tau_c = \frac{2}{\gamma_{cu}^3}[0.55G_{co}\gamma_{cu} - \tau_{cu}]\gamma_c^3 + \frac{1}{\gamma_{cu}^2}[3\tau_{cu} - 2.1G_{co}\gamma_{cu}]\gamma_c^2 + G_{co}\gamma_c \qquad (3\text{-}6)$$

where τ_c is the shear stress in the core, γ_c is the shear strain in the core, τ_{cu} is the ultimate core shear stress, γ_{cu} is the ultimate core shear strain and G_{co} is the initial modulus of the core. The equation was developed based on the following four boundary conditions: $\{\gamma_c = 0;\ \tau_c = 0\}$, $\{\gamma_c = \gamma_{cu};\ \tau_c = \tau_{cu}\}$, $\{\gamma_c = 0;\ d\tau_c/d\gamma_c = G_{co}\}$ and $\{\gamma_c = \gamma_{cu};\ d\tau_c/d\gamma_c = G_{co}/10\}$.

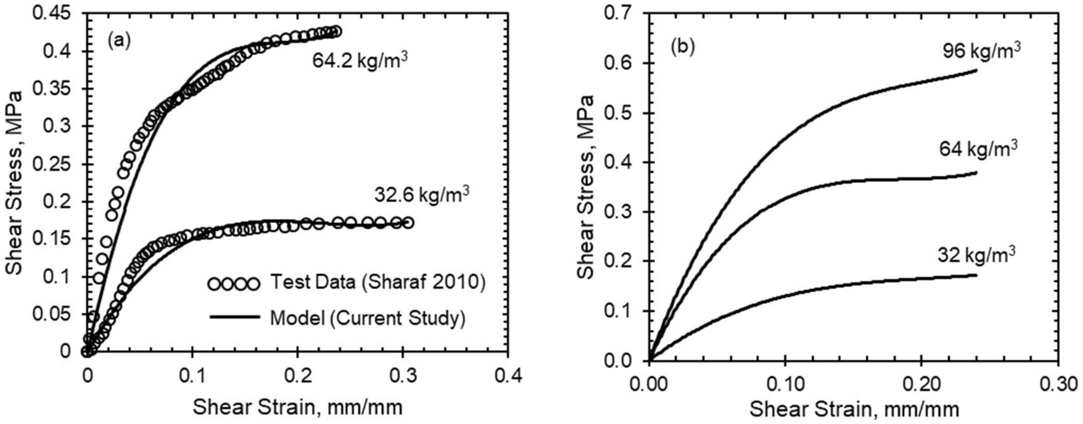

Figure 3-10. Modelling of shear stress-strain response of foam cores (a) verification using independent data and (b) models used in the current study

3.4.1.3. Modelling of Constituent Behaviour Using a Secant Moduli

To incorporate the nonlinear behaviour of the FFRP faces and foam core in the NIIM, a secant elastic modulus and a secant shear modulus were used at each energy level. This allowed the process to be incremented assuming a linear elastic behaviour at each increment while also capturing the overall nonlinear behaviour. The method of determining the secant moduli is shown in Figure 3-11. Each secant modulus was defined between a stress-strain of zero and a stress-strain point corresponding to the energy level. At each model increment an iterative procedure was used to determine the secant moduli to within an accuracy of 0.1%. The entire NIIM is presented in the form of a flowchart in Figure 3-12 and is detailed in the proceeding section.

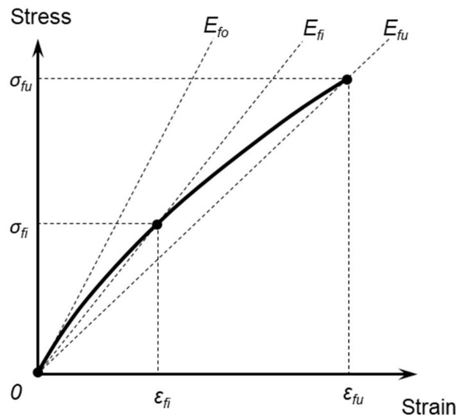

Figure 3-11. Modelling of nonlinear mechanical behaviour using variable secant moduli

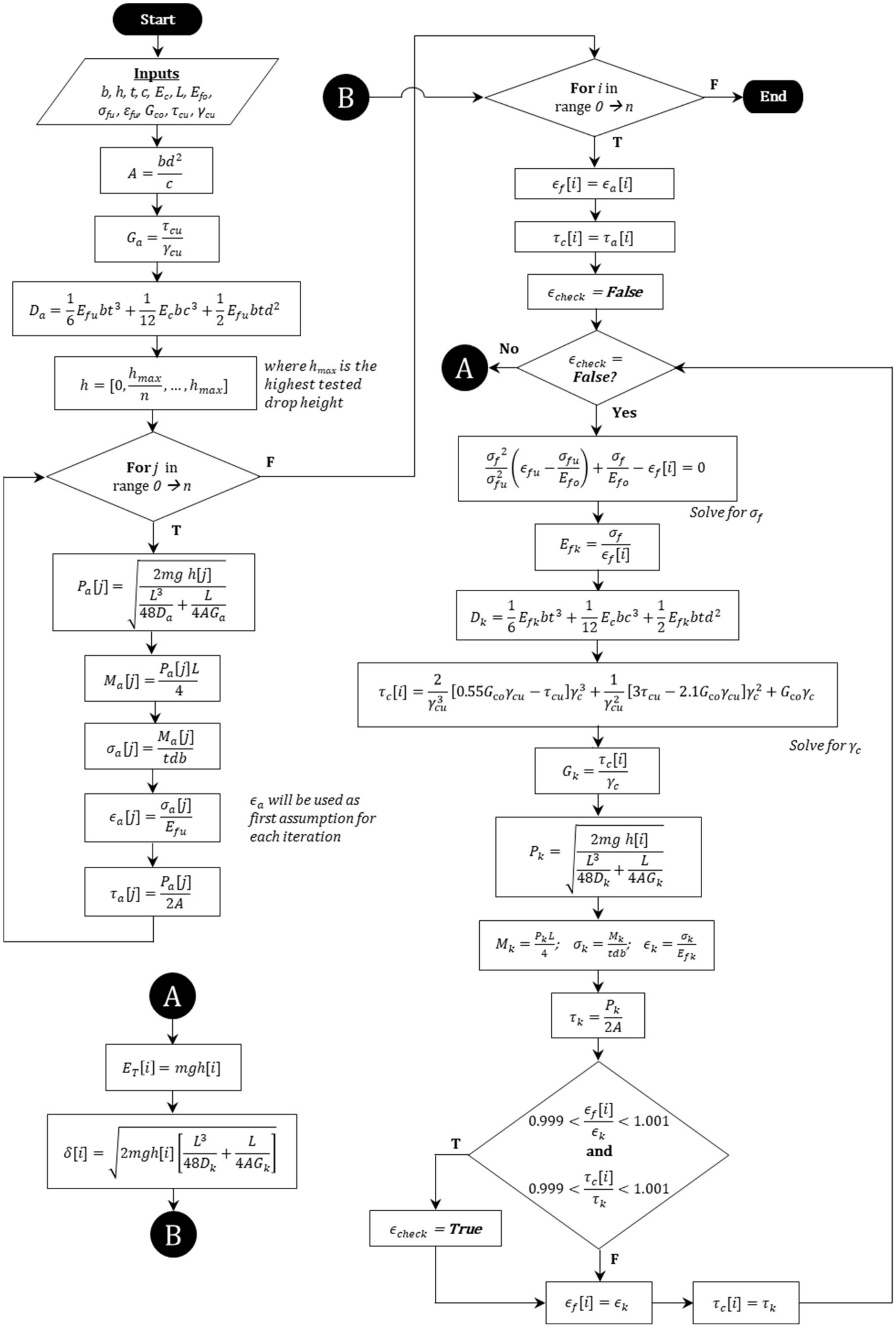

Figure 3-12. Analysis flow chart

3.4.2. Model Description

The NIIM presented in this section is an nonlinear analysis based on the energy balance method presented by Akil Hazizan and Cantwell (Akil Hazizan and Cantwell 2002) at multiple increments. A python script, presented in Appendix C was developed to run the analysis based on the flowchart presented in Figure 3-12.

At each model increment, the governing equation is as follows:

$$E_T = mgh = E_b + E_s + E_c \tag{3-7}$$

where E_T is total energy, m is the mass of the drop weight in kg, h is the drop height in m and E_b, E_s and E_c are the energies absorbed through bending, shear and contact, respectively. Eq. 3-7 assumes no loss of energy during the drop. Additionally, a steel section cut from a 150-mm wide Hollow Structural Section (HSS) was used as the impact surface to eliminate localized effects such as indentation. An HSS was chosen for its curved edges to eliminate the possibility of a stress concentration at the edge of the loading area. Additionally, the length of the impact surface was longer than the width of the specimens which ensured the entire width of each specimen was loaded. No indentation was observed during or after testing the sandwich specimens. Therefore, the model was developed with the assumption that the impact did not cause significant indentation in the top face sheet (i.e. the contact energy $E_c = 0$). Allen (Allen 1969) presented a general load-displacement relationship for one-way sandwich panels subjected to three-point bending as shown in Eq. 3-8:

$$\delta = \frac{PL^3}{48D} + \frac{PL}{4AG} \tag{3-8}$$

where δ is the deflection, P is the equivalent static load, L is the span length, G is the secant shear modulus, $A = bd^2/c$ is a geometric property (Allen 1969), b is the specimen width, t is the thickness of the faces, c is the thickness of the core and D is the flexural rigidity of the sandwich panel as follows:

$$D = \frac{1}{6}E_f bt^3 + \frac{1}{12}E_c bc^3 + \frac{1}{2}E_f btd^2 \tag{3-9}$$

where E_f is the secant modulus of elasticity of the FFRP faces. By using a variable secant modulus for the FFRP faces and foam cores, each model step can be analysed assuming linear-elastic behaviour, while capturing the overall nonlinear behaviour of the structure. Therefore, the total energy at each model increment must be equal to $E_t = P\delta_{max}/2$ and by rearranging with Eq. 3-7 and 3-8, the maximum impact force at each increment can be written as follows:

$$P_{max} = \sqrt{\frac{2mgh}{\frac{L^3}{48D} + \frac{L}{4AG}}} \tag{3-10}$$

The maximum impact force can then be used to predict the maximum strain experienced by each face during the test. To simplify this calculation, it is assumed that the neutral axis of the specimens is adequately close to the center of the cross section, such that the facing strain in the top face is equal and opposite to that in the bottom face. This assumption was used and verified by Betts et al. (2018a). The first step in converting the impact force to face strain is to determine the moment due to the impact force. As it is a three-point bending configuration, this can be determined using by $M = P_{max}L/4$. The stress in each face can then be calculated by $\sigma_f = M/tdb$ and converted to strain in each face by dividing by the secant modulus of elasticity.

Table 3-3. Comparison of the test data and results of the NIIM

		Deflection (mm)			Bottom Strain (mm/mm)			Top Strain (mm/mm)		
Specimen	Energy (J)	Test	NIIM	Test/ NIIM	Test	NIIM	Test/ NIIM	Test	NIIM	Test/ NIIM
1FL-C32	10.2	19.0	18.9	1.01	0.0034	0.0020	1.70	-0.0003	-0.0020	0.15
2FL-C32	10.2	16.0	17.2	0.93	0.0015	0.0012	1.25	-0.0010	-0.0012	0.83
3FL-C32	10.2	16.3	17.0	0.96	0.0017	0.0010	1.70	-0.0010	-0.0010	1.00
1FL-C64	30.6	26.3	24.0	1.10	0.0071	0.0048	1.48	-0.0046	-0.0048	0.96
2FL-C64	30.6	20.3	21.0	0.97	0.0046	0.0032	1.44	-0.0026	-0.0032	0.81
3FL-C64*	30.6	16.3	19.5	0.84	0.0037	0.0031	1.19	-0.0026	-0.0031	0.84
1FL-C96†	61.3	29.8	32.9	0.91	0.0091	0.0067	1.36	-0.0071	-0.0067	1.06
2FL-C96	61.3	23.0	28.0	0.82	0.0067	0.0048	1.40	-0.0036	-0.0048	0.75
3FL-C96	61.3	18.2	26.4	0.69	0.0055	0.004	1.38	-0.0034	-0.0040	0.85
AVE				0.91			1.43			0.81
SD				0.12			0.18			0.27

* *Strain data and model compared at energy level of 51.1 J as strain gauge failed during 30.3 J impact test*

† *Strain data and model compared at energy level of 51.1 J as strain gauge failed during 61.3 J impact test*

3.4.3. Model Verification

A comparison between the test data and the model at a selected energy level for each specimen is presented in Table 3-3. The table shows that, generally, the NIIM was able to accurately predict both the maximum deflection and face strain at each impact level. At the selected energy levels, the Test/NIIM ratios were 0.91 and 1.12 for midspan deflection and face strains, respectively.

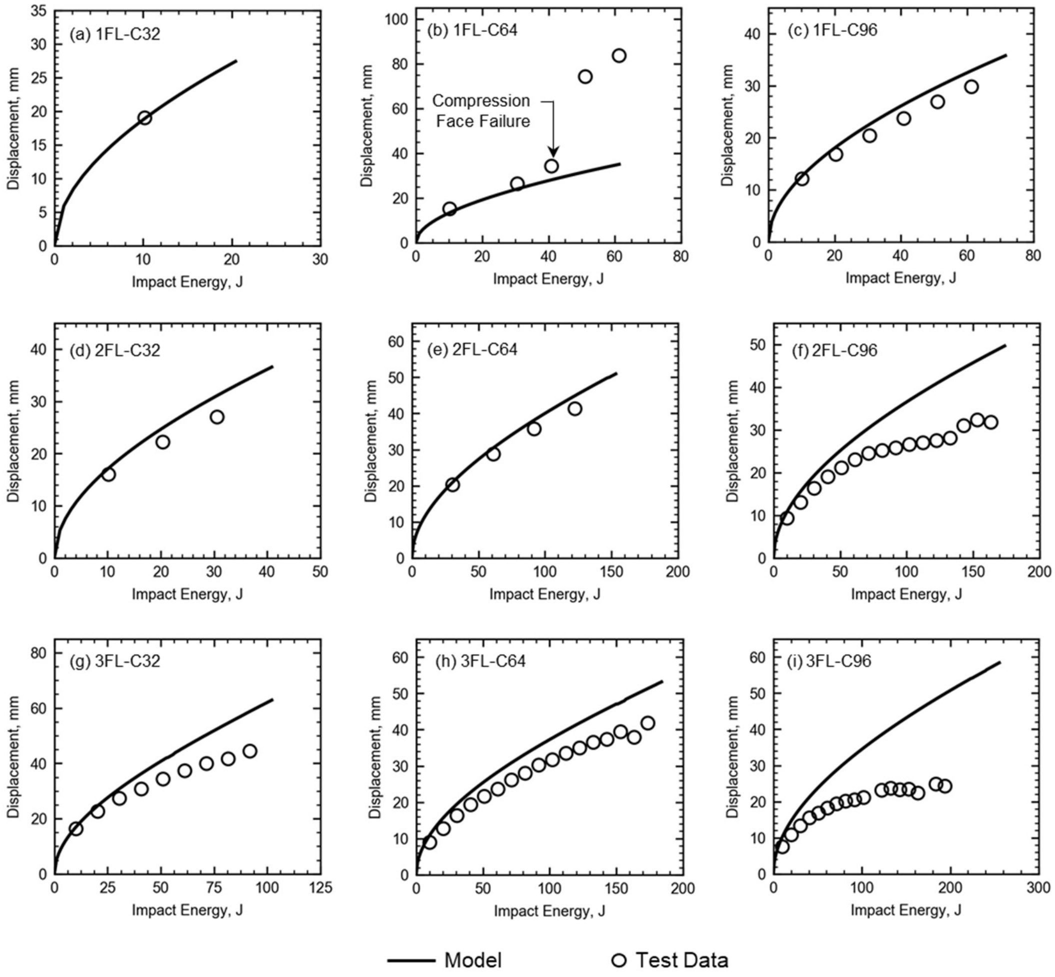

Figure 3-13. Verification of deflection model against test data: (a) 1FL-C32; (b) 1FL-C64; (c) 1FL-C96; (d) 2FL-C32; (e) 2FL-C64; (f) 2FL-C96; (g) 3FL-C32; (h) 3FL-C64; and (i) 3FL-C96

Figure 3-13 and Table 3-3 show the verification of the deflection model. The test data presented in Figure 3-13 is the maximum deflection recorded from each impact event. The models presented do not predict ultimate energies, only the deflection behaviour of the specimens. Each model was truncated at the ultimate failure energy recorded for the corresponding specimen. Note that some deflection data is missing due to instrumentation failure during the tests.

The model predicts the deflections of most specimens well, however, it over predicts deflection for all the specimens with the C96 foam cores. One hypothesis for this over prediction is that the mechanical properties of this foam are more affected by strain rate than the lower density foams. This would cause the specimen to be stiffer, reducing the overall deflection during the tests. Because specimens 2FL-C96 and 3FL-C96 reached higher energies (i.e. higher drop heights and higher strain rates) than the other specimens, this increase in stiffness could also be affected by the high strain rate behaviour of the FFRP faces not seen in lower energy tests. Generally, as natural fibres are more variable than synthetic fibres all the results could be affected by the intrinsic variability of the natural flax fibre fabrics used. Additionally, the test data may vary because the specimens were impacted multiple times which could have caused unobservable microscopic damage. However, as discussed previously, the presence of microscopic damage is not supported by the test results.

Unlike most structures, shear deformation can significantly contribute to the overall deflection of sandwich structures. Therefore, it is important to consider the effect of the test parameters on shear deformation. Figure 3-14 shows the average contribution of both shear and bending to the overall deflection calculated by the model. This was calculated by separating the amount of shear and bending deflection calculated by Eq. 3-8. This figure shows that as the core strength increases the contribution of shear deflection on the overall specimen deflection decreases. It also shows that the most significant increase in shear deflection occurs when the core density is decreased from 64 kg/m^3 to 32 kg/m^3. For instance, the average percentage of shear contribution to the overall deflection of specimen 2FL-C32 is 82% whereas the average shear contributions to the deflections of 2FL-C64 and 2FL-C96 are 61% and 55%, respectively. This information suggests that in the design of sandwich structures with FFRP faces where the deflection criteria is important, the choice of core density is significant. Figure 3-14 also shows that the face thickness affects the contribution of shear and bending to the overall specimen deflection. For all core types, as the face thickness increases, the contribution of shear deflection increases.

However, this increase in contribution is due to the increase in flexural rigidity and not due to a significant increase in shear deflection.

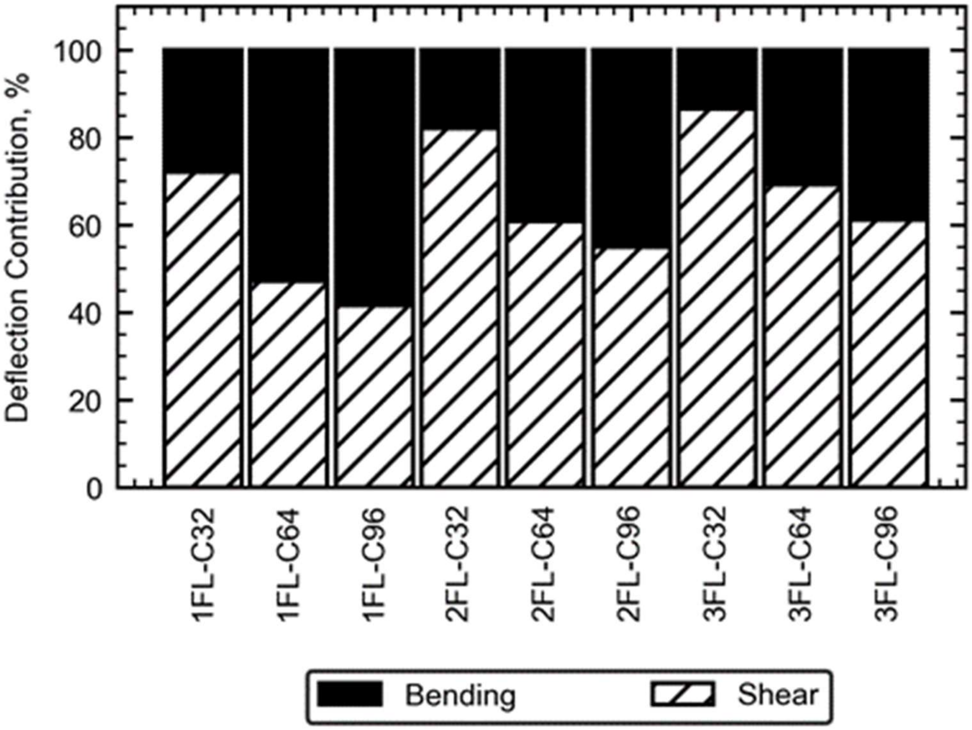

Figure 3-14. Average deflection contribution from shear and bending predicted by NIIM

Figure 3-15 and Table 3-3 show the verification of the strain model. It is important to note that this model does not predict the ultimate impact energy. Also note that some data points are missing due to failure of strain gauges in some of the tests. Generally, Figure 3-15 shows that the NIIM can reasonably predict the maximum strain in each face during the impact event.

One limitation of the NIIM is the assumption that the neutral axis is at the midsection. The accuracy of the model, specifically for predicting face strains, could be improved by determining the actual location of the neutral axis and considering the difference in tension and compression behaviour of the faces. Future research will include experimental and analytical tests of the residual strength of these sandwich panels after an impact event.

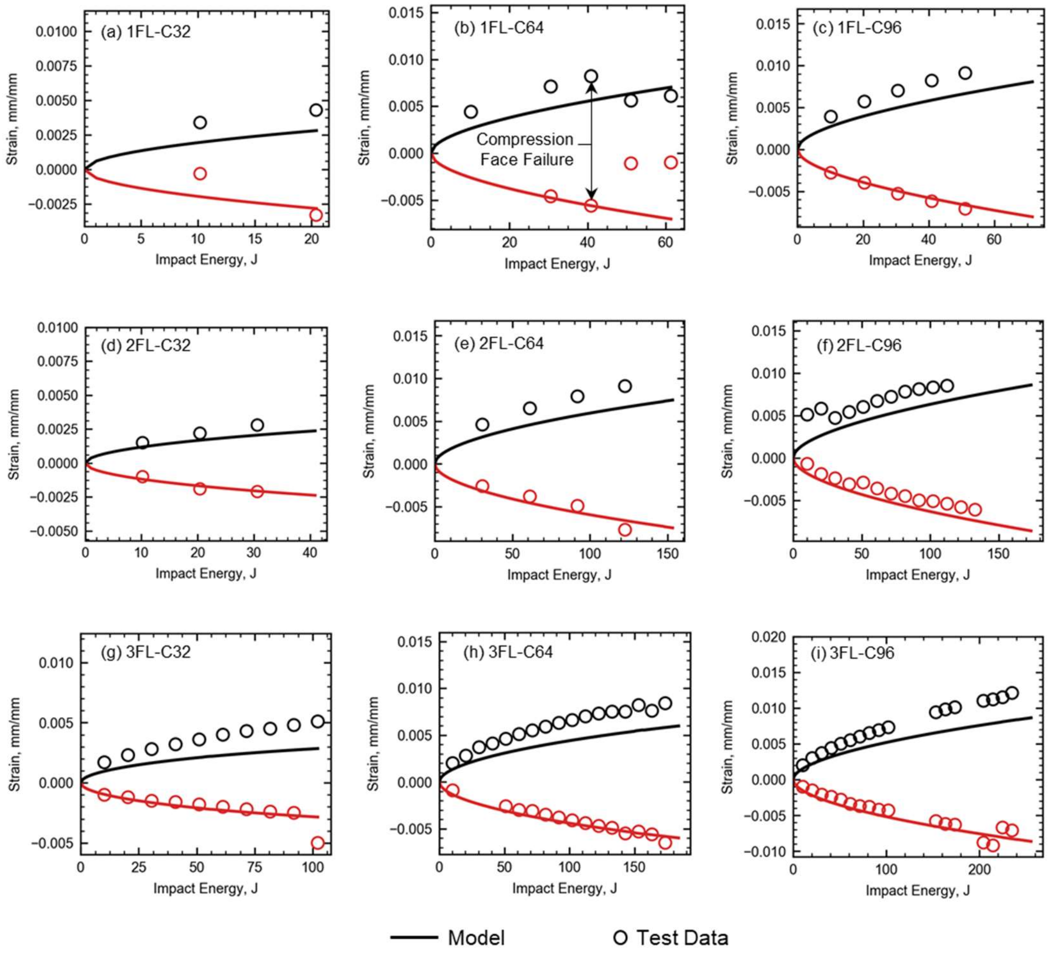

Figure 3-15. Verification of mid-span face strain model (top face strains are negative; bottom face strains are positive): (a) 1FL-C32; (b) 1FL-C64; (c) 1FL-C96; (d) 2FL-C32; (e) 2FL-C64; (f) 2FL-C96; (g) 3FL-C32; (h) 3FL-C64; and (i) 3FL-C96

3.5. SUMMARY

In this chapter, the performance of sandwich panels constructed with flax fibre-reinforced polymer (FFRP) faces and foam cores under impact loading is studied experimentally and analytically. The parameters of the tests were facing thickness (1, 2 and 3 layers of flax fabric) and core density (32, 64 and 96 kg/m^3). Each specimen was 1220 mm long, 152 mm wide and approximately 80 mm thick and was tested by a 10.41 kg drop weight impact at mid-span. Each specimen was tested multiple times starting at a drop height of 100 mm and increasing the height by 100 mm for each subsequent test until ultimate failure. The results indicate that the ultimate impact energy increases with both core density and face thickness. The four main failure modes observed were: compression face crushing, compression face wrinkling, core shear and tension face rupture. The failure modes observed generally matched those observed during similar quasi-static testing. Additionally, a nonlinear incremental iterative model (NIIM) was developed based on the conservation of energy during an impact event and the nonlinear mechanical behaviour of both the FFRP faces and foam cores. This novel model accurately predicts the total deflection and face strains based on the energy of an impact.

CHAPTER 4: POST-IMPACT RESIDUAL BEHAVIOUR OF FFRP-FOAM SANDWICH BEAMS [3]

4.1. INTRODUCTION

With the growing understanding of the effect of human activity on the environment, it is important to consider ways to reduce the environmental footprint caused by civil infrastructure including buildings. One way to improve the sustainability of building practices is the use of systems that provide dual benefits, such as sandwich panels. These are lightweight systems that are comprised of strong and stiff faces and a lightweight core, such as foam, that separates the faces and increases the moment of inertia. When used for building cladding applications, sandwich panels can provide both lateral force resistance and insulation. The environmental sustainability of sandwich panels can be further improved through the use bio-based materials. Sandwich panel faces are often constructed of metals or synthetic fibre-reinforced polymers (FRPs), such as glass FRPs. Because these materials are much stronger than the weaker core material, sandwich panel failure often occurs in the core and therefore the strength of the face material is underutilized (Fam et al. 2016; Sadeghian et al. 2018). This leaves an opportunity to replace these synthetic face materials with bio-based materials, such as FRPs made with natural fibres, such as flax and bio-based polymers. Flax fibres are relatively strong and stiff compared with other natural fibres (Ramesh et al. 2017) and have less embodied energy than glass or carbon fibres (Cicala et al. 2010). Sandwich panels with flax FRP (FFRP) faces and foam cores are a more sustainable alternative for construction applications, such as cladding for building envelopes. Before they can be implemented in the industry, it is necessary to have an in-depth understanding of the behaviour of sandwich panels with FFRP faces under various loading conditions, such as shear and flexural loading, impact loading and post-impact flexural loading.

Sandwich panels with synthetic FRP faces have been studied extensively under flexural loads (Besant et al. 2001; Dai and Hahn 2003; Fam and Sharaf 2010; Gupta

---

[3] **This chapter has been published in the *ASCE Journal of Building Engineering:***

Betts D, Sadeghian P, Fam A. Post-Impact Residual Strength and Resilience of Sandwich Panels with Natural Fiber Composite Faces. *Journal of Building Engineering.* 2021; 38:102184.

et al. 2002; Manalo et al. 2016, 2010; Petras and Sutcliffe 1999; Sharaf et al. 2010) and recently, some researchers have focused on the shear and flexural behaviour of sandwich panels with natural FFRP faces and foam cores (Betts et al. 2018a; Codyre et al. 2016; Mak et al. 2015; Mak and Fam 2019a; Sadeghian et al. 2018). Due to their light weight and insulative properties, sandwich panels are often used for building cladding. During windstorms, building envelopes can be impacted by flying debris and therefore it is important to understand their impact behaviour. Therefore, the low velocity impact behaviour of sandwich structures with synthetic faces has been well documented in the literature (Abrate 1997; Akil Hazizan and Cantwell 2002; Anderson and Madenci 2000; Atas and Potoglu 2016; Plagianakos et al. 2016; Schubel et al. 2005; Torre and Kenny 2000). Recent studies have also looked at the impact behaviour of sandwich panels with FFRP faces and foam cores (Betts et al. 2020a; Boria et al. 2018; Ude et al. 2013). Other authors have studied the high strain rate behaviour of FFRPs and other natural FRPs (Hu et al. 2018; Kim et al. 2012). Kim et al. (2012) performed high rate compression tests on hemp, glass and hybrid composites with different matrices. They found that between strain rates of 600 strain/s to 1500 strain/s the hemp-thermoset composites exhibited maximum stresses similar to that of glass composites. However, after 1500 strain/s, there was no significant increase in strength with strain rate and it was concluded that strain hardening was muted above this strain rate. Hu et al. (2018) examined the high strain rate compressive behaviour of FFRPs made with woven flax fabrics loaded in-plane and out-of-plane. They determined that FFRPs exhibited higher strength in both the in-plane and out-of-plane directions under high strain rate loads.

Building envelopes may be impacted multiple times throughout their lifespan, and therefore an understanding of their post-impact residual strength and resiliency is necessary. Numerous studies have focused on the compression after impact (CAI) test to determine the post-impact residual strength of impacted sandwich panels (Davies et al. 2004; Gustin et al. 2005; Shipsha and Zenkert 2005). However, sandwich panels in building cladding systems are typically required to resist flexural loads and therefore it is appropriate to test their flexural behaviour after impact. Tests to determine the residual flexural strength of sandwich panels with GFRP faces (Baran and Weijermars 2020) and CFRP faces (Göttner and Reimerdes 2006; He et al. 2018; Klaus et al. 2012) have been performed. Baran and Weijermars (2020) looked at the post-impact flexural behaviour of sandwich panels with GFRP faces and multiple different core types, including: balsa wood, styrene acrylonitrile foam and polyethylene terephthalate foam. They observed a reduction in both strength and stiffness of impacted specimens compared with intact specimens due to the impact event. He et al. (2018) studied sandwich panels with CFRP faces and corrugated aluminum cores. After impacting specimens at various energy levels, they tested them under three-point bending. The authors noted that there was a reduction in specimen strength due to all levels of impact and they concluded that the main cause of the decrease in strength was local buckling of the aluminum core under the area of the impact.

There is currently a gap in the literature with respect to the post-impact residual strength and resilience of sandwich panels with FFRP faces. The aim of this paper is to fill this gap by providing experimental data on the post-impact flexural behaviour of sandwich panels with FFRP faces and foam cores. Furthermore, the resiliency of these panels is tested through post-impact flexural testing of specimens that have been impacted at one energy level multiple times.

4.2. EXPERIMENTAL PROGRAM

As a part of this study, sandwich beams with FFRP faces and PIR foam cores were impacted with a drop weight and subsequently tested under three-point bending to determine the residual flexural behaviour. In this section of the paper, the test matrix will be presented as well as the specimen fabrication and test set-up and procedure.

4.2.1. Test Matrix

A total of 27 sandwich beams which were 1200 mm long, 75 mm wide and 80 mm thick, were tested. The main test parameters were the face thickness, foam core density and impact energy level. Three face thicknesses were examined: one layer, two layers and three layers of FFRP per face which were measured to be 1.41 ± 0.16 mm, 2.70 ± 0.15 and 3.90± 0.17 mm thick, respectively. The core-to-thickness ratios of the one-layer, two-layer and three-layer beam specimens were 54, 28, and 20 respectively. Foam cores with three densities were examined: 32 kg/m^3, 64 kg/m^3 and

96 kg/m^3. The effects of three impact energy levels were investigated: 100% 75% and 50% failure energy. The test matrix is presented in Table 4-1.

Table 4-1. Test matrix for post-impact residual tests of one-way sandwich beams

Specimen	Test Group	Core Density, kg/m^3	FFRP Layers	Width, mm	Impact Energy, J	No. of Impacts
1FL-C32-R100	R100	32	1	151.1	10.2	1
2FL-C32-R100	R100	32	2	149.5	30.6	1
3FL-C32-R100	R100	32	3	150.6	91.9	1
1FL-C64-R100	R100	64	1	151.0	30.6	1
2FL-C64-R100	R100	64	2	151.6	122.6	1
3FL-C64-R100	R100	64	3	151.9	173.7	1
1FL-C96-R100	R100	96	1	152.1	61.3	1
2FL-C96-R100	R100	96	2	151.9	163.4	1 †
3FL-C96-R100	R100	96	3	152.1	245.1	1
1FL-C32-R75	R75	32	1	76.0	9.8 *	6 †
2FL-C32-R75	R75	32	2	77.4	23.5 *	5 †
3FL-C32-R75	R75	32	3	79.6	48.7	3 †
1FL-C64-R75	R75	64	1	74.5	15.3	50
2FL-C64-R75	R75	64	2	74.3	27.1	50
3FL-C64-R75	R75	64	3	76.4	34.5	50
1FL-C96-R75	R75	96	1	75.7	23.7	14 †
2FL-C96-R75	R75	96	2	74.2	68.5	6 †
3FL-C96-R75	R75	96	3	72.9	100.0	24 †
1FL-C32-R50	R50	32	1	74.6	5.3	50
2FL-C32-R50	R50	32	2	72.0	11.7	50
3FL-C32-R50	R50	32	3	20.3	27.7	24 †
1FL-C64-R50	R50	64	1	75.7	10.3	50
2FL-C64-R50	R50	64	2	69.7	16.9	50
3FL-C64-R50	R50	64	3	75.0	22.6	50
1FL-C96-R50	R50	96	1	75.5	15.8	50
2FL-C96-R50	R50	96	2	77.1	47.5	50
3FL-C96-R50	R50	96	3	78.6	71.9	50

* *These specimens were tested at 90% of energy resisted by static specimens*

† *Specimen failed during impact tests*

The following naming convention was used: XFL-YC-RZ, where X is the number of FFRP layers in each face, FL represents "Flax Layers", Y is the core density in kg/m^3, C represents "Core", R represents "Residual", and Z is the energy level of the impact tests as a percentage of the energy resisted by intact specimens. For example, a specimen with two layers of FFRP on each face and a core density of 96 kg/m^3 impacted at 75% the energy resisted by an intact specimen would be labelled 2FL-C96-R75.

In this study, there were nine sets of three specimens with the same face thickness and core density. The first set (group R100) were each impacted once at 100% the failure energy resisted by similar specimens tested under ramped impact loading (Betts et al. 2020a). It was expected that this impact would cause failure in the specimens, as it had in previous tests. However, eight of the nine specimens survived the impact event. As the previously tested specimens (Betts et al. 2020a) were impacted multiple times before failure, it is assumed that the cumulative energy absorption affected the ultimate impact capacity of the panels predicted by these tests. Therefore, the impact energy for the remaining tests (groups R50 and R75), was determined based on the energy to cause failure in quasi-static tests of similar specimens (Betts et al. 2018a). The R100 specimens were subsequently tested under three-point bending to determine the post-impact residual flexural behaviour. Through these tests, as will be discussed later, it was determined that the one impact at 100% energy did not significantly affect the behaviour of the beams. The second set (group R75) were each impacted 50 times at 75% of the energy resisted by intact specimens. Only three of these specimens survived the impact tests. It should be noted that the first two specimens tested in the R75 group (1FL-C32-R75 and 2FL-C32-R75) were tested at 90% failure energy. The intent was to test the entire group at 90% energy, but when these two specimens failed after a low number of impacts, the impact level was reduced in order to avoid all specimens failing before residual tests could be performed. The third set of specimens (group R50) were each impacted 50 times at 50% of the energy resisted by intact specimens. All but one specimen survived the impacts. The R75 and R50 specimens were then tested under three-point bending to determine their post-impact residual behaviour and resiliency to multiple impacts.

It should be noted that the R100 impact energy was set to the maximum energy resisted by impact test specimens from a previous study (Betts et al. 2020a) whereas the R75 and R50 impact levels were determined by finding the energy to cause failure in specimens tested under quasi-static bending in a previous study (Betts et al. 2018a). As discussed above, this was decided after testing the R100 specimens and determining that the failure energy from the impact test specimens was potentially low due to cumulative energy absorbed from multiple impacts before failure. Also note that the R100 specimens were 150 mm wide, but in order to directly compare the results of the tests, all test data presented in this paper was normalised to a beam width of 75 mm. One notable drawback of the test matrix is that only one specimen was tested at each energy level and therefore it should be noted that the conclusions of this study are based on single tests. However, as nine different specimen types were tested under each loading condition, general conclusions of the resiliency of the FFRP-foam sandwich beams can be made with confidence.

4.2.2. Materials

All sandwich panels were constructed of FFRP faces and PIR foam cores. Foams with three different nominal densities were used, namely 32, 64 and 96 kg/m^3 (ELFOAM P200, P400 and P600, Elliott Company, Indianapolis, IN, US). The FFRP used was fabricated using a 2x2 twill flax fabric (Biotex Flax, Composites Evolution, Chesterfield, UK) with an areal density of 410 g/m^2 and a bio-based epoxy resin with an approximate bio-content of 30% after mixing (ONE Epoxy, Entropy Resins, Hayward, CA, US). Betts et al (2018a) tested these FFRPs to determine their tensile and compressive behaviour. The average (± standard deviation) initial tensile modulus, strength and ultimate strain of the FFRP faces were found to be 7.51 ± 0.69 GPa, 45.4 ± 1.8 MPa and 0.0083 ± 0.0009 mm/mm, respectively. The average (± standard deviation) initial compressive modulus, strength and corresponding strain were found to be 6.73 ± 1.59 GPa, 86.4 ± 2.2 MPa and 0.0327 ± 0.0010 mm/mm, respectively. Previous studies have also noted that FFRPs and other natural fibre composites exhibit a nonlinear behaviour (Christian and Billington 2011; Hristozov et al. 2016; Mathura and Cree 2016; Yan et al. 2016).

4.2.3. Specimen Fabrication

The specimen fabrication procedure is presented in Figure 4-1. First, the foams were cut down to a size of 600 mm by 1200 mm. A 600 mm wide sandwich panel was fabricated using this foam section that was later cut into individual beams for testing under quasi-static flexural loads (Betts et al. 2018a), ramped impact loads (Betts et al. 2020a), and post-impact residual loads in the current study.

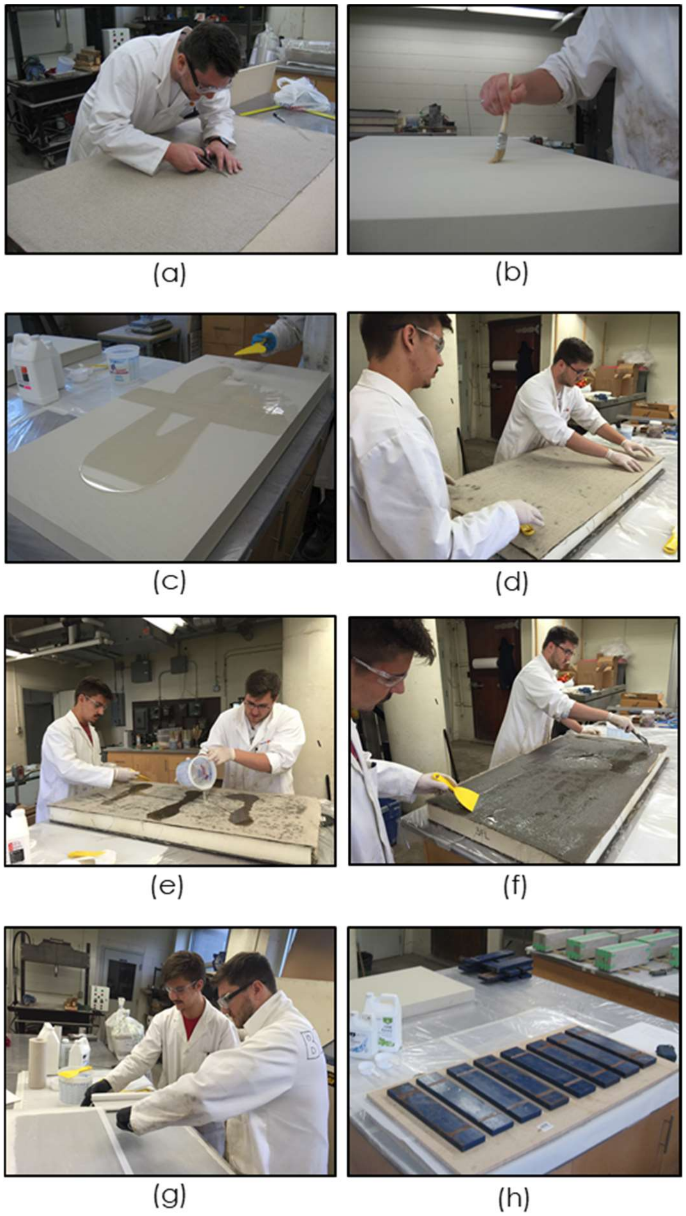

(a) (b)

(c) (d)

(e) (f)

(g) (h)

Figure 4-1. Specimen fabrication: (a) cutting fabric; (b) cleaning foam surface; (c) applying epoxy resin to foam surface; (d) placement of flax fabric; (e) placing epoxy resin flax fabric; (f) spreading epoxy resin over surface of flax fabric; (g) removal of air and excess resin; and (h) curing with weighted board

To fabricate the sandwich panel, the flax fabric was cut to the correct width using scissors as shown in Figure 4-1a. The surface of the foam was cleaned of all dust and debris using a brush as shown in Figure 4-1b. Once, the fabric was prepared and the surface of the foam was clean, the bio-based epoxy was mixed and applied to the surface of the foam as shown in Figure 4-1c. The first layer of flax fabric was then applied to the wetted foam surface with the warp direction of the fabric parallel to the longitudinal direction of the foam. Epoxy was then placed and spread across the fabric as shown in Figure 4-1d and Figure 4-1e. Depending on the desired FFRP thickness, more flax layers were placed in the same manner. When the correct amount of flax fabric layers had been added (one, two or three), parchment paper was placed on the surface and an aluminum roller was used to remove excess resin and air as shown in Figure 4-1g. A weighted board was then placed on the surface of the panel as shown in Figure 4-1h and the face was allowed to cure for a minimum of seven days before cutting. This entire procedure was repeated for the opposite face of each panel. When both faces were cured, each panel was cut into the individual specimens using a band saw. As noted previously, the R100 specimens were cut to width of 150 mm, while the R75 and R50 specimens were cut to a width of 75 mm.

4.2.4. Test Setup and Instrumentation

In this study, each beam went through two phases of testing: impact tests and post-impact quasi-static flexural testing. The R100 specimens were each impacted once before post-impact tests, while the R50 and R75 specimens were each impact 50 times before post-impact testing. In this section, the set-up of each testing phase will be presented and discussed.

4.2.4.1. Impact Tests

To impact the specimens, a drop weight frame based on ASTM D7136 (2005) was used. A photo of the test set-up with a 75 mm wide specimen in place is shown in Figure 4-2. A 10.4 kg drop weight with a 150 mm wide impact surface impacted the specimens at midspan. The 150 mm wide impact surface was chosen to mitigate premature a local failure mechanism as the intent of the tests was to observe the global response of these sandwich beams and to simulate the behaviour due to the impact of large wind-borne debris. Additionally, the 150 mm impactor matched the loading surface used in the quasi-static tests by Betts et al (Betts et al. 2018a) allowing for direct comparison of the tests. The impact surface was made using a piece of a steel hollow structural section (HSS) with rounded edges to reduce any stress concentrations occurring at the edge of the loading area. The length of the impact surface was long enough such that the full width of each specimen was impacted. At both ends a specimen rebound restraint was added to ensure the specimens did not bounce after being impacted. Each support was made using a steel roller, one end was welded to the frame to simulate a pin support while the other end was placed to simulate a roller support. Each specimen was impacted either one time (R100 specimens), 50 times (R50 and R75 specimens) or until failure.

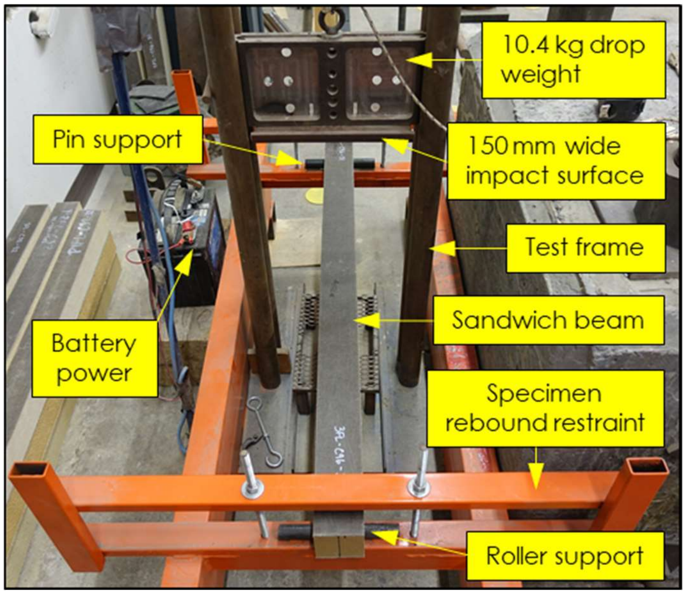

Figure 4-2. Impact test set-up

4.2.4.2. Post-Impact Flexural Tests

The post-impact flexural tests were performed based on ASTM D790 (2017) with minor modifications, such as the width and shape of the loading area. A schematic and photos of the test set-up are presented in Figure 4-3. It is important to note that the sandwich beams were tested in the same configuration as in the impact tests; the top face during the impact tests was also the top face during the post-impact flexural tests. The test frame used was bolted to a concrete strong floor. At each end the specimens were supported on roller-type supports resting on steel pedestals which were placed on the concrete strong floor. A concentrated load was applied to the beams through a 150 mm by 150 mm steel HSS section with a length long enough to ensure that each specimen was loaded across its full width. The HSS had a mass of 8.1 kg which was included in the data processing. A hydraulic actuator with a load cell attached applied displacement to the HSS a rate of approximately 15 to 20 mm per minute. For the 150 mm wide specimens, a 250 kN load cell was used. However, a 45 kN load cell was used to test the 75 mm specimens to improve the accuracy at the lower load levels. A string potentiometer was used to measure the deflection at midspan and strain gauges with 6 mm gauge lengths were used to measure the strain in each face at midspan. All data was sampled at a rate of 10 Hz.

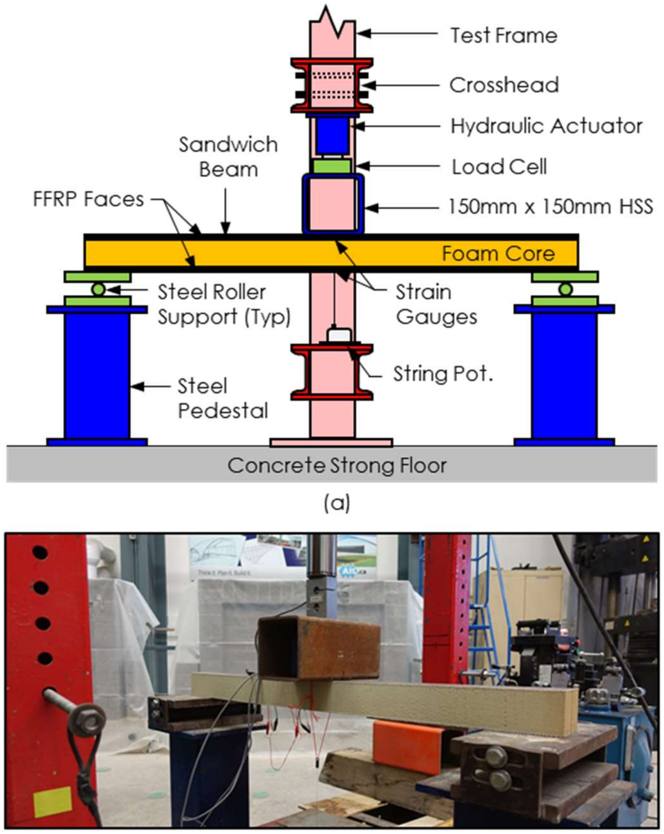

(a)

(b)

Figure 4-3. Residual bending test set-up (a) schematic (b) photo (R50 specimen)

Table 4-2. Load capacity of post-impact flexural tests

Specimen Type	Static Load Capacity (S), kN *	Static Failure Mode	Residual Load Capacity After 50 Impacts at 50% Energy (R50), kN	R50/S Ratio	R50 Failure Mode	Residual Load Capacity After 50 Impacts at 75% Energy (R75), kN	R75/S Ratio	R75 Failure Mode	Residual Load Capacity After One Impact at 100% Energy (R100), kN	R100/S Ratio	R100 Failure Mode
1FL-C32	0.65	CC/CW	0.47	0.71	CW	-	-	-	0.65	1.00	CW
2FL-C32	1.17	CS	1.27	1.08	CS	-	-	-	1.28	1.09	CS
3FL-C32	1.53	CS	-	-	-	-	-	-	1.72	1.12	CS
1FL-C64	1.18	CC/CW	1.37	1.16	CC	1.41	1.19	TR/CC	1.23	1.04	CW
2FL-C64	1.63	CW	2.32	1.42	CS	1.84	1.13	CC	2.07	1.27	CC
3FL-C64	2.31	CS	2.77	1.20	CS	2.64	1.14	CS/CC	2.73	1.18	CS
1FL-C96	1.54	TR	1.46	0.95	TR	-	-	-	1.76	1.14	TR
2FL-C96	3.35	TR	2.96	0.88	TR	-	-	-	-	-	-
3FL-C96	4.54	TR/CS	4.86	1.07	TR	-	-	-	4.80	1.06	TR
AVE				1.06			1.16			1.11	
SD				0.20			0.03			0.08	

All data was normalised to a beam width of 75 mm
AVE = Average, SD = Standard Deviation, CC = Compression Crushing, CW = Compression Wrinkling, CS = Core Shear, TR = Tensile Rupture

** Data from Betts et al (2018)*

4.3. RESULTS AND DISCUSSIONS

In this section of the paper, the results of the tests will be presented and discussed. Generally, the data processing was performed using a script written using the scientific package, Anaconda, for the programming language, Python. The results of the tests in terms of strength and stiffness are presented in Table 4-2 and Table 4-3, respectively.

Table 4-3. Stiffness of post-impact flexural test specimens

Specimen Type	Static Stiffness (S), kN/m *	Stiffness After 50 Impacts at 50% Energy (R50), kN/m	R50/S Ratio	Stiffness After 50 Impacts at 75% Energy (R75), kN/m	R75/S Ratio	Stiffness After One Impact at 100% Energy (R100), kN/m	R100/S Ratio
1FL-C32	26.77	23.77	0.89	-	-	30.26	1.13
2FL-C32	38.43	38.35	1.00	-	-	34.32 †	0.89
3FL-C32	43.38	-	-	-	-	44.06	1.02
1FL-C64	52.84	44.01	0.83	45.80	0.87	47.88	0.91
2FL-C64	58.13	62.71	1.08	66.41	1.14	69.83	1.20
3FL-C64	80.63	79.59	0.99	76.81	0.95	86.46	1.07
1FL-C96	61.36	57.58	0.94	-	-	59.26	0.97
2FL-C96	101.55	91.79	0.90	-	-	-	-
3FL-C96	124.31	120.62	0.97	-	-	116.89	0.94
AVE			0.95		0.99		1.02
SD			0.07		0.12		0.10

1. *All data was normalised to a beam width of 75 mm*
2. *Stiffnesses were determined by fitting a line to the data between load-deflection data between deflections of 1 mm and 5 mm.*

* *Data from Betts et al (2018)*

† *Stiffness was determined between deflections of 5 mm and 7 mm due to a lack of data below 5 mm.*

4.3.1. Failure Modes

The failure modes of all specimens are presented in Figure 4-4. Failure modes of all specimens [Note static specimens were tested as a part of another study by Betts et al (2018)]. In order to compare the residual failure modes with the failure modes observed during static tests, photos of sandwich specimens tested as a part of another study by Betts et al (2018a) were presented. The only notable difference in failure mode between tests of similar specimens is the failure of 1FL-C64-R75. This specimen failed due to tensile rupture during the post-impact residual flexural tests whereas the intact static specimen failed due to crushing of the compression face. This can be explained by the fact that damage in the form of visible tensile cracks was observed on the bottom face of this specimen after the impact tests. Tensile cracks were also observed in the C96-R50 specimens, sample photos of which are presented in Figure 4-5. Tensile cracking evident on bottom face of impacted specimens 2FL-C96-R50 and 3FL-C96-R50 Tensile cracking evident on bottom face of impacted specimens 2FL-C96-R50 and 3FL-C96-R50. However, the static C96 specimens failed due to tensile rupture and therefore the failure modes of the C96 specimens were not affected. Interestingly, as shown in Table 4-2, the strength of 1FL-C96-R50 and 2FL-C96-R50 were reduced, however the load capacity of 1FL-C64-R75 was higher than its static counterpart by 19%. Further research is required to determine the cause of this increase in strength of the post-impact residual tests.

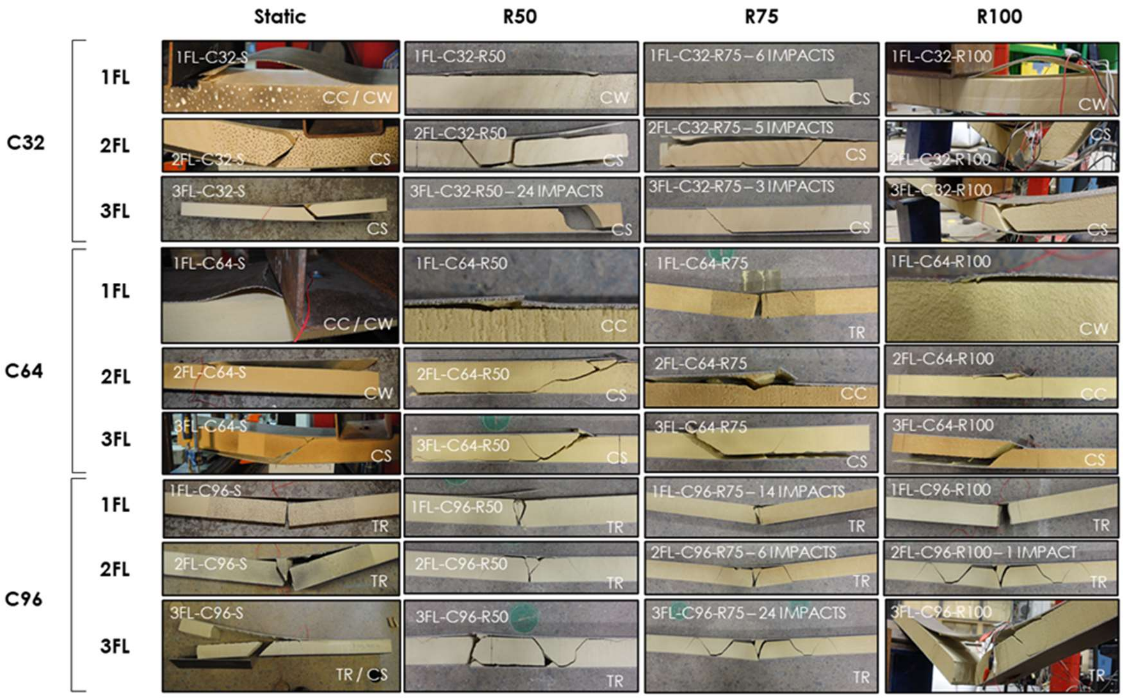

Figure 4-4. Failure modes of all specimens [Note static specimens were tested as a part of another study by Betts et al (2018)]

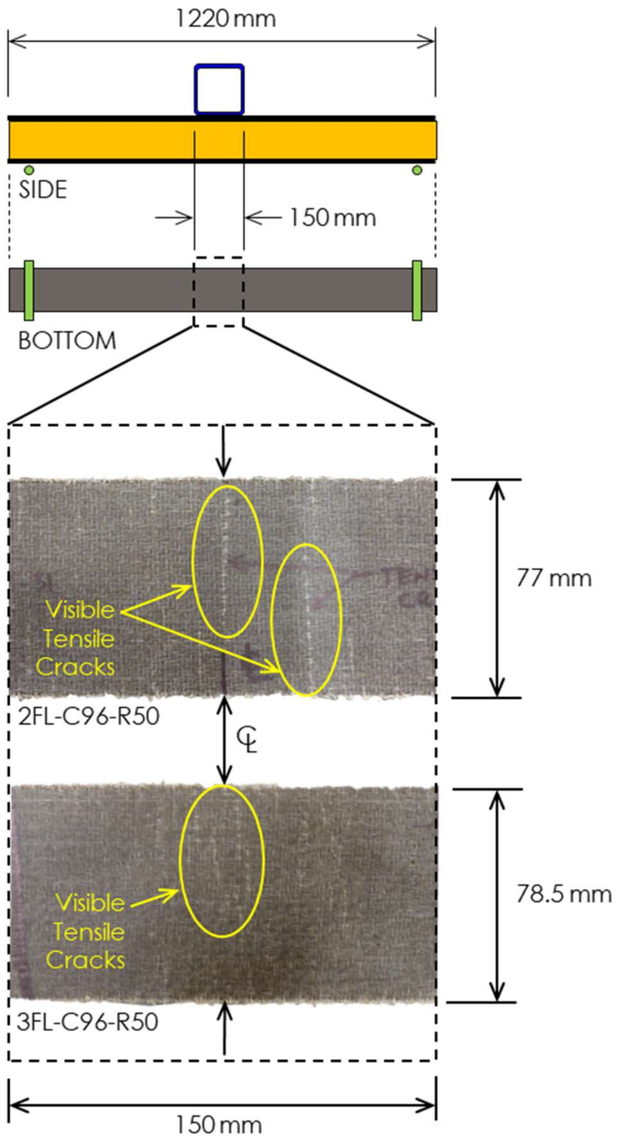

Figure 4-5. Tensile cracking evident on bottom face of impacted specimens 2FL-C96-R50 and 3FL-C96-R50

4.3.2. Impact Tests

Some specimens failed during the impact phase of the testing. The number of impacts before failure is presented in Table 4-1. One R100 specimen, 2FL-C96-R100, failed during the impact tests. The R100 impact energies were based on the energy resisted in a previous set of impact specimens that were tested by (2020a). Because these specimens were tested at drop height increments of 100 mm, it is possible that this specimen was close to energy that caused failure in the previous specimen.

For the R75 specimens, only the C64 type specimens survived the impact tests. It is hypothesized that this is based on the respective resiliency of the PIR foams and the FFRP faces. The C32-R75 specimens all failed from a core type failure, which indicates that the resiliency of the sandwich beams was limited by the 32 kg/m^3 foam. This is supported by the fact that the C64 specimens with similar face thicknesses were able to withstand higher impact energies. Similarly, it is hypothesized that as the C96-R75 specimens failed due to tensile rupture, that the resiliency of these specimens was limited by the resiliency of the FFRP faces. These hypotheses indicate that the C64-R75 specimens were at a balance point.

Of the R50 specimens, only 3FL-C32-R50 failed during the impacts. It is assumed that this is again due to the lack of resiliency of the 32 kg/m^3 foam. As specimens 1FL-C32-R50 and 2FL-C32-R50 were tested at lower energies, the capacity of the foam at the lower impact energies was sufficient enough to survive the impacts. Additionally, because 3FL-C32-R50 was tested at a lower energy than the corresponding R75 specimen, it was able to withstand more impacts before failure. As shown in Table 4-1, 3FL-C32-R50 failed after 24 impacts, whereas 3FL-C32-R75 failed after only 3 impacts.

4.3.3. Residual Behaviour After Impact

4.3.3.1. Load-Deflection Behaviour

The load-deflection curves of all specimens are presented in Figure 4-6. Residual load-deflection diagrams (normalised to a beam width of 75 mm). Additionally, the load capacity and initial stiffness of each specimen tested under residual bending are presented in Table 4-2 and Table 4-3, respectively. Initial stiffness was taken as the initial slope of the load-deflection curves presented in Figure 4-6. Residual load-deflection diagrams (normalised to a beam width of 75 mm). This initial stiffness is based on both the shear and flexural deflections which are both prevalent in sandwich beams. Therefore, it is suitable metric to investigate the effect of impact on the sandwich beams tested in this study. Figure 4-6. Residual load-deflection diagrams (normalised to a beam width of 75 mm)shows that the post-impact behaviour is similar to the behaviour of the intact specimens.

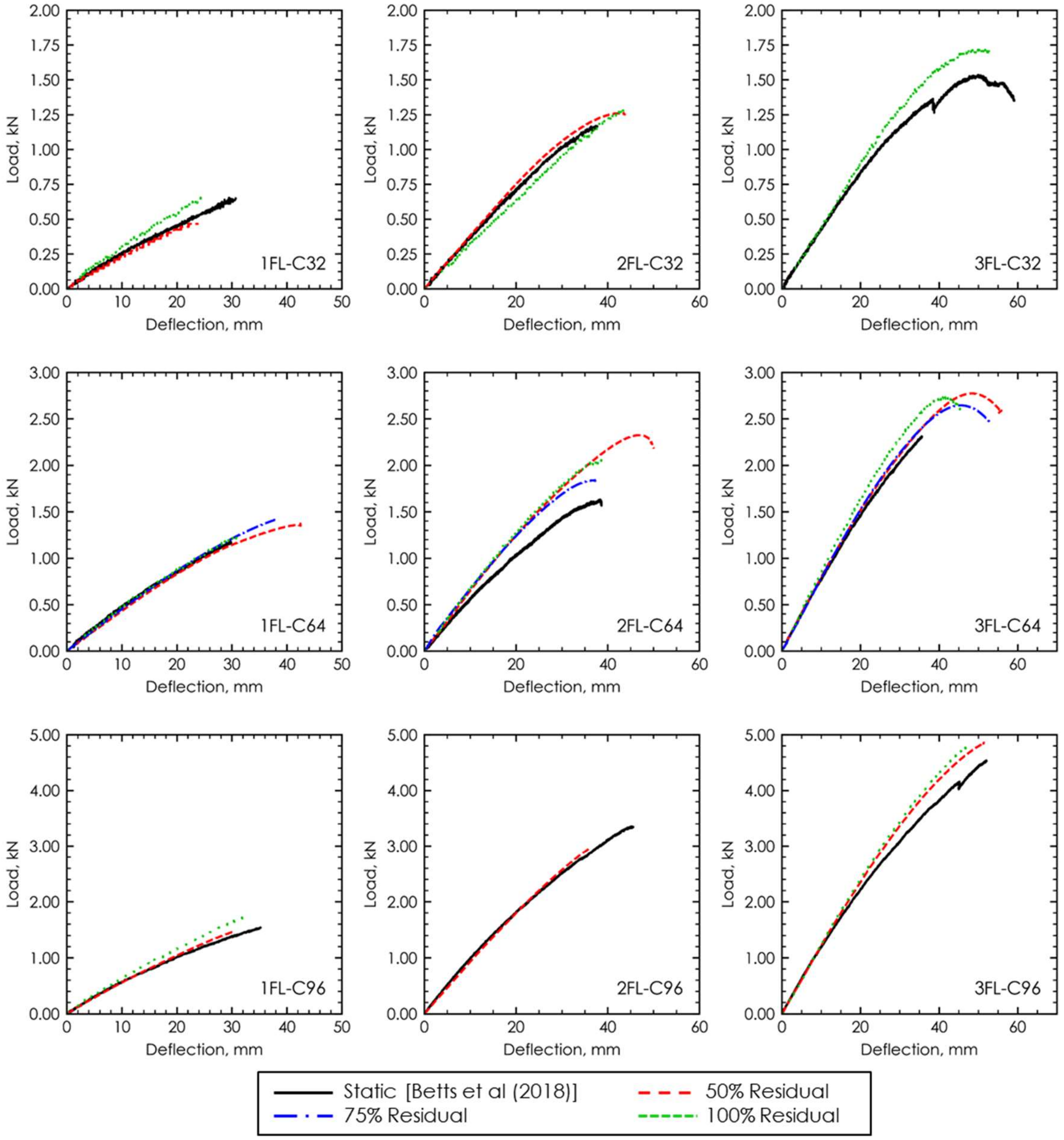

Figure 4-6. Residual load-deflection diagrams (normalised to a beam width of 75 mm)

Table 4-2 shows that there was generally no reduction of strength in the post-impact bending tests. In fact, some specimens showed an increase in strength in post-impact tests. To examine this behaviour further, paired t-tests with a confidence levels of 95% were performed using Microsoft Excel to compare each set of specimens to their intact static specimen counterparts. The results of the t-tests showed that there was no significant difference between the intact static load capacities and the load capacities of the R50 specimens. However, the t-tests indicated that, the means of the load capacities of the R75 and R100 specimen sets were statistically significantly higher than their intact static counterparts. This increase in strength is not yet well understood and requires further research. One hypothesis for this increase in strength is the potential continued curing of the faces between the quasit-static tests performed by Betts et al (Betts et al. 2018a) and the post-impact flexural tests presented in the current study. The tests performed as a part of this study were performed over a year after the initial quasi-static tests. Therefore, there is the potential that the epoxy used for the faces continued to gain strength in the period between the tests. This potential increase in FFRP strength due to curing time should be investigated in future studies by fabricated FFRP tension coupons and testing them after set amounts of curing time. Paired t-tests with confidence levels of 95% were also performed to examine the post-impact beam stiffnesses. The t-tests showed that there was no statistical difference between the stiffnesses of the intact and impacted specimens.

In order to directly compare the results of all the tests and to show that there was no effect on residual behaviour due to the impact events, the residual load capacity and stiffness of all specimens were plotted against the impact load energy, face thickness and core density in Figure 4-7. Figure 4-7a shows the effect of the energy level (regardless of number of impacts) on the residual load capacity and stiffness. This figure confirms that the energy level of the impacts did not have a significant effect on the residual load capacity of the beams. Figure 4-7b and Figure 4-7c show effects of core density and face thickness on the residual capacity and stiffness. These plots show that both the residual capacity and stiffness were significantly affected by both the core density and face thickness.

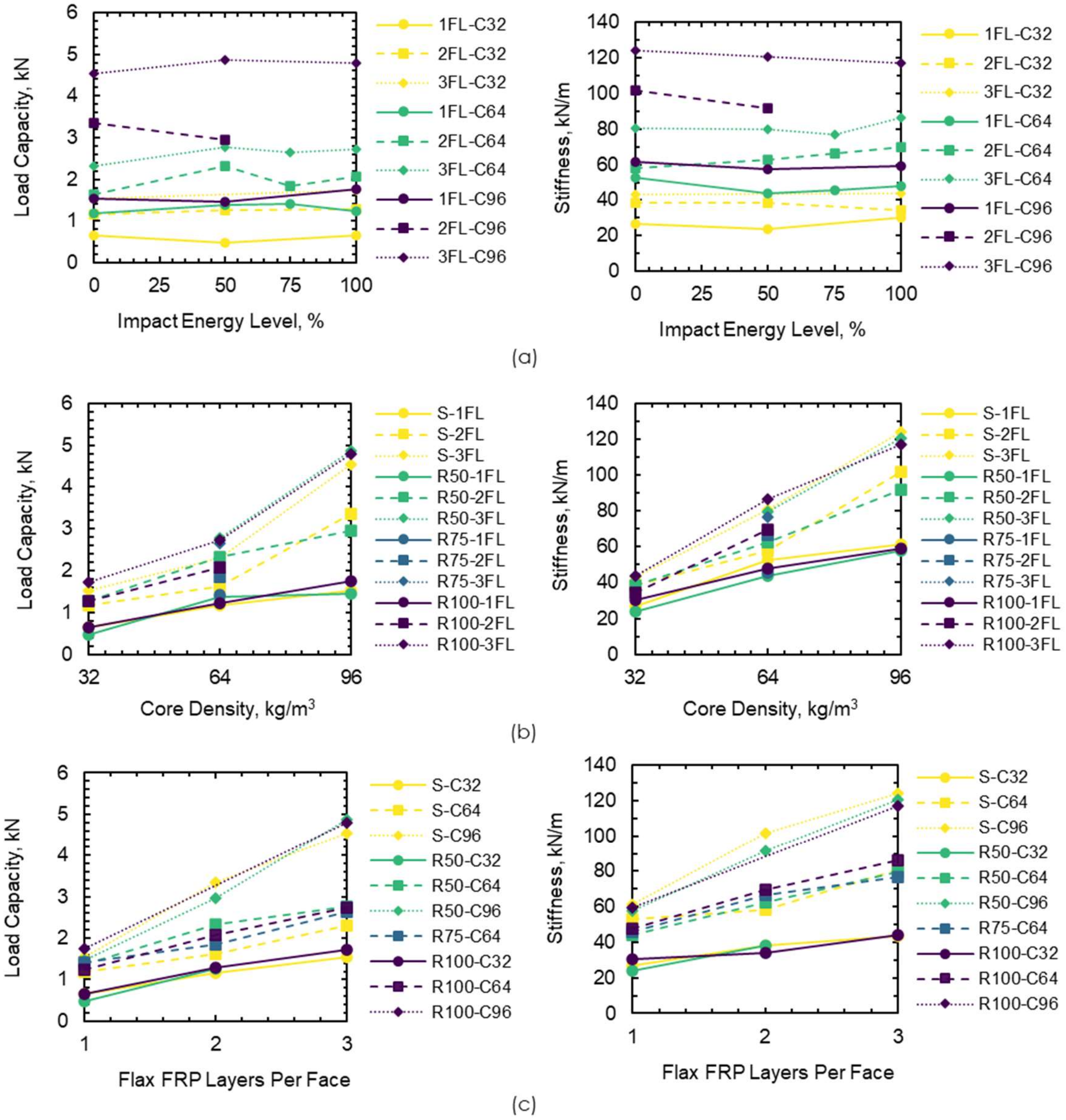

Figure 4-7. Post-impact load capacity and stiffness – effect of (a) impact energy level; (b) core density; and (c) flax FRP layers per face

4.3.3.2. Load-Strain Behaviour

The load-strain curves are presented in Figure 4-8. Based on the plots, there is some phenomenon affecting the strain in the top faces of the R50 and R75 specimens. The top face strain of these specimens is softer than the intact specimens at low load levels. It is hypothesized that this softening was caused by the development of microcracks in the matrix of the compression face during the impact events. Though there were no visible cracks observed on the compression faces, it is possible that there were cracks there that could not be seen with the naked eye.

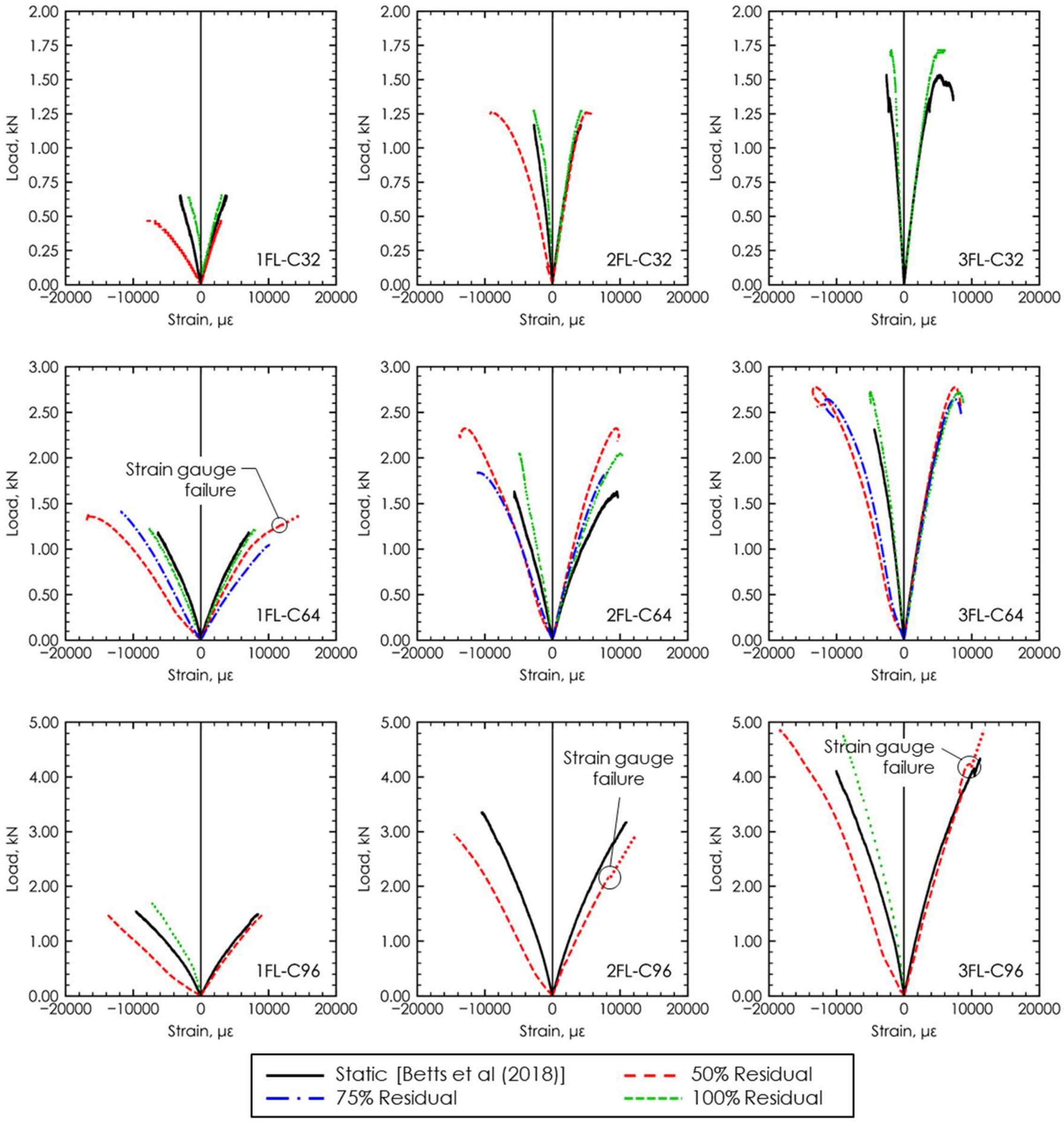

Figure 4-8. Residual load-strain diagrams with compressive strain shown as negative and tensile strain shown as positive (normalised to a beam width of 75 mm)

Figure 4-9 presents a diagram on the potential development of these cracks in the compression face and the resulting softening of the post-impact load-strain behaviour of the top face. It should be noted that previous studies on the bending after impact behaviour of sandwich structures (Baran and Weijermars 2020; Göttner and Reimerdes 2006; He et al. 2018; Klaus et al. 2012) focused on the load-deflection response and did not show the strains in the top and bottom faces. Therefore, this hypothesis has not been verified and this strain softening in the top face should be investigated further in future studies.

Each impact induced free vibration in the sandwich beams. During this free vibration the faces of the sandwich beams repeatedly changed between states of tension and compression until the beam returns to a state of rest. Therefore, it is possible for tensile cracks to have developed in the matrix of both faces during the impact events. When the sandwich beams were subsequently tested under three-point bending, the microcracks in the matrix of the top face would have to close before the full stiffness of the FFRP could be developed. This is not the case for the bottom tensile face, which is why this phenomenon was only observed on the top faces.

As shown in Figure 4-8, this load-strain softening was not observed in the R100 specimens. As it only affected the residual specimens that were impacted 50 times and not the R100 specimens, that were impacted once at a higher energy level, this indicates that this behaviour was caused by the repeated impacts.

4.3.3.3. Moment-Curvature Behaviour

The moment-curvature diagrams for all specimens are presented in Figure 4-10. Based on the diagrams, the initial flexural rigidity of the R50 and R75 specimens was significantly reduced after impacts. As the curvature was calculated based on the measured face strains, this softening of the moment-curvature diagrams is directly caused by compressive load-strain behaviour discussed earlier. The moment-curvature plots also show that the ultimate curvature of the C32 type specimens is lower than both the C64 and C96. This is because of the weaker core foams that governed failure and is evidence for these specimens, the strength of the FFRP faces was underutilized. The plots also show that the FFRP faces of the C64 specimens were underutilized as well, but to a lesser degree.

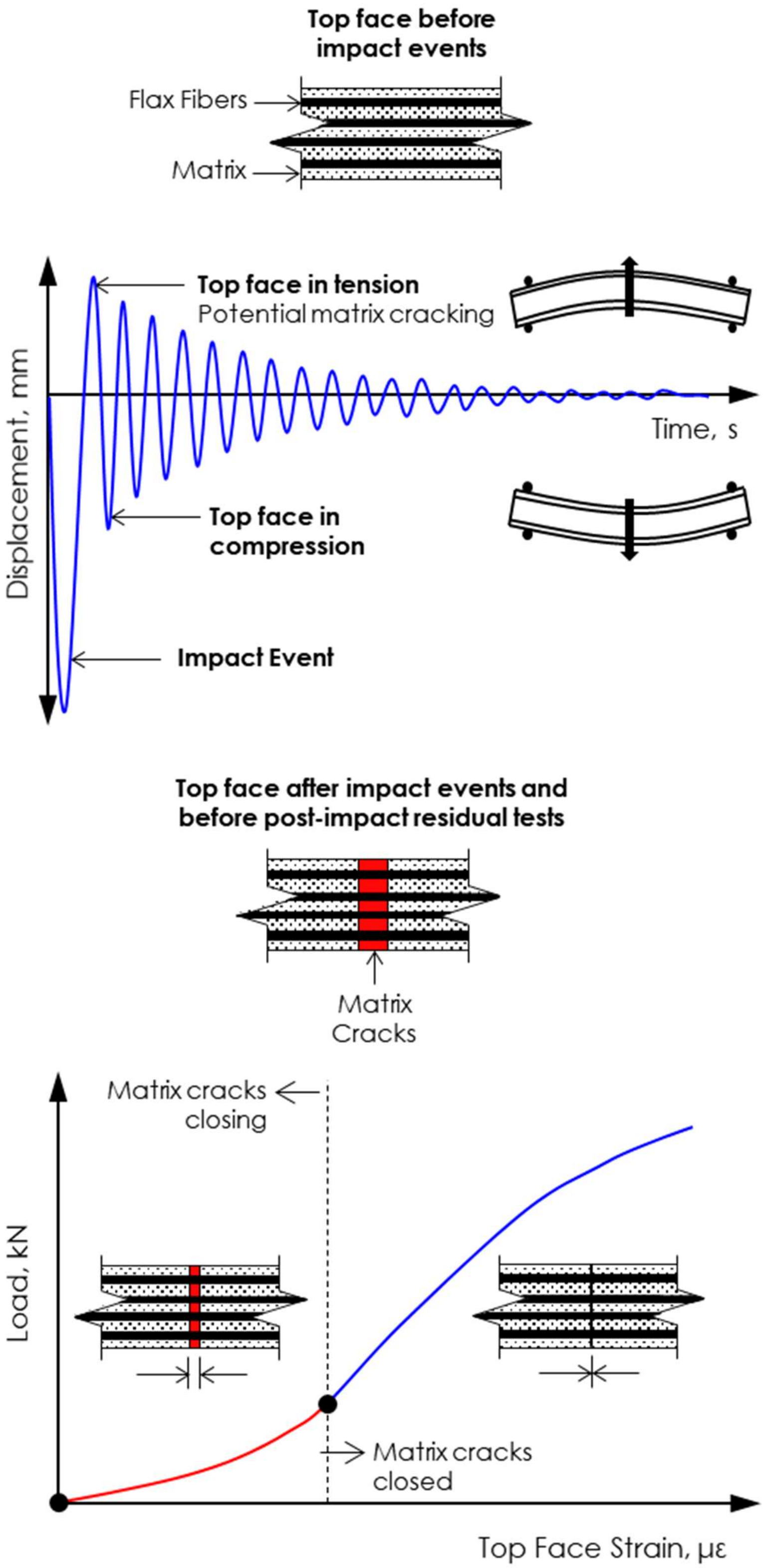

Figure 4-9. Hypothesis for the cause of increasing stiffness on compression face of impacted sandwich beams

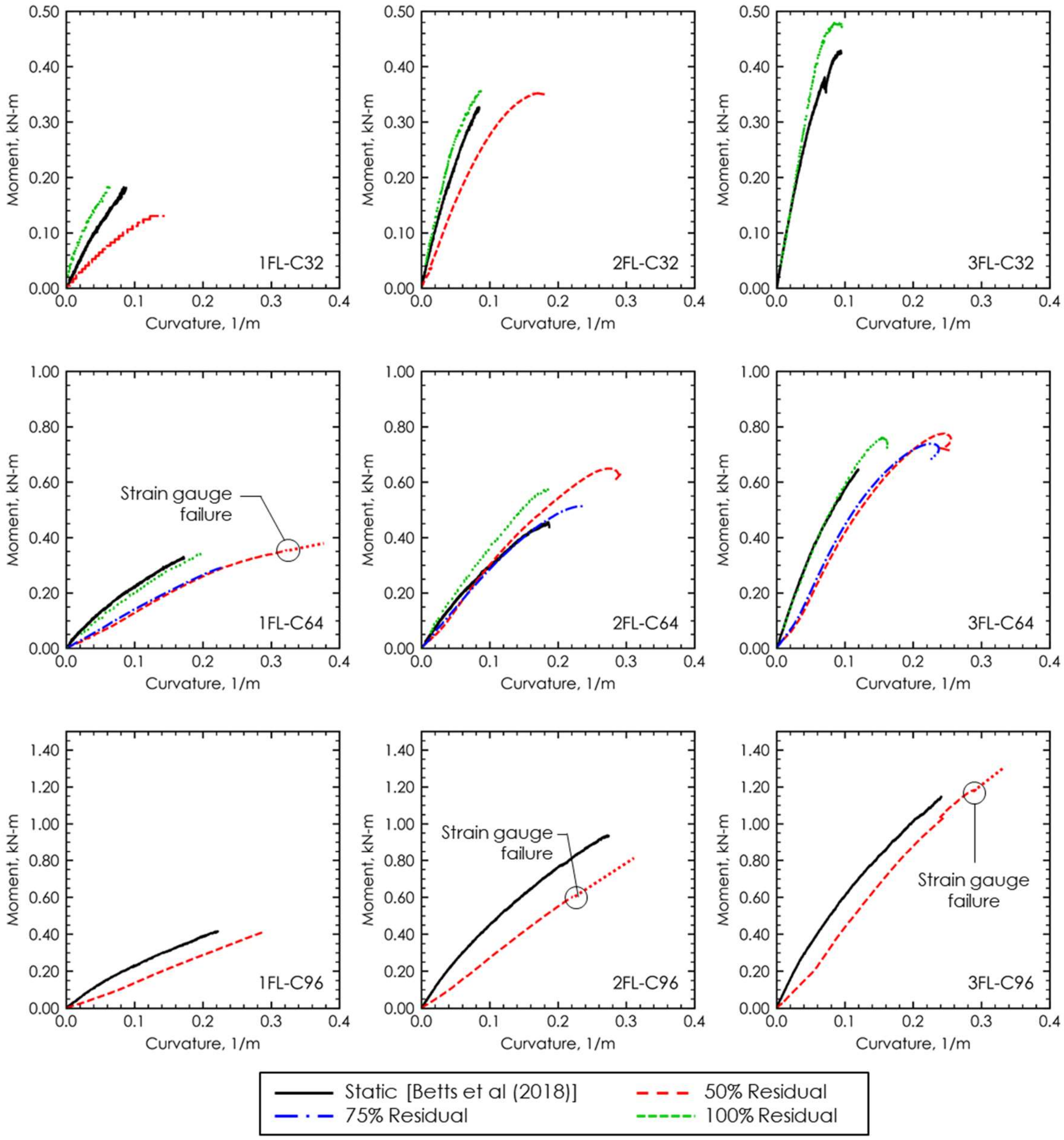

Figure 4-10. Residual moment-curvature diagrams (normalised to a beam width of 75 mm)

4.4. SUMMARY

In this chapter, the post-impact residual flexural behaviour of sandwich panels with flax fibre-reinforced polymer (FFRP) faces and polyisocyanurate (PIR) foam cores is investigated experimentally. The faces were manufactured using a wet lay-up procedure with a balanced bidirectional 2x2 twill flax fibre fabric and a bio-based epoxy with a bio-content of 30%. Each specimen was 1200 mm long x 75 mm wide x 80 mm thick. The main parameters in the study were the face thickness (one, two or three FFRP layers, representing core-to-skin thickness ratios of approximately 54, 28 and 20) and core density (32, 64 or 96 kg/m^3); a total of nine combinations. In this study, 27 specimens (three specimens for each combination) were tested under impact loads and the surviving specimens were tested under monotonic three-point bending. Each of the three identical specimens was tested under different impact condition, namely 100%, 75% and 50% of the energy resistance of an intact specimen, with the last two impacted 50 times. The results of the post-impact residual flexural tests were compared to three-point bending tests of intact specimens. The beams demonstrated remarkable resilience in that the impact events did not have a negative effect on their flexural strength or stiffness. In fact, those tested at higher energy levels exhibited a slight increase in strength after impacts. This shows their suitability for use in infrastructure applications such as building cladding panels, flooring and roofing as they retain their strength and stiffness even after multiple impacts.

CHAPTER 5: BEHAVIOUR OF FFRP-CARDBOARD SANDWICH BEAMS [4]

5.1. INTRODUCTION

With climate change being one of the major issues faced by society, it is important that new infrastructure is designed with environmental consciousness in mind. The use of natural materials, such as plant fibres in natural fibre-reinforced polymer (FRP) composites, is one method of increasing the environmental sustainability of building structures (Bensadoun et al. 2016; Christian and Billington 2011; Mak et al. 2015). Flax-FRP (FFRP) composites have gained popularity due to their comparatively high strength and stiffness (Ramesh et al. 2017) and the commercial availability of flax fabrics. To further increase the environmental sustainability of FFRPs, they can be fabricated using thermoset resins with high bio-contents (Betts et al. 2018a; Mak et al. 2015). While flax fibres have been shown to be weaker than traditional synthetic fibres, such as glass or carbon, they are biodegradable have a comparable modulus-weight ratio when compared to E-glass fibres (Mallick 2007). They also have a lower embodied energy and can be used in situations where the high strength of the synthetic FRPs have been shown to be underutilized, such as in sandwich panels where the strength of the core material often governs. (Betts et al. 2018a; CoDyre et al. 2018; Mak et al. 2015).

Sandwich structures are used when a relatively high strength and stiffness and light weight are required, such as building envelopes (Allen 1969; Fam and Sharaf 2010; Nguyen et al. 2005; Sharaf et al. 2010; Torre and Kenny 2000; Triantafillou and Gibson 1987). Sandwich structures have also been used in applications such as for floor slabs (Ferdous et al. 2019; Zhu et al. 2018), structural beams (Ferdous et al. 2018a) and railway sleepers or ties (Ferdous et al. 2018b). Sandwich structures typically have two main elements: the structural faces and the lightweight core. The core is used to resist shear forces and to separate the two faces to provide a large

---

[4] **This chapter has been published in the *ASCE Journal of Architectural Engineering:***

Betts D, Sadeghian P, Fam A. Structural Behaviour of Sandwich Beams with Flax Fibre-Reinforced Polymer Faces and Cardboard Cores under Monotonic and Impact Loads. *Journal of Architectural Engineering*. 2020; 26(2):1-12.

moment of inertia to resist flexural loading. For applications where high insulative properties are required, synthetic materials such as foam are used for the core; but when insulation is not a requirement, researchers have used natural core materials, such as cork (Boria et al. 2018; Sadeghian et al. 2018), or recycled materials, such as corrugated cardboard (Betts et al. 2019; McCracken and Sadeghian 2018; Pflug et al. 2000, 2002).

In Canada, nearly 100% of new cardboard is made from recycled materials and it is 100% biodegradable (McCracken and Sadeghian 2018; Paper & Paperboard Packaging Environmental Council 2017) making it an environmentally sustainable alternative for the traditional synthetic core materials. Because of its environmental sustainability, corrugated cardboard has been investigated for use in temperature and sound attenuation applications (Asdrubali et al. 2016; Secchi et al. 2016) as well as structural applications in small buildings (El Damatty et al. 2000) and concrete slabs (Fraile-Garcia et al. 2019). One obvious potential limitation for the use of corrugated cardboard as a core material is its susceptibility to moisture absorption which can lead to reduced capacity and permanent damage. In situations where cardboard could be exposed to high amounts of moisture, cardboard manufacturers protect the cardboard by applying a layer of wax after manufacturing. There is the potential to use this waxed cardboard as cores for sandwich panels where there is increased risk to moisture exposure. Another limitation is the low fire resistance of these structures. However, even with this limitation, these structures are potentially suitable for use as non-fire rated wall partitions in buildings due to their light weight, environmental-friendliness and aesthetic appeal.

Another potential application for these sandwich structures is non-load bearing building enclosures or cladding systems. These enclosure systems are primarily loaded in the lateral direction due to wind and air pressure and therefore it is important to understand their flexural behaviour. For this reason, sandwich structures have been examined under flexural loads (CoDyre et al. 2018; Ferdous et al. 2018a; Manalo et al. 2016; Petras and Sutcliffe 1999; Sadeghian et al. 2018; Sharaf and Fam 2012; Vitale et al. 2017). Additionally, during storm events, building exteriors can be subject to impact loads from flying debris during storm events. Therefore, it is also important to understand the impact behaviour of the panels and the residual properties after an impact event and as such sandwich structures have been studied extensively under impact loads (Anderson and Madenci 2000; Atas and Potoglu 2016; Betts et al. 2018b; Chai and Zhu 2011; Plagianakos and Papadopoulos 2014; Schubel et al. 2005; Torre and Kenny 2000; Zhu and Chai 2013) and air blast loads (Andrews and Moussa 2009) .

The currently available research on sandwich panels with cardboard cores has focused on small-scale specimens with plain cardboard cores under static loads (McCracken and Sadeghian 2018; Pflug et al. 2000, 2002). There remains a gap in the research on the performance of large-scale sandwich beams with FFRP faces and natural or recycled cores under static loads and especially on their behaviour under impact loads. It is important to understand the behaviour of large-scale panels as they more accurately represent the behaviour of actual structures. Large scale tests also remove the potential for size effects to influence the test results, especially under impact loads. In the current study, large-scale sandwich beams constructed with plain and waxed corrugated cardboard cores and FFRP faces were fabricated and tested under monotonic, impact and post-impact residual monotonic loads. The aim of the current study is to show that these panels have the required strength and impact resistance to act as wall partitions in buildings. Additionally, through the use of the waxed cardboard cores with higher resistance to moisture absorption, these panels also have potential for use in applications with more exposure to moisture, such as in building cladding systems. Finally, an existing model developed for similar large-scale sandwich beams with FFRP faces and foam cores was used to accurately predict the monotonic behaviour of the beams in the current study.

5.2. REASEARCH SIGNIFICANCE

As the effects of climate change become increasingly evident, it is important that engineers and designers consider the environmental impact of new infrastructure designs. This research provides new information to the field of sustainable infrastructure design through the testing and analysis of building materials comprised of natural and recyclable materials. The use of natural materials, such as flax fibres, for the construction of sandwich structures with foam cores has been studied in the recent past (Betts et al. 2018a; CoDyre et al. 2018; Mak et al. 2015; Mak and Fam 2019a; Sadeghian et al. 2018). To further increase the sustainability of these structures, the current study is examining a more sustainable alternative for the core material in the form of corrugated cardboard, which is both recyclable and biodegradable. While the potential limitations of using cardboard as a core material are recognized, there are applications for sandwich structures with these cores, especially as non-fire-rated wall partitions. The aim of this study is to provide test data and analysis methods for the use of biodegradable sandwich panels for use in environmentally sustainable structural and architectural design of buildings. These panels could especially be used as part of new environmentally sustainable structures and innovative construction projects. This paper presents the test data of these sandwich panels under monotonic loads and impact loads and shows that they can be accurately analysed using a simplified procedure which makes structural and architectural design using these structures feasible.

5.3. EXPERIMENTAL PROGRAM

In this section, the experimental program is discussed. First, the test matrix is presented, and the naming convention is explained. The materials used are described and the specimen fabrication procedure is discussed at length. Finally, the test set-ups and procedures are presented.

5.3.1. Test Matrix

Twelve sandwich beams with cardboard cores and FFRP faces were tested: six specimens with plain cardboard cores and six with waxed cardboard cores. Each specimen was 1200 mm long, 150 mm wide and approximately 80 mm thick. The specimens were constructed of two-layer FFRP faces and 75 mm thick corrugated cardboard cores. Three specimens of each type were tested under monotonic three-point bending and three of each type were tested under a drop weight impact at midspan. The monotonic tests were performed first, and the first drop height of the impact tests was based on the results of the static tests. The naming convention for the specimens was as follows: [P/W]C-[S/D]-X, where P is plain, W is waxed, S is static, D is dynamic, and X is a sequential number used to distinguish identical specimens. The test matrix is presented in Table 5-1.

Table 5-1. Test matrix for one-way sandwich beams with cardboard cores

Specimen Group	Quantity	Core Type	Test Type
2FL-PC-S	3	Plain Cardboard	Static
2FL-PC-D	3	Plain Cardboard	Dynamic (Impact)
2FL-WC-S	3	Waxed Cardboard	Static
2FL-WC-D	3	Waxed Cardboard	Dynamic (Impact)

5.3.2. Materials

The FFRP faces were fabricated using a bio-based epoxy resin and a balanced bidirectional flax fabric. The resin matrix was bisphenol A epoxy with a reported tensile strength and modulus of 53.2 MPa and 2.65 GPa, respectively and a compressive strength of 77.9 MPa (Entropy Resins 2013a, 2015). This resin was used for the fabrication of the FFRPs as well as the connection between the faces and core. It should be noted that the reported strength and modulus are based on using the epoxy matrix with a fast-setting hardener (Entropy Resins 2013a). For the current project, a longer pot life was required and therefore a slow-setting cycloaliphatic polyamine hardener was used (Entropy Resins 2013b). Therefore, to understand of the constitutive behaviour of the FFRP matrix material the epoxy-hardener combination used in this study was tested under uniaxial tension. The tensile strength and modulus of the epoxy mixed with the slow-setting hardener were tested and measured to be 57.9 MPa and 3.20 GPa, respectively (Betts et al. 2018a). The flax fabric used was a balanced bidirectional 2x2 twill fabric with a reported areal mass of 400 g/m^2, which was measured to be 410 g/m^2.

The properties of the FFRPs used in this study were investigated previously by Betts et al (2018a). The tensile strength, modulus and elongation of the FFRP faces were found to be 45.4 MPa, 7.51 GPa and 0.0083 mm/mm, respectively. Betts et al (2018b) used a novel test method to determine the properties of the FFRPs in compression. The compressive modulus was found to be 6.73 GPa and ultimate strength and corresponding strain were found to be 86.4 MPa and 0.0327 mm/mm, respectively.

Two types of cardboard were supplied by a local manufacturer for this study: plain corrugated cardboard and waxed corrugated cardboard. For each type of cardboard, ten random samples were selected, and their properties measured. The plain cardboard strips used had an average thickness of 4.1 mm and an average density of 127 kg/m^3. The waxed cardboard strips used had an average thickness of 4.1 mm and an average density of 166 kg/m^3.

5.3.3. Specimen Fabrication

To construct the sandwich beams, the first step was the manufacturing of the core. Each plain cardboard core was created by adhering multiple strips of cardboard together, as shown in Figure 5-1, to achieve the required specimen width. The strips were provided by the cardboard manufacturer and adhered using the same glue used in the manufacturing of the cardboard. As shown in Figure 5-1a, two rails were fastened to a worktable at right angles. The first strip of plain cardboard was placed firmly against each rail by hand. For each subsequent strip, a small amount of glue was applied before placement next to the previous strip as show in Figure 5-1b. The fabrication of the waxed cores was altered slightly because the glue did not cure as quickly, which allowed it to migrate downwards before curing. Therefore, the waxed strips were stacked vertically as opposed to horizontally. That is, that the first strip of waxed cardboard was placed flat on the table surface and glue was applied to the top face. Each subsequent strip was then placed on top of the previous strip.

After all cardboard strips were placed (i.e. such that the overall width was 150 mm), weights were placed against the core and glue while allowed to cure. This is shown in Figure 5-1c. Once the glue had cured, the top and bottom surfaces of the cardboard cores were sanded to create a flat surface for applying the FFRP faces as shown in Figure 5-1d. As will be discussed further in the results section of this paper, this part of the fabrication procedure is vital to ensure a secure bond between the core and faces. The densities of the plain cardboard cores and waxed cardboard cores were 136 kg/m^3 and 174 kg/m^3 respectively.

The faces were made using a wet lay-up procedure. First, a layer of parchment paper was placed on a flat work surface. Once the work surface was prepared, the bio-based epoxy was mixed with slow-set hardener. A layer of the mixed epoxy was applied to the parchment paper to cover the area of the flax fabric, which was 600 mm wide and 1200 mm long, and a layer of flax fabric was placed on the wetted section of parchment paper. A plastic scraper was then used to push out any air from under the placed section of flax fabric. This was done by pushing the plastic scraper longitudinally along fabric in one direction, which also worked to soak the fabric in resin layer below. Then, a second layer of epoxy was applied to the surface of the flax fabric and another layer of flax fabric was placed and smoothed with a plastic scraper as described above. The surface of the fabric was then wetted with another layer of epoxy and three cardboard cores were placed on the wetted surface as shown in Figure 5-1e. The face was allowed to cure at room temperature for seven days at which point the entire procedure was completed again for the second face. It should be noted that the curing took place in a ventilated air-conditioned room. Once the second face was cured, the specimens were cut out using a band saw and all cut edges were sanded smooth.

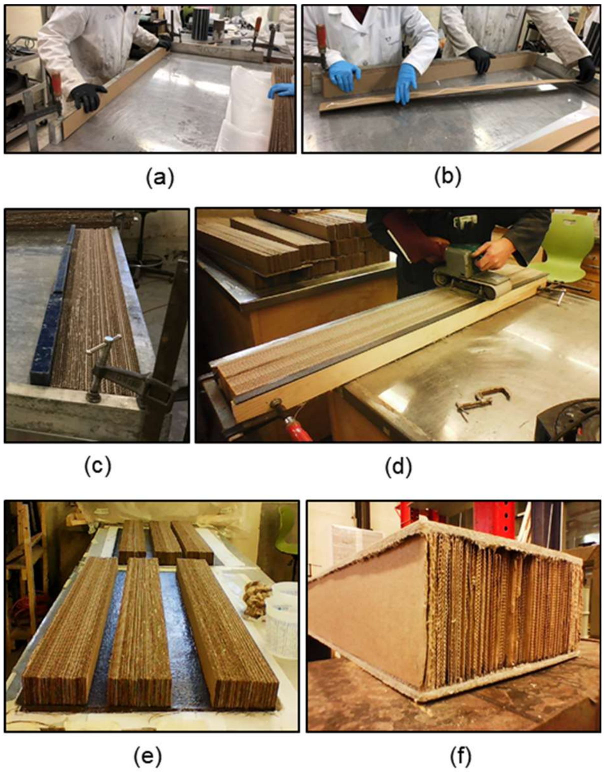
(a) (b) (c) (d) (e) (f)

Figure 5-1. Specimen fabrication: (a) placement of first cardboard strip; (b) gluing and placement of subsequent cardboard strips; (c) glue drying on plain cardboard core; (d) sanding top of cardboard core (e) cardboard cores placed on FFRP face and; (f) finished specimen

5.3.4. Test Setup and Instrumentation

As a part of this study, two types of tests were performed: static tests and impact tests. For both tests, the load/impact was applied at the midspan through a 150 mm wide loading surface made from a steel hollow structural section (HSS) to mitigate the local failure mechanisms, such as indentation. The specimens were instrumented with strain gauges on the top and bottom faces at midspan as well as a connection point for a string potentiometer on the bottom face at midspan. For both tests, the same fast-action string potentiometer was used.

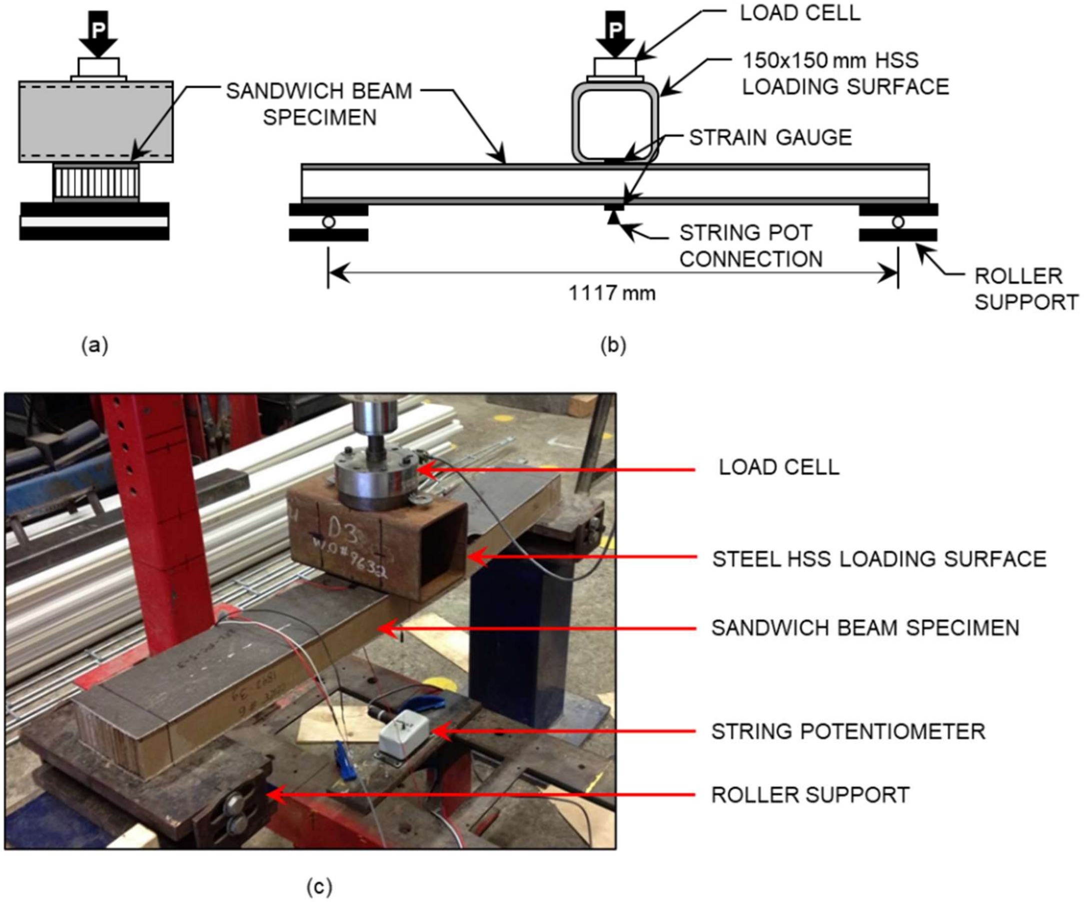

Figure 5-2. Monotonic test set-up (a) end view schematic; (b) side view schematic and; (c) photo

5.3.4.1. *Monotonic Tests*

The procedure for ASTM D790 (ASTM 2017) was adopted for these tests, with some changes, such as the width and shape of the loading surface. All details for the tests are shown in the three-point bending test set-up presented in Figure 5-2. Both supports were roller type supports. The test frame used was bolted to a concrete strong floor. An actuator with a load cell attached applied load to the specimen through a 150 mm wide HSS. All data was sampled at a rate of 10 Hz.

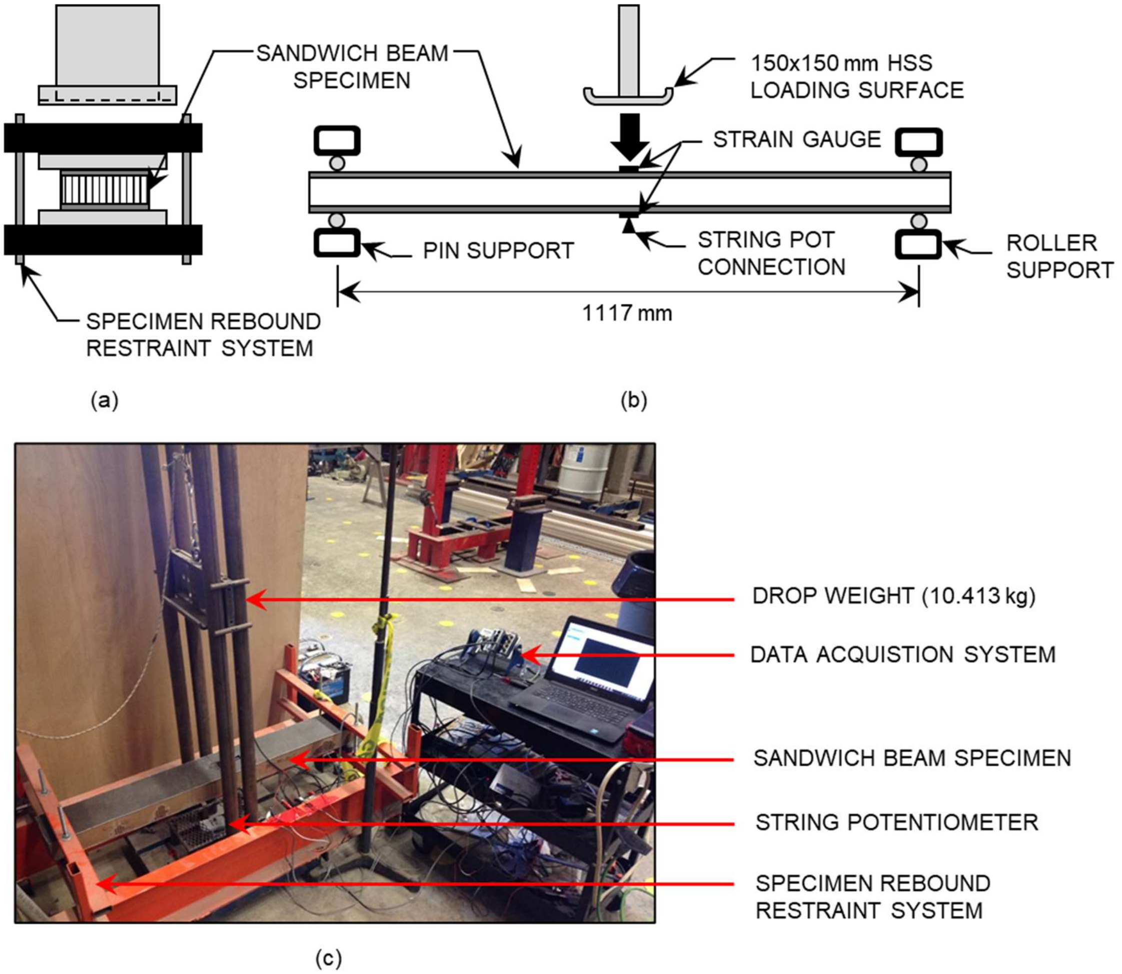

Figure 5-3. Impact test set-up (a) end view schematic; (b) side view schematic and; (c) photo

5.3.4.2. Impact Tests

The impact test set-up is presented in Figure 5-3. In order to directly compare the impact tests with the monotonic tests and to observe the one-way bending during impact of the panels, almost the same test set-up was used as in the monotonic tests. For the design of the drop weight frame and test, ASTM D7136 (ASTM 2005) was adopted where applicable. A 10.4 kg weight was used to impact the specimens at midspan in a self reaction test frame. The first drop height was determined based on the average energy that caused failure in monotonic tests of all specimens. Then, based on the performance of the first drop test, the subsequent drop heights were selected. This will be discussed in detail in the results section of this paper. As shown in Figure 5-3, each sandwich beam was simply supported by one pin-type support and one roller support. At both supports, an upper fixture was used to stop specimens from lifting off supports after impact. An accelerometer was attached to the drop weight. All data was sampled at a rate of 25 kHz. A 25 mm diameter hole was cut into the center of HSS impact surface to ensure that the top face strain gauge was not damaged during the impact.

5.4. RESULTS AND DISCUSSIONS

In this section the experimental and analytical results are discussed. The behaviour of the specimens under monotonic three-point bending are presented and the effect of waxing the core is examined. Then, the use of design-oriented model developed by Betts et al. (2018b) for sandwich panels with foam cores is used to examine its applicability to predict the behaviour of cardboard core FFRP-sandwich beams. The behaviour of the specimens under a single impact event is presented and discussed. After the impact event the specimens were tested to determine their post-impact residual strength. The results of these tests are presented and compared to the results of the monotonic test results of the intact specimens.

5.4.1. Monotonic Behaviour

The results of the monotonic three-point bending tests are presented in Table 5-2 and a photo of the failed specimens is presented in Figure 5-4. As shown in Table 5-2 there is a high variance in the maximum loads sustained by identical sandwich beam specimens. The maximum load results of the plain core specimens and waxed core specimens had coefficient of variation (CV) of 22% and 47%, respectively. The load capacity was greatly affected by the strength of the connection between the faces and core, specifically on the compression face. This was evidenced by the failure modes observed during the tests.

Table 5-2. Monotonic test results

Specimen	Mass, kg	Ultimate Load, kN	Max Deflection, mm	Specific Strength, kN/kg	Stiffness, N/mm	Ultimate Moment, kN-m	Max Curvature, 1/km	Flexural Rigidity, kN-m^2	Failure Mode
2FL-PC-S-1	2.844	2.91	15.4	1.02	271.0	0.81	115	10.39	CW
2FL-PC-S-2	2.823	4.26	22.6	1.51	263.2	1.19	169	11.27	CW
2FL-PC-S-3	2.769	4.51	24.8	1.63	236.3	1.26	132	14.21	CW
AVE	2.812	3.89	20.9	1.4	256.9	1.09	139	11.96	
SD	0.038	0.86	4.9	0.3	18.2	0.24	27	2.00	
2FL-WC-S-1	3.267	3.96	17.9	1.21	348.6	1.10	129	11.86	CW
2FL-WC-S-2	3.258	2.10	14.3	0.64	344.1	0.59	53	12.46	CW
2FL-WC-S-3	3.456	5.84	38.2	1.69	390.9	1.63	254	13.92	CS
AVE	3.327	3.96	23.5	1.2	361.2	1.11	145	12.74	
SD	0.112	1.87	12.9	0.5	25.8	0.52	101	1.06	

* *CW = Compression Face Wrinkling; CS = Core Shear, AVE = Average, SD = Standard Deviation*

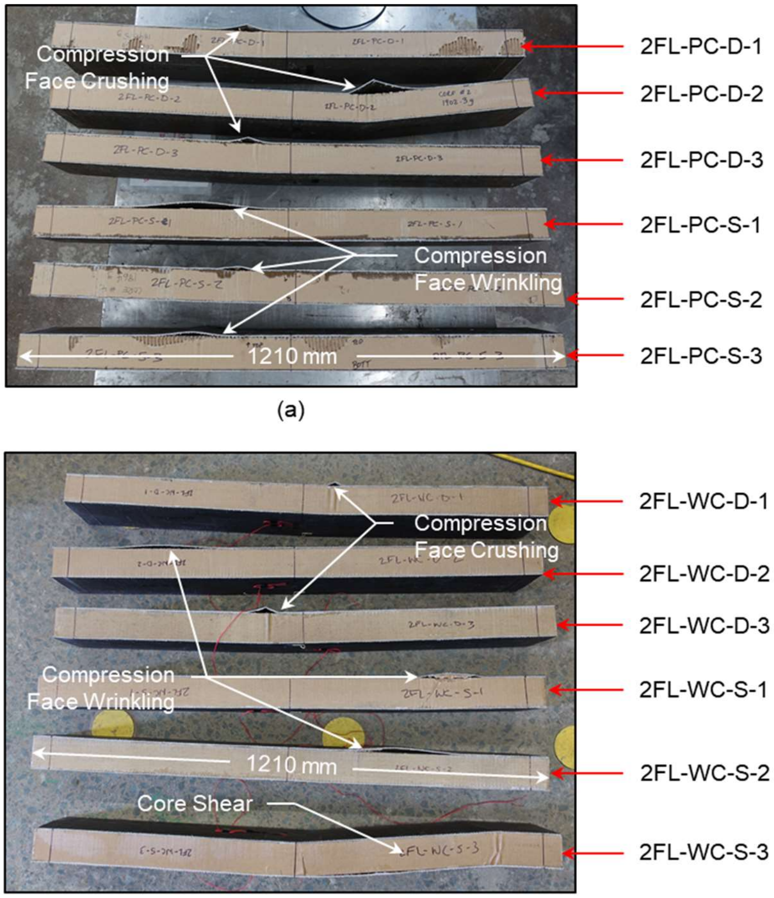

(a)

(b)

Figure 5-4. Failed specimens (a) plain core specimens; (b) waxed core specimens (note that specimens 2FL-WC-D-2 and 2FL-PC-D-2 failed under impact and were not tested for residual properties)

5.4.1.1. Failure Modes

Figure 5-4 shows each specimen after testing and the failure of each specimen. All statically tested specimens failed by compression face wrinkling save 2FL-WC-S-3 which failed due to core shear. As shown in Table 5-2, this specimen exhibited the highest peak load. This indicates that if the connection between the face and core could be improved, the failure load could be increased for specimens that failed in compression wrinkling. The compression wrinkling could be considered as a premature failure of these specimens and highlights the importance of the connection between the face and core. The authors believe that the separation between the compression face and the core was due to an increase of tensile stresses between the two layers as the compression face buckles away from the core. To resist this compression face wrinkling there needs to enough surface area between the face and core to withstand the tensile stresses developed at the interface. Therefore, in future studies, additional measures should be implemented to improve the interface between the core and faces, such as: the use of a plane flatten the surface of the cardboard cores and the use of a veil to provide more area for the adhesive between the face and the core.

5.4.1.2. Load-Deflection Behaviour

Figure 5-5a shows the load-deflection results of the static tests. From the plot, it can be seen that the specimens exhibited a nonlinear load-deflection behaviour before ultimate failure. It can also be seen that the specimens exhibited a high variance in strength. This is due to the assumed premature failure due to the weak interface between the cardboard cores and the FFRP faces. Table 5-2 shows the results of the tests. Note that the specific strength of the beams was calculated by dividing the ultimate load by the specimen mass within the span length. The stiffnesses shown in Table 2 were calculated by applying a linear fit of the data between a load of 0 kN and 1.5 kN, which is within the first linear portion of all tested specimens, as seen in Figure 5-5a. Table 5-2 shows that the average stiffness of the WC specimens is 361.2 ± 25.8 N/mm, which is 41% higher than the PC specimens which have an average stiffness of 256.9 ± 18.2 N/mm. However, due to the high variability of the data, there was no significant difference in the peak loads or specific strengths sustained by specimens with different core types.

5.4.1.3. Moment-Curvature Behaviour

Figure 5-5b shows the moment-curvature behaviour of the static tests. All specimens exhibited a nonlinear moment-curvature relationship. By examining the plot and the results presented in Table 5-2, it can be seen that the flexural rigidities of the sandwich beams are not significantly affected by the core type. The average flexural rigidity of the WC specimens was 12.74 ± 1.06 kN-m^2 and the average flexural rigidity of the PC type specimens was 11.96 ± 2.00 kN-m^2. The flexural rigidities were determined by fitting a line to the first linear portion of the plots between a moment of 0 kN-m and 0.3 kN-m. As the moment was calculated based on the load, there is also no significant difference in the moment capacity of the beams, as discussed above.

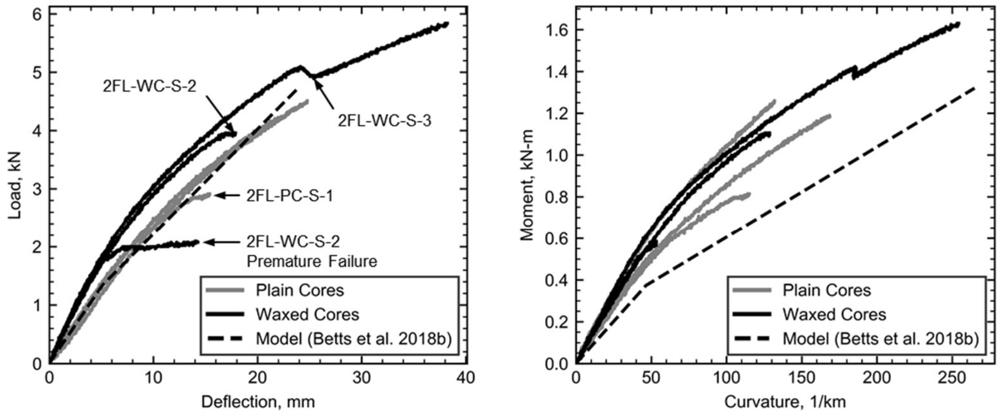

(a) (b)

Figure 5-5. Test results of monotonic three-point bending tests (a) load-deflection; (b) moment-curvature

5.4.1.4. Modelling

The load-deflection and moment-curvature plots for all specimens were nonlinear. In a previous study, Betts et al. (2018b) attributed this nonlinear behaviour to the intrinsic nonlinear behaviour of the FFRP faces. They presented a design-oriented model to predict the load-deflection and moment-curvature behaviour of sandwich beams with nonlinear FFRP faces and foam cores under three-point and four-point bending. Numerous authors have noted the approximately bilinear behaviour of FFRPs and other natural fibre FRPs (Bensadoun et al. 2016; Betts et al. 2018a; Christian and Billington 2011; Hristozov et al. 2016; Mak et al. 2015; Sadeghian et al. 2018). Through preliminary testing of flax fibres and their composites, Betts et al. (2017, 2018c) have shown that the nonlinearity of FFRPs is likely due to the behaviour of the flax fibres. Therefore, the model by Betts et al. (2018b) assumes that the faces act in a bilinear fashion which in turn causes a bilinear behaviour of the sandwich panels. The same face material used in the study by Betts et al. (2018b) was used in the current study and therefore the same bilinear model was adopted for the faces. The model allows the user to find the stiffness and strength of the sandwich beams. Some authors in this field have performed tests on sandwich beams with multiple spans and were able to determine the shear modulus (Ferdous et al. 2017; McCracken and Sadeghian 2018). However, with only one span length in these tests, this was not possible for these tests.

The model assumes that the FFRP faces in a perfectly bilinear fashion and that the neutral axis is located approximately at the midplane (Betts et al. 2018a). The primary and secondary moduli are determined using Eq. 5-1 and Eq. 5-2.

$$E_{f_1} = \frac{1}{2}(E_{f_t} + E_{f_c}) \tag{5-1}$$

$$E_{f_2} = \frac{1}{2}(\frac{2}{3}E_{f_t} + \frac{2}{5}E_{f_c}) = \frac{1}{3}E_{f_t} + \frac{1}{5}E_{f_c} \tag{5-2}$$

where E_{f1} is the initial modulus, E_{f2} is the secondary modulus, E_{ft} is the initial tensile modulus and E_{fc} is the initial compression modulus.

The load-deflection behaviour based on two points: a "point-of-transition" where the FFRP changes from its initial modulus to its secondary modulus and the ultimate point, where the ultimate strain of the FFRP is reached. The point-of-transition load and deflection can be calculated using Eq. 5-3 and Eq. 5-4, respectively, and the ultimate load and deflection can be determined using Eqs. 5-5 through 5-7 (Betts et al. 2018a, 2020b).

$$P_0 = \frac{4tbdE_{f_1}\epsilon_{f_0}}{L} \tag{5-3}$$

$$\Delta_0 = \frac{L^2}{6d}\epsilon_{f_o} + \frac{P_0 L}{4G_c(\frac{bd^2}{c})} \tag{5-4}$$

$$P_u = \frac{4tbd[E_{f_1}\epsilon_{f_0} + E_{f_2}(\epsilon_{f_u} - \epsilon_{f_0})]}{L} \tag{5-5}$$

$$\Delta_u = \frac{L^2}{12d}\left[(1+\lambda)\epsilon_{f_0} + (2-\lambda-\lambda^2)\epsilon_{f_u}\right] + \frac{P_u L}{4G_c(\frac{bd^2}{c})} \tag{5-6}$$

where t is the thickness of the FFRP faces, b is the beam width, d is the distance between the face centroids, ϵ_{fo} is the strain at the point-of-transition determined by Betts et al. (2018b) to be 0.0018 mm/mm, ϵ_{fu} is the ultimate tensile strain of the FFRPs, L is the span length, G_c is the shear modulus of the core and λ is a parameter found using Eq. 5-7.

$$\lambda = \frac{1}{2 + 2\frac{E_{f_2}}{E_{f_1}}\left(\frac{\epsilon_{f_u}}{\epsilon_{f_0}} - 1\right)} \tag{5-7}$$

The corresponding moments can be found by simply converting the loads to moments using the relation for three-point bending, $M_i = P_i L / 4$. The corresponding curvatures can be found simply by $\psi_i = 2\epsilon_i / d$. After the general model has been developed the failure loads are found by using the procedure presented by Triantafillou and Gibson (1987) and subsequently used by Betts et al. (2018b).

The cardboard core material used in this study does not have data available. However, the same C-type flute cardboard was used by McCracken and Sadeghian (2018) and through their tests, they determined an approximate shear modulus (G_c) of 121.9 MPa. However, the compressive modulus and shear strength are unknown. To allow for modelling, these values were assumed based on the shear modulus by examining the relationship between the same properties of the foam cores used in the study by Betts et al. (2018b). It was found that the compressive modulus of the foams was typically 2.5 times that of the shear modulus and that the shear strength of the foams was typically 0.075 times that of the shear modulus of the foams. Therefore, in this study, the compressive modulus of the cardboard was assumed to be $E_c = 2.5G_c$ and the shear strength was assumed to be $\tau_{cu} = 0.075G_c$.

Table 5-3. Results of monotonic design-oriented model

Specimen Group	Ultimate Load, kN	Max Deflection, mm	Stiffness, N/mm	Ultimate Moment, kN-m	Max Curvature, 1/km	Rigidity, kN-m^2	Failure Mode
Model	4.72	23.9	262.3	1.32	218	8.02	TR/CC
PC Tests	3.89	20.9	256.9	1.09	139	11.96	CW
PC-Model Ratio	0.82	0.88	0.98	0.82	0.63	1.49	N/A

The results of the model are presented in Figure 5-5 and Table 5-3. The model is able to predict the load-deflection behaviour of the sandwich beams well as presented in Figure 5-5a. The stiffness predicted by the model was 262.3 N/mm compared to the average stiffness of the PC specimens of 256.9 N/mm, a difference of less than 2.5%. However, the model overpredicts the ultimate load capacity and ultimate deflection with PC test-to-model ratios of 0.82 and 0.88, respectively. The moment-curvature model shown in Figure 5-5b captures the behaviour of the beams well, however, it slightly underpredicts the initial flexural rigidity (*EI*, initial slope of the plot). As shown in Table 5-3, the PC test-to-model ratio of the flexural rigidity is 1.49.

5.4.2. Impact Behaviour

The results of the impact tests are presented in Table 5-4 and the tested specimens are shown in Figure 5-4. The impact data was sampled at a rate of 25 kHz and included the strain in the top and bottom face at midspan and the specimen displacement at midspan. These specimen displacement measurements were used to calculate the specimen damping ratio, ξ, and specimen stiffness, K.

To determine the damping ratio, the damped period of each specimen was needed. This was found by measuring the average time between the local maxima and minima displacements during free vibration. The damped angular frequency was then calculated using Eq. 5-8.

$$\omega_d = \frac{2\pi}{T_d} \tag{5-8}$$

where ω_d is the damped angular frequency and T_d is the damped period of the structure. To find both the natural angular frequency and damping ratio, the exponential equation, Eq. 5-9, was used.

$$f(t) = Ae^{Bt} = Ae^{\xi\omega_n t} \tag{5-9}$$

where ω_n is the natural angular frequency and A and B are constants solved by fitting the exponential equation to both the maxima or minima displacement measurements during free vibration, as shown in Figure 5-6. Using the value of B determined this way, the natural angular frequency and damping ratio were solved by iterating Eq. 5-10 and Eq. 5-11 until the natural angular frequency converged to within 1%. To begin the iteration ω_n was assumed to be ω_d.

$$\xi = \frac{B}{\omega_n} \tag{5-10}$$

$$\omega_n = \frac{\omega_d}{\sqrt{1-\xi^2}} \tag{5-11}$$

Table 5-4. Impact test results

Specimen	Mass, kg	Drop Height, mm	Absorbed Energy, J	Specific Absorbed Energy, J/kg	Maximum Deflection, mm	Maximum Bottom Face Strain, mm/mm	Minimum Top Face Strain, mm/mm	Calculated Stiffness, N/mm	Damping Ratio, %
2FL-PC-D-1	2.81	614	62.72	22.30	18.5	0.0073	-0.0077	277	8.9
2FL-PC-D-2 †	2.78	1075	Break	Break	N/A	N/A	N/A	N/A	N/A
2FL-PC-D-3 *	2.75	845	86.32	31.39	23.3	0.0096	-0.0087	N/A	N/A
2FL-WC-D-1	3.36	614	62.72	18.69	18.6	0.0071	-0.0055	256	11.4
2FL-WC-D-2 †	3.32	1517	Break	Break	N/A	N/A	N/A	N/A	N/A
2FL-WC-D-3	3.32	1075	109.81	33.07	25.6	0.0086	-0.0060	284	8.7

* *String potentiometer failed after maximum deflection*

† *Specimen experienced ultimate failure*

In this study, the procedure was completed twice: once fitting the equation to the maxima displacements and once fitting the equation to the minima displacements. Then, the damping ratio and natural angular frequency were taken as the average of the two results. The specimen stiffness was then calculated as follows:

$$K = \frac{{\omega_n}^2\, mL}{2} \tag{5-12}$$

where m is the specimen mass per unit length and L is the span length.

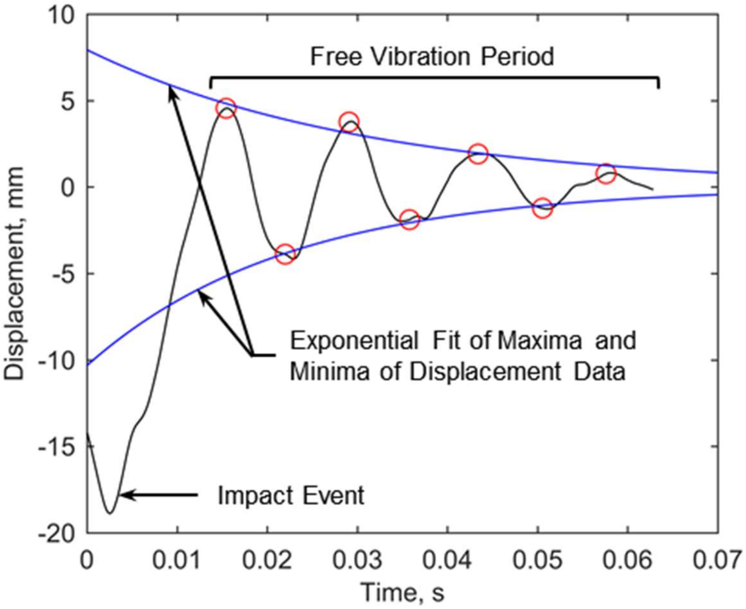

Figure 5-6. Specimen 2FL-PC-D-1 – damping ratio calculation

5.4.2.1. Impact Energy

For both the PC and WC type specimens, the first impact was based on the average energy to cause failure in all the monotonic tests, which was found to be approximately 62.7 J. Both PC and WC type specimens were able to resist the impact of 62.72 J (i.e. a drop height of 614 mm with a drop weight mass of 10.413 kg). The next impact test for both PC and WC type specimens was then performed at an energy of 109.81 J, a 75% increase from the first impact. The PC type specimen failed at this impact level and therefore the remaining specimen was tested at 86.32 J, the average of the first two impact test energy levels. The WC type specimen resisted the impact energy of 109.81 J and the remaining specimen was tested at an energy level of 154.96 J, an increase of approximately 150% from the initial impact of 62.72 J. The WC specimen failed at this impact level.

Because the types of structures are often used where reduced weight is a design requirement, an important property is the specific absorbed energy (SAE). The SAE of each specimen is presented in Table 5-4. Due to the lack of test data available, the ultimate SAEs of these beams are still unknown, but it can be concluded from these tests that the SAE of the WC and PC specimens is at a minimum 33.07 J/kg and 31.39 J/kg, respectively.

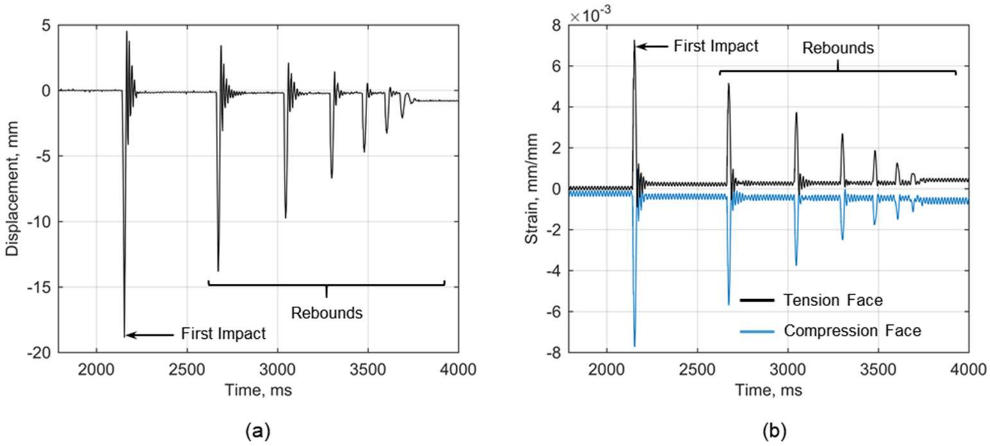

Figure 5-7. Specimen 2FL-PC-D-1 impact test data (a) midspan displacement vs. time; (b) face strain at midspan vs. time

5.4.2.2. *Strain and Displacement*

Both strain and displacement at midspan were measured throughout the impact event. Sample test results of specimen 2FL-PC-D-1 are presented in Figure 5-7. This figure shows that after the impact event, there is a period of free vibration and that the drop weight was allowed to rebound during the tests. During the impact tests causing failure, there was no significant displacement data to report as the specimen failure caused the string potentiometer to disconnect. However, the energies resisted by both specimens caused deflections greater than those experienced during monotonic testing. The PC specimen impacted by 86.32 J deflected 23.3 mm compared to an average of 20.9 mm during the monotonic tests and the WC specimen impacted by 109.81 J deflected 25.6 mm compared to an average of 23.5 mm during the monotonic tests. These high levels of deflection indicate that the specimens were potentially close to their ultimate capacity during these impact tests. This is also supported by the fact that the maximum strains at these impacts in the bottom face exceeded the average ultimate FFRP tensile strain of 0.0083 mm/mm.

5.4.3. Residual Behaviour After Impact

Specimens that did not fail during impact testing were tested under monotonic loading to determine post-impact residual properties. The results of these tests are presented in Figure 5-8 and Table 5-5. The tested specimens are presented in Figure 5-4.

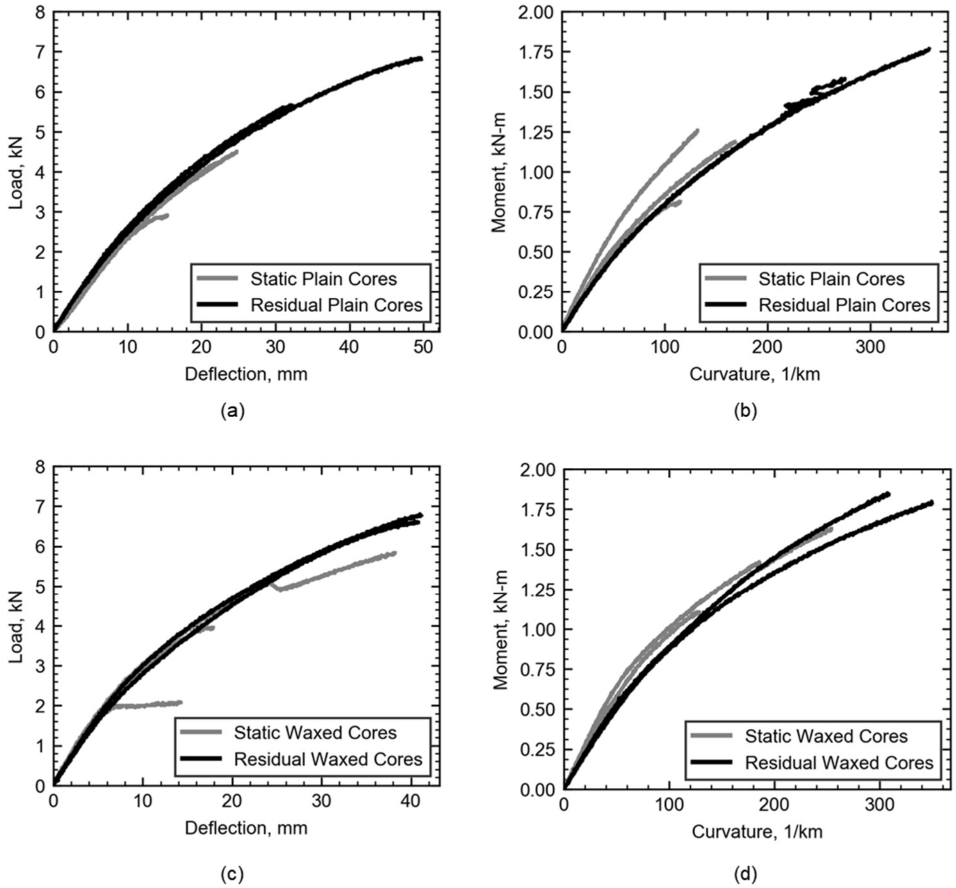

(a) (b)

(c) (d)

Figure 5-8. Comparison of the residual properties of cardboard core sandwich beams and intact static properties (a) load-deflection of plain core specimens; (b) moment-curvature of plain core specimens; (c) load-deflection of waxed core specimens and; (d) moment-curvature of waxed core specimens.

Table 5-5. Residual monotonic test results

Specimen	Mass, kg	Ultimate Load, kN	Max Deflection, mm	Specific Strength, kN/kg	Stiffness, N/mm	Ultimate Moment, kN-m	Max Curvature, 1/km	Flexural Rigidity, kN-m^2	Failure Mode
2FL-PC-D-1-R	2.799	5.67	32.3	2.02	285.2	1.58	275	9.80	CC
2FL-PC-D-3-R	2.743	6.84	49.7	2.49	268.2	1.91	357	9.99	CC
AVE	2.771	6.25	41.0	2.26	276.7	1.75	316	9.89	
SD	0.039	0.83	12.3	0.33	12.0	0.23	58	0.13	
2FL-WC-D-1-R	3.359	6.81	41.2	2.03	353.3	1.90	350	10.40	CC
2FL-WC-D-3-R	3.315	6.63	40.8	2.00	336.7	1.85	309	11.67	CC
AVE	3.337	6.72	41.0	2.01	345.0	1.88	329	11.03	
SD	0.031	0.12	0.2	0.02	11.8	0.03	29	0.90	

* *CC = Compression Face Crushing, AVE = Average, SD = Standard Deviation*

5.4.3.1. Failure Mode (comparison with monotonic)

All residually tested specimens failed due to compression face crushing (CC), which is a face material failure mechanism. This contrasts the behaviour exhibited by the monotonic tests of the intact specimens, five of which failed due to an interface stability failure between the core and face. All the residually tested specimens also resisted a larger ultimate load than their intact counterparts. These two facts indicate that either the intact specimens failed prematurely or that there is some phenomenon causing an increase in strength after an impact event. In previous tests of sandwich panels with FFRP faces and polyisocyanurate foam cores performed by the authors, a similar increase was observed during residual testing which suggests that there is an unknown condition causing this increase in strength and stiffness. Currently, it is suspected that this increase in strength and stiffness after impact is caused by a densification of the core material under the impact. However, this phenomenon is not yet fully understood and requires further detailed investigation. Future work to investigate this behaviour will include removing sections of the core material from under the impact area of tested sandwich specimens and comparing the results with the behaviour of intact core materials. Additionally, the hysteretic behaviour of the FFRP faces will be examined through further tension and compression testing. This will show the behaviour of the FFRPs after prior loading and unloading, such as after an impact event.

5.4.3.2. Load-Deflection Behaviour (comparison with monotonic)

The load-deflection and moment-curvature behaviour of the residual tests are compared to the intact monotonic tests in Figure 5-8. The results of the residual tests are presented in Table 5-5. As discussed previously, the residual PC specimens and residual WC specimens resisted higher ultimate loads than their intact counterparts. The average ultimate load resisted by residual PC specimens was 6.25 kN which is an increase of 60.7% from the 3.89 kN resisted by intact PC specimens. Likewise, the residual WC specimens resisted an average ultimate load of 6.72kN, a 69.7% from the 3.96 kN resisted by the intact WC specimens. By examining Figure 5-8a and Figure 5-8c, the stiffnesses of both WC and PC type specimens were not affected by the impact event. The average stiffness of the residual PC specimens was 276.6 N/mm, which is within 7.7% of the average stiffness of the intact PC specimens. Likewise, the stiffness of the residual WC specimens was within 4.5% of the WC intact specimens.

5.4.3.3. Moment-Curvature Behaviour (comparison with monotonic)

By examining Figure 5-8b and Figure 5-8d, it can be seen that the moment-curvature behaviour of the beams was affected by the respective impact events. The average flexural rigidity exhibited by the residual PC type specimens was 9.89 kN-m^2 which is a reduction by 17.3% compared to the intact PC specimens. The rigidity of the residual WC type specimens also showed a reduction in rigidity of 13.4% when compared to the intact WC type specimens.

5.4.4. Comparison with Foam-Core Sandwich Beams

Figure 5-9 shows the comparison the cardboard core sandwich beams with similar sandwich beams with PIR foam cores tested by Betts et al. (2018b). The figure shows that the sandwich beams perform well compared to beams using more traditional core materials. Both the PC and WC specimens exhibited higher stiffness than all PIR foam core specimens tested in the previous study. However, the PC and WC cores have an average measured density of 136 kg/m^3 and 174 kg/m^3 which is higher than even the most dense foam tested in the study by Betts et al. (2018b) at 96 kg/m^3. Generally, the PC and WC core specimens exhibited a higher ultimate strength than the similar sandwiches with PIR foam core densities of 32 kg/m^3 and 64 kg/m^3, but a lower ultimate strength than the 96 kg/m^3 PIR foam core specimens. Therefore, further research should be performed to examine the shear strength of the face-core interface to have a better understanding of the ultimate load capacity of these structures. Additionally, further research should be performed to understand the freeze-thaw behaviour and effect of fire on these structures.

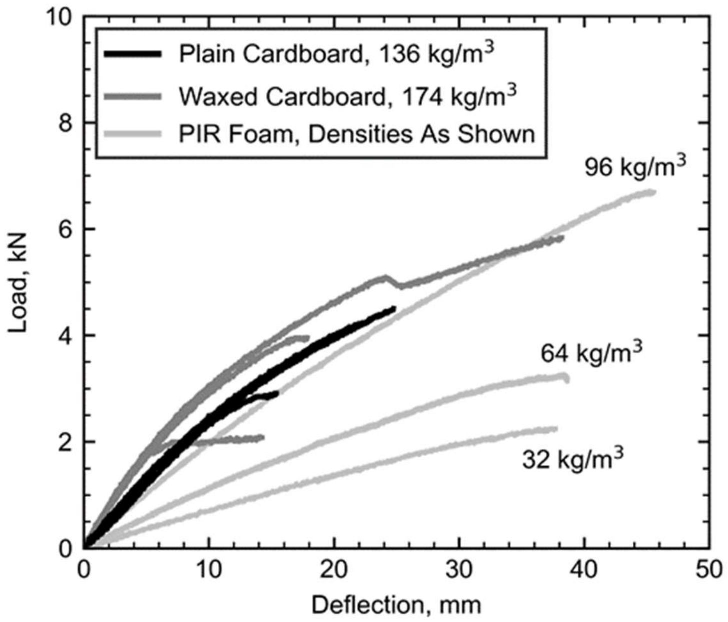

Figure 5-9. Load-deflection comparison of plain and waxed cardboard core FFRP-sandwich beams with foam core FFRP-sandwich beams – PIR foam core data from Betts et al. (2018b)

5.5. SUMMARY

In this chapter, twelve sandwich beams constructed with flax fibre-reinforced polymer (FFRP) faces and recycled corrugated cardboard cores were studied experimentally under monotonic and impact loading. Each sandwich beam was 1200 mm long, 150 mm wide and was constructed of two-layer FFRP faces and a 75 mm thick corrugated cardboard core. Six specimens were prepared using a plain cardboard core and six with a waxed cardboard core. Two separate test methods were employed in this study: a three-point bending test and a drop weight impact test. Three specimens of each type with a span length of 1120 mm of each type were tested under monotonic load. The load was applied through a 150 mm wide steel hollow structural section (HSS) and was measured with a 250 kN load cell. The midspan deflection was measured with a string potentiometer and the strains in the top and bottom faces at midspan were measured using strain gauges. The monotonic test data was recorded at a rate of 10 Hz. Three specimens of each type were tested under a drop weight impact load. The drop weight was applied to the midspan. To match the monotonic tests, the drop weight was affixed with a 150 mm HSS section loading surface. The midspan displacement was measured with a fast-action string potentiometer and the midspan face strains were measured using strain gauges. The impact data was recorded at a rate of 25 kHz. Additionally, a high-speed video (500 frames per second) was taken of each impact test.

The residual monotonic flexural behaviour after impact was also investigated for specimens that survived the impact testing (that is, they were additionally tested under monotonic three-point bending). The results of the tests were compared with the results of similar tests on sandwich beams with conventional petroleum-based foam cores and showed that the cardboard core beams behaved similarly to the foam core beams. It was determined that core manufacturing and specimen preparation had a significant effect on the overall specimen behaviour and potentially caused premature failure in some of the tests. The residual monotonic tests of specimens after impact showed that there was no significant reduction in specimen strength or stiffness after an impact event. Existing models used for predicting the behaviour of foam-core FFRP-sandwich beams were used to predict the behaviour of the cardboard specimens tested in this study.

CHAPTER 6: EXPERIMENTAL BEHAVIOUR OF TWO-WAY FFRP-FOAM SANDWICH STRUCTURES

6.1. INTRODUCTION

Sandwich panels are structural members comprised of two stiff faces and a weaker lightweight core that separates the faces, providing a relatively large moment of inertia. These structures are ideal for situations requiring a lightweight panel with a relatively high strength and stiffness. Often, they are made using fibre-reinforced polymer (FRP) faces and foam cores. When foam cores are used, these panels can provide dual benefits for applications such as for building cladding systems. In this application, a sandwich structure can provide insulation and act as a structural member. Foam cores are relatively weak when compared to traditional FRPs such as carbon FRP (CFRP) or glass FRP (GFRP) and therefore they typically control the failure of the panel. This presents an opportunity to replace the synthetic FRPs with more sustainable natural FRPs (Betts et al. 2018a, 2020a; CoDyre et al. 2018; Mak et al. 2015; Sadeghian et al. 2018). The behaviour of plant-based FRPs, such as flax FRPs (FFRPs) and hemp FRPs, have been studied extensively in the recent literature (Baley et al. 2012; Bambach 2017; Bensadoun et al. 2016; Christian and Billington 2011; Hristozov et al. 2016; Mak and Fam 2019b; Ramesh et al. 2017; Sparnins 2006; Yan et al. 2016). FFRPs have been shown to have a lower embodied energy than both GFRPs and CFRPs (Cicala et al. 2010) and have a relatively high strength ad stiffness when compared to other natural FRPs (Ramesh et al. 2017).

As building cladding systems can be exposed to high wind events, it is necessary to understand the behaviour of sandwich panels under both flexural and shear loading due to wind and impact loads due to flying debris. For this reason, sandwich structures with synthetic faces have been investigated extensively under one-way flexural loads (Besant et al. 2001; Dai and Hahn 2003; Fam and Sharaf 2010; Gupta et al. 2002; Manalo et al. 2016, 2010; Petras and Sutcliffe 1999; Sharaf et al. 2010) and impact loads (Abrate 1997; Akil Hazizan and Cantwell 2002; Daniel et al. 2012; Torre and Kenny 2000). Recently, sandwich structures with FFRP faces and cardboard cores (Betts et al. 2020c; McCracken and Sadeghian 2018) and foam cores

(Betts et al. 2018a; CoDyre et al. 2018; Mak et al. 2015) have been investigated under one-way flexural and shear loads and under impact loads (Betts et al. 2020a; c, 2021).

Depending on the structural or architectural design, sandwich panels used for cladding materials can be also be loaded in two-way bending. There has been substantial research on the two-way flexural (Dawood et al. 2010; Huo et al. 2015; Qi et al. 2016; Satasivam et al. 2018) and impact behaviour (Anderson and Madenci 2000; Nemes and Simmonds 1992; Schubel et al. 2005) of sandwich structures with synthetic FRP faces. Dawood et al (2010) tested 1200 mm by 1200 mm sandwich panels with GFRP faces and 25 mm and 50 mm thick foam cores with 3-D insertions. They developed a finite element model and used it to perform a parametric study to examine the effect of different parameters, including, panel thickness, face thickness and aspect ratio. Anderson and Madenci (2000) tested 76.2 by 76.2 mm^2 sandwich panels with CFRP faces and 12.7 mm thick foam and honeycomb cores. They tested the panels using a drop weight impact test and found that sandwich panels subjected to low velocity impacts with little or no visible damage have the potential for significant internal damage. Schubel et al (2005) tested 279 mm by 279 mm by 28.2 mm sandwich plates with CFRP faces and a PVC foam cores under low velocity impacts. They found that general impact behaviour of the sandwich panels could be predicted by quasi-static testing. However, the indentation is more pronounced in plates tested under quasi-static loading.

Currently, there is a gap in the field of research concerning the two-way flexural, shear and impact behaviour of FFRP-foam sandwich panels. This is especially true for large-scale panels and large mass impacts to simulate the potential loading of building cladding systems due to wind-borne debris. The aim of this study is to fill the current gap in the literature by investigating the flexural, shear and impact behaviour of large-scale (1220 mm by 1220 mm by 80 mm) sandwich panels with FFRP faces and 96 kg/m^3 polyisocyanurate foam cores.

6.2. EXPERIMENTAL PROGRAM

In this section, the experimental test matrix will be presented, the constituent material behaviour will be discussed, and the static and impact test set-ups will be presented.

6.2.1. Test Matrix

As a part of this study, a total of 12 large scale sandwich panels were fabricated and tested under a concentrated load or an impact at the center. The sandwich panels were comprised of flax fibre-reinforced polymer faces and polyisocyanurate foam cores with a density of 96 kg/m^3. Each sandwich panel was 1220 mm by 1220 mm and approximately 80 mm thick. The main test parameters were the effect of face thickness, namely one, two or three layers of flax fabric per face, and the effect of impact energy. The impact energies were chosen based on the results of the static tests, namely 50%, 70% or 95% the static failure energy (SFE). The naming convention used in this study is as follows: XFL-[S/DY], where X is the number of flax layers per face, FL stands for "Flax Layers", S stands for "Static", D stands for "Dynamic", and for dynamic specimens, Y is the impact energy in joules (J). As an example, a panel with one flax layer per face tested under static load would be named 1FL-S and a panel with three layers per face tested under an impact load of 656 J would be named 3FL-D656. The test matrix is presented in Table 6-1.

Table 6-1. Test matrix for 1220 mm x 1220 mm two-way sandwich panels

Specimen ID	Face Layers	Impact Energy, J	Impact Energy, % Failure Energy	Number of Specimens	Number of Impacts
1FL-S	1	-	-	1	-
1FL-D119	1	119	50	1	20
1FL-D167	1	167	70	1	100
1FL-D227	1	227	95	1	100
2FL-S	2	-	-	1	-
2FL-D306 *	2	306	50	1	52
2FL-D428 †	2	428	70	1	12
2FL-D581	2	581	95	1	5
3FL-S	3	-	-	1	-
3FL-D345 *	3	345	50	1	100
3FL-D483 †	3	483	70	1	8
3FL-D656	3	656	95	1	15
Total	-	-	-	12	412

* *Tested once at an impact energy of 119 J before subsequent testing*

† *Tested once at an impact energy of 167 J before subsequent testing*

6.2.2. Materials

The flax fibre-reinforced polymer (FFRP) faces were fabricated using a bidirectional flax fabric and a bio-based epoxy resin. The flax fabric had a reported areal mass of 400 g/m^2. The bio-based epoxy resin used has an approximate bio-content of 25%. The epoxy properties were determined in a previous study by Betts et al (2018a) using ASTM D638 (2013). Their tests showed that the epoxy had a mean (± standard deviation) tensile strength, initial elastic modulus and ultimate strain of 57.9 ± 0.4 MPa, 3.20 ± 0.13 GPa and 0.0287 ± 0.0018 mm/mm, respectively.

The tensile properties of the bidirectional FFRPs were determined in both the warp and weft directions using ASTM D3039 (2014) and the shear properties were found using ASTM D3518 (2018a). For each test type, five identical 250 mm x 25 mm coupons were tested. The tension coupons were comprised of two layers of flax fabric whereas the shear coupons comprised of four layers of flax fabric in a ±45° layup. The coupons were all fabricated using a wet lay-up procedure. The tensile strength, initial elastic modulus and ultimate strain were found to be 70.0 ± 3.4 MPa, 6.35 ± 0.71 GPa and 0.0202 ± 0.0022 mm/mm, respectively, in the warp direction and 51.3 ± 1.4 MPa, 5.64 ± 0.90 GPa and 0.0204 ± 0.0024 mm/mm, respectively, in the weft direction. The shear strength, shear modulus and ultimate shear strain were found to be 23.1 ± 0.4 MPa, 1.26 ± 0.02 GPa, and 0.0562 ± 0.0053 mm/mm, respectively. The stress-strain responses in tension and shear were averaged and are presented in Figure 6-1.

The shear properties of the foams were determined experimentally using ASTM C273 (2018b). Five identical 240 mm long, 50 mm wide and 20 mm thick specimens were tested. The shear strength, shear modulus and ultimate shear strain of the 96 kg/m^3 polyisocyanurate foam were found to be 0.476 ± 0.102 MPa, 12.5 ± 0.8 MPa and 0.59 ± 0.018 mm/mm, respectively. The shear stress-strain behaviour and photos of the test set-up and a typical failure are presented in Figure 6-2. Note that the test data for one of the shear coupons was not included in the averaging as it was perceived to have failed prematurely. This data is represented in Figure 6-2 with a dashed line.

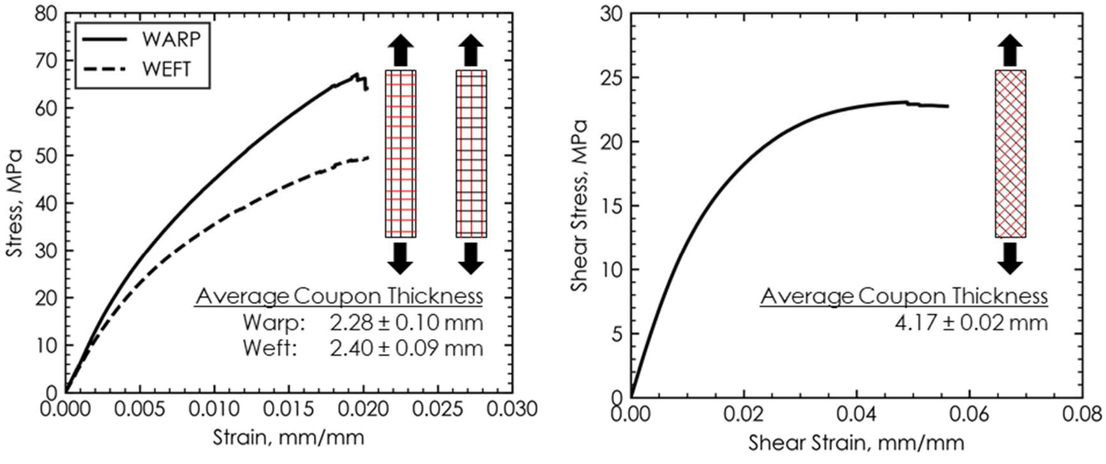

(a) (b)

Figure 6-1. Stress-strain response of FFRPs in (a) tension and (b) shear

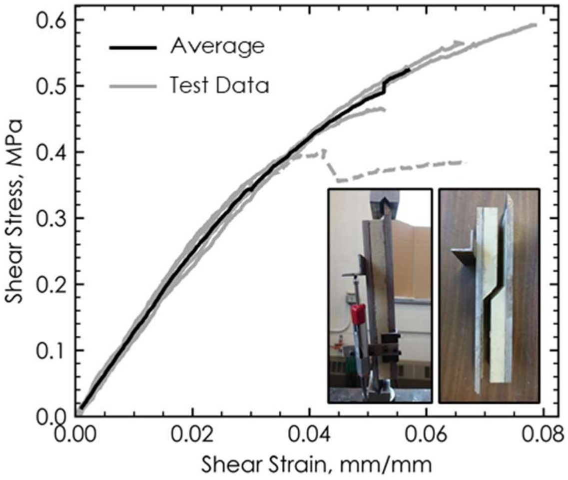

Figure 6-2. Shear stress-strain behaviour of 96 kg/m^3 polyisocyanurate foam (data represented by dashed line was not included in average plot)

6.2.3. Specimen Fabrication

The specimen fabrication procedure for each panel is presented in Figure 6-3. The 75 mm thick foam was supplied in 2400 mm by 1220 mm panels. The foam was cut to 1220 mm by 1220 mm using a circular saw. The foam surface was cleared of any dust and debris using a bristle brush. A layer of epoxy was evenly applied to the surface of the foam (Figure 6-3b). Then, a layer of the bidirectional flax fabric was placed on the specimen (Figure 6-3c) and the warp direction was recorded on the side of the foam. A plastic scraper was then used to gently press the fabric into the epoxy layer below (Figure 6-3d). Then, a layer of epoxy was evenly applied to the flax fabric (Figure 6-3e). These last three steps were repeated as necessary to achieve different face thicknesses, namely, one two or three layers. Note that all layers were placed with the warp direction of the fabric along the same axis. Sheets of parchment paper were applied in the warp direction of the fabric and an aluminum roller or plastic scraper was used to remove any air and excess epoxy (Figure 6-3f). A weighted board was then placed on the specimen (Figure 6-3g) and the face was allowed to cure for 24 hours under the weighted board. After 24 hours, the opposite face was completed following the same procedure. After seven days of curing at room temperature, the edges of the faces were cut flush using a jig saw (Figure 6-3h). After fabrication, all specimens were stored in a dry environment until testing.

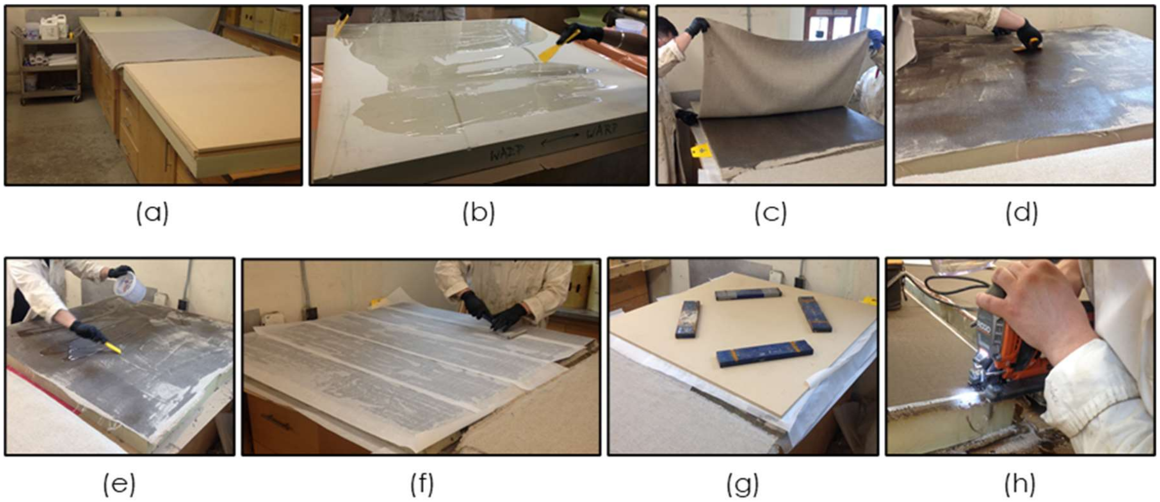

Figure 6-3. Specimen fabrication: (a) materials and workstation; (b) epoxy application to foam; (c) placement of fabric; (d) removal of air under flax layer; (e) epoxy application on fabric; (f) placement of parchment paper; (g) curing with weight board; and (h) cutting edges

6.2.4. Test Set-up and Instrumentation

As a part of this study, two types of tests were performed: quasi-static tests and impact tests. In both tests the load was applied at the center of a 1220 mm x 1220 mm panel. In this section of the paper, the test set-ups and instrumentation will be presented.

6.2.4.1. *Quasi-Static Tests*

Figure 6-4 shows the quasi-static test set-up. The load was applied to the center of 1220 mm by 1220 mm sandwich panel specimen using a hydraulic actuator through a 150 mm diameter steel disc. To protect the wires of the strain gauges, a piece of rubber was placed under the applied load. The sandwich panel was supported by steel roller supports on a steel frame which sat on a concrete strong floor. In each direction, one of the steel rollers was welded to the frame to simulate a pin connection.

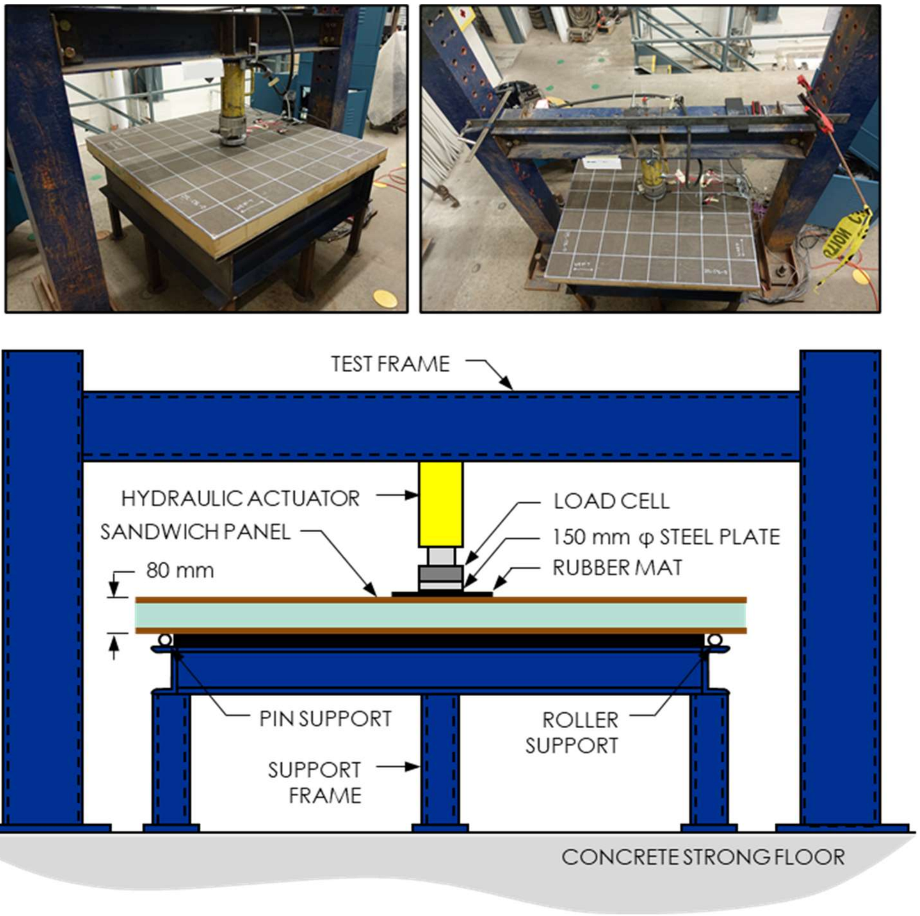

Figure 6-4. Quasi-static test set-up

The data instrumentation layout is presented in Figure 6-5. The load was measured using a 250 kN load cell and the center deflection was measured using a string potentiometer connected to the sandwich panel on the bottom face. Additionally, four linear potentiometers (LPs) measured the deflection at the quarter points of the panel, that is, halfway between the panel center and the corners of the supports. Strain gauges with a 6 mm gauge length and a resistance of 350-ohms measured the strain in the warp, weft and 45° directions at the center on both the top and bottom faces. All data was measured at a sample rate of 10 samples per second.

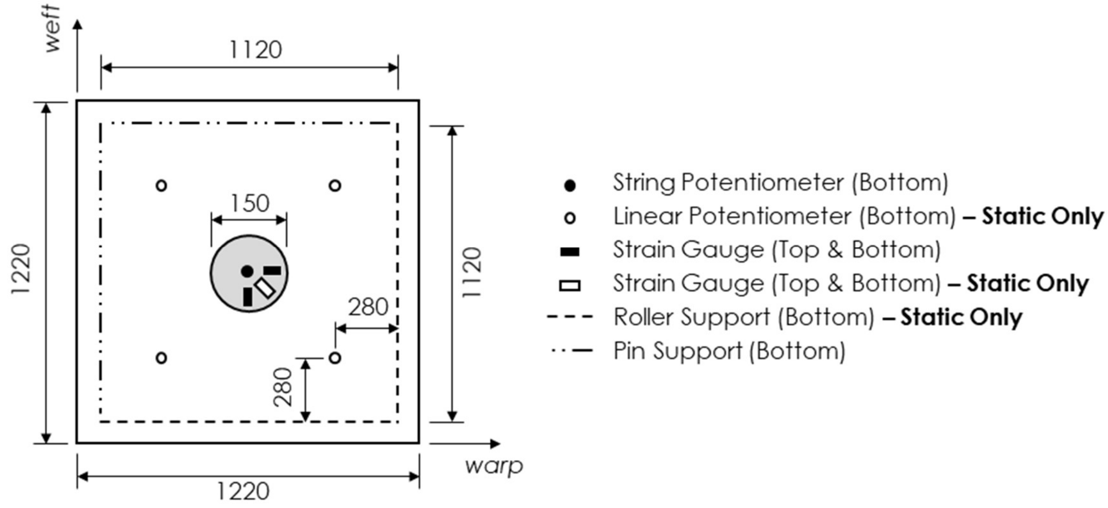

Figure 6-5. Test instrumentation

6.2.4.2. *Impact Tests*

Figure 6-6 shows the impact test set-up. The specimens were supported on a steel frame with a simulated pin connection at each side. The support frame was secured to a concrete strong floor. To stop the specimen from rebounding after an impact, a top frame of steel rods secured the sandwich specimens to the bottom steel frame using a u-bolt in each corner.

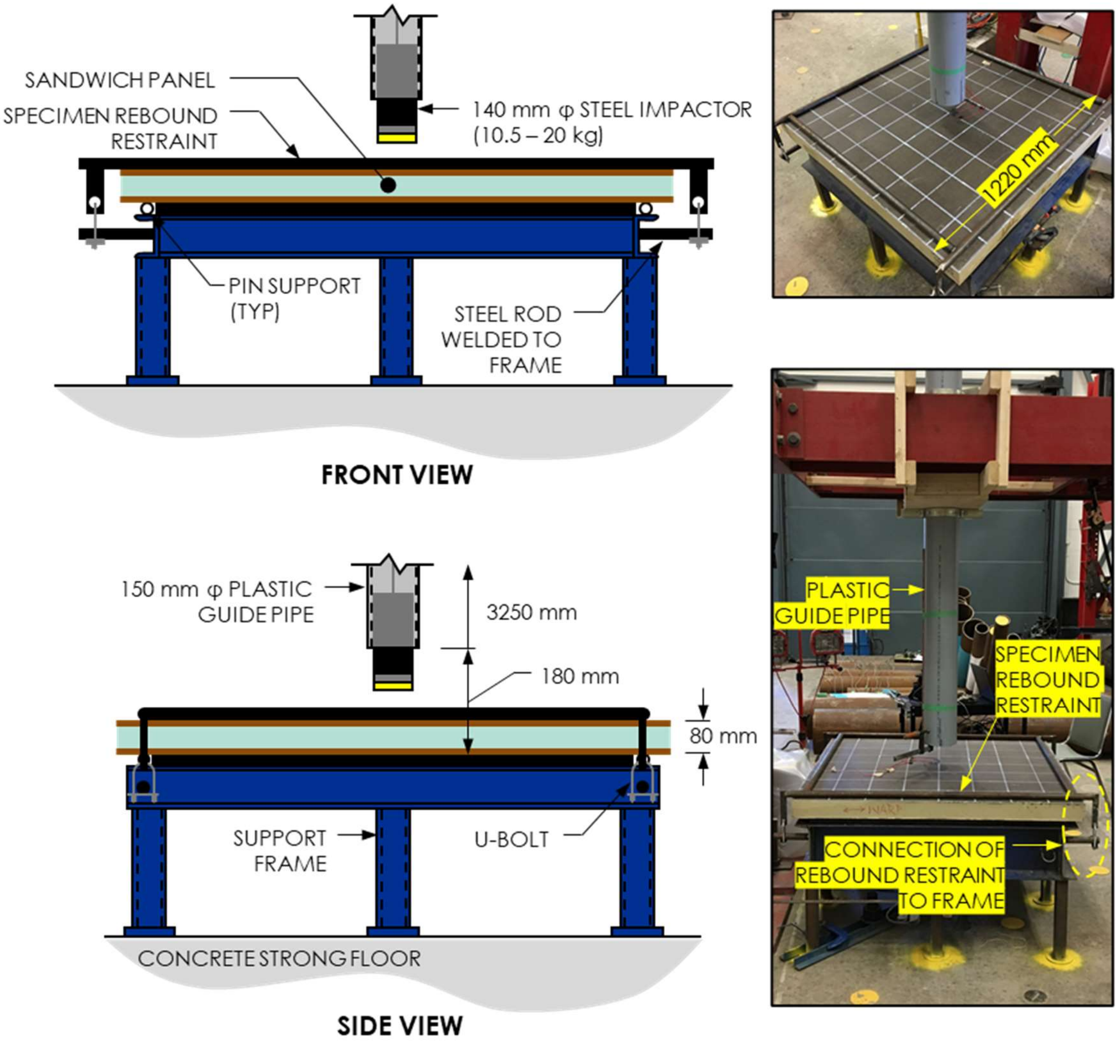

Figure 6-6. Impact test set-up

The specimens were impacted at the center by a 200 mm long, 140 mm diameter cylindrical impactor. The impactor weight was set for each test in order to achieve the desired impact energy. The impactor weights varied between a minimum weight of 10.5 kg to a maximum weight of 20 kg. The impactor was dropped through a 150 mm diameter plastic guide pipe and the maximum drop height possible was 3250 mm. The bottom of the plastic guide pipe was set approximately 100 mm above the top face of the specimens, to ensure that the impactor did not fully leave the guide pipe during the tests. To protect the strain gauge wires, a rubber mat was placed on the specimen at the impact location.

The test instrumentation is presented in Figure 6-5. The center deflection was recorded using a fast-action string potentiometer. The strains in both the warp and weft direction were measured using 350-ohm strain gauges with a 6 mm gauge length. All impact test data was recorded at a sample rate of 25 000 samples per second.

6.3. RESULTS AND DISCUSSIONS

In this section, the results of the quasi-static and impact tests are presented and discussed. All data presented in this study was processed using Python, specifically the scientific package, Anaconda.

6.3.1. Quasi-Static Tests

The failure modes of the quasi-static tests are shown in Figure 6-7. As the face thickness increased, the failure mode transitioned from a tension face-controlled failure (1FL-S) to a core shear failure, which lead to local failure of the compression face (3FL-S). Specimen 2FL-S failed due to tension at the bottom face, however, as the top face showed signs of the start of local failure, it is assumed that this specimen was close to the core shear failure as well.

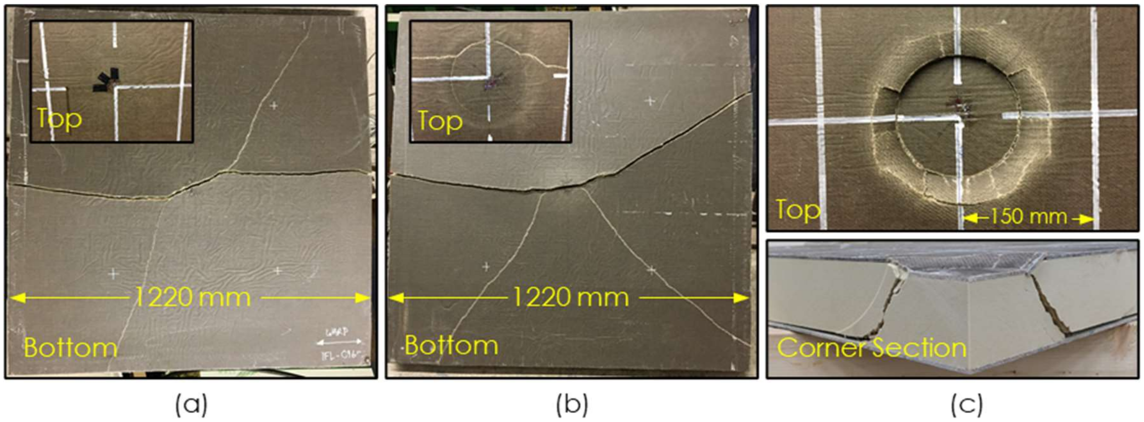

(a) (b) (c)

Figure 6-7. Quasi-static failure modes (a) 1FL-S; (b) 2FL-S; and (c) 3FL-S

The results of the quasi-static tests are presented in Figure 6-8 and Table 6-2. As shown in Figure 6-8a, the ultimate strength and stiffness of the panels increased with face thickness. The load-deflection diagrams also show that there was a larger increase in both strength and stiffness between specimens 1FL-S and 2FL-S than between 2FL-S and 3FL-S. The ultimate strength and initial stiffness increased by 78% and 51%, respectively, between specimens 1FL-S and 2FL-S. However, the ultimate strength and initial stiffness only increased by 12% and 4%, respectively, between specimens 2FL-S and 3FL-S. This is likely caused by the more prominent effect of local deformation of the 2FL-S and 3FL-S panels, which is shown in the load-strain diagrams shown in Figure 6-8b. The load-compression strain curves show the top faces of the 2FL-S and 3FL-S panels started the tests by going into a state of compressive strain, as expected. At a load of approximately 29 kN, the top faces started to transition into a state of tensile strain. This is indicative of local indentation under the load application.

Based on the static tests, the failure energy of each specimen was calculated by finding the area under the load-displacement curves shown in Figure 6-8. The ultimate energy of each specimen type is presented in Table 6-2. These energies were used to calculate the impact energies used for the drop weight impact tests, namely 50%, 70% and 95% static failure energy.

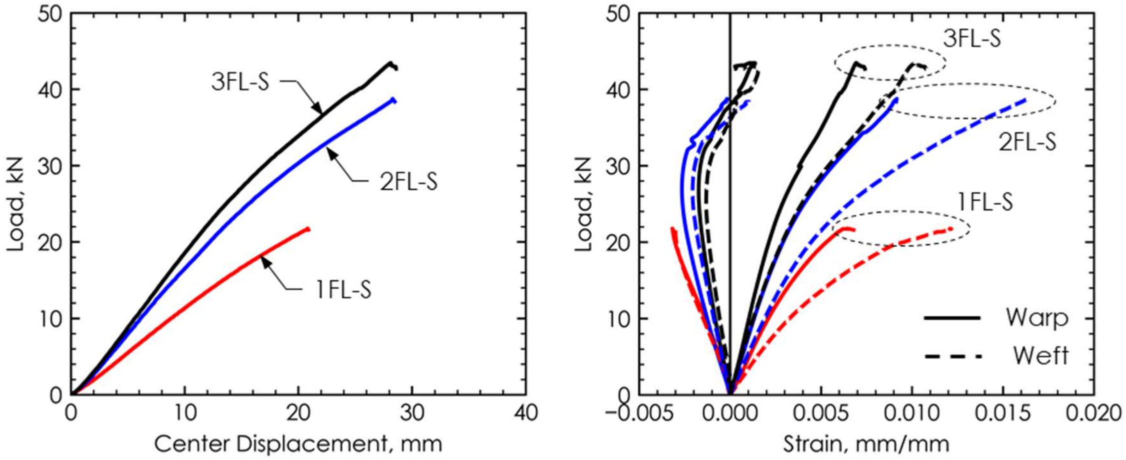

(a)

(b)

Figure 6-8. Quasi-static test results (a) load-displacement curves and (b) load-strain curves

Table 6-2. Quasi-static test results

Specimen ID	Initial Stiffness, N/mm	Ultimate Load, kN	Ultimate Deflection, mm	Failure Energy, J
1FL-S	1210	21.8	20.9	239.0
2FL-S	1781	38.8	28.5	612.4
3FL-S	1975	43.5	28.6	691.1

6.3.2. Impact Tests

As a part of this study, panels were impacted multiple times under a drop weight impact. For the first impact, strain and displacement data were recorded for analysis. The subsequent impacts were (for the most part) performed without data acquisition to determine the number of impacts that a specimen could withstand before failure.

6.3.2.1. First Impact

Each specimen was impacted multiple times at a drop weight with a fixed energy level: 50% static failure energy (SFE), 70% SFE or 95% SFE. The strain data of an impact at 95% SFE is presented in Figure 6-9. As shown in the figure, the bottom strains behaved similarly for each specimen. However, the strains in the top faces were significantly different between the 1FL specimen and the 2FL and 3FL specimens. The top face strains in 1FL-D227 specimen went fully into compression, as would be expected of a panel loaded under flexural load. However, the top faces strains of specimens 2FL-D581 and 3FL-D656 show that the top face of these specimens did not go into significant compression under the load. This observation is consistent with the results of the quasi-static tests and shows there was likely significant energy absorbed by local indentation of the core and top face for the 2FL and 3FL panels.

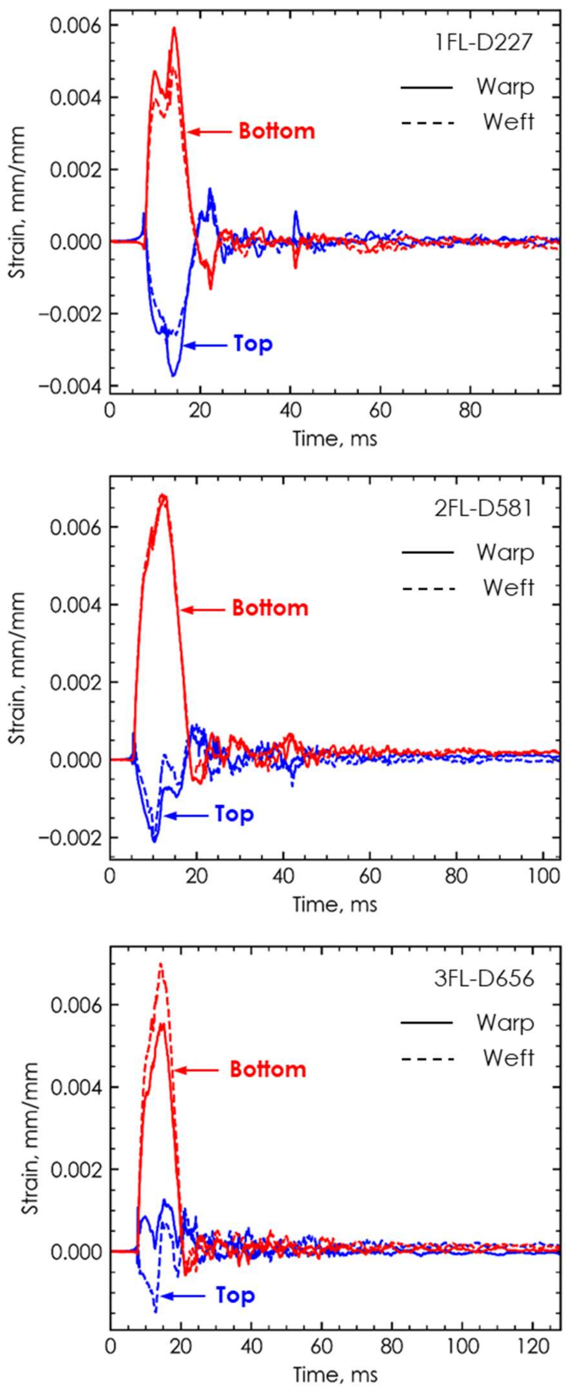

Figure 6-9. Strain data of 95% static failure energy impact on intact specimens

In order to see the effect of the energy level on the impulse response of the sandwich panels, Figure 6-10 presents the impulse deflection and bottom warp strain response of each impact test. As shown in Figure 6-10, the impact energy did not have a significant effect on the maximum center displacement for most panels. The exception to this is specimen, 3FL-D483, which was the only specimen that showed signs of damage for which displacement data was obtained. Because of the displacement data acquisition failure, it is difficult to make conclusions based on the displacement data only. Therefore, to present a more complete comparison, the bottom warp strain impulse response is also presented in Figure 6-10. Based on the bottom warp strain data, the length of time for most of the impulses was unaffected by energy level. However, specimens impacted with the highest-level energies (2FL-D581, 3FL-D483 and 3FL-D656) presented a longer impulse duration. This is prolonged impulse duration is attributed to the fact that these three specimens were the only specimens to exhibit signs of damage after the first impact as shown in Figure 6-11.

For each face thickness (ie. 1FL, 2FL and 3FL), the specimen impacted at 95% SFE showed a significant increase of strain in the bottom face when compared with the 70% SFE test. It should be noted that for the 2FL and 3FL specimens, this is also paired with damage and a prolonged impulse duration as discussed above. However, based on the observations of 3FL-D483 and 3FL-D656, which both showed signs of damage, it is evident that this increase in strain was not necessarily caused by the damage. Therefore, it seems that there is a threshold between 70% and 95% where the strain developed in the bottom face increases dramatically.

Upon further examination of Figure 6-10, it is evident that the shape of the bottom warp strain impulse response is affected by the panel face thickness, but not affected by the impact energy. Generally, the shape of the impulse was approximately in the shape of a half sine-wave. However, as the panel face thickness decreased, the presence of a higher frequency response becomes evident. The higher frequency response is likely suppressed in the thicker faced specimens due to the local deformation developed in these panels. It should be noted that this behaviour is also present in the 1FL specimens' displacement responses, however it is not as prominent as in the strain responses.

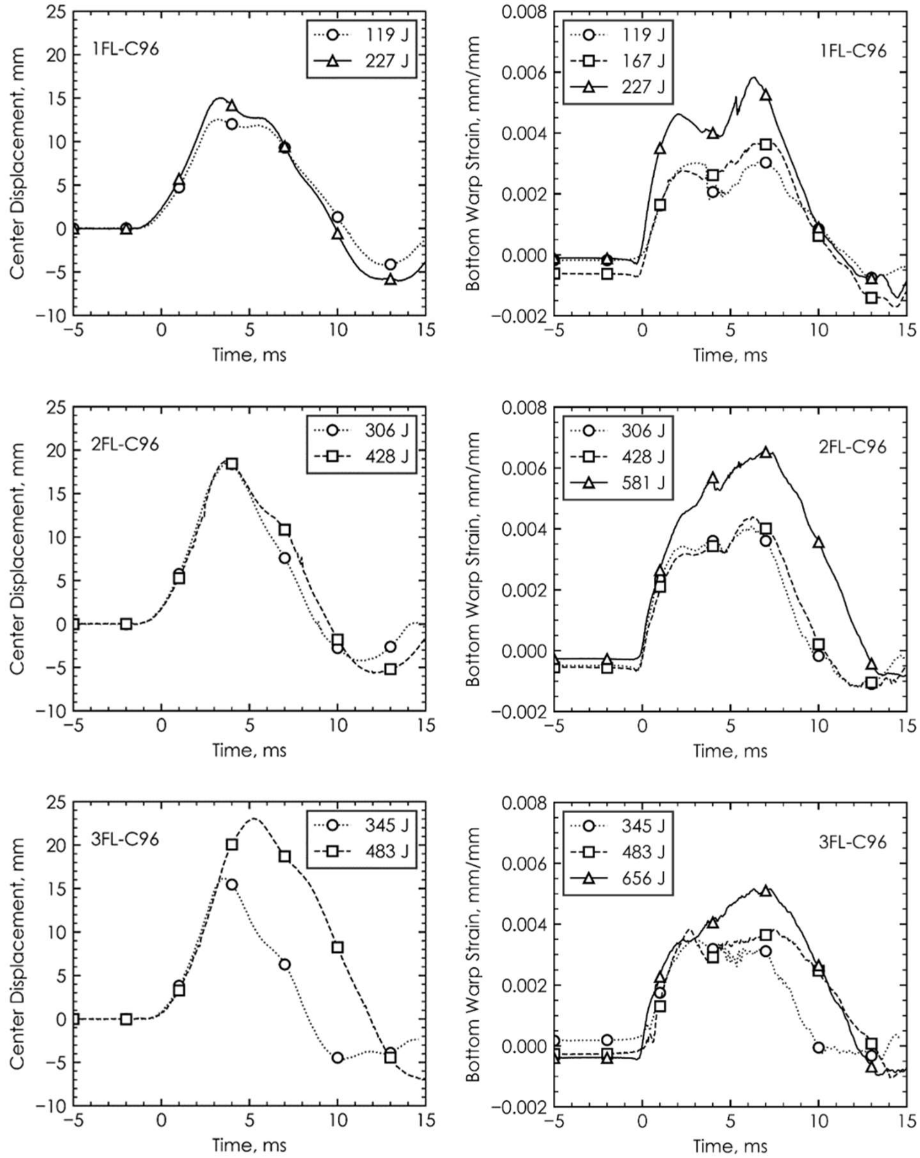

Figure 6-10. Deflection and bottom warp strain data for the impact on intact specimens

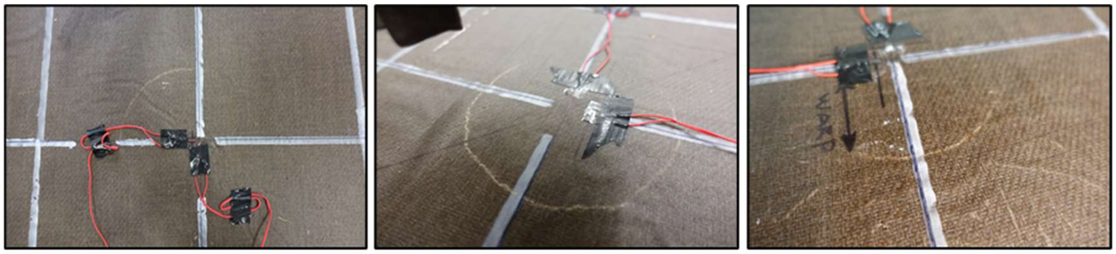

2FL-D581 3FL-D483 2FL-D656

Figure 6-11. Visible damage indicating internal core shear damage after first impact

Prior to testing specimens 2FL-D306 and 3FL-D345, each was tested once at 119 J to directly compare their impulse response with 1FL-D119. Similarly, 2FL-D428 and 3FL-D483 were each tested once at 167 J to directly compare their impulse response with 1FL-D167. It was assumed that these specimens could be tested once at these low energy levels (< 30% SFE) and still be considered intact for their subsequent tests.

Figure 6-12 presents the effect of face thickness on the impulse response of the sandwich panels. As expected, for each energy level, 119 J and 167 J, the center displacement increased with a decrease in face thickness. Additionally, the impulse duration increased with a decrease in face thickness. This indicates that specimens with a more global loading response (ie. plate deflection) have a longer impulse duration than specimens with a more local loading response (ie. indentation of core and top face). In future studies, it would be beneficial to measure the indentation of the top face during an impact event. However, this would present considerable challenges with the test set-up.

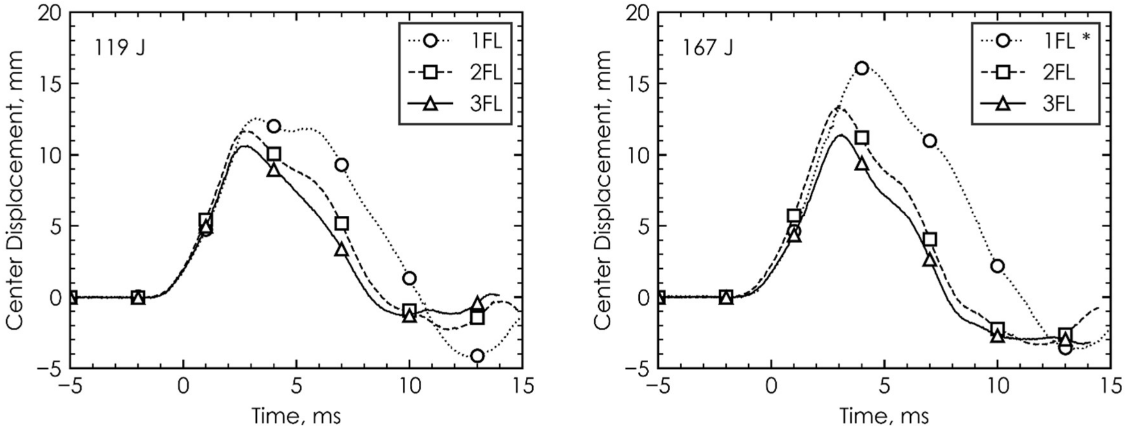

Figure 6-12. Effect of face thickness on displacement behaviour of a panel subjected to a set energy level (* deflection data for 1FL-D167 is presented for the second impact event as the deflection data was not captured during first impact event)

6.3.2.2. *Effect of Multiple Impact Events*

To understand the panels' resiliency, each specimen was impacted multiple times targeting a total number of 100 impacts or until obvious ultimate failure. The number of impacts before obvious ultimate failure for each specimen is presented in Table 6-3.

It should be noted that determining the ultimate failure visibly in the two-way panels was not accurate, and that these tests were performed to gain understanding of the behaviour during damage development. One observation made by performing these additional impacts was that panels susceptible to core shear failure under quasi-static testing were less resilient than panels susceptible to tensile failure of the bottom face. For the 95% SFE specimens, 1FL-D227, 2FL-D581 and 3FL-D656, only the 1FL-D227 specimen remained relatively undamaged after multiple impact events. This shows that the FFRP faces are likely more resilient than the foam cores. Therefore, FFRP-foam sandwich structures that will be subjected to impact loads should be designed such that a ultimate failure is controlled by the FFRP faces, if possible.

Table 6-3. Number of impacts to failure

Specimen ID	Impacts to Ultimate Failure	Notes
1FL-D119	20	Tests stopped. Probable delamination in top face
1FL-D167	DNF	Visible tensile crack in matrix on bottom face
1FL-D227	DNF	Visible tensile cracks in matrix on bottom face
2FL-D306	52	Probable delamination in top face before 52 impacts
2FL-D428	11 / 12	Substantial cracking and fibre rupture in top face
2FL-D581	4 / 5	Assumed shear failure within and significant cracking of top face
3FL-D345	DNF	No visible signs of damage
3FL-D483	8	Assumed shear failure within and significant cracking of top face
3FL-D656	6	Assumed shear failure within and significant cracking of top face

For two specimens, 3FL-D345 and 3FL-D483, the strain data was recorded for each impact event to show the damage progression due to multiple impacts. Note that panel 3FL-D345 did not experience perceived ultimate failure during the impact tests and was impacted 100 times whereas panel 3FL-D483 was impacted only 8 times due to perceived ultimate failure by delamination of the top face under the impact area. The bottom warp strain impulse responses for each specimen after multiple impacts are presented in Figure 6-13.

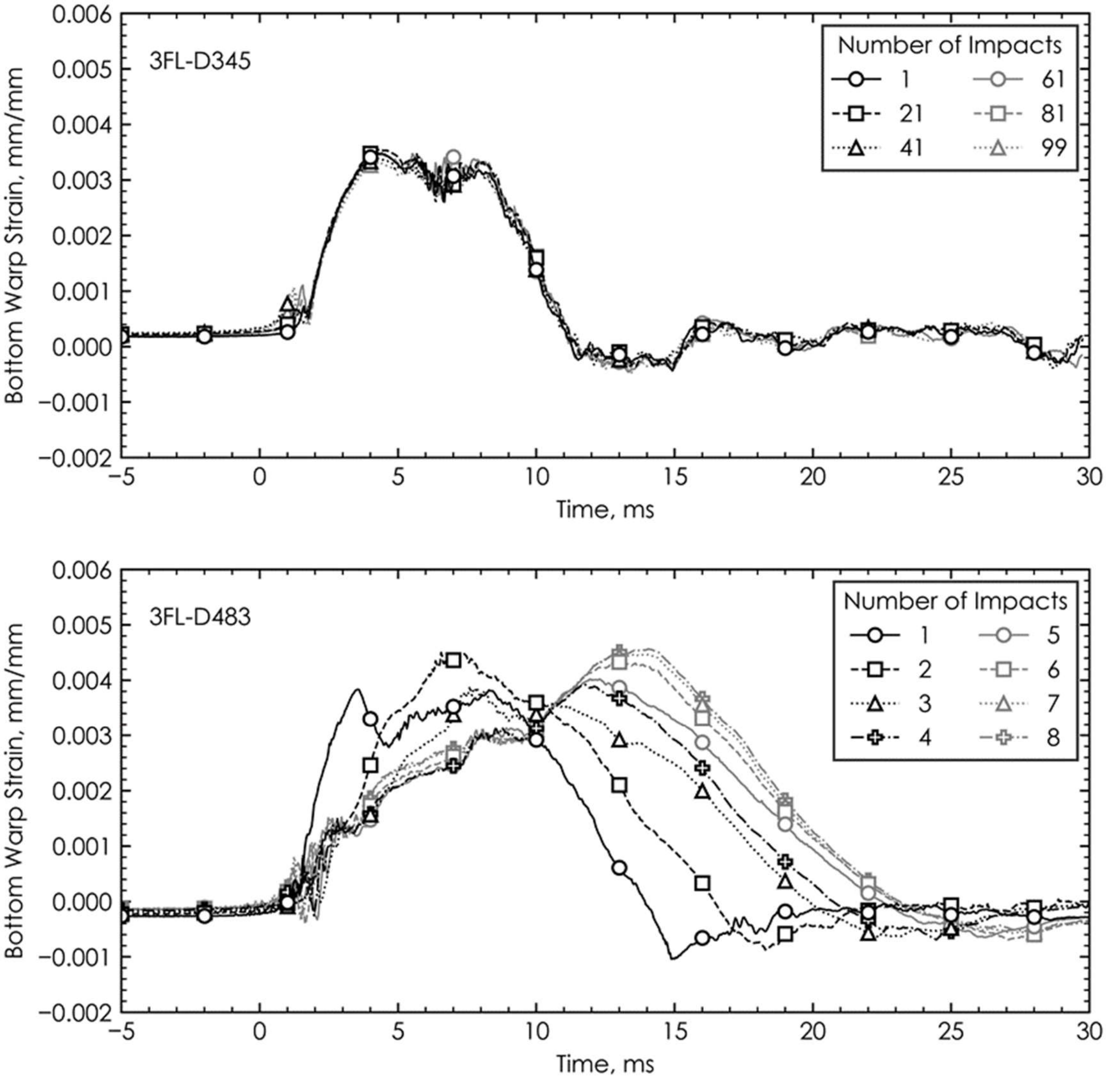

Figure 6-13. Impulse responses of 3FL-D345 and 3FL-D483 after multiple impact events

For panel 3FL-D345, the impulse response was not affected by multiple impacts. However, panel 3FL-D483 was significantly affected by the number of impacts and shows a clear damage progression as the number of impacts increased. As previously mentioned, panel 3FL-D483 showed visible damage after the first impact event and it also showed a prolonged impulse duration (Figure 6-10). As shown in Figure 6-13, the impulse duration increased further, and the strain response became softer after each subsequent impact. The visible progression of the damage is presented in Figure 6-14. There was an obvious visible damage progression, but the delamination was not observed until the eighth impact at which point the tests were stopped. However, upon examination of the impulse response plots shown in Figure 6-13, the progression of internal damage was more substantial than the damaged observed during testing.

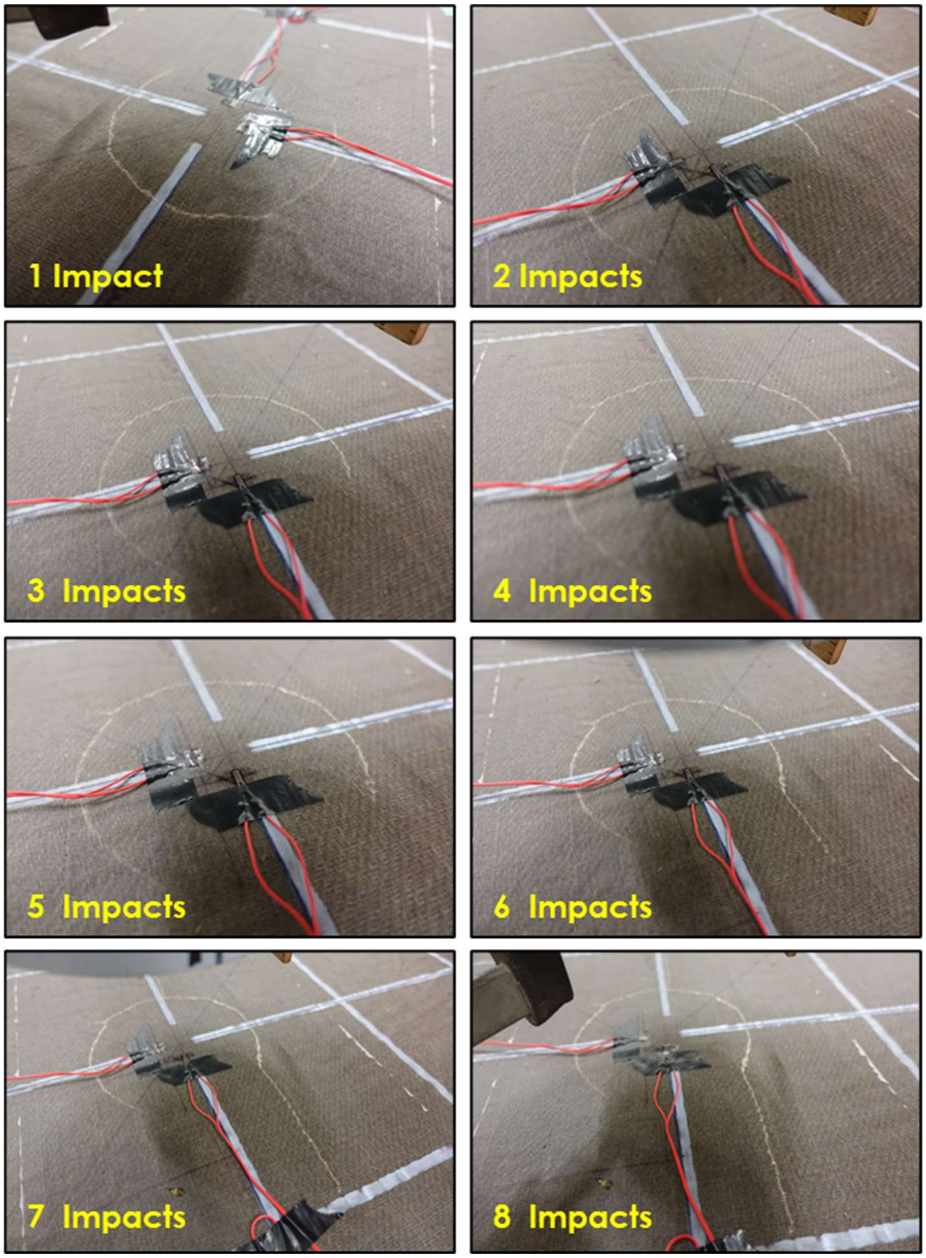

Figure 6-14. Visible damage indicating internal core shear damage progression of 3FL-D483 – significant damage observed after first impact, followed by slow increase of damage until, after six impacts, damage increases significantly and continues after next two impacts

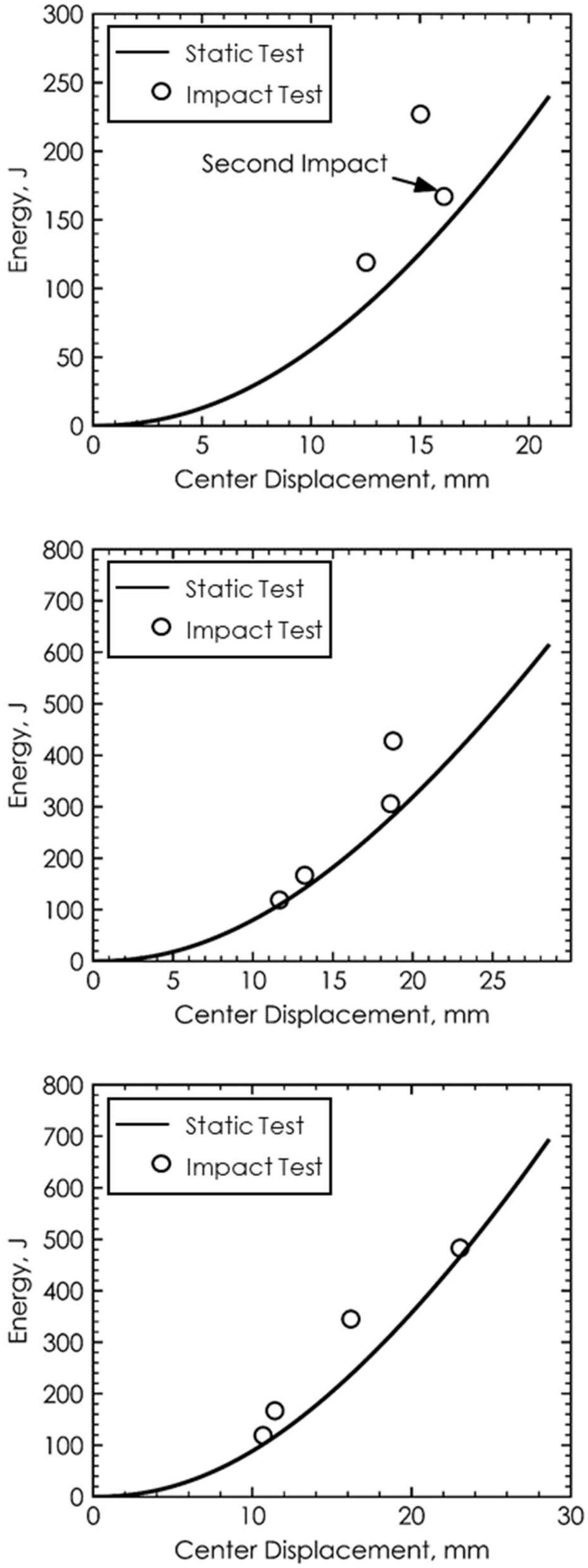

Figure 6-15. Comparison of the center displacement under impact and quasi-static tests

6.3.3. Comparison of Static and Impact Tests

To compare the behaviour of the panels under impact loads and under quasi-static loads, the cumulative energy was calculated at each load level during the quasi-static tests. Figure 6-15 shows the energy-displacement curves for the static tests and shows the deflections due to each impact at their respective energies. As shown in the figure, in all cases, the panels deflected less under impact loads than under the same cumulative energy applied quasi-statically. This shows that the panels have a higher stiffness when loaded under impact.

6.4. SUMMARY

As a part of this chapter, sandwich panels with flax fibre-reinforced polymer (FFRP) faces and polyisocyanurate (PIR) foam cores were tested in two-way bending and shear under quasi-static and impact loads. Each panel was 1220 mm by 1220 mm and approximately 80 mm thick. The main test parameters were the effect of face thickness (one, two or three layers of FFRP) and impact energy (50%, 70% and 95% of failure energy) on the panel behaviour. For each face thickness, four identical panels were fabricated and tested, totalling in twelve panels. One set of panels was tested under quasi-static loading by a 150 mm diameter circular load area applied at the center of a panel with a span length of 1120 mm in each direction. The results of the static tests were used to determine the required energy levels for the impact tests. The impact tests were performed using a drop weight (10.5 kg to 20 kg) with a maximum height of 3250 mm. The quasi-static results indicate that there is an increase in both strength and stiffness with face thickness and that the panels become more susceptible to punching shear failure as the face thickness increases. The results of the impact tests showed that the panels are susceptible to hidden internal damage after impacts, such as core shear failure. The analyses of the impact test data showed that the impulse duration of a panel increased with an increase of damage. Additionally, based on a comparison of the quasi-static and impact test data showed that the panels exhibited a higher stiffness when loaded under impact.

CHAPTER 7: ANALYTICAL MODELLING OF TWO-WAY FFRP-FOAM SANDWICH STRUCTURES

7.1. INTRODUCTION

Research on the use of more sustainable building materials is important in limiting the effect of new infrastructure on the environment. In the field of sustainable infrastructure, sandwich plates fabricated with natural materials, such as plant fibre-reinforced polymers (FRPs), have gained significant attention (Betts et al. 2018a, 2020a; Codyre et al. 2016; Mak and Fam 2019a; McCracken and Sadeghian 2018; Sadeghian et al. 2018). Due to their high moment of inertia and light weight, these natural sandwich panels have potential to be used for cladding systems and wall panels in new buildings. For these applications, it is important to understand the two-way behaviour of these sandwich plates and to have an efficient method with which to predict their behaviour under different loading conditions. Additionally, plant FRPs, such as flax FRPs (FFRPs), have been shown to exhibit a nonlinear stress-strain behaviour (Christian and Billington 2011; Hristozov et al. 2017; Mak et al. 2015; Mathura and Cree 2016; Yan et al. 2016) and in turn sandwich plates fabricated with FFRP faces have been shown exhibit a nonlinear load-deflection response (Betts et al. 2018a, 2020c; Mak et al. 2015). Therefore, to properly model sandwich plates fabricated with FFRP faces, it is necessary to consider the nonlinear stress-strain behaviour of both the faces and the core.

The behaviour of sandwich structures in general has been studied extensively in the past 70 years. Allen (1969) first presented a standard approach for predicting the behaviour of sandwich beams based on the ordinary-beam theory. Frostig et al (1992) developed a higher order procedure to predict the flexural behaviour of sandwich beams with transversely flexible cores under various loading conditions. Later, Frostig and Baruch (1996) studied the localised effect of a load on a sandwich plate under two-way loading. They developed a higher-order model to predict the two-way behaviour of the sandwich panels by analyzing the faces as thin panels and the core as a three-dimensional elastic solid. One limitation of the analytical models developed in the available literature is that the materials were assumed to behave in a linear fashion. Furthermore, higher-order modelling, while accurate, is quite comprehensive and requires advanced knowledge in mathematics. This means that it is less feasible for use by practicing engineers.

In the current study a simple model based on the first-order shear deformation Mindlin plate theory was developed for use by practicing engineers. The Mindlin plate model was chosen because shear deflections are significant in sandwich panels. The model incorporates the nonlinear behaviour of both the faces and the core material through the use of secant moduli. The intent of this study is to provide a simple and accurate method to predict the behaviour of sandwich plates made with nonlinear materials, specifically flax FRP faces and foam cores, such that they can be used in new infrastructure projects.

7.2. MODEL DEVELOPMENT

In this study, a model to predict the flexural behaviour of simply supported sandwich plates with thin faces and foam cores was developed. The model is based on the Mindlin plate model and therefore includes deflection due to shear. It also accounts for the nonlinear behaviour of both the faces and the core using a secant modulus. The undeformed and deformed geometries considered in the analysis are presented in Figure 7-1.

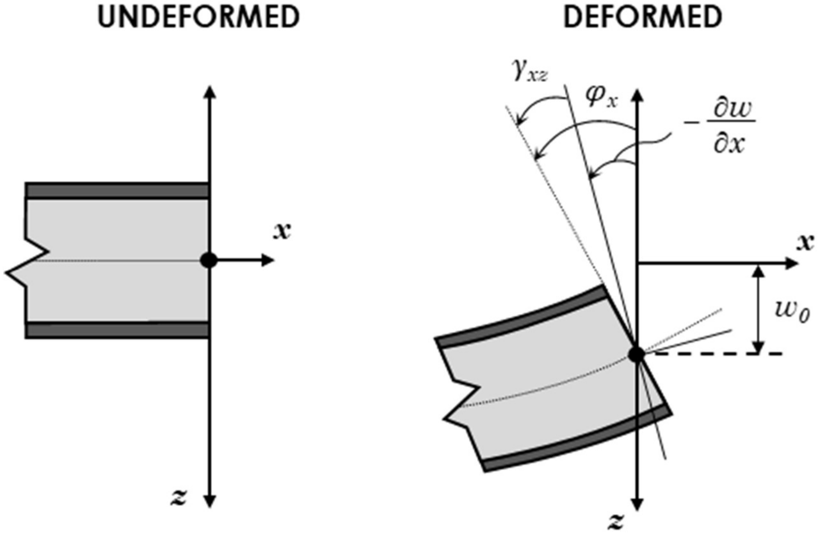

Figure 7-1. Assumed geometries used in the Mindlin Plate Theory

7.2.1. Assumptions

To allow for the development of a closed form solution for this problem, some assumptions were required. These assumptions are as follows:

- the face material is isotropic with different failure stress in x and y;
- the face material behaves same in tension and compression;
- the shear strain is constant through thickness (i.e. Mindlin Plate Theory);
- the core resists all shearing forces
- the faces resist all bending forces.

7.2.2. Governing Equations

The governing equations of the Mindlin plate theory, also known as the First-Order Shear Deformation Plate Theory (FSDT) are shown below as derived by Wang et al. (2000) with the following changes: $G_c = E/(2–2v)$ and $c = h$. These changes were implemented such that the core material resists all shearing forces.

$$-K_s G_c c\left(\frac{\partial^2 w_o}{\partial x^2}+\frac{\partial^2 w_o}{\partial y^2}+\frac{\partial \phi_x}{\partial x}+\frac{\partial \phi_y}{\partial y}\right)=q(x,y) \tag{7-1}$$

$$-\frac{D(1-\nu)}{2}\left(\frac{\partial^2 \phi_x}{\partial x^2}+\frac{\partial^2 \phi_x}{\partial y^2}\right)-\frac{D(1+\nu)}{2}\frac{\partial}{\partial x}\left(\frac{\partial \phi_x}{\partial x}+\frac{\partial \phi_y}{\partial y}\right)+K_s G_c c\left(\frac{\partial w_0}{\partial x}+\phi_x\right)=0 \tag{7-2}$$

$$-\frac{D(1-\nu)}{2}\left(\frac{\partial^2 \phi_y}{\partial x^2}+\frac{\partial^2 \phi_y}{\partial y^2}\right)-\frac{D(1+\nu)}{2}\frac{\partial}{\partial y}\left(\frac{\partial \phi_x}{\partial x}+\frac{\partial \phi_y}{\partial y}\right)+K_s G_c c\left(\frac{\partial w_0}{\partial y}+\phi_y\right)=0 \tag{7-3}$$

where w_0 is the deflection of the sandwich plate in the z-direction as shown in Figure 7-1, ϕ_x is the angle of rotation in the x-direction as shown in Figure 7-1, ϕ_y is the rotation in the y-direction, v is the Poisson's ratio, D is the flexural rigidity of the sandwich plate as shown in Eq. 7-4, G_c is the shear modulus of the core material, c is the thickness of the core and q is the loading. Note that K_s is a shear correction factor which, for rectangular sections, is typically assumed to be 5/6. This assumption will be used for these sandwich panel equations as the core material is assumed to resist all shearing forces.

$$D = \frac{E_f t d^2}{2(1-\nu^2)} \tag{7-4}$$

where E_f is the modulus of elasticity of the face material, t is the thickness of each face and d is the distance between the centroids of the two faces (d=c+t).

Using the Navier Solution, the loading on the square sandwich plate with side lengths L as shown in Figure 7-2 can be represented as a double trigonometric series as shown in Eq. 7-5 (Timoshenko and Woinowsky-Krieger 1987).

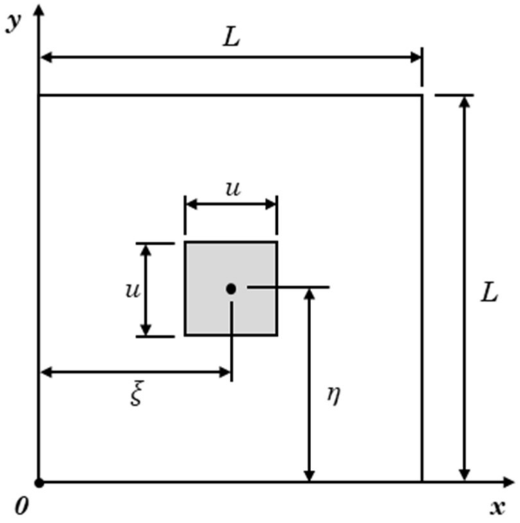

Figure 7-2. Square sandwich plate partially loaded over an area

$$q(x,y) = \sum_{m=1}^{\infty}\sum_{n=1}^{\infty} a_{mn} \sin\left(\frac{m\pi x}{L}\right)\sin\left(\frac{n\pi y}{L}\right) \tag{7-5}$$

For a simply supported plate, the boundary conditions are shown in Eq. 7-6.

$$\begin{aligned} &w_0 = 0;\quad \phi_y = 0;\quad M_{xx} = D\left(\frac{\partial\phi_x}{\partial x} + \frac{\nu\partial\phi_y}{\partial y}\right) = 0 \qquad \text{for } x = 0 \text{ and } x = L \\ &w_0 = 0;\quad \phi_x = 0;\quad M_{yy} = D\left(\frac{\partial\phi_y}{\partial y} + \frac{\nu\partial\phi_x}{\partial x}\right) = 0 \qquad \text{for } y = 0 \text{ and } y = L \end{aligned} \tag{7-6}$$

Upon examination, the boundary conditions are satisfied for Eq. 7-1 and Eq. 7-5 if the deflections are represented as shown in Eq. 7-7, 7-8 and 7-9.

$$w_0 = \sum_{m=1}^{\infty}\sum_{n=1}^{\infty} C_w \sin\left(\frac{m\pi x}{L}\right)\sin\left(\frac{n\pi y}{L}\right) \tag{7-7}$$

$$\phi_x = \sum_{m=1}^{\infty}\sum_{n=1}^{\infty} C_x \cos\left(\frac{m\pi x}{L}\right)\sin\left(\frac{n\pi y}{L}\right) \tag{7-8}$$

$$\phi_y = \sum_{m=1}^{\infty}\sum_{n=1}^{\infty} C_y \sin\left(\frac{m\pi x}{L}\right)\cos\left(\frac{n\pi y}{L}\right) \tag{7-9}$$

By substituting Eqs. 7-7, 7-8 and 7-9 into Eqs. 7-1, 7-2 and 7-3 and solving the system of equations, the coefficients C_w, C_x and C_y can be found and are presented in Eqs. 7-10, 7-11 and 7-12.

$$C_w = \frac{L^2 a_{mn}}{\pi^2}\left(\frac{1}{K_s G_c c(m^2+n^2)} + \frac{L^2}{D\pi^2(m^2+n^2)^2}\right) \tag{7-10}$$

$$C_x = -\frac{L^3 m a_{mn}}{D\pi^3(m^2+n^2)^2} \tag{7-11}$$

$$C_y = -\frac{L^3 n a_{mn}}{D\pi^3(m^2+n^2)^2} \tag{7-12}$$

Timoshenko and Woinowsky-Krieger (1987) showed that for the case shown in Figure 7-2 of a force *P* applied over a square area centered at $x=\xi$ and $y=\eta$, a_{mn} can be represented by Eq. 7-13.

$$a_{mn} = \frac{16P}{\pi^2 mnu^2}\sin\left(\frac{m\pi\xi}{L}\right)\sin\left(\frac{n\pi\eta}{L}\right)\sin\left(\frac{m\pi u}{2L}\right)\sin\left(\frac{n\pi u}{2L}\right) \tag{7-13}$$

where u is the side length of the load area. Therefore, by combining Eqs. 7, 10 and 13 the deflection of the simply supported plate can be presented as shown in Eq. 7-14.

$$w_0 = \frac{16P}{\pi^2 u^2}\sum_{m=1}^{\infty}\sum_{n=1}^{\infty}\frac{1}{mn} C_w \sin\left(\frac{m\pi x}{L}\right)\sin\left(\frac{n\pi y}{L}\right)\sin\left(\frac{m\pi\xi}{L}\right)\sin\left(\frac{n\pi\eta}{L}\right)\sin\left(\frac{m\pi u}{2L}\right)\sin\left(\frac{n\pi u}{2L}\right) \tag{7-14}$$

For the specific case of determining the center deflection of a sandwich plate loaded at the center by a square area with side length u, the equation can be simplified by noting that for $x = y = \xi = \eta = L/2$ the respective sine terms are 0 when m or n is even or 1 when m or n is odd. The center deflection for this specific case is presented in Eq. 7-15.

$$w_0 = \frac{16PL^2}{\pi^4 u^2} \sum_{m=1,3,5\ldots}^{\infty} \sum_{n=1,3,5\ldots}^{\infty} \frac{1}{mn} \left(\frac{1}{K_s G_c c(m^2+n^2)} + \frac{L^2}{D\pi^2 (m^2+n^2)^2} \right) \sin\left(\frac{m\pi u}{2L}\right) \sin\left(\frac{n\pi u}{2L}\right) \tag{7-15}$$

The face strains in the principle directions can also be found knowing that:

$$\epsilon_x = z\frac{\partial \phi_x}{\partial x} \tag{7-16}$$

where z is the distance from the neutral axis. To determine the strains in the faces, z is set as half of the distance between the center of the top and bottom faces, $d/2$. By combining Eqs. 7-8, 7-11 and 7-16, the face strains at the center for the case described above can be represented as shown in Eq. 7-17.

$$\epsilon_{fx} = \frac{8PL^2 d}{D\pi^4 u^2} \sum_{m=1,3,5\ldots}^{\infty} \sum_{n=1,3,5\ldots}^{\infty} \frac{m}{n(m^2+n^2)^2} \sin\left(\frac{m\pi u}{2L}\right) \sin\left(\frac{n\pi u}{2L}\right) \tag{7-17}$$

7.3. ANALYSIS PROCEDURE

The model presented above was used in a program written in the programming language Python to predict the behaviour of sandwich plates load by a concentrated load at the center. In this program the model was expanded to include the nonlinear behaviour and failure of both the face and core materials. The flowchart of the analysis is presented in Figure 7-3.

7.3.1. Incorporating Nonlinear Material Behaviour

To incorporate the nonlinear behaviour of the face and core materials, the stress-strain behaviour of both the materials was required. At the first and second steps in the modelling, the initial moduli of both the core and the faces were used to perform the calculations. In all subsequent steps, the strains calculated in the previous step and the corresponding material stresses were used to calculate a secant modulus as shown in in Figure 7-4.

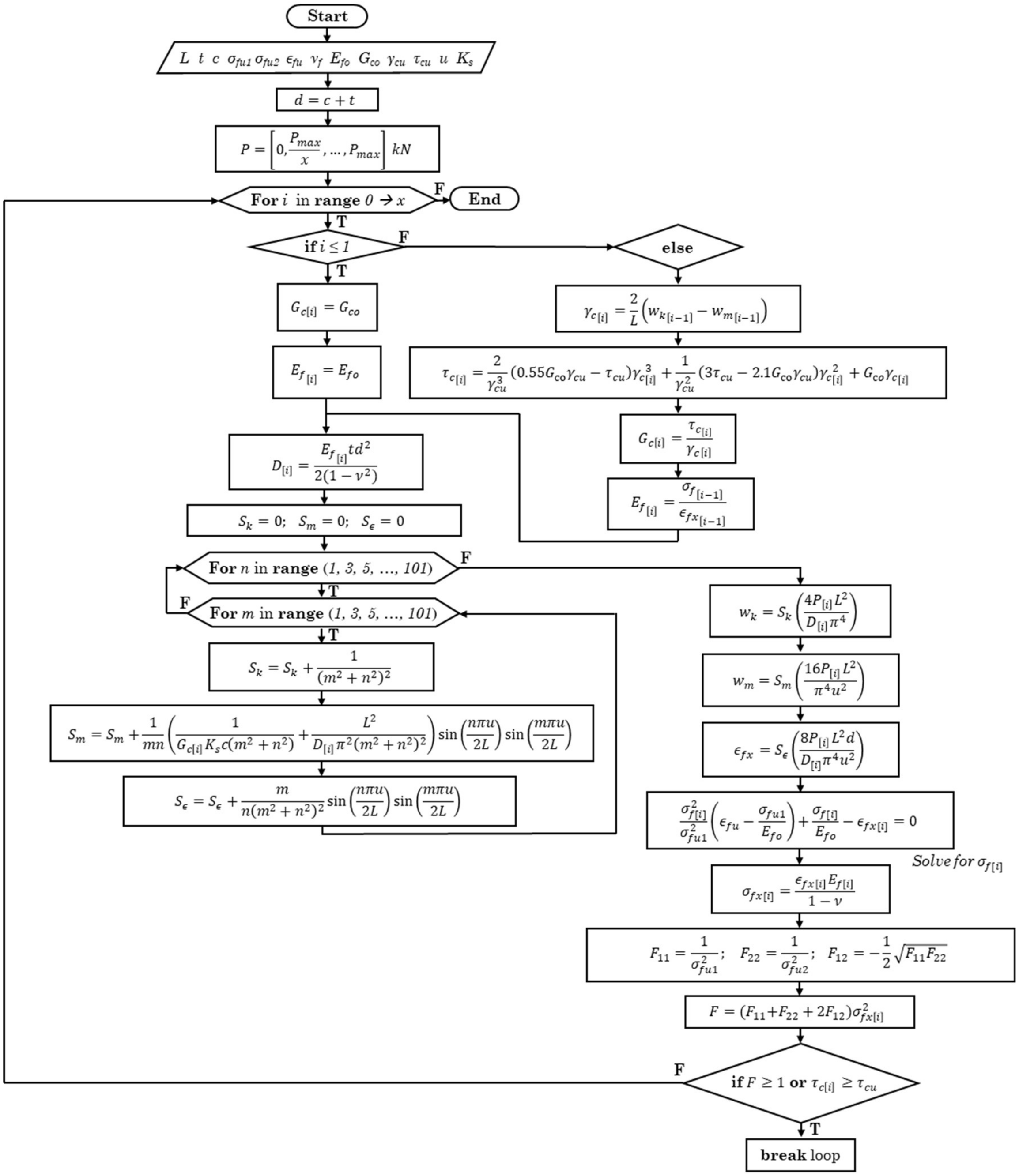

Figure 7-3. Analysis flow chart

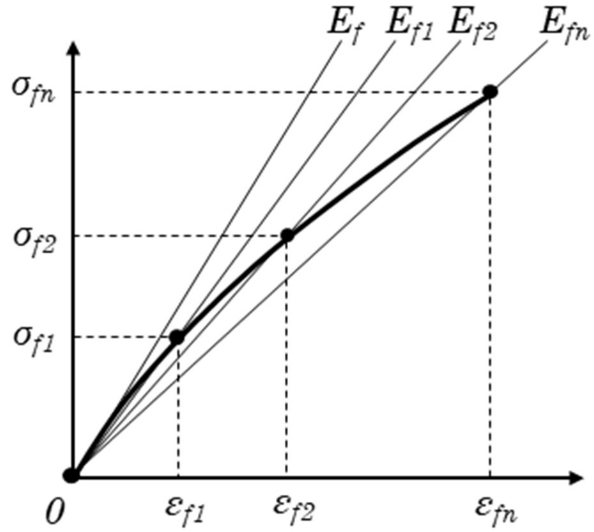

Figure 7-4. Incorporating nonlinear behaviour using a secant modulus

Determining the secant elastic modulus for the face material is straightforward. The face strain in the *x*-direction is calculated at each model step using Eq. 17. Knowing the stress-strain relationship of the material, the corresponding stress, σ_f, can be determined and the secant modulus can be calculated through $E_f = \sigma_f \ / \ \epsilon_{fx}$.

To determine the secant shear modulus in the core at each model step, a simplified method was used. The deflection due to bending only, w_k, was calculated based on the Kirchhoff Plate Theory as shown in Eq. 7-18.

$$w_k = \frac{16PL^4}{D\pi^6u^2} \sum_{m=1,3,5\ldots}^{\infty} \sum_{n=1,3,5\ldots}^{\infty} \frac{1}{mn(m^2+n^2)^2} \sin\left(\frac{m\pi u}{2L}\right) \sin\left(\frac{n\pi u}{2L}\right) \tag{7-18}$$

Then, the deflection due to shear was calculated as $w_{shear} = w_0 - w_k$ and shear strain in the core was calculated as $\gamma_c = 2w_{shear} \ / \ L$. Using the known shear stress-strain relationship of the core material, the shear stress in the core, τ_c, can be determined. Finally, the secant shear modulus was calculated as $G_c = \tau_c \ / \ \gamma_c$.

7.3.2. Ultimate Conditions

The ultimate condition of the model is based on material failure and considers both failure of the face material or failure of the core material. As many sandwich plates are constructed using fibre-reinforced polymers, the Tsai Wu criterion (Tsai and Wu 1971) was chosen to predict the failure of the faces and failure due to shear was considered in the core.

To predict the face failure, the state of stress in the face is required. During each step of the analysis, the stress in the face was calculated using Eq. 7-19, which was derived based on the stress-strain relationship presented by Bank (2006).

$$\sigma_{fx} = \frac{\epsilon_{fx} E_f}{1 - \nu} \tag{7-19}$$

As the behaviour of the faces was considered to be isotropic with different failure stresses in the x and y-directions, the Tsai Wu failure criterion (Tsai and Wu 1971) was reduced to the following form:

$$\left(\frac{1}{\sigma_{fu1}^2} + \frac{1}{\sigma_{fu2}^2} - \frac{1}{\sigma_{fu1}\sigma_{fu2}}\right)\sigma_{fx}^2 \leq 1 \tag{7-20}$$

where σ_{fu1} is the ultimate stress in the x-direction and σ_{fu2} is the ultimate stress in the y-direction. If this statement becomes false, then the face material was considered to have failed. The core was considered to have failed if the shear stress in the core, τ_c, was larger than the ultimate shear stress, τ_{cu}.

7.4. MODEL VERIFICATION

To verify the analysis method presented in the previous section, the panels tested in Chapter 6 were modelled. In this section, the material properties, fabrication methods and behaviour of the tested sandwich plates will be briefly discussed, and the verification of the model will be presented.

7.4.1. Test Specimen Properties

7.4.1.1. Material Properties

The sandwich plates were fabricated with FFRP faces and polyisocyanurate (PIR) foam cores. It has been reported by various authors that plant FRPs, such as FFRPs, exhibit a nonlinear stress-strain behaviour (Christian and Billington 2011; Hristozov et al. 2016; Mak et al. 2015; Mathura and Cree 2016; Yan et al. 2016). In the current study, the FFRPs were made with a balanced bidirectional 2x2 twill flax fabric and a bio-based epoxy resin. The same FFRPs were also used and tested in Chapter 6. They tested two-layer FFRP tension coupons warp (average thickness of 2.28 mm) and weft (average thickness of 2.40 mm) directions and found that the FFRPs exhibited a nonlinear behaviour in both directions. The ultimate tensile strength, initial tensile modulus and ultimate tensile strain 70.0 ± 3.4 MPa, 6.35 ± 0.71 GPa, and 0.0202 ± 0.0022 mm/mm, respectively in the warp direction, and 51.3 ± 1.4 MPa, 5.64 ± 0.90 GPa, and 0.0204 ± 0.0024 mm/mm, respectively in the weft direction. To incorporate the nonlinear behaviour of the FFRPs in the model, a parabolic stress-strain relationship was assumed. The relationship, presented in Eq. 7-21 and shown in Figure 7-5a, was based on the assumptions that the initial slope is the modulus of the FFRP, E_{fo}, and that the ultimate stress, σ_{fu}, corresponds with the ultimate strain, ϵ_{fu}. In the current study, it was assumed that the FFRPs behaved similarly in the warp and weft direction and that the compressive and tensile behaviour were the same. In future studies, this analysis can be improved by incorporating the orthotropic behaviour of the FFRPs as well as their compressive behaviour.

$$\epsilon_f = \frac{\sigma_f^2}{\sigma_{fu}^2}\left(\epsilon_{fu} - \frac{\sigma_{fu}}{E_{fo}}\right) + \frac{\sigma_f}{E_{fo}} \tag{7-21}$$

The sandwich panel cores were made of a PIR foam with a density of 96 kg/m^3. It is also known that foams typically exhibit a nonlinear behaviour (Sharaf 2010). In a previous study by Betts et al (Betts et al. 2020a), a cubic shear stress-shear strain relationship based on the following boundary conditions presented in Eq. 7-22 and was shown to work well for PIR foams. That relationship was adopted for this model and is presented in Eq. 7-23 and is shown in Figure 7-5b compared to the shear stress-strain data for the foams presented in Chapter 6.

$$\tau_c = 0;\ \frac{d\tau_c}{d\gamma_c} = G_{co} \ \text{ for } \gamma_c = 0 \qquad \text{and} \qquad \tau_c = \tau_{cu};\ \frac{d\tau_c}{d\gamma_c} = \frac{G_{co}}{10} \ \text{ for } \gamma_c = \gamma_{cu} \tag{7-22}$$

$$\tau_c = \frac{2}{\gamma_{cu}^3}[0.55G_{co}\gamma_{cu} - \tau_{cu}]\gamma_c^3 + \frac{1}{\gamma_{cu}^2}[2\tau_{cu} - 2.1G_{co}\gamma_{cu}]\gamma_c^2 + G_{co}\gamma_c \tag{7-23}$$

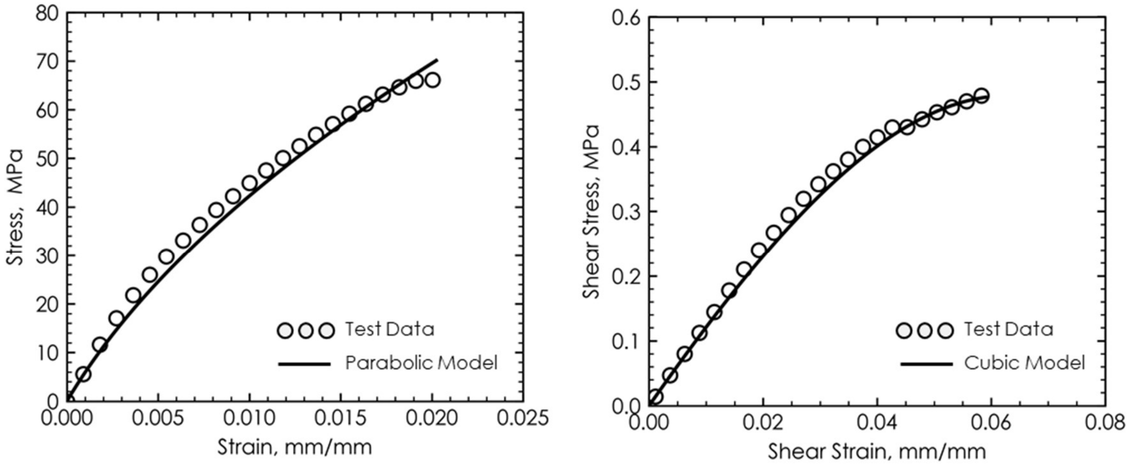

(a) (b)

Figure 7-5. Material models (a) FFRP in tension and (b) 96 kg/m³ PIR foam in shear

7.4.1.2. Specimen Fabrication

Figure 6 shows the fabrication and test set-up used for the model verification tests. Each plate was 1200 mm x 1200 mm with a thickness of approximately 80 mm. As shown in the figure, the sandwich plate faces were fabricated using a wet lay-up procedure. The foam surface was cleaned of any dust and debris and the surface was wetted with the bio-based epoxy. Once the surface was evenly coated with epoxy (shown in Figure 7-6a), the first layer of fabric was placed on the wetted surface noting the warp direction of the fabric. Epoxy was applied to the surface of the fabric. For the sandwich plate with two-layer FFRP faces, this process was repeated for the second layer as shown in Figure 7-6b. Parchment paper was placed on the face and a plastic scraper was used to remove any air and excess epoxy. The face was then allowed to cure at room temperature for at least seven days before cutting the excess FFRP from the plate edges. This entire procedure was repeated for the opposite face.

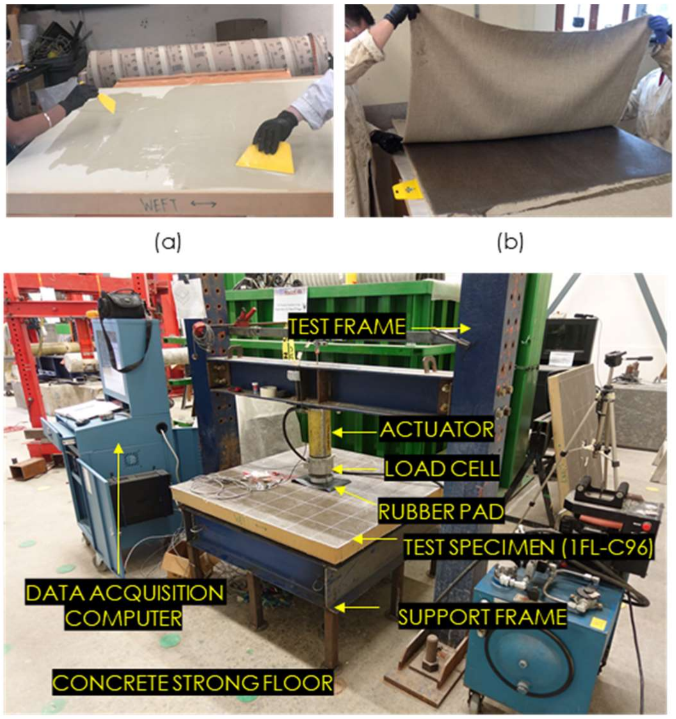

(a) (b)

(c)

Figure 7-6. Fabrication and testing of sandwich panels: (a) applying epoxy to foam surface; (b) placing a layer of flax fabric; and (c) test set-up

7.4.1.3. *Test Set-up*

A photo of the test set-up is presented in Figure 6c and the instrumentation layout is shown in Figure 7-7. The span length in both directions was 1120 mm. The plates were simply supported by 32 mm diameter steel tubes on a frame sitting on a concrete strong floor. Two of the steel tubes (one in each direction) were welded to the frame to simulate a pin connection, while the other two were allowed to roll. The deflection at the center of the plate was measured by a string potentiometer. Additionally, the deflections at quarter points as shown in Figure 7-7 were measured using LVDTs with a 100 mm stroke length. At the center of the top and bottom faces, strains were measured using strain gauges with 6 mm gauge lengths in the warp and weft directions and also at 45°. The load was applied to the specimens through a circular disc with a diameter 150 mm attached to a 250 kN load cell.

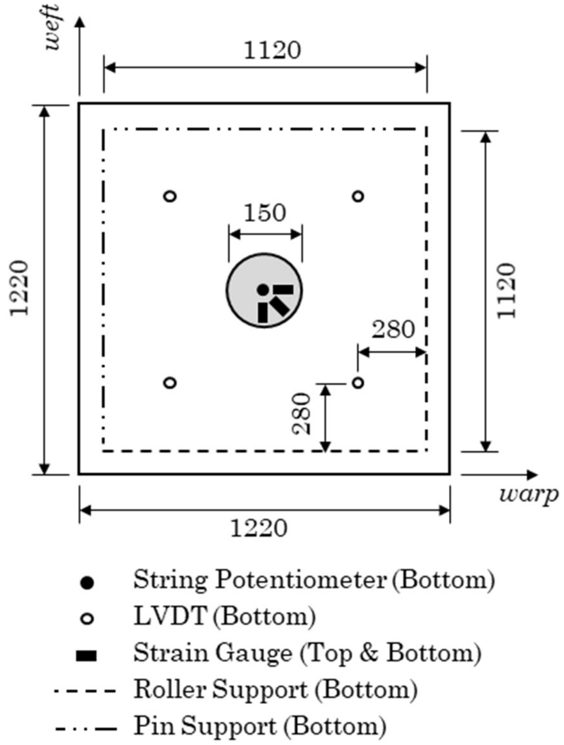

Figure 7-7. Test Instrumentation

7.4.2. Modelling

The analysis procedure (shown in Figure 7-3) was implemented using a computer program (provided in Appendix D) written in the Python programming language using the scientific package, Anaconda. The FFRP properties determined in Chapter 6 were used to model the faces. The properties of the FFRPs were normalized to a thickness of 2.5 mm and it was assumed that each individual layer had a thickness of 1.25 mm. The 96 kg/m^3 foam core shear strength and modulus were determined through testing according to ASTM C273 (ASTM 2018b) and presented in Chapter 6. One notable difference between the tests and the model is the loading area. In the model, a square loading area with a side length of 150 mm is assumed for simplicity. However, to avoid a local failure at corners, a circular loading area with a diameter of 150 mm was used in the tests.

Table 7-1. Comparison of test and model results

	Ultimate Load, kN			Ultimate Deflection, mm			Ultimate Quarter-Point Deflection, mm			Stiffness, N/mm			Quarter-Point Stiffness, N/mm			Failure Mode	
No. Flax Layers	Model	Test	Model/ Test Ratio	Model	Test	Model/ Test Ratio	Model	Test	Model/ Test Ratio	Model	Test	Model/ Test Ratio	Model	Test	Model/ Test Ratio	Model	Test
1	21.5	21.8	0.99	23.4	20.9	1.12	11.72	7.75	1.51	1205	1210	1.00	2152	2861	0.75	FR	FR
2	43.3	38.8	1.12	29.2	28.5	1.03	14.62	9.65	1.51	1887	1781	1.06	3503	4519	0.78	FR	FR/CS
3	66.1	43.5	1.52	37.1	28.6	1.30	18.56	8.49	2.19	2320	1975	1.17	4384	5385	0.81	FR	CS
AVE			1.21			1.15			1.74			1.08			0.78		

AVE = average, FR = Face Rupture, CS = Core Shear

7.4.3. Comparison of Tests and Models

A comparison of the test results and models is presented in Table 7-1 and Figure 7-8 and Figure 7-9. As shown in Table 7-1, the model predicted the load-deflection behaviour of the plates with one-layer and two-layer FFRP faces (1FL) well. The model-test ratios of ultimate load, ultimate deflection and initial stiffness were 0.99, 1.12 and 1.00, respectively. The same model-test ratios of two-layer (2FL) model were 1.12, 1.03, and 1.06, respectively. However, the model over predicted the load and stiffness of the 3FL plate significantly. This is due to the development of a local failure mechanism which was not captured by the model. This will be discussed further in this section.

7.4.3.1. Ultimate Conditions

Photos of the test plate failures are presented in Figure 7-8. Both the 1FL and 2FL specimens experienced a bottom face tensile rupture in the weft direction. As shown in the Table 7-1, the model also predicts a face rupture type failure. However, as shown in Figure 7-8b, the 2FL plate was close to core shear failure as evidenced by the cracking observed on the top face. The 3FL plate tested failed due to core shear whereas the model predicted a face rupture failure. This discrepancy is due to the observed indentation that occurred under the loading are during testing as it caused significant shear stresses to develop in the core.

Therefore, the model was able to accurately capture the failure mechanism of panels with thinner faces but was not able to capture the localised indentation failure mechanism that was present in the thicker faced sandwich plates. As a result, the prediction of ultimate capacity is affected by the face thickness. The model was able to predict accurately the ultimate capacity of the 1FL plate (within 1%) and the 2FL plate (with 12%) which both failed due to face rupture. However, the ultimate capacity of the 3FL plate was overestimated by 52%. In future studies, indentation should be included in models as a potential failure mode. This will likely require the use of finite element analysis.

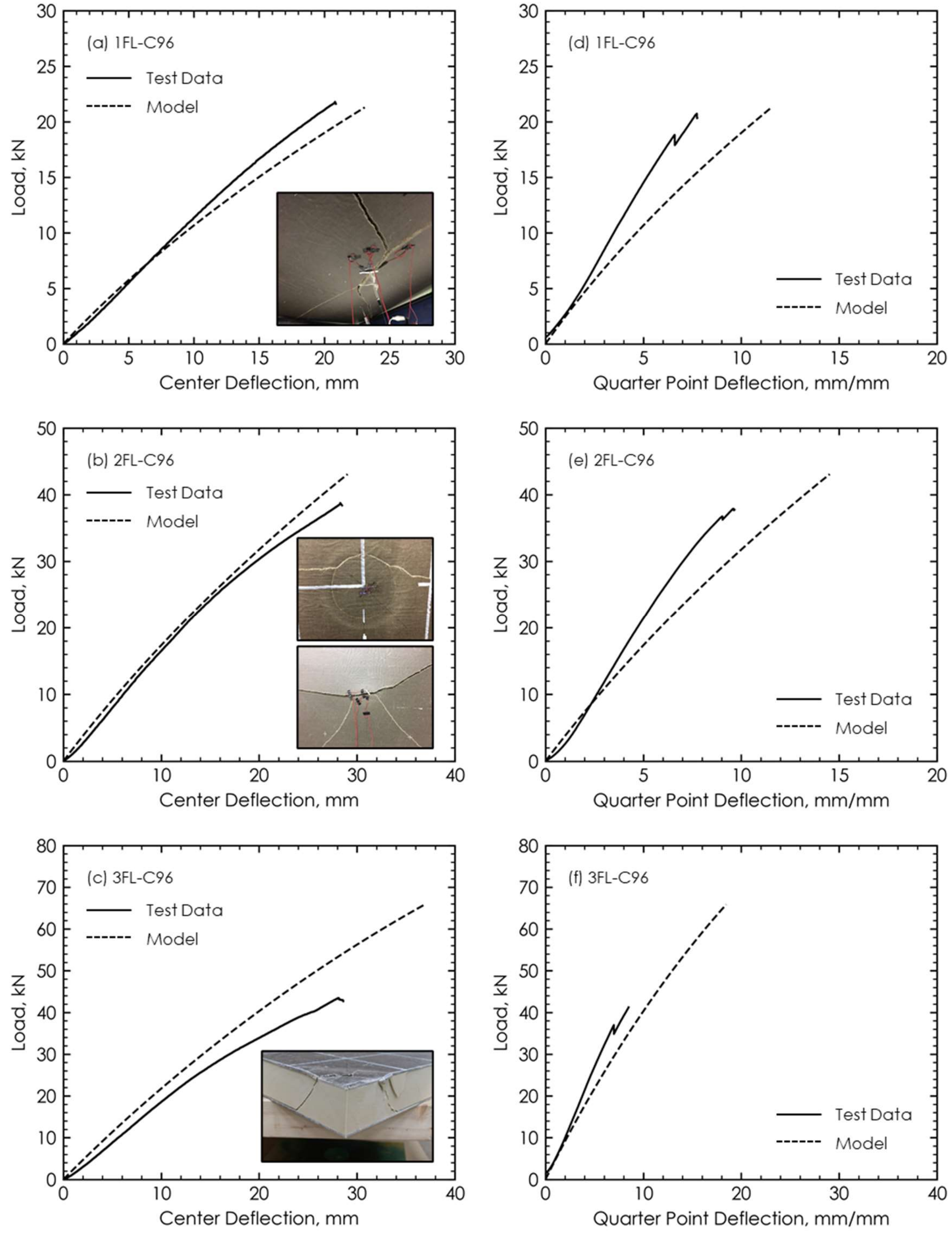

Figure 7-8. Load-deflection curves (a) 1FL-C96 center; (b) 2FL-C96 center; (c) 3FL-C96 center (d) 1FL-C96 quarter point; (e) 2FL-C96 quarter point and; (f) 3FL-C96 quarter point

7.4.3.2. Load-Deflection Behaviour

Comparisons of the midspan load-deflection behaviours of the models and tests are presented in Figure 7-8a-c. These plots show that the load-deflection behaviour of the plates was predicted accurately, especially for the thinner faced specimens. As mentioned previously, this accuracy is also shown by the test-model ratios of the stiffness. For the 1FL, the initial stiffness was predicted within 1%. However, as the face thickness increased, the accuracy of the stiffness was reduced. The initial stiffnesses of the 2FL and 3FL plates were predicted to with 6% and 17% respectively.

The quarter-point load-deflection behaviours were also modelled and compared with the test data shown in Figure 7-8c-d. This modelling was performed by using Eq. 14 and setting both x and y to $L/4$. As shown in Figure 7-8 and Table 7-1, the quarter-point deflection was overestimated, and the quarter-point stiffness was underestimated for each panel. This discrepancy between the model and the test results is likely due to localised effects that happen closer to the loading point that are not captured by the model.

7.4.3.3. Load-Strain Behaviour

The comparisons of the load-strain behaviour of the tests and the models are presented in Figure 7-9. The model is shown to accurately predict the load-strain behaviour of the bottom face for all the sandwich plates. However, as shown in Figure 9, the strains in the top face are drastically overestimated by the model.

Upon examination of the data and based on test observations, it is hypothesized that this softness is due to localised indentation of the top face under the load area as shown in Figure 7-10. As the top face experiences localised deflection, it experiences some tensile strain, thereby lessening the compression strain in the face and producing a stiffer load-strain diagram. In the case of the 3FL sandwich plate, the top face under the loading area goes fully into tension before failure occurs. Upon examining Figure 7-9c, in the early portion of the load-strain diagram, the test data and model prediction are closely matched. Then, there is an observable increase in slope which supports the presented hypothesis. Based on these results, it is evident that it is necessary to capture the localised indentation of these plates in order to accurately predict their flexural behaviour under concentrated loads.

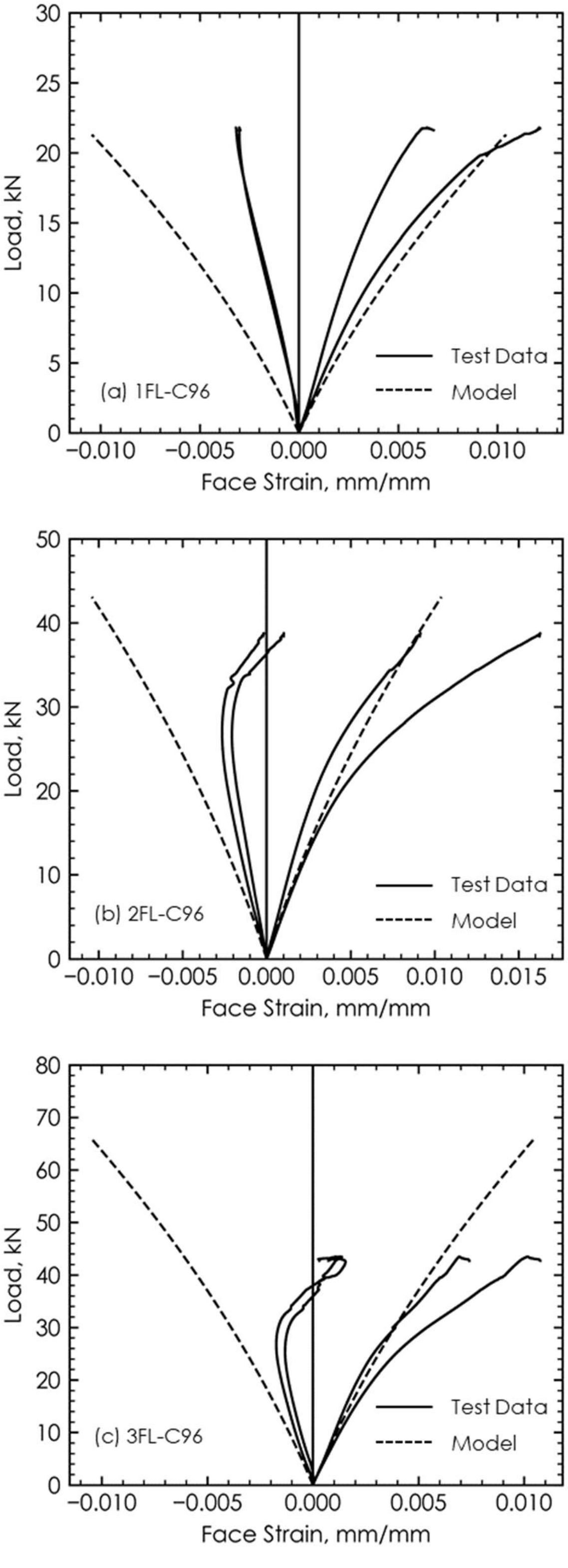

Figure 7-9. Load-strain curves (a) 1FL-C96; (b) 2FL-C96 and (c) 3FL-C96

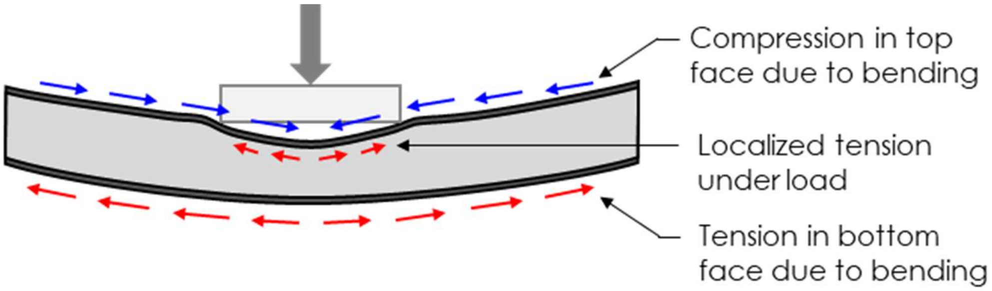

Figure 7-10. Development of tensile forces in top face under loading area

7.5. SUMMARY

In this chapter, a novel method to predict the flexural behaviour of sandwich plates constructed with nonlinear materials is presented. The model is based on the First-Order Shear Deformation Plate Theory (FSDT), also known as the Mindlin Plate Theory. It captures the nonlinear behaviour of both the face material and the core material through the use of a secant modulus. Three sandwich plates were fabricated and tested under a concentrated load applied through a 150 mm diameter circular plate. Both plates were constructed of a 75 mm thick, 96 kg/m^3 polyisocyanurate core and flax fibre-reinforced faces which were fabricated with bidirectional flax fabric with an areal density of 400 g/m^2 and a bio-based epoxy. Each plate was fabricated with a different face thickness, namely one, two or three layers of flax fibre-reinforced polymer (FFRP). The developed model was compared with the test results of the tested sandwich plates. It was determined that the model was able to accurately predict the behaviour of the thin faced sandwich plate (one-layer FFRP). However, localised indentation was prevalent in the thicker faces plates which load to overprediction of ultimate strength by the model. The intent of the model is to provide a simple model to predict the load-deflection behaviour of simply supported sandwich plates loaded by a partial uniformly distributed load.

CHAPTER 8: FINITE ELEMENT MODELLING OF TWO-WAY FFRP-FOAM SANDWICH STRUCTURES UNDER QUASI-STATIC AND IMPACT LOADS [5]

8.1. INTRODUCTION

Sandwich panels are efficient structures made of two relatively strong and stiff faces separated by a lightweight core. The separation of the two faces provided by the core increases the moment of inertia which gives these panels a high stiffness and flexural rigidity. The faces resist the majority of the bending force, while the core resists shear force. As lightweight foams with high insulative properties can be used as the core material, these structures are ideal for applications where light weight and high insulation are required, such as building cladding materials.

As the core material is typically significantly weaker than the face materials, the capacity of these structures is often limited by the core strength. Traditional sandwich panel faces include aluminium, glass fibre-reinforced polymers (GFRPs) and carbon fibre-reinforced polymers (CFRPs). As these traditional face materials are underutilized, there is an opportunity to replace these materials with weaker, but more sustainable, materials such as flax fibre-reinforced polymers (FFRPs). The material properties of FFRPs and other natural fibre-reinforced polymers have been investigated extensively in the literature and the results show that they exhibit a nonlinear stress-strain response (Betts et al. 2018a; Christian and Billington 2011; Sadeghian et al. 2018).

Sandwich panels with traditional face materials have been studied extensively using finite element (FE) modelling under quasi-static loads (Dawood et al. 2010; Satasivam et al. 2018; Sharaf and Fam 2012) and impact loads (Besant et al. 2001; Feng and Aymerich 2013; Meo et al. 2005; Zhang et al. 2016; Zhou et al. 2012). Dawood et al (2010) tested and numerically modelled two-way 1220 mm x 1220 mm x 25 or 50

---

[5] **Preliminary results for this study were published in the proceedings of the *7th Asia-Pacific Conference on FRP in Structures:***

Betts D, Sadeghian P, Fam A. Parametric Study of the Flexural Behaviour of Sandwich Panels with Flax FRP Faces and Foam Cores Using Finite Element Analysis. *7th Asia-Pacific Conference on FRP in Structures.* Surfers Paradise, Gold Coast, Australia, 2019.

mm thick sandwich structures with glass FRP (GFRP) faces and foam cores. They used an FE model paired with a rational analysis to develop a simplified analysis procedure with which they performed a parametric study. Sharaf and Fam (2012) developed a numerical FE model to predict the one-way bending behaviour sandwich panels with GFRP faces and foam cores with and without ribs. Their model accounted for material and geometric nonlinearity and was validated against experimental data. The model was then used to determine the most efficient GFRP rib configuration of the panels. Sandwich panels have also been investigated using fibre element modelling (Fam et al. 2016). In this study Fam et al (2016) examined the behaviour of one-way sandwich beams with glass FRP faces and soft cores and looked at the effect of shear deformation of the core on the behaviour of the sandwich beams. They showed that both face thickness and core density affected the failure modes observed in the beams and that as the core density increased from low density (32 kg/m^3) to high density (192 kg/m^3), the contribution of shear deflection decreased significantly.

Recently, FFRP-foam sandwich panels have been investigated under flexural loads (Betts et al. 2018a; Mak et al. 2015; Mak and Fam 2019a; Sadeghian et al. 2018) and axial loads (Codyre et al. 2016) and impact loads (Betts et al. 2020a, 2021). Some studies have been completed on experimental and FE modelling of FFRP-cork sandwich panels under impact loads (Boria et al. 2018). However, in the study by Boria et al. (2018), the nonlinear behaviour of the FFRP faces was not considered. There are currently no studies providing an in-depth look at the behaviour of FFRP-foam sandwich structures under flexural loads using FE modelling. Additionally, there is still a major gap in the literature concerning the two-way behaviour of sandwich structures with FFRP faces. In this chapter, FE models considering the material and geometric nonlinearity of the two-way behaviour of FFRP-foam sandwich panels loads are developed and verified using experimental data. Then, the modelling program is expanded to perform a parametric study to determine the effect of face thickness, core thickness, foam core density and the load area size on their flexural and shear behaviour under both quasi-static and impact loads.

8.2. QUASI-STATIC MODELLING

8.2.1. Summary of Experimental Program

In Chapter 6, the experimental program of the sandwich panels was presented. Three quasi-static concentrated load tests were performed on 1220 mm x 1220 mm x 80 mm sandwich panels with FFRP faces and 96 kg/m^3 PIR foam cores. The main test parameter was the effect of face thickness, namely one, two or three layers of FFRP per face.

In the tests, the load was applied through a 150 mm diameter loading disc at a constant displacement rate. The panels were supported on a steel frame on a concrete strong floor by two pin supports (welded rollers) and two roller supports (free rollers) such that the span length was 1120 mm in each direction. The strains in the warp and weft directions were measured at the center of both the top and bottom faces. Additionally, the applied load was measured using a 250 kN load cell and the center deflection was measured using a string potentiometer attached to the bottom face.

8.2.2. FE Model Development

The quasi-static finite element modelling presented in this study was performed using the commercially available program, LS DYNA, using the implicit solver. The models were developed using 3D solid elements with element formulation -2, as suggested in the implicit guideline from Dynamore (2018). This is an accurate element formulation for fully integrated S/R solid elements with poor aspect ratios. To lessen the computational effort required, only a quarter of the panels were modelled assuming a roller support on each side. A photo of the 3FL sandwich panel model is presented in Figure 8-1. In this section, material models, boundary conditions and mesh sizes will be presented and discussed.

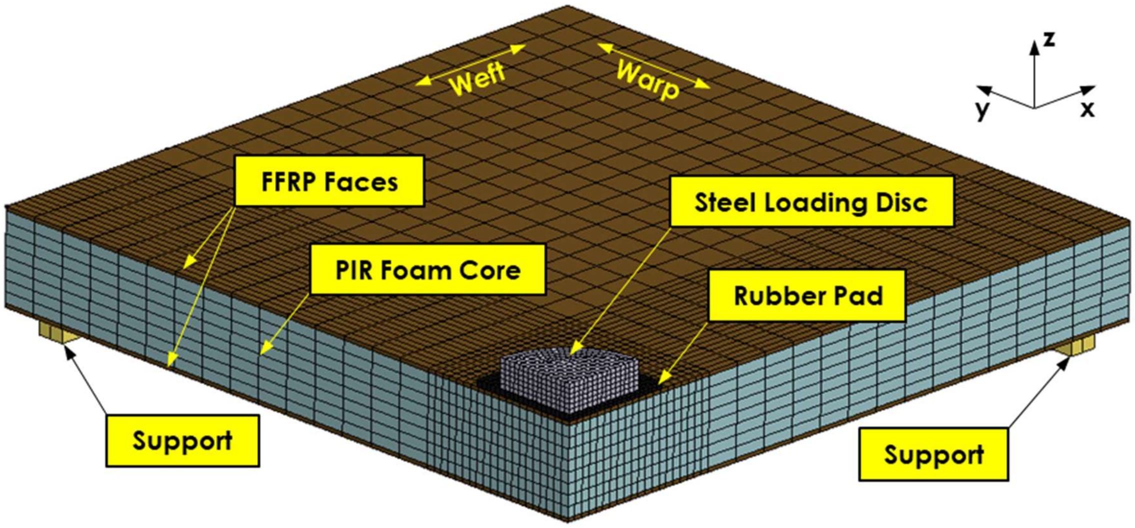

Figure 8-1. Quarter model of 3FL sandwich panel

8.2.2.1. Material Models

The bidirectional flax fibre-reinforced polymers (FFRPs) used for the faces have been shown in Chapter 6 to exhibit a nonlinear behaviour in both the warp and weft direction. The tensile strength, initial modulus and ultimate strain were found to be 70.0 MPa, 6.35 GPa and 0.0202 mm/mm, respectively in the warp direction and 51.3 MPa, 5.64 GPa and 0.0204 mm/mm, respectively in the weft direction. These results were based on tests of two-ply FFRP coupons with an average thickness of 2.34 mm. Therefore, the faces were modelled based on this thickness. The 1FL specimen faces were modelled as 1.17 mm thick; the 2FL specimen faces were modelled as 2.34 mm thick and the 3FL specimen faces were modelled as 3.51 mm thick.

In order to capture the nonlinear behaviour, the FFRP faces were modelled using MAT_040, NONLINEAR_ORTHOTROPIC. This material model takes the material stress-strain curves as inputs and therefore is able to accurately predict the behaviour of the FFRPs in both the warp and weft direction. To verify this material model, a tension coupon was modelled in both the warp and weft direction and compared to the test data presented in Chapter 6. This verification is presented in Figure 8-2.

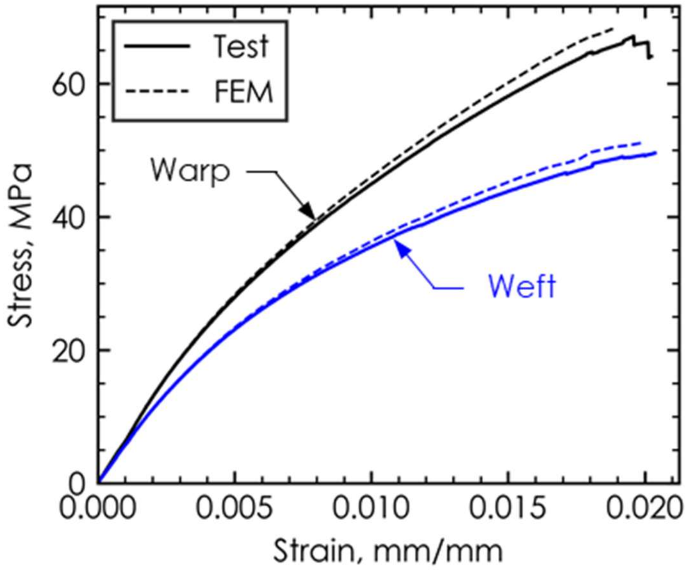

Figure 8-2. Verification of finite element material model for FFRP faces

It is also known that the FFRPs behave differently under tensile and compressive loads (Betts et al. 2018a). However, the material model used is unable to account for this difference. Therefore, knowing that for quasi-static loads, the top face is generally under compression and the bottom face is generally under tension, the top face was modelled using the warp compressive stress-strain data from Betts et al. (2018a) and the bottom face was modelled using the tensile stress-strain data from Chapter 6. The FFRPs in the warp direction were found have an initial compressive modulus of 6.73 GPa and a compressive strength and corresponding strain of 86.4 MPa and 0.0327 mm/mm (Betts et al. 2018a).

The core was modelled using material model MAT_057, LOW_DENSITY_FOAM. This model takes the compressive stress-strain curve of the foam as an input. The stress-strain curve for the 96 kg/m^3 PIR foam presented by Codyre et al (2018) was used for the modelling.

The supports were modelled as steel using the MAT_001, ELASTIC. The loading disc was also made of steel, but was modelled as MAT_020, RIGID. This allowed for the use of the prescribed motion boundary condition that can be used with rigid parts. The rubber beneath the loading disc was modelled as MAT_007, BLATZ-KO_RUBBER with a shear modulus, G, of 15 MPa. However, the actual shear modulus of the rubber pad used in the tests is not known.

8.2.2.2. *Contacts and Boundary Conditions*

The faces of the sandwich panel were connected to the core in the model using a tied mortar contact. As noted by the LS DYNA implicit guidelines (Dynamore 2018), solid to solid mortar contacts can lead to noticeably large penetrations. In the guideline, it is suggested that increasing the contact penalty stiffness can alleviate this problem, however it may lead to convergence problems. To increase the penalty stiffness, two parameters can be changed: the scale factor on default slave penalty stiffness (SFS) and the IGAP parameter. The IGAP parameter controls how quickly the penalty force increases due to penetration distance. In the model presented in this study, the penalty stiffness for the contacts was increased from the default by setting SFS = 5 and IGAP = 5.

To take advantage of symmetry, it was assumed that the supports were roller-type supports in both directions. Figure 8-3 shows the modelling of the panel supports. They were modelled with solid elements which were allowed to rotate about the bottom centerline. These supports were connected to the panel using automatic surface to surface mortar contacts which allowed the panel to slide simulating a roller behaviour. This sliding was allowed by setting the coefficient of friction of the contact to a low value of 0.0001. The panels were also allowed to separate from the supports. This is important because the corners of two-way panels often lift off the supports when subjected to flexural loads. It should be noted that in the tests, two of the roller supports were welded to the support frame to simulate a pin-type support. However, it was assumed that this simplification would not significantly affect the model results and allowed the computational effort to be reduced by a factor of four. To use the quarter model, the cut edges required special boundary conditions due to symmetry. In the cut along the yz-plane, the nodes were restricted from moving in the x-direction and likewise, in the xz-plane, the nodes were restricted from moving in the y-direction.

The load was applied to the panel through a steel loading disc which was placed on a rubber pad. Between both the loading disc and the rubber pad and between the rubber pad and the panel, automatic surface to surface mortar contacts were used. For these contacts the static coefficient of friction was assumed to be 0.8.

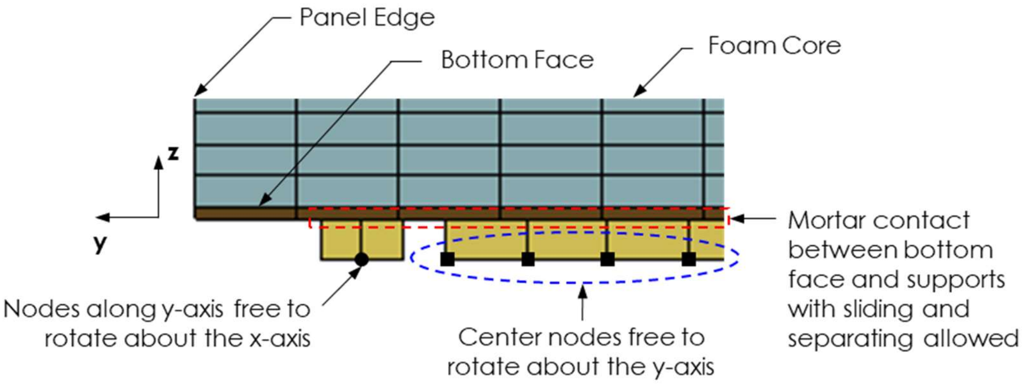

Figure 8-3. Modelling of panel supports

8.2.2.3. Failure Modes

Failure was considered in the post-processing of the model using a script written in Python using the scientific package, Anaconda. Material failure was considered in both the FFRP faces and the PIR foam core and the stability type failure, face wrinkling was considered on the top face.

To check for material failure in the faces, the maximum stress criterion was used. The normal stresses in elements at the center of the top and bottom faces were exported from the model. Then, a python script checked the stress in the warp (y) and weft (x) direction at each model step. The stresses were checked against both the compressive and tensile strength of FFRP. If, at any point, the stress in any direction exceeded the ultimate material strength, the model was terminated, and the failure mode noted.

The foam core was checked for shear failure using the tresca failure criterion. As shown in Figure 8-4b, it was observed that, for a 3FL-C96 sandwich panel, shear failure began at the edge of the loading disc. This is an expected result as stress concentrations typically develop at the edge of the load applications. From this initialization of foam shear failure, the failure area propagated downward as shown in Figure 8-4c. Total failure due to foam shear was then assumed when the maximum shear stress (tresca) exceeded the ultimate shear stress of the foam in over half the thickness of the foam, as shown in Figure 8-4d. To implement this failure mechanism into the post-processing, the tresca stress in the element just below the midplane of the core was exported from the model. In the case of the 3FL-C96 panel, this is the element shown in Figure 8-4d. The core was considered to have failed when the tresca stress in this element exceeded the ultimate shear strength of foam material.

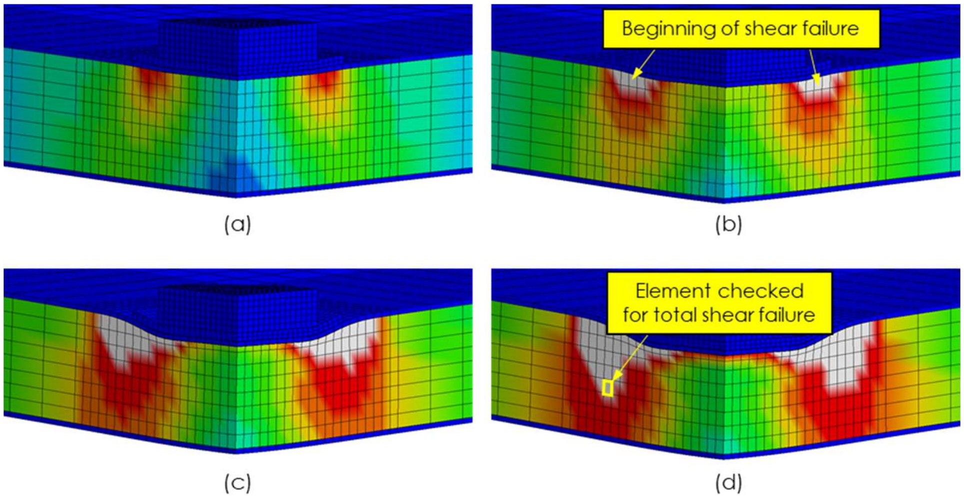

Figure 8-4. Development of shear failure in foam core (a) no shear failure; (b) beginning of foam shear failure at stress concentration area; (c) shear failure propagates downward through core; and (d) shear failure in over half of core – assumed total failure [Note white color elements denote shear failure development]

Compression face wrinkling failure was considering using the critical stress equation presented by Allen (1969) and given by Eq. 8-1:

$$\sigma_{cr} = B_1 E_f^{1/3} E_c^{2/3} \tag{8-1}$$

where σ_{cr} is the critical compressive stress in the face causing wrinkling, B_1 is a parameter given by Eq. 8-2, E_f is the elastic modulus of the face and E_c is the elastic modulus of the core. Because FFRPs exhibit a nonlinear behaviour, the elastic modulus was taken conservatively as the ultimate secant modulus, that is: $E_f = \sigma_{fu} / \epsilon_{fu}$, where σ_{fu} is the ultimate strength of the FFRP and ϵ_{fu} is the ultimate strain of the FFRP.

$$B_1 = 3[12(3 - \nu_c)^2(1 + \nu_c)^2]^{1/3} \tag{8-2}$$

where ν_c is the Poisson's ratio of the core material. For the PIR foams used in this study, the Poisson's ratio is not known and therefore a typical value of 0.3 was chosen. Allen (1969) showed that B_1 is not significantly affected by the Poisson's ratio and therefore this assumption does not have a significant effect on the prediction of the critical wrinkling stress. The stress history for the element exhibiting the highest compressive stress in each direction was exported from the model and checked at each model step. If the compressive stress was found to be greater than the critical stress, the model was considered to have failed.

Chapter 6 found the average (± standard deviation) ultimate foam shear stress, $\tau_{cu,a}$, of the 96 kg/m^3 foam to be 0.476 ± 0.102. Because the tests showed a high variance in strength, a region of potential total shear failure was determined. The lower bound, $\tau_{cu,l}$, of the potential shear failure was set as the average shear strength minus one standard deviation and the upper bound, $\tau_{cu,u}$, was set as the average plus one standard deviation. Each point was noted in the post processing and if the tresca stress exceeded the upper bound, it was assumed that the panel failed due to core shear.

8.2.2.4. Mesh Convergence

To determine the most appropriate mesh, a mesh size convergence study was performed on both the 3FL and the 1FL specimen. The study was performed on these two specimens, to ensure that the effect of the mesh size was observed for both failure of the face material (1FL) and for failure of the core material (3FL). Four meshes were considered as presented in Figure 8-5: a coarse mesh (Coarse), a refined coarse mesh (Coarse-R), a refined moderate mesh (Moderate-R) and a refined fine mesh (Fine-R).

The mesh size analysis for the 1FL and 3FL-C96 sandwich panels are shown in Figure 8-6 and Figure 8-7, respectively. As shown in Figure 8-6 the ultimate load capacity decreased with a decrease in mesh size (ie. changing from Coarse to Fine-R). The smallest percentage decrease in ultimate load capacity was 3.1% between Moderate-R and Fine-R whereas the decreases between Coarse and Coarse-R, and Coarse-R and Moderate-R were 5.4% and 5.8%, respectively. Figure 8-6 also shows that the mesh size did not have a significant effect on the initial stiffness of the panels.

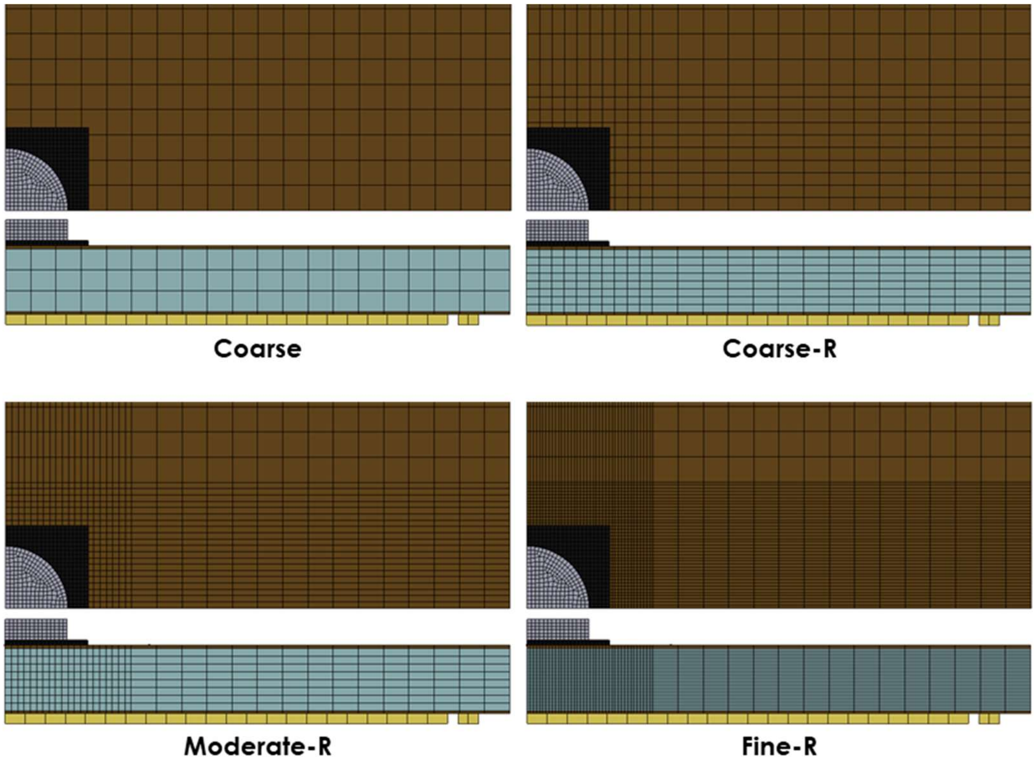

Figure 8-5. Mesh sizes considered in convergence study

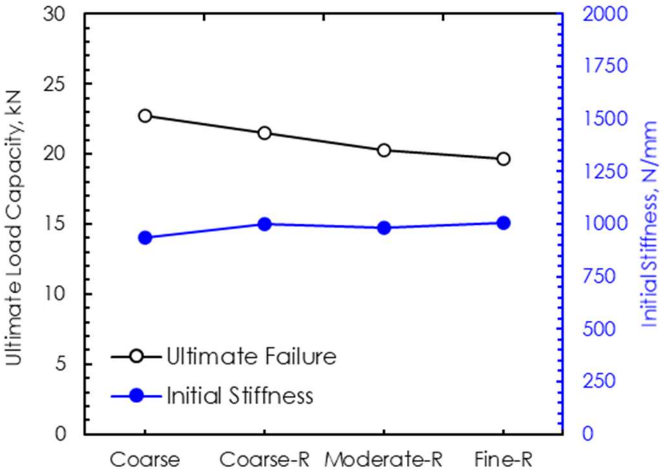

Figure 8-6. Mesh size analysis for 1FL-C96

Figure 8-7 shows the effect of the mesh size on the ultimate capacity, initial stiffness and computational runtime for the 3FL-C96 panels. As the shear failure is predicted as a region, the mesh size effect was presented for the average shear failure capacity as well as the lower and upper bounds. As shown in the figure, there was no significant effect on the average core shear failure load, the maximum difference was 3.1% between the Coarse-R mesh and the Moderate-R mesh. Additionally, Figure 8-7a shows that the initial stiffness increased slightly with a decrease in mesh size. Figure 8-7b shows the effect of the mesh size on the computational runtime of the 3FL-C96 specimen. As the mesh size decreases, the runtime increases significantly, especially between the Moderate-R and Fine-R meshes. Therefore, to ensure accurate results for specimens failing due to face rupture (as panel 1FL-C96) while maintaining a reasonable computational runtime, the Moderate-R mesh was selected for the model verification and parametric study.

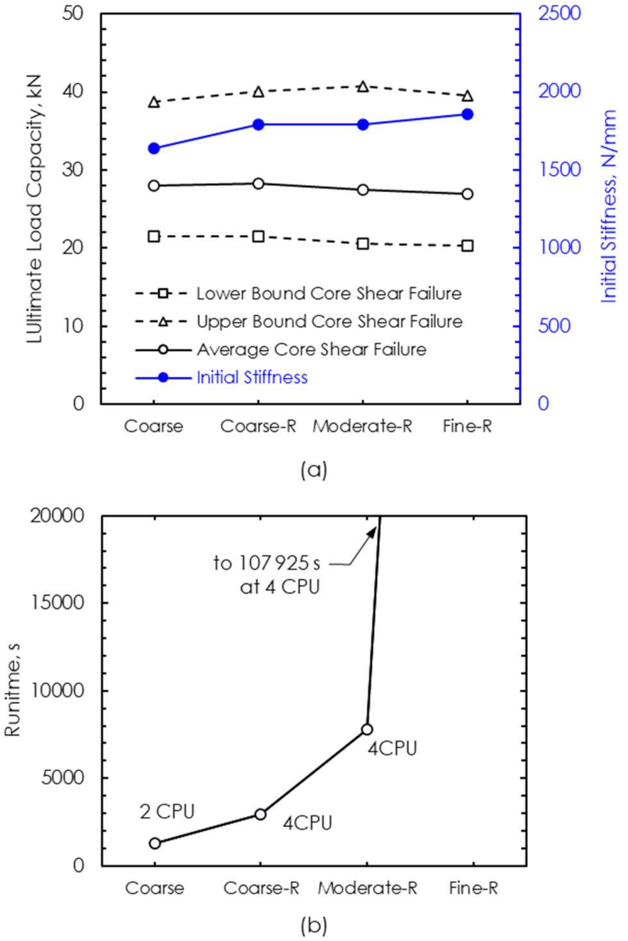

Figure 8-7. Mesh size analysis for 3FL-C96 (a) effect on ultimate load and initial stiffness and (b) effect on computational runtime

8.2.3. Model Verification

The FE models developed in this study were verified using the quasi-static test data presented in Chapter 6. Table 8-1 shows the comparisons of the ultimate loads and ultimate deflections, initial stiffnesses and failure modes between the models and the tests.

As shown in Table 8-1, the average model-test ratio for the prediction of ultimate load and deflection are 0.96 and 0.97, respectively. Additionally, the failure mode was accurately predicted for the 1FL-C96 and 3FL-C96 specimens. Visual comparisons of the model and test failure modes for the 1FL-C96 and 3FL-C96 specimens are presented in Figure 8-8 and Figure 8-9, respectively. Upon examination of the model results, 2FL-C96 specimen was close to a balance point between core shear failure and bottom face tensile rupture. At failure, the stress in the weft direction of the bottom face was 50.0 MPa, which is 97.5% of the ultimate strength.

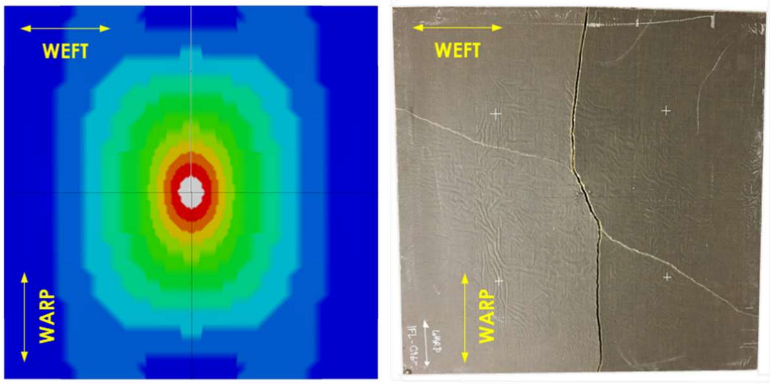

(a) (b)

Figure 8-8. Visual comparison (a) weft stress in FE model and (b) experimental failure [Note: white color in (a) represents weft stress > ultimate face tensile strength]

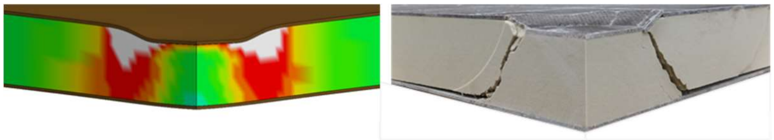

(a) (b)

Figure 8-9. Visual comparison of (a) core tresca stress in FE model and (b) experimental failure [Note: white color in (a) represents core tresca stress > ultimate core shear strength (upper bound)]

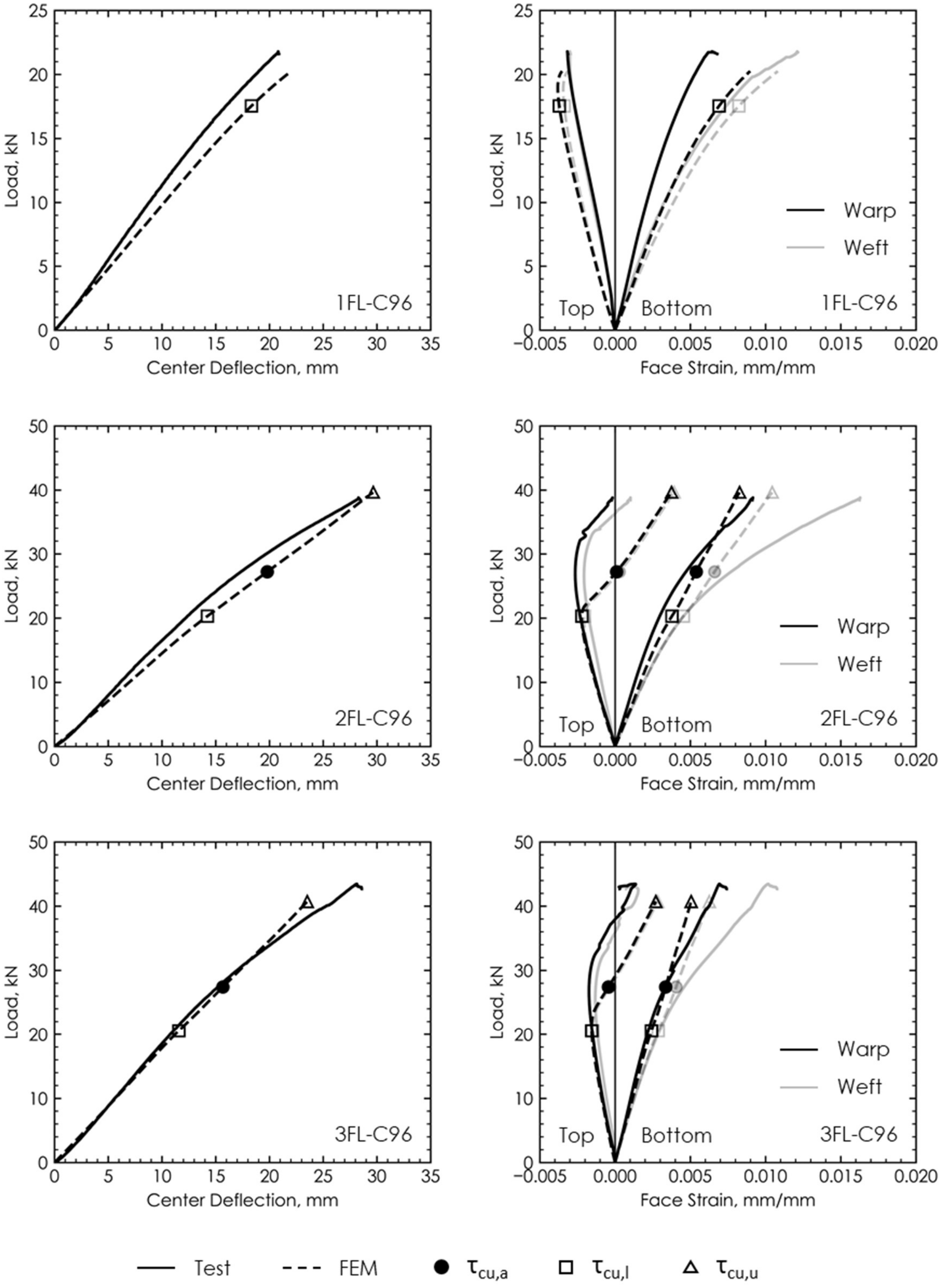

Figure 8-10. Verification of FE models

Figure 8-10 shows a comparison of the load-deflection and load-strain behaviour of the models and experiments. Though Table 8-1 indicates that the initial stiffness is slightly under-predicted by the models, Figure 8-10 shows that the overall slope of the load-deflection diagrams are predicted well. The figure also shows that the model was able to accurately predict the strain behaviour at the center of the top face. Based on the information presented in this section, this two-way model can be considered successfully verified when using the upper bound of the shear failure region. Therefore, for the remainder of this paper, the upper bound of the shear failure region will be considered as the shear failure criteria.

Table 8-1. Verification of quasi-static FE models using test data

	Ultimate Load [1], kN			Ultimate Deflection, mm			Initial Stiffness [2], N/mm			Failure Mode	
Model ID	Test	Model	Model -Test Ratio	Test	Model	Model-Test Ratio	Test	Model	Model-Test Ratio	Test	Model
1FL-C96	21.8	20.3	0.93	20.9	22.0	1.05	1210	985	0.81	B-WFT	B-WFT
2FL-C96	38.8	39.6	1.02	28.5	29.7	1.04	1781	1453	0.82	B-WFT	CS
3FL-C96	43.5	40.7	0.94	28.6	23.5	0.82	1975	1791	0.91	CS	CS
Average			0.96			0.97			0.85		

[1] *Ultimate load for core shear failure is based on upper bound core shear failure,* $\tau_{cu,u}$

[2] *Initial stiffnesses were calculated between deflections of 3 mm and 6 mm*

8.2.4. Parametric Study

A parametric study was performed using the verified model to observe the effect of the core density, face thickness, core thickness and the load area diameter on the behaviour of the panels. In this section, the results of both parametric studies will be presented and discussed. Additionally, the material models for the different core densities will be verified.

8.2.4.1. Verification of Additional Foam Material Models

For the parametric study, the behaviour of sandwich panels with two additional PIR foam core densities were investigated: 32 kg/m^3 and 64 kg/m^3. These additional foams were modelled using their respective compressive stress-strain curves presented by Codyre et al (2018). In their study, they showed that the compressive moduli of the C32, C64 and C96 foams were 4.9 MPa, 12.6 MPa and 35.1 MPa, respectively (CoDyre et al. 2018). However, they did not perform any shear tests and therefore the manufacturer data (Elliott Company 2016a; b) was used to predict core shear failure. The manufacturer data provides shear strength parallel to the rise of the foam and perpendicular to the rise of the foam. These two values were used to predict a shear failure region and it was assumed that the larger of the two caused ultimate shear failure.

To accurately model panels with these additional core densities, the material models for the foams first had be verified. This was done by modifying the two-way FE model to examine the behaviour of the sandwich beams tested by Betts et al (2018a). This beam model is presented in Figure 8-11. Note that to save on computational time, the principle of symmetry was used to model half of the beam length. Additionally, because the beams are under a state of plane stress, only a third of the beam width was modelled.

The comparisons of the load-deflection behaviour of the FE beam models and the tests by Betts et al (Betts et al. 2018a) is presented in Figure 8-12. The figure shows that the behaviour of the beams was predicted accurately by the FE models. Therefore, the foam material models were considered acceptable for use in the parametric study of the two-way panels.

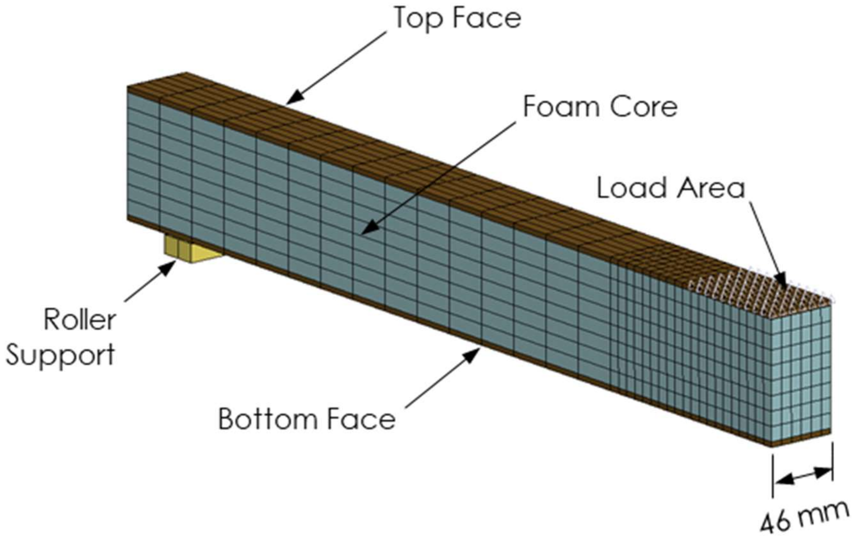

Figure 8-11. Beam FE model

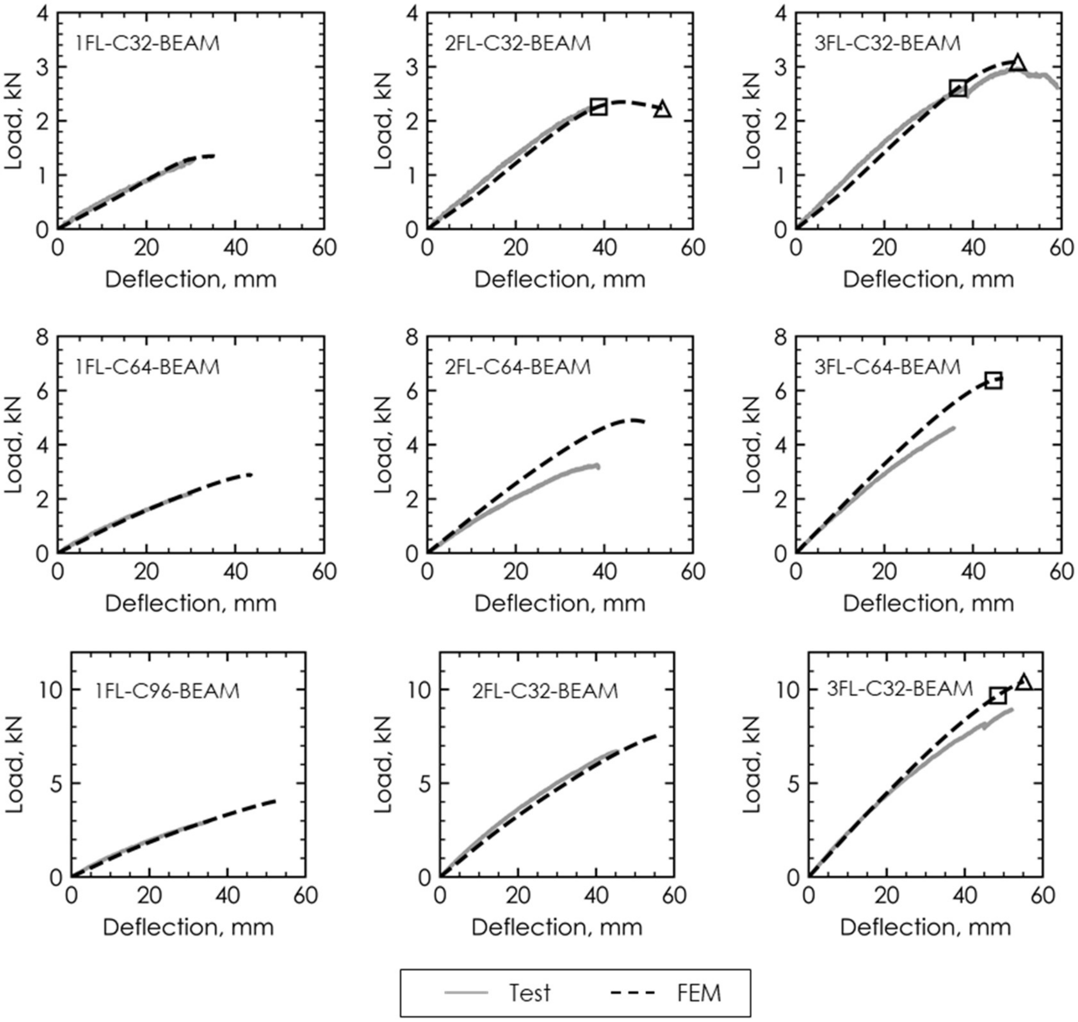

Figure 8-12. Load-deflection verification of sandwich beam FE models

8.2.4.2. *Effect of Core Density*

The effect of core density on the ultimate load, ultimate deflection and initial stiffness of the two-way sandwich panels is presented in presented in Table 8-2 and Figure 8-13. Figure 8-13a shows that the ultimate load capacity increases with core density for all face thicknesses. Note that the increase is not linear as it is affected by the failure mode. As shown in Table 8-2, the failure of the C32 and C64 panels was due to compression face wrinkling and for the C96 specimens the failures were due to tensile rupture or core shear. The core density did not have a significant effect on the ultimate deflection for the 1FL and 2FL panels. However, the ultimate deflections of the 3FL panels decreased with an increase in core density.

Table 8-2. Parametric study results for two-way sandwich panels

Model ID	Core Density kg/m^3	Core Thickness mm	Flax Layers	Load Diameter mm	Ultimate Load kN	Ultimate Deflection mm	Stiffness N/mm	Failure Mode
1FL-C32	32	76.2	1	150	7.7	23.7	309	CW
2FL-C32	32	76.2	2	150	15.1	31.8	366	CW
3FL-C32	32	76.2	3	150	26.9	40.4	408	CW
1FL-C64	64	76.2	1	150	14.3	21.6	724	CW
2FL-C64	64	76.2	2	150	24.7	26.1	970	CW
3FL-C64	64	76.2	3	150	37.5	30.9	1133	CW
1FL-C96	96	76.2	1	150	20.3	22.0	985	TR
2FL-C96	96	76.2	2	150	39.6	29.7	1453	CS
3FL-C96	96	76.2	3	150	40.7	23.5	1791	CS
1FL-C96-L300	96	76.2	1	300	37.9	28.7	1420	TR
2FL-C96-L300	96	76.2	2	300	54.1	27.8	2090	CS
3FL-C96-L300	96	76.2	3	300	56.8	22.8	2515	CS
1FL-C96-L600	96	76.2	1	600	76.4	37.7	2266	TR
2FL-C96-L600	96	76.2	2	600	101.1	29.4	3692	CS
3FL-C96-L600	96	76.2	3	600	108.4	22.5	4677	CS
1FL-C96-CT25	96	25.4	1	150	9.3	46.7	172	TR
2FL-C96-CT25	96	25.4	2	150	11.8	34.6	302	CS
3FL-C96-CT25	96	25.4	3	150	12.2	26.2	424	CS
1FL-C96-CT51	96	50.8	1	150	14.9	29.2	516	TR
2FL-C96-CT51	96	50.8	2	150	19.1	23.9	807	CS
3FL-C96-CT51	96	50.8	3	150	20.6	19.8	1040	CS

Naming convention: XFL-CYY-(LZZZ or CT##): X is number of FFRP layers, YY is core density, ZZZ is load area diameter (optional), ## is nominal core thickness (optional)
CW = Compression Wrinkling, TR = Tensile Rupture, CS = Core Shear

Figure 8-14 shows the effect of panel core density on the load-deflection and load-strain behaviour of two-way the sandwich panels. The load-deflection diagrams for the panels with lower density cores (32 kg/m^3) showed an increasing slope until failure. As the compressive yield stress and modulus of the 32 kg/m^3 foam is significantly less than the 96 kg/m^3 foam, it is assumed that this stiffness gain is attributed to densification of the foam under the load area. Specifically, this densification would occur under the edge of the load area.

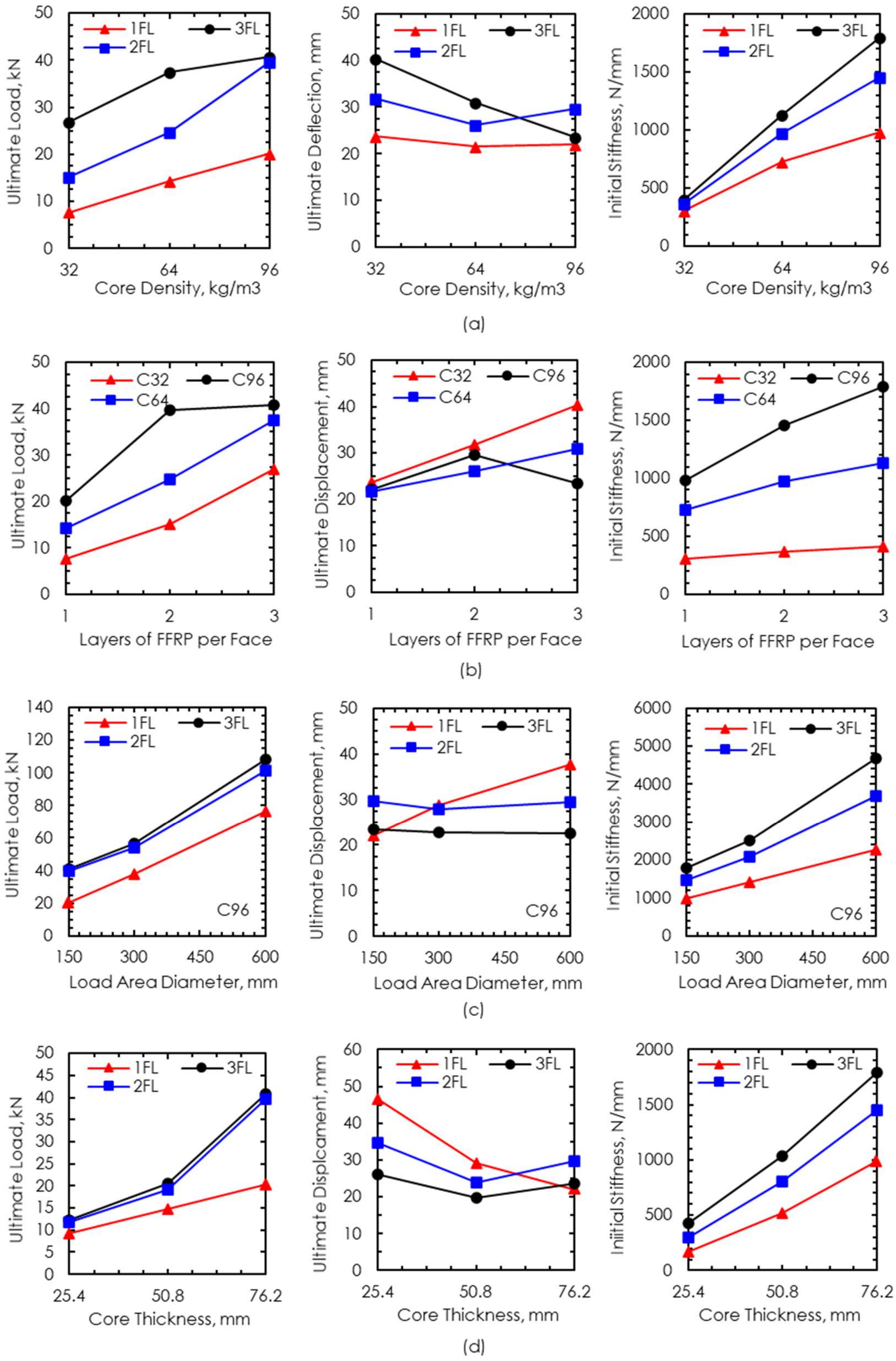

Figure 8-13. Parametric study results – effect of (a) core density; (b) FFRP face thickness; (c) load area diameter; and (d) core thickness

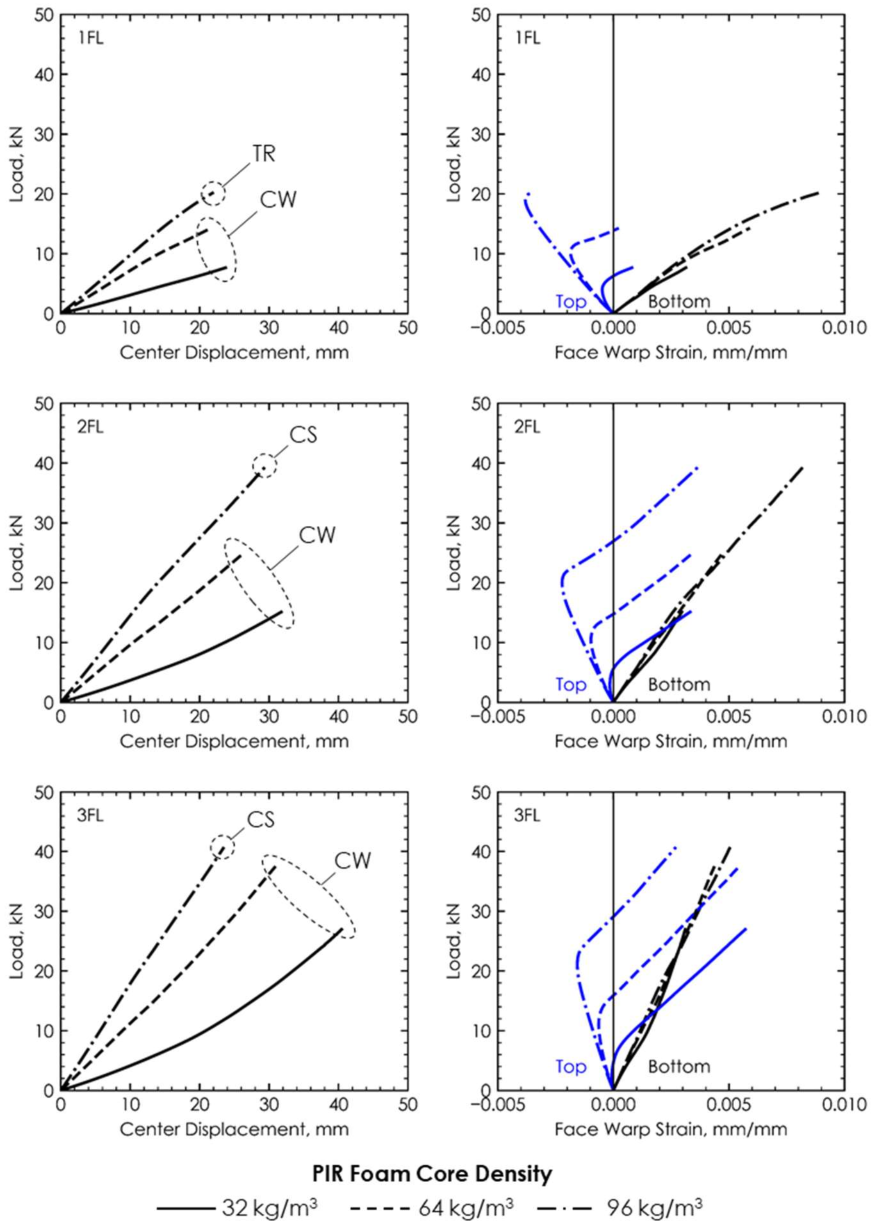

Figure 8-14. Effect of core density on load-deflection and load-strain behaviour of two-way sandwich panels (Note: TR = Tensile Rupture, CS = Core Shear and CW = Compression Wrinkling)

As shown in Figure 8-14, the initial load-face strain behaviour is similar for all core densities. For all panels, the strains in the top face transition into a state of tensile strain. This phenomenon was discussed in Chapter 6 and it was assumed that this was caused by the onset of local deformation. The results of the models confirm this hypothesis and show that this behaviour is specifically due to the onset of core indentation under the edge of the load area. Because the yield stress and compressive moduli of the cores decrease with core density, this indentation starts at lower load levels for the lower density foams. Therefore, the transition from compression to tensile strain at the center of the top face occurs at an earlier stage for the panels with the lower density cores, as shown in Figure 8-14.

8.2.4.3. *Effect of Face Thickness*

The effect of face thickness on the ultimate load capacity, ultimate deflection and initial stiffness of the two-way sandwich panels is presented in Table 8-2 and Figure 8-13b. The ultimate load capacity increased with an increase in the number of FFRP layers per face. For the C96 panels, the increase between one and two layers of FFRP is more significant than the increase between two and three layers. This is due to the failure modes of the panels. As the 1FL-C96 panel failed due to tensile rupture and it has been shown that 2FL-C96 panel was close to tensile rupture before ultimately failing due to core shear, the ultimate capacity is largely dependent on the face thickness. However, as the 2FL-C96 and 3FL-C96 panels both failed due to core shear, the increase in FFRP layers per face has a less significant effect on the ultimate panel capacity. Similarly, the ultimate deflections of the C96 panels were not significantly affected by the face thickness. However, both the ultimate load and displacement of the C32 and C64 panels increased with an increase in face thickness. This is expected as these panels failed due to compression face wrinkling which is affected by both the face and core material properties.

The initial stiffness of all panels increased with the number of FFRP layers per face. By comparing the plots in Figure 8-14, it can be seen that the slope of the load-strain diagrams increased with an increase in face thickness. Additionally, the amount of compressive strain and tensile strain experienced by the top faces decreased with an increase in face thickness.

8.2.4.4. *Effect of Load Area Diameter*

To develop an understanding of the effect of the load area diameter, additional models were developed for the C96 panels. As shown in Figure 8-15, three load size diameters were considered: 150 mm (original), 300 mm and 600mm. The only change implemented in the models was the size of the loading disc; the contact formulations, material models and boundary conditions were not altered. Note that, as they are quarter models, the load sizes shown in Figure 8-15 are half of the load area diameters.

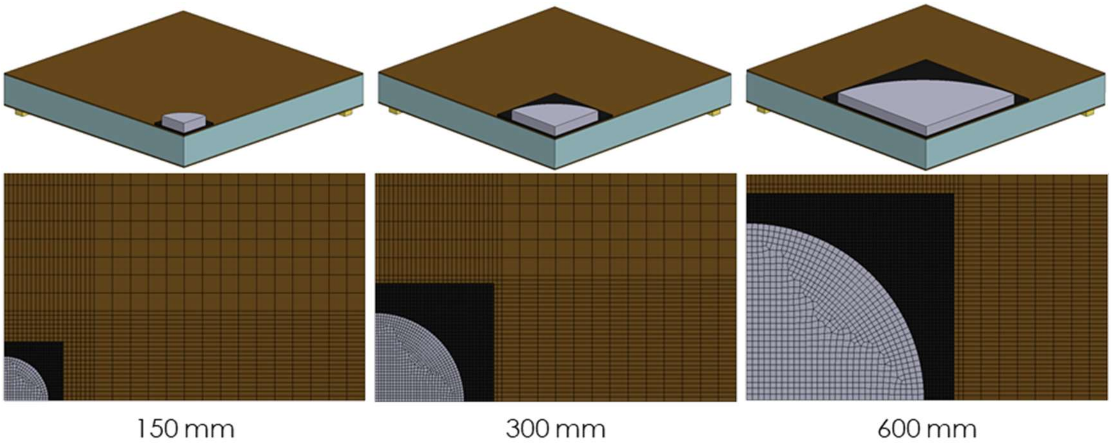

Figure 8-15. Comparison of models with different load size diameters

The effect of load area diameter on the ultimate load capacity, ultimate deflection and initial stiffness of the two-way sandwich panels is presented in Table 8-2 and Figure 8-13c. Additionally, the effect on the load-displacement and load-face strain behaviour is presented in Figure 8-16. As expected, the ultimate load capacity and initial stiffness, increased with an increase in load area. The ultimate deflection of the 1FL-C96 specimens increased with an increase in the load area, however the 2FL-C96 and 3FL-C96 panels were relatively unaffected. This is due to the different failure modes of the panels as shown in Figure 8-16. The 1FL-C96 panels all failed due to tensile rupture of the bottom face whereas the 2FL-C96 and 3FL-C96 panels all failed due to core shear.

The slopes of the load-face strain plots increased with an increase in the load area diameter. Additionally, Figure 8-16 shows that the top faces of the models with larger load areas (300 mm and 600 mm) did not go into a state of tensile strain. This is an expected result as the stress concentration developed at the edge of the load area was distributed over a larger perimeter. Therefore, as the effects of local deformation were reduced when the load area diameter was increased, these models could be used to verify the analytical model presented in Chapter 7 for large load areas. Future work should include comparing the results of the FE and analytical sandwich panel models for large load areas.

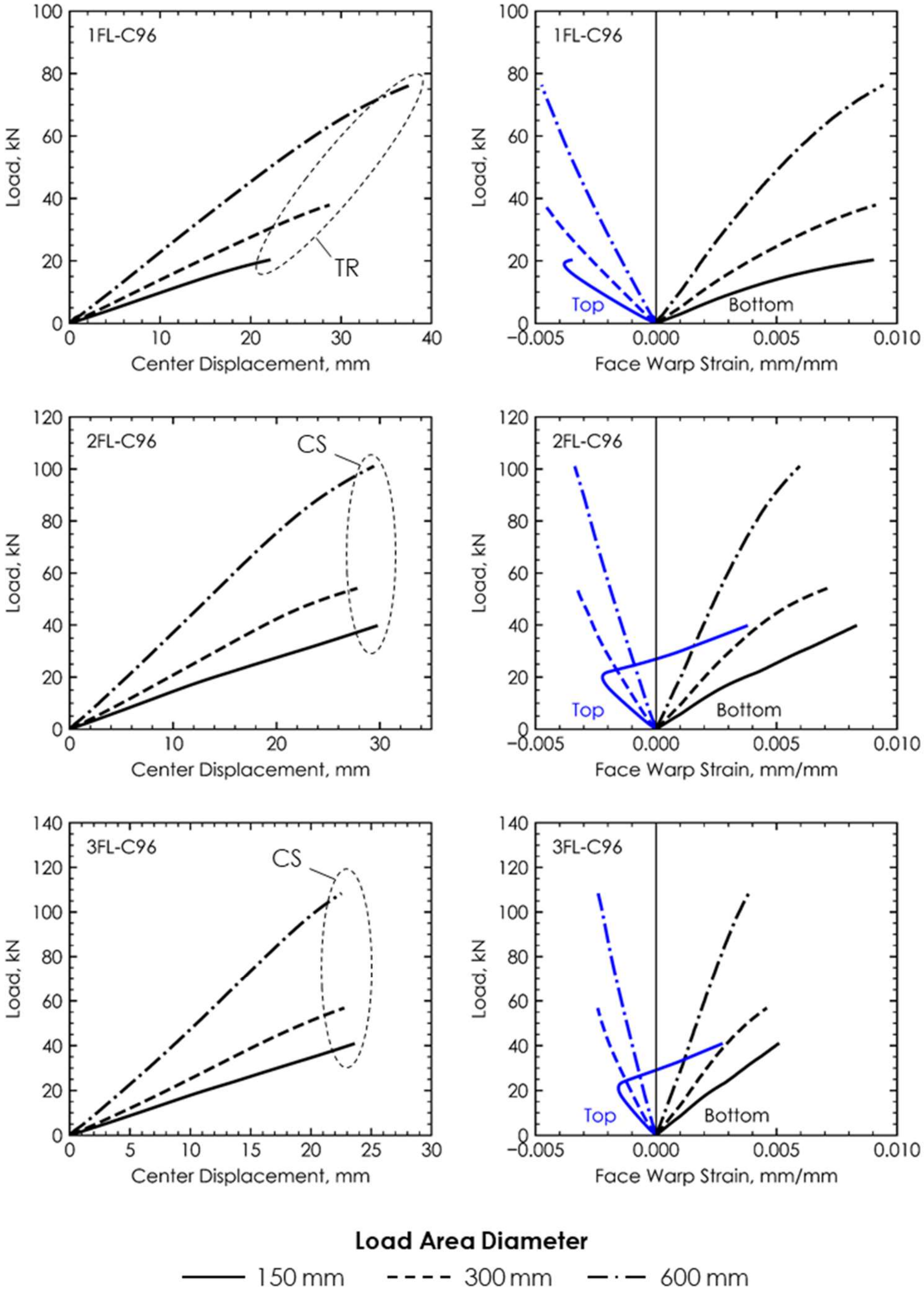

Figure 8-16. Effect of load size diameter on load-deflection and load-strain behaviour of two-way sandwich panels (Note: TR = Tensile Rupture, CS = Core Shear and CW = Compression Wrinkling)

8.2.4.5. *Effect of Core Thickness*

The effect of the core thickness was examined for sandwich panels with core densities of 96 kg/m^3. As shown in Figure 8-17, three core thicknesses were considered: 25.4 mm, 50.8 mm and 76.2 mm (as tested).

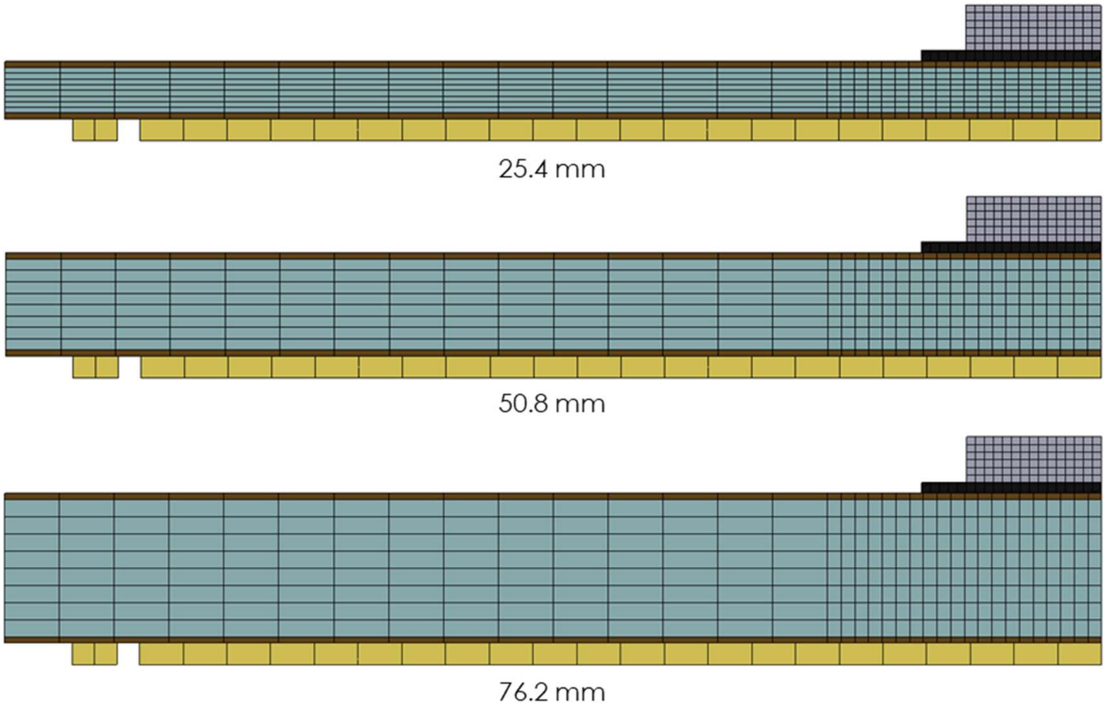

Figure 8-17. Comparison of models with different core thicknesses

The effect of the core density on the load-displacement and load-strain behaviour of the sandwich panels is presented in Figure 8-18. The ultimate load capacity and stiffness increased with an increase in core thickness for all panels. For the 1FL panels, the ultimate center displacement also increased with an increase in core thickness. However, for the 2FL and 3FL panels, the effect of core thickness on the ultimate displacement was not clear. As these panels failed due to core shear, it is likely that the ultimate displacement was heavily influenced by the localized deformation at the ultimate point. As shown in Figure 8-18, the slope of the load-strain increased with an increase in core thickness. This is expected as an increase in core thickness is an increase in moment of inertia, thereby increasing the flexural rigidity of the structure.

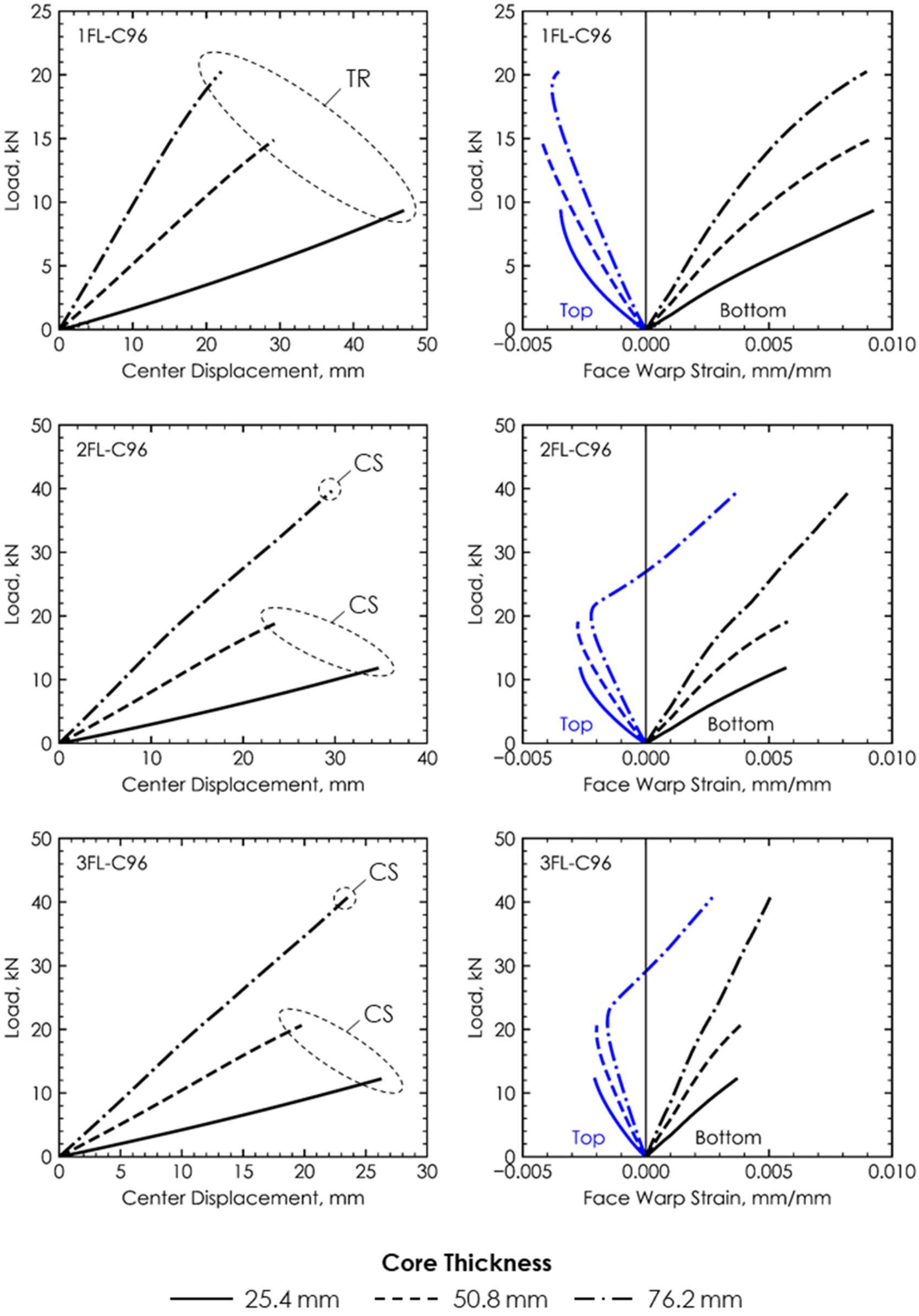

Figure 8-18. Effect of core thickness on load-displacement and load-strain behaviour of two-way sandwich panels

8.3. IMPACT MODELLING

8.3.1. Summary of Experimental Program

In Chapter 6, the experimental program of the sandwich panels under various impact loads was presented. Each panel was 1220 mm x 1220 mm x 80 mm with flax fibre-reinforced polymer (FFRP) faces and a 96 kg/m^3 foam core. The main test parameters were the effect of face thickness (one, two or three layers of FFRP per face) and impact energy on the impulse behaviour of the sandwich panels. Each panel was subjected once to a drop weight impact with data acquisition. The impact energies were set as 50%, 70% and 95% static failure energy (SFE) of the respective panel. Subsequently, the panels were tested multiple times until failure, however, the FE modelling presented in this study focuses on the behaviour of these panels under one impact at a set energy level. Additionally, the intact 2FL and 3FL were also impacted once at the 119 J and 167 J (50% and 70% SFE of the 1FL panel) before their tests. This was done to directly compare the effect of face thickness on the impulse behaviour of the panels under a constant impact energy.

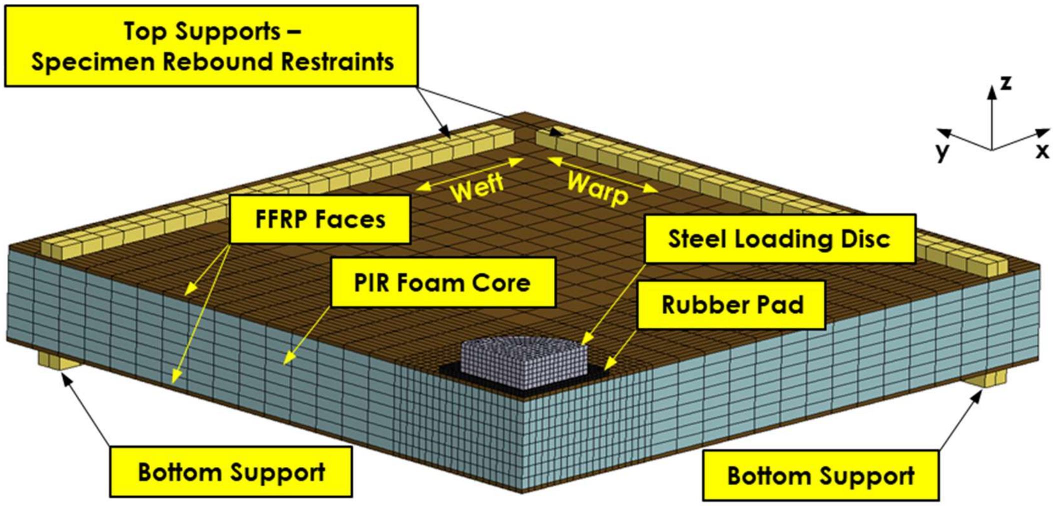

Figure 8-19. Impact FE model of 3FL-C96 sandwich panel

8.3.2. FE Model Development

The quasi-static finite element models were modified to perform impact analysis of the two-way sandwich panels. In this section, these modifications will be presented and discussed. A comparison of the quasi-static and impact FE models is presented in

Table 8-3 and a photo of the impact FE model is presented in Figure 8-19. It should be noted that as the models examined only low velocity impacts, it is assumed that the strain rate would have little effect on the results. Therefore, the effect of strain rate was not considered in the modelling.

Table 8-3. Comparison of quasi-static and impact FE models

Item	Quasi-Static Models	Impact Models
Solver	Implicit	Explicit
Element Types	All solids	All solids
Element Formulations	-2	-2
Face Material	NONLINEAR_ORTHOTROPIC	NONLINEAR_ORTHOTROPIC
Core Material	LOW_DENSITY_FOAM	LOW_DENSITY_FOAM
Supports Material	ELASTIC	ELASTIC
Impactor Material	RIGID	ELASTIC
Rubber Material	BLATZ-KO_RUBBER	BLATZ-KO_RUBBER
Face-Core Contacts	AUTOMATIC_SURFACE_TO_SURFACE_MORTAR_TIED	TIED_SURFACE_TO_SURFACE
Panel-Support Contacts	AUTOMATIC_SURFACE_TO_SURFACE_MORTAR_TIED	AUTOMATIC_SURFACE_TO_SURFACE
Support Locations	Bottom edges	Top and bottom edges
Load Application	PRESCRIBED_MOTION_RIGID	INITIAL_VELOCITY_GENERATION
Mesh Type	Moderate-R	Moderate-R
Failure	Compression wrinkling, face failure and core shear failure considered in post-processing	N/A

In both the quasi-static and impact models, the element formulation -2 was used. This is an accurate formulation for elements with poor aspect ratios. It is suggested that this be used for implicit analyses, which is why it was chose for the quasi-static analysis. However, as shown in Table 8-3, the impact analysis was completed using the explicit solver. The same element formulation was used for consistency between the models.

The same material models were used in the impact model, except for the steel impactor, which was changed from the RIGID material model in the quasi-static modelling to the ELASTIC material model for the impact modelling. This is because the boundary condition did not require a rigid part as in the quasi-static model.

The support conditions were changed to match the experimental tests presented in Chapter 6. To do this, supports were added to the top face of the panel as shown in Figure 8-19. These top supports were modelled to simulate the specimen rebound restraint present in the experiments and are shown in detail in Figure 8-20.

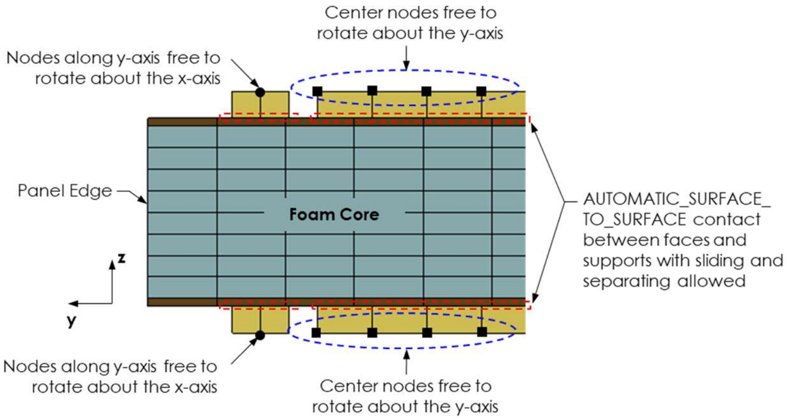

Figure 8-20. Modelling of panel supports in impact FE model

Mortar contacts were used in the quasi-static model as it was suggested by the implicit guidelines by Dynamore (2018). However, it was determined that fer explicit analyses, the mortar contacts caused significant penetration the non-mortar variation of the same contact types was more accurate. The contact parameters were kept the same for consistency. That is that the static and dynamic coefficient of friction was set to 0.0001 between the panel and the supports and to 0.8 between the impactor, rubber pad and the top face of the panel.

A mesh convergence study was completed for the quasi-static models. It was determined that the Moderate-R mesh offered adequate accuracy while maintaining a reasonable computation runtime. Therefore, for consistency, the Moderate-R mesh was also used for the impact modelling.

8.3.3. Model Verification

The FE models developed in this study were verified using the impact data presented in Chapter 6. Figure 8-21 shows a comparison of the face strains between the FE models and the respective experimental tests at impact levels of 50%, 70% and 95% static failure energy (SFE). As shown in the figure, the models were able to accurately capture the impulse duration and the maximum strains induced in the top and bottom faces.

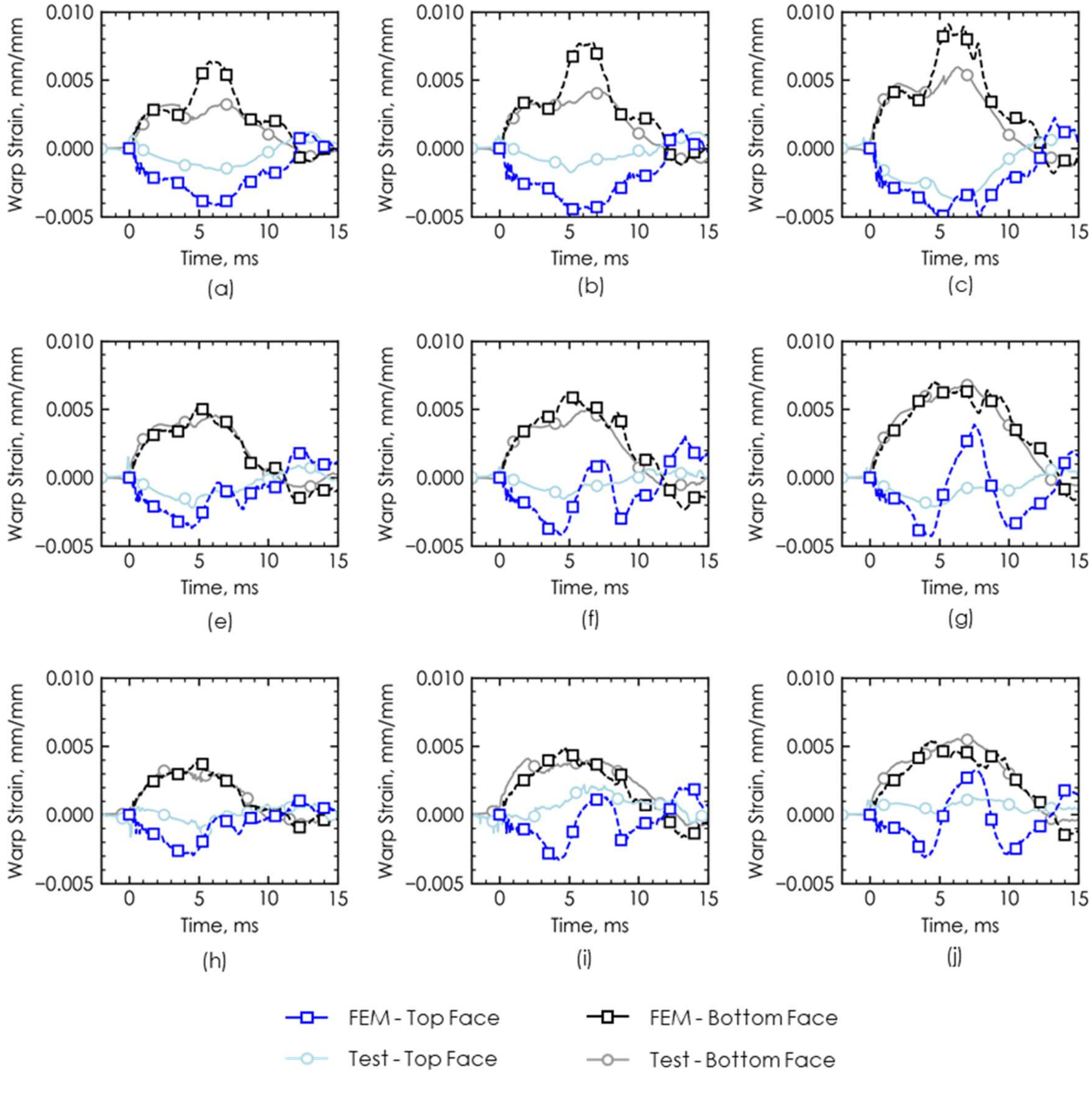

Figure 8-21. Impact FE model verification for 1FL panel at (a) 50% static failure energy (SFE); (b) 70% SFE and (c) 95% SFE, for the 2FL panel at (e) 50% SFE; (b) 70% SFE and (c) 95% SFE and for the 3FL panel at (h) 50% SFE; (i) 70% SFE and (j) 95% SFE

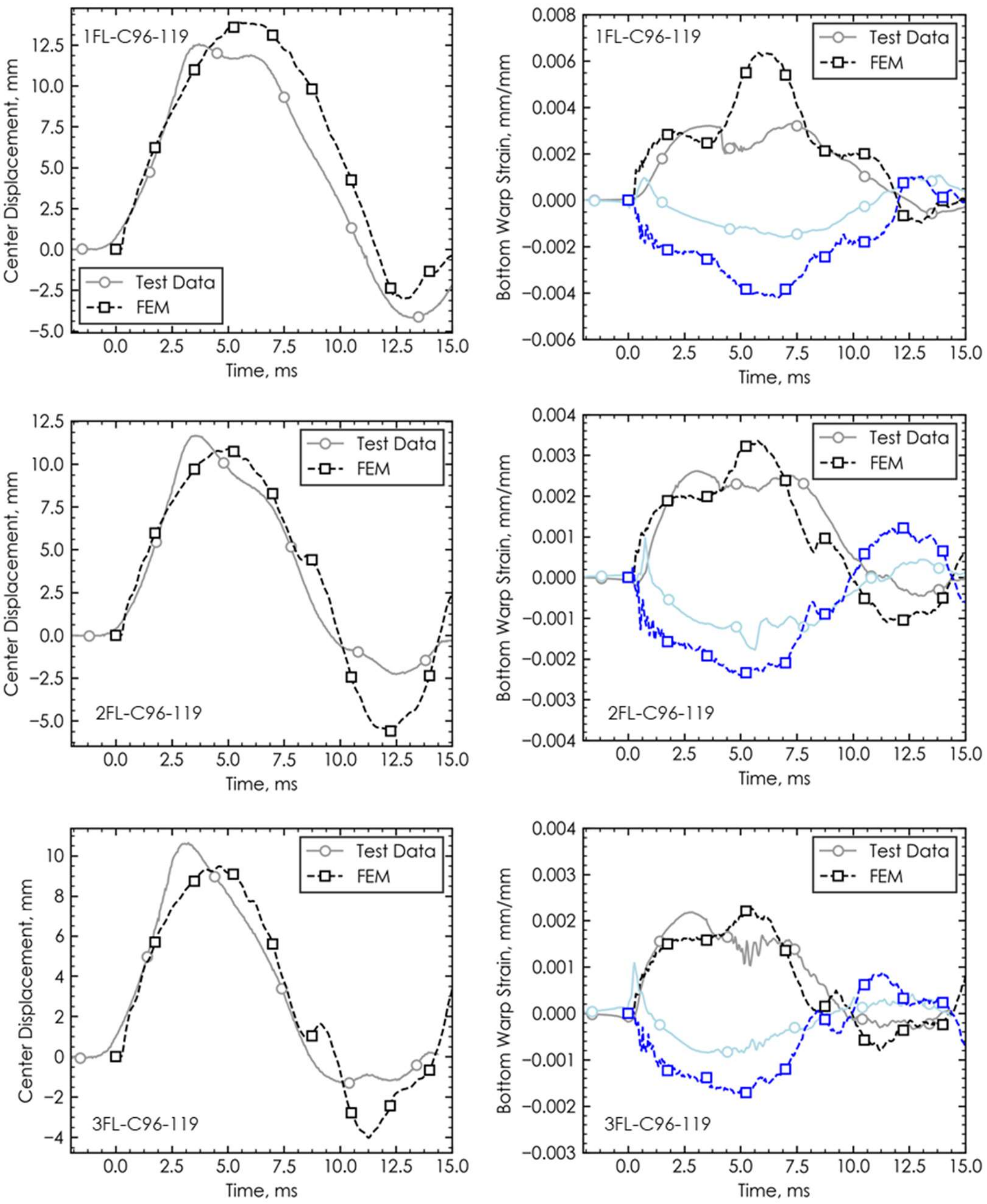

5p

Figure 8-22. FE model verification for two-way sandwich panels subjected to 119 J impacts

The models were also verified using the displacement data for the specimens tested under constant energy levels 119 J and 167 J which are the equivalents of the 50% and 70% SFE for the 1FL panel. The verification of the models impacted at 119 J and 167 J are presented in Figure 8-22 and Figure 8-23, respectively. These figures show that for low level impacts, the model was able to accurately capture both the center displacement and face strain behaviour of the panels. Therefore, the models were considered verified and were used to perform a parametric study to examine the effect of core density and core thickness.

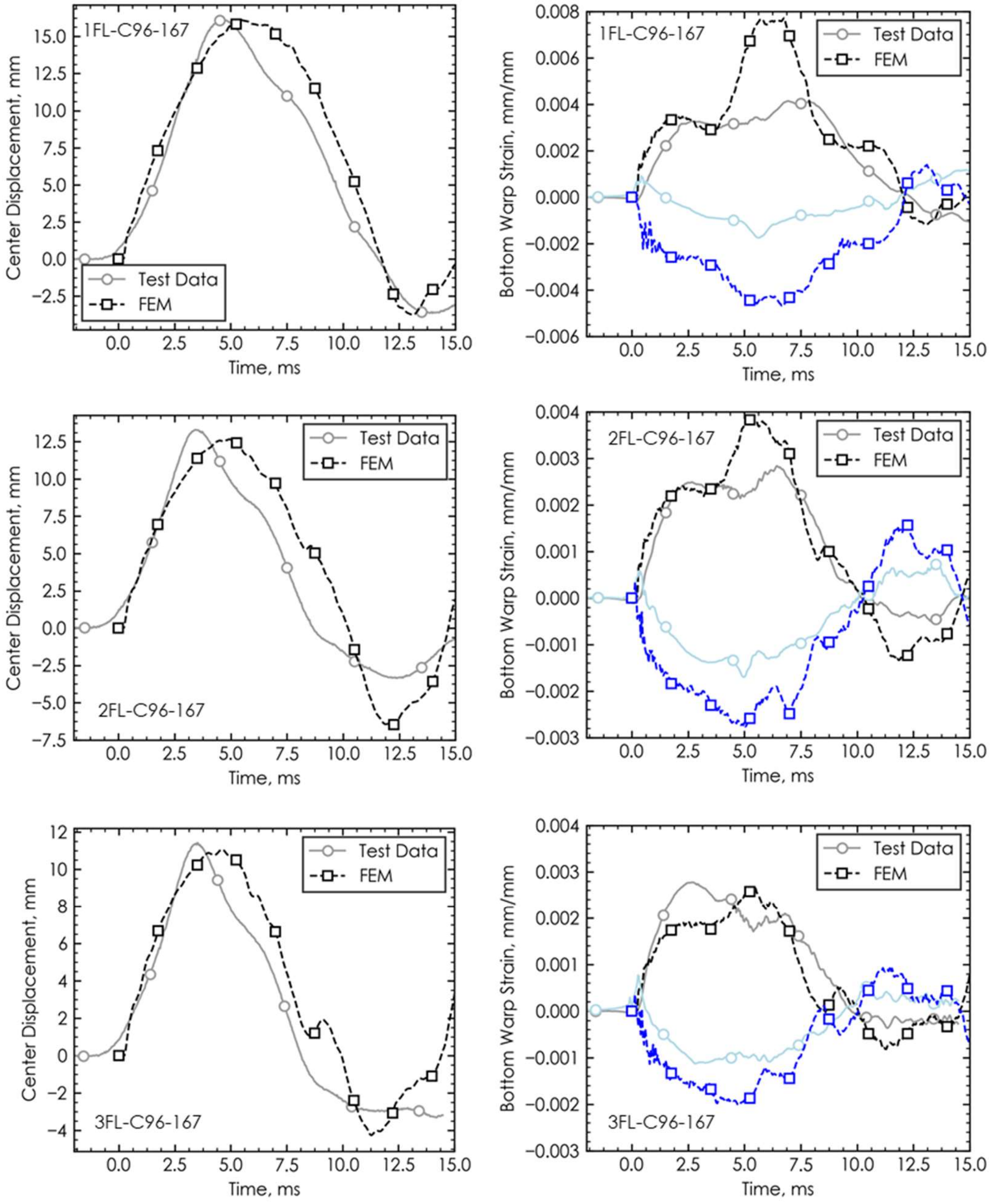

Figure 8-23. FE model verification for two-way sandwich panels subjected to 167 J impacts

8.3.4. Parametric Study

A parametric study was completed to see the effect of core density, core thickness, and face thickness. To directly compare the low velocity impact behaviour of the sandwich panels, the impulse due to an impact energy of 80 joules (J) was examined for each model. This energy level was chosen using 90% of the least amount of energy absorbed by the quasi-static models presented earlier. Panel 1FL-C32-CT25, which has one FFRP layer per face and a 25.4 mm thick 32 kg/m^3 foam core, resisted the smallest amount of static energy at 88.4 J. Therefore, the impact models for the parametric study were impacted at 80 J (approximately 90% of 88.4 J). This was modelled by having a 2.51 kg drop weight impact the panels at a velocity of 7.96 m/s.

8.3.4.1. Effect of Core Density

To examine the effect of core density, panels with three core densities were modelled: 32 kg/m^3, 64 kg/m^3 and 96 kg/m^3 (C32, C64 and C96). The effect of core density on the center displacement caused by an impact of 80 J is presented in Figure 8-24. Based on the figure, the impulse duration increased with a decrease in core density for panels with all face thicknesses. Considering the impulse duration to be from the start of the downward displacement the panel returns to the original position, the impulses of the 3FL panels were approximately 5.6 ms, 7.5 ms, and 10.6 ms for C96, C64 and C32 panels, respectively. That is an increase of 34% between C96 and C64 panels and an increase of 89% between the C96 and the C32 panels. However, the general shape of the impulses remained the same. Additionally, the maximum center displacement also increased with a decrease in core density and the largest increases were between the C64 and C32 panels.

8.3.4.2. Effect of Face Thickness

The effect of the face thickness on the impulse behaviour can be seen in Figure 8-24 by comparing the plots of the same core densities in the sub-figures (a), (b) and (c). As expected, the maximum displacement decreased with and increase in face thickness. The face thickness did not have a significant affect on the impulse duration of the panels with C32 cores. However, upon examination, the impulse duration was affected by face thickness for panels with higher density cores (C64 and C96). For instance, the impulse durations of the C64 panels were approximately 8.1 ms, 7.5 ms, and 6.9

ms for the 1FL, 2FL and 3FL panels, respectively. A similar trend is also seen in the C96 panels.

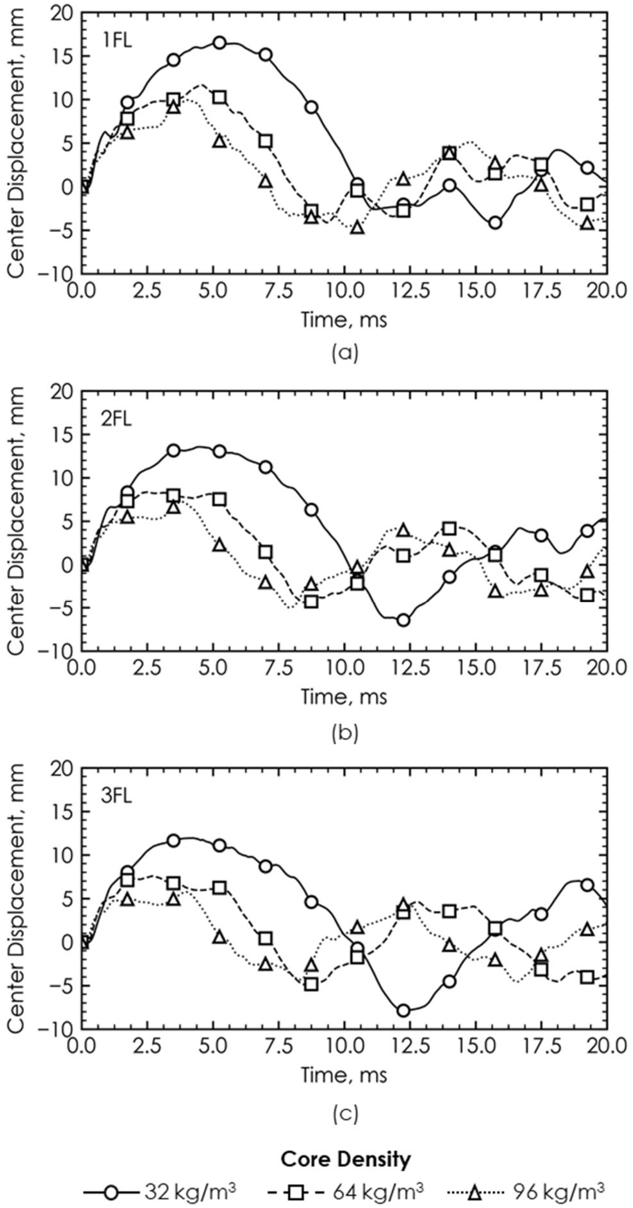

Figure 8-24. Effect of core density on the center displacement response of sandwich panels subjected to an 80 J impact (a) 1FL; (b) 2FL; and (c) 3FL [Note downward displacement is shown as positive]

It is likely that the impulse duration of the C32 panels was not affected by face thickness due to a higher amount of shear deformation. A visual comparison of the maximum downward displacement shape of panels, 3FL-C32, 3FL-C64 and 3FL-C96 is presented in Figure 8-25. The comparison shows that the C32 panel undergoes significantly more shear deformation than the C64 and C96 panel as evidenced by the straight line between the support and the load area.

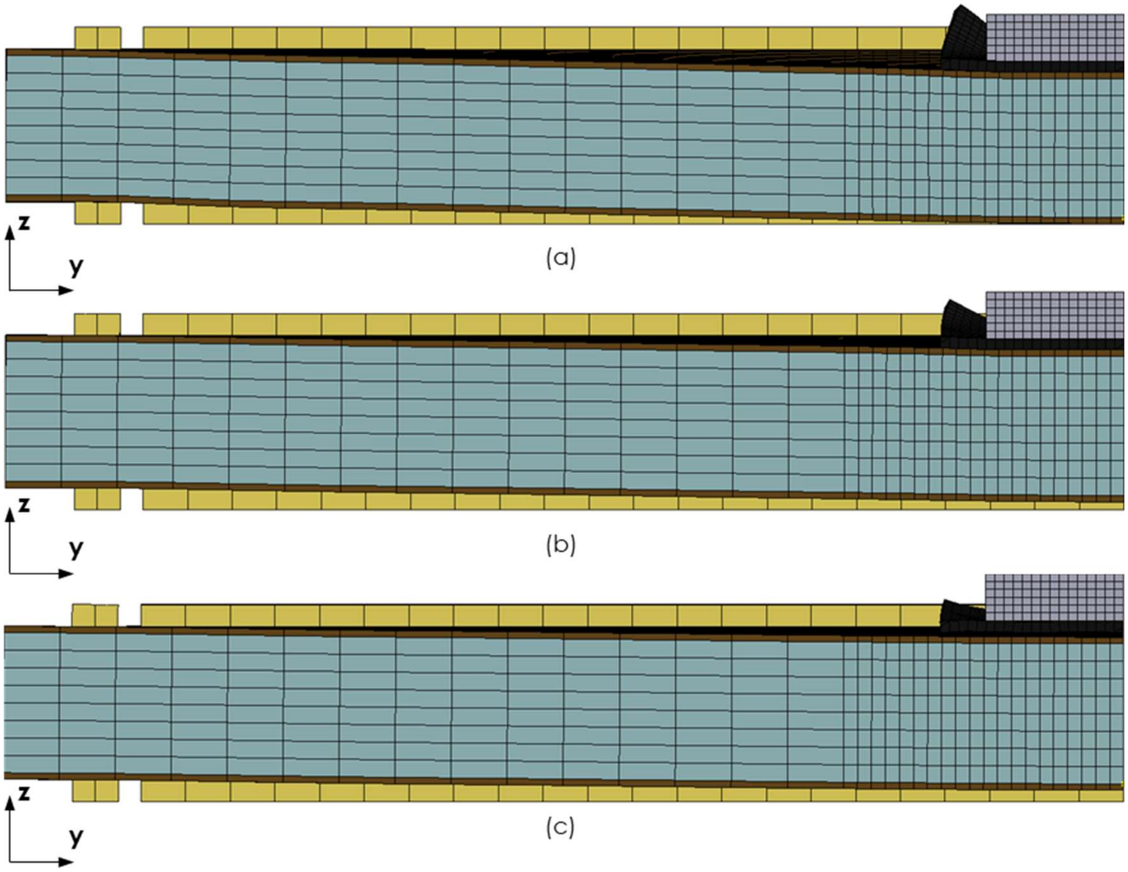

Figure 8-25. Maximum downward displacement shapes of panels (a) 1FL-C32; (b) 2FL-C32; and (c) 3FL-C32

8.3.4.3. *Effect of Core Thickness*

The effect of the core thickness on the impulse response of the sandwich panels is presented in Figure 8-26. The maximum displacements and impulse durations increased with a decrease in core thickness for all panels, as expected. The largest increase in impulse duration due to one step increase in core thickness was 77% between 2FL-C96-CT25 and 1FL-C96-CT50, increasing from approximately 8.75 ms to 15.63 ms, Additionally, note that for panels with thin cores (CT25), the face thickness had a significant effect on the maximum displacement and impulse duration. This is because the thinner panels experienced more a more flexural type of deformation than the thicker core panels (50.8 mm and 76.2 mm). Therefore, as the faces resist the majority of the flexural stresses, the face thickness is an important parameter for panels with thin cores.

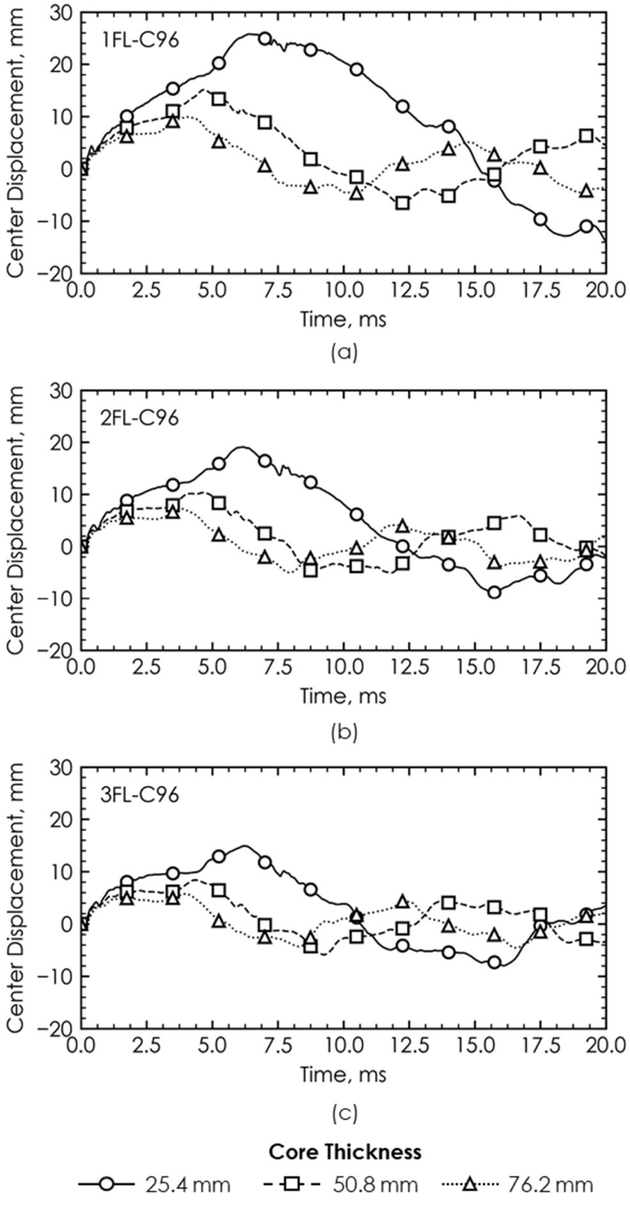

(a)

(b)

(c)

Figure 8-26. Effect of core thickness on the center displacement response of sandwich panels subjected to an 80 J impact (a) 1FL-C96; (b) 2FL-C96; and (c) 3FL-C96 [Note downward displacement is shown as positive]

8.4. SUMMARY

In this chapter, finite element (FE) modelling of sandwich panels with bidirectional flax fibre-reinforced polymer (FFRP) faces and polyisocyanurate foam cores under quasi-static and impact concentrated loads was performed. The modelling was performed using the commercially available software, LS DYNA. The material nonlinearity of both the FFRPs and the foam cores was considered as well as the geometric nonlinearity due to localized deformation. For the quasi-static models, four failure modes were considered: FFRP compression failure, FFRP tensile failure, core shear failure and compression face wrinkling. Failure was not considered for the impact modelling. The models were verified using test data from a previous study and then used to perform a parametric study to investigate the effect of foam core density, core thickness, face thickness and the size of the loading area. Through the parametric study, it was discovered that panels with low density cores were more susceptible to face wrinkling failure and panels with high density cores are susceptible to both tensile rupture and core shear failure. For the quasi-static models, it was shown that an increase in the load area diameter lessened the effect of localized deformation for panels with high density 96 kg/m^3 cores. For the impact models, it was shown that the impulse duration and maximum displacement experienced under low energy impacts increased with a decrease in core thickness, face thickness and core density. Additionally, it was shown that face thickness was less significant on the impulse behaviour for panels with lower density cores.

CHAPTER 9: CONCLUSIONS AND RECOMMENDATIONS

9.1. BEHAVIOUR OF FFRP-FOAM SANDWICH BEAMS UNDER MONOTONIC LOADS

Nine sandwich beams were constructed using FRPs comprised of bidirectional flax fabrics and bio-based epoxy resin for the facings and a polyisocyanurate foam for the core. The specimens were tested under three-point bending. Based on the test data, it can be concluded that the facings provide the majority of the flexural strength of the sandwich beams. Also, the C96 (96 kg/m^3 density) type foam is stiff enough that a balanced design can be achieved using FFRP facings. The balanced design is defined here as a simultaneous material failure, where the tension facing fails by tensile rupture while the foam core simultaneously fails by shear (i.e. both materials reach their full potential strengths). Increasing the facing thickness creates a change in the failure mode, moving from a facing-controlled failure to a core-controlled failure. Using the established material test data, moment-curvature and load-deflection models were developed and compared with the experimental results of the panels. A failure mode map was established for the tested panels and a simple design procedure was developed. The design procedure is simple enough that it could be easily used by designers. A design example using this procedure was presented. The proposed bilinear models and design-oriented analysis are applicable for analysis and design of sandwich beams with foam cores and FRP facings made of both unidirectional and bidirectional flax fabrics. Future work in this research area should include the development of appropriate safety factors for design and further testing and analysis of sandwich panels with FFRP facings.

9.2. BEHAVIOUR OF FFRP-FOAM SANDWICH BEAMS UNDER LOW VELOCITY IMPACT LOADS

The results of drop weight impact tests on nine sandwich panels with flax fibre-reinforced polymer facings were discussed. The main parameters of the tests were the facing thickness (1, 2 or 3 layers of a balanced bidirectional flax fabric) and core density (32 kg/m^3, 64 kg/m^3 or 96 kg/m^3). A Nonlinear Incremental Iterative Model (NIIM) based on the energy balance method was used to accurately predict the deflection and face strain based on the impact energy. The NIIM was also shown to predict well the contribution of shear and bending to the overall deflection of each specimen due to an impact load. Based on the test results and the model predictions the following conclusions were made:

- The impact resistance of the foam core FFRP sandwich panels increases with both facing thickness and core density. For example, by increasing the face thickness by one layer, 2FL-C64 was able to resist a 122.6 J impact whereas 1FL-C64 resisted only 30.6 J. Likewise, by increasing the core density, 2FL-C96 was able to resist 163.4 J of energy, an increase of 40.8 J when compared to 2FL-C64.
- As shown in Figure 3-3, failure energies and failure modes under impact closely matched those observed during quasi-static testing on counterpart specimens. This is also true of specimen stiffness, the average Impact/Static stiffness ratio being 1.07.
- The panel stiffnesses increased with both face thickness and core density and were not significantly affected by the impact tests.
- The contribution of shear deflection decreased with an increase in core density and was most affected when core density was reduced from 64 kg/m^3 to 32 kg/m^3. This indicates that in designs where the deflection is a limiting factor the choice of core density is important.

The nonlinear model was able to accurately predict the experimental behaviour. The average Test/NIIM ratios at the selected energy levels were 0.91 and 1.12 for the specimen deflection and face strains, respectively.

9.3. POST-IMPACT RESIDUAL BEHAVIOUR OF FFRP-FOAM SANDWICH BEAMS

The results of post-impact flexural tests on sandwich beams with flax fibre-reinforced polymer faces and polyisocyanurate foam cores were presented. A total of 27 sandwich beams were tested as a part of this study. The main parameters of the tests were the face thickness (one, two or three layers of flax fabric), the core density (32 kg/m^3, 64 kg/m^3 or 96 kg/m^3), and the impact energy and quantity (50 impacts at 50% the energy resisted by an intact sandwich beam, 50 impacts at 75% energy or one impact at 100% energy). Based on the tests, the following conclusions were made:

- The FFRP-foam sandwich beams exhibited notable resiliency. The post-impact flexural tests showed that the impacts did not cause a reduction in strength or stiffness of the sandwich beams.
- For specimens impacted at higher impact energies (75% and 100% of the energy resisted by intact specimens), there was a statistically significant increase in specimen strength after the impact events. Further research is required to explain this phenomenon.
- The failure modes of the sandwich beams were relatively unaffected by the impact events. The only specimen that exhibited a significant change in failure mode was 1FL-C64-R75 which failed due to tensile rupture of the bottom face whereas the intact beam failed due to compression face crushing. This change in failure mode was caused by the development of tensile cracks during the impact testing procedure.
- Sandwich beams impacted 50 times exhibited a softening of the load-top face strain behaviour and reduction in initial flexural rigidity during the post-impact flexural tests. This reduction was attributed to the hypothesized development of microcracks in the matrix of the top face. However, this has not been verified and should be investigated further in future studies.

9.4. BEHAVIOUR OF FFRP-CARDBOARD SANDWICH BEAMS

Twelve sandwich beams with two-layer flax fibre-reinforced polymer faces and corrugated cardboard cores were fabricated and tested under monotonic and impact loads. The main test parameter was the effect of using plain or waxed cardboard for a core material on the flexural behaviour of these beams. Additionally, the residual behaviour of these sandwich beams after an impact event was investigated. During the tests, the top and bottom face strains and specimen displacement were measured at midspan. Based on the results of the tests, the following conclusions can be drawn:

- Cardboard cores were shown to be comparable with traditional polyisocyanurate (PIR) foam cores. Sandwich beams made with both plain and waxed cardboard cores exhibited a higher stiffness than sandwich beams made with 32 kg/m^3, 64 kg/m^3 and 96 kg/m^3 density PIR cores and a higher ultimate strength than sandwich beams made with the 32 kg/m^3 and 64 kg/m^3 PIR cores.

- There was no significant difference between the load capacity or flexural rigidity of sandwich beams constructed with plain cardboard cores (PC) and waxed cardboard cores (WC). However, the stiffness of the WC specimens was 40.6% higher than the PC specimens.
- An existing design-oriented model was able to predict the static load-deflection behaviour of the PC core beams well. The moment-curvature behaviour was also predicted well, however the model behaviour was softer than the test results.
- Specimens with WC cores and PC cores resisted impact energies of 75% and 37.5% higher than the average static energy to cause failure, respectively.
- Beam strength and stiffness were not adversely affected after being subjected to an impact load. However, the flexural rigidity of both PC and WC type specimens were reduced after being subjected to an impact event. Interestingly, the beam residual strength was higher than the strength of the intact specimens. The current hypothesis is that this increase in strength after an impact event is caused by the densification of the core material during the impact event.
- The interface between the cardboard cores and FFRP faces has a major effect on the overall strength of the panels. Therefore, this is a major design problem for these types of panels and shows that the resin curing temperature, humidity and core surface quality are important parameters. In future studies, to improve the connection between the core and the faces, the core surface should be planed, and a veil should be included in the design.

Future work on these structures should include interlaminar shear testing of the face-core interface, testing of the effect freeze-thaw on these structures and examining the behaviour of these structures when exposed to fire

9.5. EXPERIMENTAL BEHAVIOUR OF TWO-WAY FFRP-FOAM SANDWICH STRUCTURES

Twelve 1220 mm x 1220 mm x 80 mm sandwich panels with FFRP faces and foam cores were tested by a concentrated center load both quasi-statically and dynamically. The main test parameters were the effect of face thickness, namely one, two or three layers of flax FRP (FFRP) per face (1FL, 2FL and 3FL, respectively) and impact energy level, namely, 50% failure energy, 70% failure energy or 95% failure energy. Based on the tests results, the following conclusions were drawn:

- The results of the quasi-static tests showed that as face thickness increased, the initial stiffness and ultimate load capacity of the panels increased. However, the increase of initial stiffness and load capacity was largest between the 1FL and 2FL specimens, increasing by 51% and 78%, respectively.
- The quasi-static failure mode changed from a bottom face-controlled tensile failure of the 1FL panel to a core-controlled shear failure of the 3FL panel.
- The results of the first impact on each panel were analysed to determine the effect of the impact energy level on the panel response. It was shown that the impact energy level did not have a significant effect on the center displacement or impulse duration. However, when visible damage was present, both the center displacement and the impulse duration increased significantly.
- The impact specimens were tested multiple times under set impact energies up to 100 times or until failure was observed. For specimens without damage, the impulse shape and duration were not changed due to number of impacts. However, for damaged panels, the impulse duration increased, and the impulse shape changed.
- A comparison of the quasi-static and impact displacement data showed that the panels exhibited a higher stiffness under impact loads than under quasi-static loads.

9.6. ANALYTICAL MODELLING OF TWO-WAY FFRP-FOAM SANDWICH STRUCTURES

A simple method to predict the load-deflection behaviour of sandwich panels constructed with nonlinear materials was developed based on the Mindlin plate theory. The model was verified using the test results of sandwich plates with flax fibre-reinforced polymer face and polyisocyanurate cores. From the study, the following conclusions were drawn:

- The model was able to accurately predict the ultimate load capacity of the thin-faced plate. The model-test ratio of the strength of the 1FL-C96 plate was 0.99. The ultimate capacities of the plates with thicker faces (2FL and 3FL) were overestimated because the model is not able to capture localised failure. To improve the accuracy of the model, in future studies, indentation should be considered as a failure mode.
- The model was able to predict the stiffness of the plates. The model-test ratios of the plate stiffness were 1.00 and 1.06 for the 1FL-C96 and 2FL-C96 plates respectively.
- The model is not able to capture localised failure mechanisms, such as indentation, which leads to an overprediction of plate capacity and stiffness for sandwich plates with thick faces. Future studies should include the incorporation of more failure modes, such as indentation under the load area. To capture this localised behaviour, it is expected that finite element analysis will be needed.

9.7. FINITE ELEMENT MODELLING OF FFRP-FOAM SANDWICH STRUCTURES

The behaviour of large-scale sandwich panels with flax fibre-reinforced polymer (FFRP) faces and foam cores under a concentrated load was examined numerically. Finite element models were created using the commercially available software, LS DYNA, for both quasi-static and impact loading conditions. Both the material nonlinearity of the FFRP faces and foam cores and the geometric nonlinearity were accounted for in the models. In the quasi-static models, material failure was considered in the faces using the maximum stress criterion and, in the core, using the tresca failure criterion. Additionally, the stability type failure of compression face wrinkling, was considered in the top faces. The impact models examined were of low energy impacts and therefore did not consider failure. Both the quasi-static and impact models were successfully verified and validated using test data from a previous study.

A parametric study investigated the effect of the foam core density, core thickness, FFRP face thickness and the size of the load area. Based on the parametric study the following conclusions were drawn for the quasi-static models:

- The models were able to accurately capture the strain state in the center of the top faces observed in the tests. The top faces started in a state of compression, but after the onset of indentation under the load edge, transitioned to a state of tensile strain.
- Panels examined experienced failure due to core shear, tensile rupture and compression face wrinkling. The failure modes were affected by both core density and face thickness, but not load area diameter.
- Ultimate load capacity and initial stiffness both increased with and increase of core density, face thickness and load area diameter.
- Increasing the size of the load area mitigated the effect of localized deformation under the load edge. Future work should use FE models to verify the analytical model presented in Chapter 7 for use with larger load areas.

For the impact models, a parametric study was performed to observe the effect of a low energy impact of 80 J. The parameters investigated were core density, core thickness and face thickness. The impulse duration and maximum center displacement generally increased with a decrease in core density, core thickness and face thickness. Face thickness did not have a significant effect on panels with low density cores (32 kg/m^3) due to the significant contribution of shear to the overall displacement. Conversely, panels with thin cores were significantly affected by face thickness. This was attributed to the significant contribution of flexure to the overall displacement.

9.8. RECOMMENDATIONS FOR FUTURE RESEARCH

The intent of this thesis research was to show the viability of sandwich structures with flax fibre-reinforced polymer (FFRP) faces for use in infrastructure. The thesis research has shown that these sandwich structures exhibit remarkable resilience and relatively high strengths. However, in order to incorporate these structures into new design codes and subsequently new infrastructure, more research is required including, but not limited to:

- Performing more tests to build the experimental database and to ensure that there is enough experimental data to develop design resistance factors and to perform reliability studies.
- Exploring the size effect on the behaviour of sandwich panels with FFRP faces, specifically looking at the effects of larger span lengths and different core thicknesses.
- Studying the effect of strain rate on the behaviour of FFRPs and sandwich structures with FFRP faces.
- Examining the fire resistance of sandwich panels with FFRP faces.
- Investigating the effect of wet/dry and freeze/thaw environmental conditions on sandwich panels with FFRP faces.

BIBLIOGRAPHY

Abrate, S. (1997). “Localized Impact on Sandwich Structures With Laminated Facings.” *Applied Mechanics Reviews*, 50(2), 69.

Abrate, S. (1998). *Impact on Composite Structures*. Cambridge University Press, Cambridge, UK.

Akil Hazizan, M., and Cantwell, W. J. (2002). “The low velocity impact response of foam-based sandwich structures.” *Composites Part B: Engineering*, 33(3), 193–204.

Allen, H. G. (1969). *Analysis and Structural Design of Sandwich Panels*. Pergamon Press, Oxford, UK.

Anderson, T., and Madenci, E. (2000). “Experimental investigation of low-velocity impact characteristics of sandwich composites.” *Composite Structures*, 50(3), 239–247.

Andrews, E. W., and Moussa, N. A. (2009). “Failure mode maps for composite sandwich panels subjected to air blast loading.” *International Journal of Impact Engineering*, 36(3), 418–425.

Asdrubali, F., Pisello, A. L., D’Alessandro, F., Bianchi, F., Fabiani, C., Cornicchia, M., and Rotili, A. (2016). “Experimental and numerical characterization of innovative cardboard based panels: Thermal and acoustic performance analysis and life cycle assessment.” *Building and Environment*, Elsevier Ltd, 95, 145–159.

ASTM. (2005). “ASTM D7136, Standard test method for measuring the damage resistance of a fiber-reinforced polymer matrix composite to a drop-weight impact event.” *Annual Book of ASTM Standards*, 1–16.

ASTM. (2013). “ASTM D638, Standard test method for tensile properties of plastics.” *Annual Book of ASTM Standards*, ASTM International, West Conshohocken, Pennsylvania, US.

ASTM. (2014). “ASTM D3039/D3039M - Standard Test Method for Tensile Properties of Polymer Matrix Composite Materials.” *Annual Book of ASTM Standards*, ASTM, West Conshohocken, Pennsylvania, US.

ASTM. (2017). “D790, Standard Test Methods for Flexural Properties of Unreinforced and Reinforced Plastics and Electrical Insulating Materials.” *Annual Book of ASTM Standards*.

ASTM. (2018a). “ASTM D3518/D3518M, Standard Test Method for In-Plane Shear Response of Polymer Matrix Composite Materials by Tensile Test of a ± 45° Laminate.” *Annual Book of ASTM Standards*, ASTM International, West Conshohocken, Pennsylvania, US.

ASTM. (2018b). “ASTM C273/C273M, Standard Test Method for Shear Properties of Sandwich Core Materials.” *Annual Book of ASTM Standards*, ASTM International, West Conshohocken, Pennsylvania, US.

Atas, C., and Potoglu, U. (2016). “The Effect of Face-Sheet Thickness on Low-Velocity Impact Response of Sandwich Composites with Foam Cores.” *Journal of Sandwich Structures and Materials*, 18(2), 215–228.

Baley, C., Le Duigou, A., Bourmaud, A., and Davies, P. (2012). "Influence of drying on the mechanical behaviour of flax fibres and their unidirectional composites." *Composites Part A: Applied Science and Manufacturing*, Elsevier Ltd, 43(8), 1226–1233.

Bambach, M. R. (2017). "Thin-Walled Structures Compression strength of natural fi bre composite plates and sections of flax , jute and hemp." *Thin Walled Structures*, Elsevier Ltd, 119(May), 103–113.

Bank, L. C. (2006). *Composites for Construction: Structural Design with FRP Materials*. *Composites for Construction*, John Wiley & Sons, Inc., Hoboken, New Jersey.

Baran, I., and Weijermars, W. (2020). "Residual bending behaviour of sandwich composites after impact." *Journal of Sandwich Structures and Materials*, 22(2), 402–422.

Bensadoun, F., Vallons, K. A. M., Lessard, L. B., Verpoest, I., and Van Vuure, A. W. (2016). "Fatigue behaviour assessment of flax-epoxy composites." *Composites Part A: Applied Science and Manufacturing*, Elsevier Ltd, 82, 253–266.

Besant, T., Davies, G. A. O., and Hitchings, D. (2001). "Finite element modelling of low velocity impact of composite sandwich panels." *Composites - Part A: Applied Science and Manufacturing*, 32(9), 1189–1196.

Betts, D., Sadeghian, P., and Fam, A. (2017). "Tensile properties of flax frp composites." *Asia Pacific Conference on FRP in Structures*, International Institute for FRP in Construction, Singapore.

Betts, D., Sadeghian, P., and Fam, A. (2018a). "Experimental Behavior and Design-Oriented Analysis of Sandwich Beams with Bio-Based Composite Facings and Foam Cores." *Journal of Composites for Construction*, 22(4), 1–12.

Betts, D., Sadeghian, P., and Fam, A. (2018b). "Impact Behaviour of Sandwich Panels Made of Flax Fiber-Reinforced Bio-Based Polymer Face Sheets and Foam Cores." *Structures Congress 2018*, 1–7.

Betts, D., Sadeghian, P., and Fam, A. (2018c). "Tensile Preperties of Single Flax Fibres." *CSCE Annual Conference*, CSCE, Fredericton, NB, Canada, 1–10.

Betts, D., Sadeghian, P., and Fam, A. (2019). "Impact behavior of sustainable sandwich panels with flax FRP faces and cardboard cores." *AEI Conference 2019*, American Society of Civil Engineers, Tysons, Virginia, 1–6.

Betts, D., Sadeghian, P., and Fam, A. (2020a). "Experiments and nonlinear analysis of the impact behaviour of sandwich panels constructed with flax fibre-reinforced polymer faces and foam cores." *Journal of Sandwich Structures and Materials*.

Betts, D., Sadeghian, P., and Fam, A. (2020b). "Erratum for 'Experimental Behavior and Design-Oriented Analysis of Sandwich Beams with Bio-Based Composite Facings and Foam Cores .'" *Journal of Composites for Construction*, 24(1), 08219001–1.

Betts, D., Sadeghian, P., and Fam, A. (2020c). "Structural Behavior of Sandwich Beams with Flax Fiber-Reinforced Polymer Faces and Cardboard Cores under Monotonic and Impact Loads." *Journal of Architectural Engineering*, 26(2), 1–12.

Betts, D., Sadeghian, P., and Fam, A. (2021). "Post-Impact Residual Strength and Resilience of Sandwich Panels with Natural Fiber Composite Faces." *Journal of Building Engineering*, 38, 102184.

Boria, S., Raponi, E., Sarasini, F., Tirillò, J., and Lampani, L. (2018). "Green sandwich structures under impact: experimental vs numerical analysis." *Procedia Structural Integrity*, Elsevier B.V., 12, 317–329.

Chai, G. B., and Zhu, S. (2011). "A review of low-velocity impact on sandwich structures." *Proceedings of the Institution of Mechanical Engineers, Part L: Journal of Materials Design and Applications*, 225(4), 207–230.

Christian, S. J., and Billington, S. L. (2011). "Mechanical response of PHB- and cellulose acetate natural fiber-reinforced composites for construction applications." *Composites Part B*, Elsevier Ltd, 42(7), 1920–1928.

Christoforou, A. P., and Yigit, A. S. (2009). "Scaling of low-velocity impact response in composite structures." *Composite Structures*, Elsevier Ltd, 91, 358–365.

Cicala, G., Cristaldi, G., Recca, G., and Latteri, A. (2010). "Composites Based on Natural Fibre Fabrics." *Woven Fabric Engineering*, P. D. Dubrovski, ed., IntechOpen.

De Cicco, D., and Taheri, F. (2018a). "Robust numerical approaches for simulating the buckling response of 3D fiber-metal laminates under axial impact – Validation with experimental results." *Journal of Sandwich Structures and Materials*.

De Cicco, D., and Taheri, F. (2018b). "Delamination Buckling and Crack Propagation Simulations in Fiber-Metal Laminates Using xFEM and Cohesive Elements." *Applied Sciences*, 8(12), 2440.

Codyre, L., Mak, K., and Fam, A. (2016). "Flexural and axial behaviour of sandwich panels with bio-based flax fibre-reinforced polymer skins and various foam core densities." *Journal of Sandwich Structures and Materials*, 1–22.

CoDyre, L., Mak, K., and Fam, A. (2018). "Flexural and axial behaviour of sandwich panels with bio-based flax fibre-reinforced polymer skins and various foam core densities." *Journal of Sandwich Structures and Materials*, 20(5), 595–616.

Dai, J., and Hahn, H. T. (2003). "Flexural behavior of sandwich beams fabricated by vacuum-assisted resin transfer molding." *Composite Structures*, 61(3), 247–253.

El Damatty, A. A., Mikhail, A., and Awad, A. A. (2000). "Finite element modeling and analysis of a cardboard shelter." *Thin-Walled Structures*, 28, 145–165.

Daniel, I. M., Abot, J. L., Schubel, P. M., and Luo, J. J. (2012). "Response and Damage Tolerance of Composite Sandwich Structures under Low Velocity Impact." *Experimental Mechanics*, 52(1), 37–47.

Davies, G. A. O., Hitchings, D., Besant, T., Clarke, A., and Morgan, C. (2004). "Compression after impact strength of composite sandwich panels." *Composite Structures*, 63(1), 1–9.

Dawood, M., Taylor, E., and Rizkalla, S. (2010). "Two-way bending behavior of 3-D GFRP sandwich panels with through-thickness fiber insertions." *Composite Structures*, Elsevier Ltd, 92(4), 950–963.

Dynamore. (2018). "Guideline for implicit analyses using LS-DYNA." Dynamore.

Elliott Company. (2016a). "ELFOAM P400 Polyisocyanurate Foam." Elliott Company, Indianapolis, IN.

Elliott Company. (2016b). "ELFOAM P200 Polyisocyanurate Foam." Elliott Company, Indianapolis, IN.

Entropy Resins. (2013a). *Super SAP ONE Epoxy Resin*. Hayward, CA.

Entropy Resins. (2013b). *Material Safety Data Sheet - Super Sap CLS Hardener*. Hayward, CA.

Entropy Resins. (2015). *Safety Data Sheet - Super Sap ONE Epoxy Resin*. Hayward, CA.

Fam, A., and Sharaf, T. (2010). "Flexural performance of sandwich panels comprising polyurethane core and GFRP skins and ribs of various configurations." *Composite Structures*, Elsevier Ltd, 92(12), 2927–2935.

Fam, A., Sharaf, T., and Sadeghian, P. (2016). "Fiber element model of sandwich panels with soft cores and composite skins in bending considering large shear deformations and localized skin wrinkling." *Journal of Engineering Mechanics*, 142(5), 1–14.

Feng, D., and Aymerich, F. (2013). "Damage prediction in composite sandwich panels subjected to low-velocity impact." *Composites Part A: Applied Science and Manufacturing*, Elsevier Ltd, 52, 12–22.

Ferdous, W., Bai, Y., Ngo, T. D., Manalo, A., and Mendis, P. (2019). "New advancements, challenges and opportunities of multi-storey modular buildings – A state-of-the-art review." *Engineering Structures*, Elsevier, 183(October 2018), 883–893.

Ferdous, W., Manalo, A., and Aravinthan, T. (2017). "Effect of beam orientation on the static behaviour of phenolic core sandwich composites with different shear span-to-depth ratios." *Composite Structures*, Elsevier Ltd, 168, 292–304.

Ferdous, W., Manalo, A., Aravinthan, T., and Fam, A. (2018a). "Flexural and shear behaviour of layered sandwich beams." *Construction and Building Materials*, Elsevier Ltd, 173, 429–442.

Ferdous, W., Manalo, A., Van Erp, G., Aravinthan, T., and Ghabraie, K. (2018b). "Evaluation of an Innovative Composite Railway Sleeper for a Narrow-Gauge Track under Static Load." *Journal of Composites for Construction*, 22(2).

Fraile-Garcia, E., Ferreiro-Cabello, J., Pernia-Espinoza, A., and Martinez-de-Pison, F. J. (2019). "Technical-economic assessment of redesigned reinforced concrete pre-slabs: Incorporating corrugated cardboard." *Structural Concrete*, (August 2018), 1340–1349.

Frostig, B. Y., Baruch, M., Vilnay, O., and Sheinman, I. (1992). "High-order theory for sandwich-beam behavior with transversely flexible core." *Journal of Engineering Mechanics*, 118(5), 1026–1043.

Frostig, Y., and Baruch, M. (1996). "Localized Load Effects in High-Order Bending of Sandwich Panels with Flexible Core." *Journal of Engineering Mechanics*, 122(11), 1069–1076.

Göttner, W., and Reimerdes, H. G. (2006). "Bending strength of sandwich panels with different cores after impact." *Fracture of Nano and Engineering Materials and Structures - Proceedings of the 16th European Conference of Fracture*, 1261–1262.

Gupta, N., Woldesenbet, E., Kishore, and Sankaran, S. (2002). "Response of Syntactic Foam Core Sandwich Structured Composites to Three-Point Bending." *Journal of Sandwich Structures and Materials*, 4(3), 249–272.

Gustin, J., Joneson, A., Mahinfalah, M., and Stone, J. (2005). "Low velocity impact of combination Kevlar/carbon fiber sandwich composites." *Composite Structures*, 69(4), 396–406.

He, W., Liu, J., Wang, S., and Xie, D. (2018). "Low-velocity impact response and post-impact flexural behaviour of composite sandwich structures with corrugated cores." *Composite Structures*, Elsevier, 189(December 2017), 37–53.

Hristozov, D., Wroblewski, L., and Sadeghian, P. (2016). "Long-term tensile properties of natural fibre-reinforced polymer composites: Comparison of flax and glass fibres." *Composites Part B: Engineering*, Elsevier Ltd, 95, 82–95.

Hristozov, D., Wroblewski, L., and Sadeghian, P. (2017). "Durability of Flax FRPs Exposed to Accelerated Environmental Conditions." *5th International Conference on Durability of Fibre Reinforced Polymer (FRP) Composites for Construction and Rehabilitation of Structures*, Sherbrooke, QC, 1–8.

Hu, J., Yin, S., Yu, T. X., and Xu, J. (2018). "Dynamic compressive behavior of woven flax-epoxy-laminated composites." *International Journal of Impact Engineering*, 117(December 2017), 63–74.

Huo, R., Liu, W., Wan, L., Fang, Y., and Wang, L. (2015). "Experimental Study on Sandwich Bridge Decks with GFRP Face Sheets and a Foam-Web Core Loaded under Two-Way Bending." *Advances in Materials Science and Engineering*, Hindawi Publishing Corporation, 2015.

Icardi, U., and Ferrero, L. (2009). "Impact analysis of sandwich composites based on a refined plate element with strain energy updating." *Composite Structures*, Elsevier Ltd, 89, 35–51.

Kalantari, M., Nami, M. R., and Kadivar, M. H. (2010). "Optimization of composite sandwich panel against impact using genetic algorithm." *International Journal of Impact Engineering*, Elsevier Ltd, 37(6), 599–604.

Kim, W., Argento, A., Lee, E., Flanigan, C., Houston, D., Harris, A., and Mielewski, D. F. (2012). "High strain-rate behavior of natural fiber-reinforced polymer composites." *Journal of Composite Materials*, 46(9), 1051–1065.

Klaus, M., Reimerdes, H. G., and Gupta, N. K. (2012). "Experimental and numerical investigations of residual strength after impact of sandwich panels." *International Journal of Impact Engineering*, Elsevier Ltd, 44, 50–58.

Mak, K., and Fam, A. (2016). “Bio Resins and Bio Fibers for FRP Applications in Structural Engineering Applications.” *7th International Conference on Advanced Composite Materials in Bridges and Structures*, Vancouver, BC, Canada, 1–6.

Mak, K., and Fam, A. (2019a). “Performance of flax-FRP sandwich panels exposed to different ambient temperatures.” *Construction and Building Materials*, Elsevier Ltd, 219, 121–130.

Mak, K., and Fam, A. (2019b). “Freeze-thaw cycling effect on tensile properties of unidirectional flax fiber reinforced polymers.” *Composites Part B: Engineering*, Elsevier Ltd, 174(March), 106960.

Mak, K., Fam, A., and Macdougall, C. (2015). “Flexural Behavior of Sandwich Panels with Bio-FRP Skins Made of Flax Fibers and Epoxidized Pine-Oil Resin.” *Journal of Composites for Construction*, 19(2003), 1–13.

Malekzadeh, K., Khalili, M. R., Olsson, R., and Jafari, A. (2006). “Higher-order dynamic response of composite sandwich panels with flexible core under simultaneous low-velocity impacts of multiple small masses.” *International Journal of Solids and Structures*, 43, 6667–6687.

Mallick, P. K. (2007). *Fiber-Reinforced Composites: Materials, Manufacturing and Design*. CRC Press, NW.

Manalo, A. C., Aravinthan, T., Karunasena, W., and Islam, M. M. (2010). “Flexural behaviour of structural fibre composite sandwich beams in flatwise and edgewise positions.” *Composite Structures*, Elsevier Ltd, 92(4), 984–995.

Manalo, A., Surendar, S., van Erp, G., and Benmokrane, B. (2016). “Flexural behavior of an FRP sandwich system with glass-fiber skins and a phenolic core at elevated in-service temperature.” *Composite Structures*, Elsevier Ltd, 152, 96–105.

Mathura, N., and Cree, D. (2016). “Characterization and mechanical property of Trinidad coir fibers.” *Journal of Applied Polymer Science*, 133(29), 1–9.

McCracken, A., and Sadeghian, P. (2018). “Corrugated cardboard core sandwich beams with bio-based flax fiber composite skins.” *Journal of Building Engineering*, Elsevier Ltd, 20(January), 114–122.

Meo, M., Vignjevic, R., and Marengo, G. (2005). “The response of honeycomb sandwich panels under low-velocity impact loading.” *International Journal of Mechanical Sciences*, 47(9), 1301–1325.

Nemes, J. A., and Simmonds, K. E. (1992). “Low-Velocity Impact Response of Foam-Core Sandwich Composites.” *Journal of Composite Materials*, 26(4), 500–519.

Nguyen, M. Q., Jacombs, S. S., Thomson, R. S., Hachenberg, D., and Scott, M. L. (2005). “Simulation of impact on sandwich structures.” *Composite Structures*, 67(2 SPEC. ISS.), 217–227.

Paper & Paperboard Packaging Environmental Council. (2017). “PPEC Factsheet.” <http://www.ppec-paper.com/pdfFiles/factsheets/2017/Packaging/FS03-2017.pdf> (Mar. 8, 2019).

Petras, A., and Sutcliffe, M. P. F. (1999). “Failure mode maps for honeycomb sandwich panels.” *Composite Structures*, 44(4), 237–252.

Pflug, J., Verpoest, I., and Vandepitte, D. (2000). "Folded Honeycomb Cardboard and Core Material for Structural Applications." *Proceedings of the 5th International Conference on Sandwich Construction*, European Society for Composite Materials, Zurich, Switzerland.

Pflug, J., Xinyu, F., Vangrimde, B., Verpoest, I., Bratfisch, P., and Vandepitte, D. (2002). "Development of a sandwich material with polypropylene / natural fibre skins and paper honeycomb core Development of a sandwich material with polypropylene / natural fibre skins and paper honeycomb core." *Proceedings of the 10th European Conference on Composites Materials*, EMAS Publishing.

Plagianakos, T. S., Lika, K., and Papadopoulos, E. G. (2016). "Low-velocity impact response of smart sandwich composite plates with piezoelectric transducers : Modeling and experiments." *Journal of Intelligent Material Systems and Structures*, 27(6), 774–785.

Plagianakos, T. S., and Papadopoulos, E. G. (2014). "Low-energy impact response of composite and sandwich composite plates with piezoelectric sensory layers." *International Journal of Solids and Structures*, Elsevier Ltd, 51(14), 2713–2727.

Qi, Y., Fang, H., and Liu, W. (2016). "Experimental study of the bending properties and deformation analysis of web-reinforced composite sandwich floor slabs with four simply supported edges." *PLoS ONE*, 11(2), 1–26.

Ramesh, M., Palanikumar, K., and Reddy, K. H. (2017). "Plant fibre based bio-composites : Sustainable and renewable green materials." *Renewable and Sustainable Energy Reviews*, Elsevier Ltd, 79(May), 558–584.

Sadeghian, P., Hristozov, D., and Wroblewski, L. (2018). "Experimental and analytical behavior of sandwich composite beams: Comparison of natural and synthetic materials." *Journal of Sandwich Structures and Materials*, 20(3), 287–307.

Satasivam, S., Bai, Y., Yang, Y., Zhu, L., and Zhao, X. L. (2018). "Mechanical performance of two-way modular FRP sandwich slabs." *Composite Structures*, Elsevier, 184(March 2017), 904–916.

Schubel, P. M., Luo, J.-J., and Daniel, I. M. (2005). "Low velocity impact behavior of composite sandwich panels." *Composites Part A: Applied Science and Manufacturing*, 36(10), 1389–1396.

Secchi, S., Asdrubali, F., Cellai, G., Nannipieri, E., Rotili, A., and Vannucchi, I. (2016). "Experimental and environmental analysis of new sound-absorbing and insulating elements in recycled cardboard." *Journal of Building Engineering*, Elsevier, 5, 1–12.

Sharaf, T. A. M. (2010). "Flexural Behaviour of Sandwich Panels Composed of Polyurethane Core and GFRP Skins and Ribs." 374.

Sharaf, T., and Fam, a. (2012). "Numerical modelling of sandwich panels with soft core and different rib configurations." *Journal of Reinforced Plastics and Composites*, 31(11), 771–784.

Sharaf, T., Shawkat, W., and Fam, A. (2010). "Structural performance of sandwich wall panels with different foam core densities in one-way bending." *Journal of Composite Materials*, 44(19), 2249–2263.

Shipsha, A., and Zenkert, D. (2005). “Compression-after-impact strength of sandwich panels with core crushing damage.” *Applied Composite Materials*, 12(3–4), 149–164.

Sparnins, E. (2006). “Mechanical properties of flax fibers and their composites.” Lulea University of Technology.

Thomsen, O. T., and Rits, W. (1998). “Analysis and design of sandwich plates with inserts—a high-order sandwich plate theory approach.” *Composites Part B: Engineering*, 29(6), 795–807.

Timoshenko, S., and Woinowsky-Krieger, S. (1987). *Theory of Plates and Shells*. McGraw-Hill Book Company.

Torre, L., and Kenny, J. M. (2000). “Impact testing and simulation of composite sandwich structures for civil transportation.” *Composite Structures*, 50(3), 257–267.

Triantafillou, T. C., and Gibson, L. J. (1987). “Failure Mode Maps for Foam-Core Sandwich Beams.” *Materials Science and Engineering*, 95, 37–53.

Tsai, S. W., and Wu, E. M. (1971). “A General Theory of Strength for Anisotropic Materials.” *Journal of Composite Materials*, 5(1), 58–80.

Tuo, H., Lu, Z., Ma, X., Zhang, C., and Chen, S. (2019). “An experimental and numerical investigation on low-velocity impact damage and compression-after-impact behavior of composite laminates.” *Composites Part B*, Elsevier, 167, 329–341.

Ude, A. U., Arif, A. K., and Azhari, C. H. (2013). “Impact damage characteristics in reinforced woven natural silk / epoxy composite face-sheet and sandwich foam, coremat and honeycomb materials.” *International Journal of Impact Engineering*, 58, 31–38.

Vitale, J. P., Francucci, G., Xiong, J., and Stocchi, A. (2017). “Failure mode maps of natural and synthetic fiber reinforced composite sandwich panels.” *Composites Part A: Applied Science and Manufacturing*, Elsevier Ltd, 94, 217–225.

Wang, C. M., Reddy, J. N., and Lee, K. H. (2000). *Shear Deformable Beams and Plates: Relationships with Classical Solutions*. Elsevier Science, Kidlington, Oxford, UK.

Wroblewski, L., Hristozov, D., and Sadeghian, P. (2016). “Durability of bond between concrete beams and FRP composites made of flax and glass fibers.” *Construction and Building Materials*, Elsevier Ltd, 126, 800–811.

Xiao, L., Wang, G., Qiu, S., Han, Z., Li, X., and Zhang, D. (2019). “Exploration of energy absorption and viscoelastic behavior of CFRPs subjected to low velocity impact.” *Composites Part B*, Elsevier, 165(November 2018), 247–254.

Yan, L., Kasal, B., and Huang, L. (2016). “A review of recent research on the use of cellulosic fibres, their fibre fabric reinforced cementitious, geo-polymer and polymer composites in civil engineering.” *Composites Part B: Engineering*, Elsevier Ltd, 92(April), 94–132.

Zhang, D., Jiang, D., Fei, Q., and Wu, S. (2016). "Experimental and numerical investigation on indentation and energy absorption of a honeycomb sandwich panel under low-velocity impact." *Finite Elements in Analysis and Design*, Elsevier, 117–118, 21–30.

Zhang, J., Pan, S., and Chen, L. (2019). "Dynamic thermal buckling and postbuckling of clamped–clamped imperfect functionally graded annular plates." *Nonlinear Dynamics*, Springer Netherlands, 95(1), 565–577.

Zhou, J., Hassan, M. Z., Guan, Z., and Cantwell, W. J. (2012). "The low velocity impact response of foam-based sandwich panels." *Composites Science and Technology*, Elsevier Ltd, 72(14), 1781–1790.

Zhu, D., Shi, H., Fang, H., Liu, W., Qi, Y., and Bai, Y. (2018). "Fiber reinforced composites sandwich panels with web reinforced wood core for building floor applications." *Composites Part B: Engineering*, Elsevier, 150(April), 196–211.

Zhu, S., and Chai, G. B. (2013). "Damage and failure mode maps of composite sandwich panel subjected to quasi-static indentation and low velocity impact." *Composite Structures*, Elsevier Ltd, 101, 204–214.

APPENDIX A: TENSILE PROPERTIES OF FLAX FRP COMPOSITES [6]

A.1. INTRODUCTION

Interest in sustainable materials is increasing around the world. One new material type that is currently being studied is natural fibre-reinforced polymers (FRPs), specifically flax FRPs. Flax is a plant that is grown in many locations around the world and its fibres have moderate strength and stiffness (Sparnins 2006). In Canada, the use of the flax fibres is often over-looked and the fibres are mainly considered a waste product of the flax seed industry. An interesting property of flax FRPs reported by numerous authors is that stress-strain behaviour is nonlinear (Mak et al. 2015; Sadeghian et al. 2018; Bensadoun et al. 2016). The objective of this study was to determine the source of the nonlinear behaviour of flax FRPs. It was first hypothesized that as flax fibres are weaker and less stiff than glass or carbon fibres, there is the potential that the matrix has a larger influence over the composite mechanical properties, specifically on the nonlinear properties of flax FRPs. Another hypothesis was that the nonlinear behaviour was influenced by the shape of the test specimens. Finally, the third hypothesis was that the source of the nonlinearity was the flax fibre material. A series of coupons were prepared and tested to evaluate the aforementioned hypotheses.

A.2. EXPERIMENTAL STUDY

A unidirectional flax fabric with a reported unit weight of 275 g/m^2 (gsm) was used. The technical fibre diameter, tensile strength and modulus were not available from the manufacturer, but are typically cited as 50 – 100 µm, 500-900 MPa and 50-70 GPa, respectively (Sparnins 2006). Three different resins, namely, West System Epoxy, Super Sap ONE Epoxy, and Altek General Purpose Polyester resin were used. West System Epoxy has a reported tensile strength, modulus and elongation of 50.33 MPa,

---

[6] **This appendix was published in the proceedings of the 6th *Asia-Pacific Conference on FRP in Structures*:**

Betts, D., Sadeghian, P., and Fam, A. (2017). "Tensile properties of flax frp composites." *Asia Pacific Conference on FRP in Structures*, International Institute for FRP in Construction, Singapore.

3.17 GPa and 4.596 %, respectively. Super Sap ONE has a reported tensile strength, modulus and elongation of approximately 53.23 MPa, 2.65 GPa and 6 %, respectively. Altek General Purpose Polyester Laminating Resin has a reported tensile strength, modulus, and elongation of 84 MPa, 3.9 GPa, and 3.6%, respectively.

A total of 45 tension coupons (9 groups x 5 identical specimens) were fabricated and tested. To manufacture the unreinforced specimens, the resin was first mixed with the hardener and placed into a vacuum chamber for degassing. The degassed resin was then poured into a template in accordance with ASTM D638 (2013). Both types of reinforced specimens started as a 300 mm by 300 mm square sheet of polymer reinforced with two layers of unidirectional flax fibres manufactured using the wet lay-up technique as shown in Figure 2a. After performing the wet lay-up, parchment paper was placed on top of the sheets and any additional resin and air was removed by a steel roller as shown in Figure 2b. After the sheets had cured, they were cut and made into either the tabbed specimen shape as prescribed by ASTM 3039 (2014) or the dumbbell specimen shape as prescribed by ASTM D638 (2013).

Table A-1. Mechanical properties of unidirectional FFRP tensile coupons

Group ID	Thickness (mm)		Tensile Strength (MPa)		Ultimate Strain (mm/mm)		Primary Modulus (GPa)		Secondary Modulus (GPa)		
	AVG	SD	AVG	SD	AVG	SD	AVG	SD	AVG	SD	Red.
E-R-D	1.74	0.03	186.0	14.8	0.0134	0.0011	18.95	0.42	12.66	0.60	66.8
B-R-D	1.53	0.11	159.5	14.0	0.0126	0.0008	16.46	0.96	11.45	0.37	69.5
P-R-D	1.36	0.07	144.1	4.9	0.0106	0.0006	17.83	2.00	11.09	0.68	62.2
E-R-T	1.66	0.07	192.5	7.6	0.0165	0.0025	17.49	2.41	10.73	1.34	61.4
B-R-T	1.97	0.09	198.0	9.3	0.0153	0.0006	17.09	0.63	11.93	0.39	69.8
P-R-T	1.57	0.02	167.7	6.7	0.0136	0.0011	17.74	2.48	10.83	1.05	61.1
E-U-D	2.95	0.42	55.6	0.6	0.0234	0.0005	3.84	0.06	N/A	N/A	N/A
B-U-D	3.49	0.29	57.9	0.4	0.0287	0.0018	3.20	0.13	N/A	N/A	N/A
P-U-D	4.07	0.37	48.4	4.8	0.0185	0.0032	3.55	0.37	N/A	N/A	N/A

AVG=average, SD=standard deviation, E=epoxy, B=bio-based epoxy, P=polyester, R=reinforced, U=unreinforced, D=dumbbell, T=tabbed, Red.=percent reduction, N/A=not applicable.

The specimens in this study were all tested in uniaxial tension at a rate of 2 mm/min using an Instron 8501 test frame. This testing rate was chosen as it satisfied the requirements for both ASTM D638 (2013) for the dumbbell-shaped unreinforced and reinforced polymers and ASTM D3039 (2014) for the tabbed reinforced polymers. The elongation of the coupons was measured using an Instron extensometer with a gauge length of 25 mm and a maximum travel of 25 mm in tension. To directly compare the data of the different reinforced specimens, a nominal thickness of 1 mm was used. The test results for the study are presented in Table 1.

A.3. RESULTS AND DISCUSSIONS

As seen in Figure A-1a, the flax FRPs displayed bi-linear mechanical behaviour. It was hypothesized that the type of polymer would have an effect on the mechanical properties of the flax-FRPs, specifically on the secondary modulus. The mechanical behaviour of the tabbed specimens was proven to be unaffected by the matrix type with 95% confidence by a single factor analysis of variance (ANOVA). Contrary to the results of the tabbed specimens, an ANOVA analysis with 95% confidence showed that the secondary moduli of the dumbbell specimens were affected by the matrix type. Another ANOVA analysis showed with 95% confidence that there was a significant difference in the maximum tensile strengths of the composites manufactured with different matrices for both of the specimen types. Also, a series of ANOVA analyses at 95% confidence were performed to determine if there was a significant difference in any of the mechanical properties between different specimen shapes. For both the bio-based epoxy and polyester specimens the maximum tensile strength was significantly reduced for the dumbbell type specimens when compared with the tabbed specimens of the same matrix type.

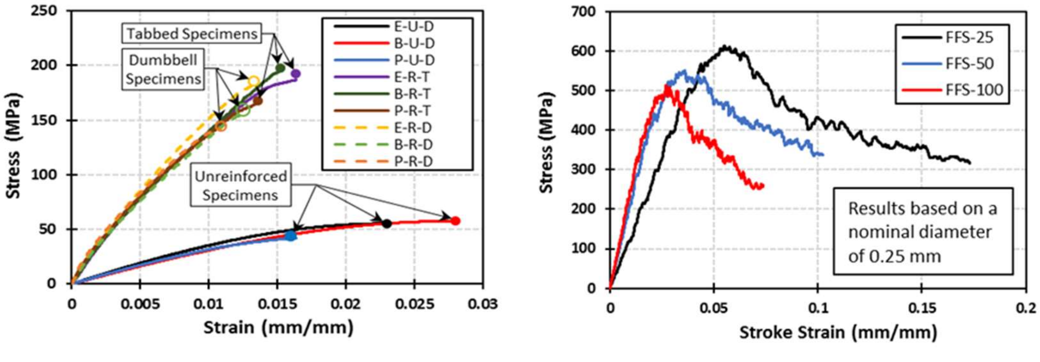

(a) (b)

Figure A-1. Stress-strain plots: (a) averages of all coupons (b) averages of fibre strands (FFS = Flax Fibre Strand, (25,50,100) = gauge length in mm).

Based on the analysis of the data, it was determined that the matrix type was not the source of the nonlinear behaviour of the flax FRPs. While it was shown that, for the dumbbell specimens, the matrix type affected the secondary modulus, it was not the cause of the reduction in modulus. It was also determined that the specimen shape was not the source of the nonlinear behaviour. Though, the specimen shape for the epoxy specimens seemed to have some effect, it was not the source of the nonlinear behaviour.

A series of flax fibre strands, as seen in Figure A-2e, were tested in uniaxial tension to determine whether the source of the nonlinear behaviour was the flax fibres. Each fibre strand in the unidirectional fabric is a group of single short flax fibres bound together. A total of 30 strands were tested: 10 tests at three different gauge lengths. The stress was calculated using a nominal strand diameter of 0.25 mm and the strain shown in Figure A-1b is based on the stroke of the test frame as a more accurate method was not available at the time. Three gauge lengths were selected to account for the fact that the single flax fibres within each strand are short. It was hypothesized that as the gauge length increased, the peak load would decrease due to the fact that at shorter gauge lengths, some fibres could span the full gauge length.

As shown in Figure A-1b, each specimen tested reached a peak stress in the range of 500-600 MPa, after which the stress reduced while the strain continued to increase. These peak stresses are in agreement with the previously reported strengths in the range of 500-900 MPa (Sparnins 2006). The reduction in strength after the peak load could be indicative that the fibres are the source of the nonlinear behaviour of the composites as this reduction in fibre strength could cause the reduction in the secondary modulus of a composite. A single factor ANOVA analysis was performed to determine whether there was a significant difference in the peak loads between the different gauge lengths. Due to the high variability of the results, the ANOVA analysis could not prove there to be any difference between the peak loads. However, looking at Figure A-1b, there is a trend showing that as the gauge length increases, the peak load decreases. To more accurately compare the data, a new set of tests will include the diameter of the flax strands and a two-way ANOVA analysis will be performed.

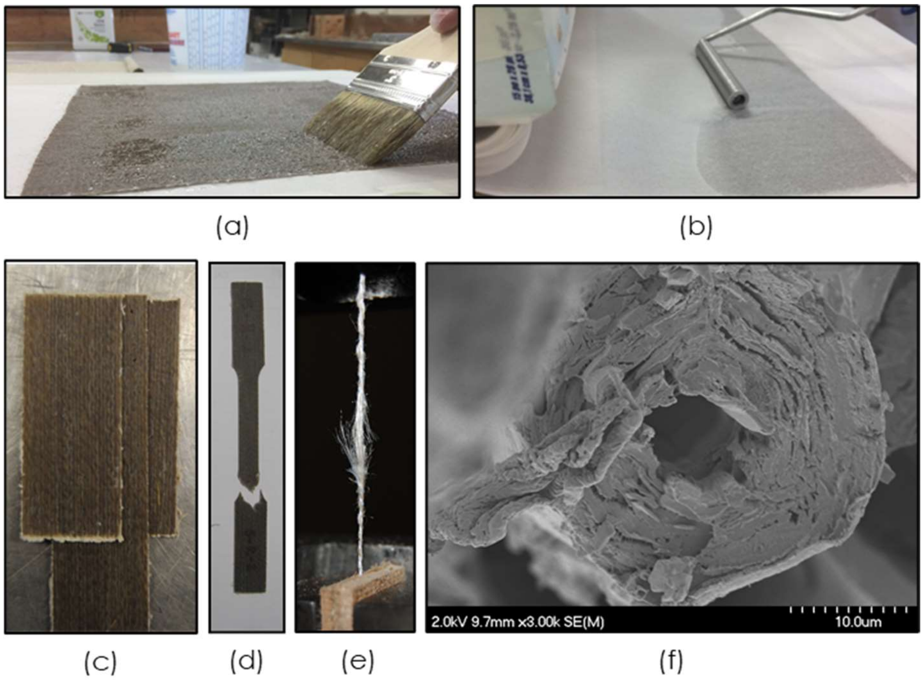

Figure A-2. Experimental procedure: (a) Applying epoxy (b) air removal (c) tabs before placement (d) tested reinforced specimen (e) tested flax fibre strand (f) SEM of tested flax FRP.

A.4. CONCLUSIONS

In this paper, a series of tensile tests was performed on flax strands, pure polymer, and composite coupons in order to identify the source of materials nonlinearity. It was verified that the mechanical behaviour of flax FRPs are nonlinear and can be simplified to an approximately bi-linear behaviour. The primary modulus of the specimens is typically in the range of 16 to 19 GPa. The secondary modulus of each specimen was approximately two thirds of the primary modulus. The nonlinear mechanical behaviour of the flax FRPs was not significantly affected by the matrix type or the specimen shape. It was determined that there is the potential that the nonlinear behaviour is caused by the fibres. This is an ongoing research project. To further this research, the following tests will be performed: more strand tests including an accurate measurement of strand diameter and strain, uniaxial tension tests of single flax fibres, and strips of dry fabric will be tested in uniaxial tension.

A.5. REFERENCES

E. Sparnins. Mechanical properties of flax fibers and their composites. *Licentiate thesis, Luleå University of Technology,* 2006.

K. Mak, A. Fam, and C. MacDougall. Flexural behavior of sandwich panels with bio-FRP skins made of flax fibers and epoxidized pine-oil resin. *Journal of Composites for Construction,* 19.6:04015005, 2015.

P. Sadeghian, D. Hristozov, and L. Wroblewski. Experimental and analytical behavior of sandwich composite beams: Comparison of natural and synthetic materials. *Journal of Sandwich Structures and Materials,* 1099636216649891, 2016.

F. Bensadoun, K.A.M. Vallons, L.B. Lessard, I. Verpoest, and A.W. Van Vuure. Fatigue behaviour assessment of flax–epoxy composites. *Composites Part A: Applied Science and Manufacturing*, 82:253-266, 2016.

ASTM. Standard test method for tensile properties of plastics. *D638,* 2014.

ASTM. Standard test method for tensile properties of polymer matrix composite materials. *D3039*, 2014.

APPENDIX B: TENSILE PROPERTIES OF SINGLE FLAX FIBRES [7]

B.1. INTRODUCTION

As environmental awareness increases across the globe, it is important that the sustainability of infrastructure is improved. One option to improve sustainability of some structures is the implementation of natural materials. One potential structural application of natural materials is the use of plant fibres, such as flax or hemp, in fibre-reinforced polymer (FRP) composites. FFRPs can be used as sustainable alternatives to synthetic FRPs, such as fibre-glass or carbon-fibre, in structural sandwich panel applications (Mak et al. 2015). These FFRP-foam sandwich panels have been studied under flexure and axial loading in recent past (Codyre et al. 2016; Betts et al. 2017a; Betts et al. 2017b).

To properly model FFRPs and their contribution to structural systems, it is necessary to fully understand their mechanical response. Numerous authors have shown that natural FRPs, including hemp FRPs and FFRPs, exhibit a nonlinear mechanical behaviour (Christian and Billington 2011; Mathura and Cree 2016; Yan et al. 2016; Mak et al. 2015). However, the cause of the nonlinearity is still unknown. The study by Betts et al. (2017c) examines the cause of this nonlinear behaviour by looking at the effect of the FFRP resin, the test specimen shape and the properties of the fibre tows. One conclusion of their study was the hypotheses that the cause of the nonlinear behaviour of FFRPs is the mechanical behaviour of the individual fibres. Therefore, the current study examines this hypothesis by testing a series of flax fibres under uniaxial tension to determine if the fibres have a nonlinear mechanical behaviour.

To complete the fibre tension tests, a load cell was designed, fabricated, and calibrated. Fibre grips were fabricated and attached to the load cell and a hydraulic

---

[7] **This appendix was published in the proceedings of the *CSCE Annual Conference 2018*:**

Betts, D., Sadeghian, P., and Fam, A. (2018). "Tensile Properties of Single Flax Fibres." *CSCE Annual Conference*, CSCE, Fredericton, NB, Canada, 1–10.

piston. Eleven fibres were extracted from bidirectional and unidirectional flax fabrics and tested in tension using the proposed test method.

B.2. PROPOSED TEST METHOD

Elementary flax fibres typically have a diameter of 10 to 20 µm and an ultimate strength of 500 to 900 MPa (Sparnins 2006). Therefore, to measure the tensile load applied to a flax fibre, a small-scale load cell (<1 N) is required. As the smallest available load cell at the university had a capacity of 100 N, a small-scale load cell was designed and fabricated. The load cell design is shown in Figure B-1.

Due to the small scale of the tests, the strain measurement was based on the test stroke. As shown in Figure B-1, the bottom fibre grip was attached to the hydraulic piston of an Instron 8501 test frame. The tests were performed at a constant displacement rate of 0.01 mm/s and the test specimens had a gauge length of 10 mm. Therefore, the strain could be calculated based on the time, displacement rate and gauge length.

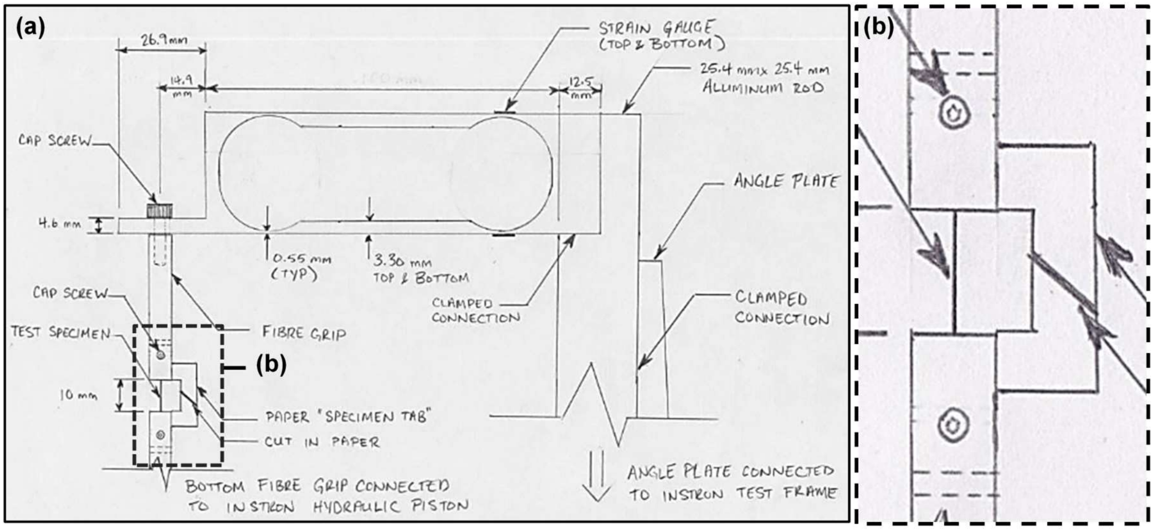

Figure B-1. Load cell design: (a) general schematic and (b) detail of fibre grips

The fibre grip was fabricated using an aluminium rod with a diameter of 10 mm. The grip design is shown in Figure B-2. Each fibre was glued to a paper tab which had been cut to the correct gauge length. The prepared fibre was then placed into the bottom grip which was closed by tightening the cap screw using an Allen Key. The bottom grip and fibre were then raised into the top grip which was tightened in the same manner. Once both grips were tightened, the bottom grip was raised to ensure that there was no tensile force on the specimen (ie. the distance between the grips was less than the gauge length of the specimen). The paper tab was then cut as shown in Figure B-1a. Finally, the bottom grip was lowered until the fibre specimen was almost taut. The test was then ready to start.

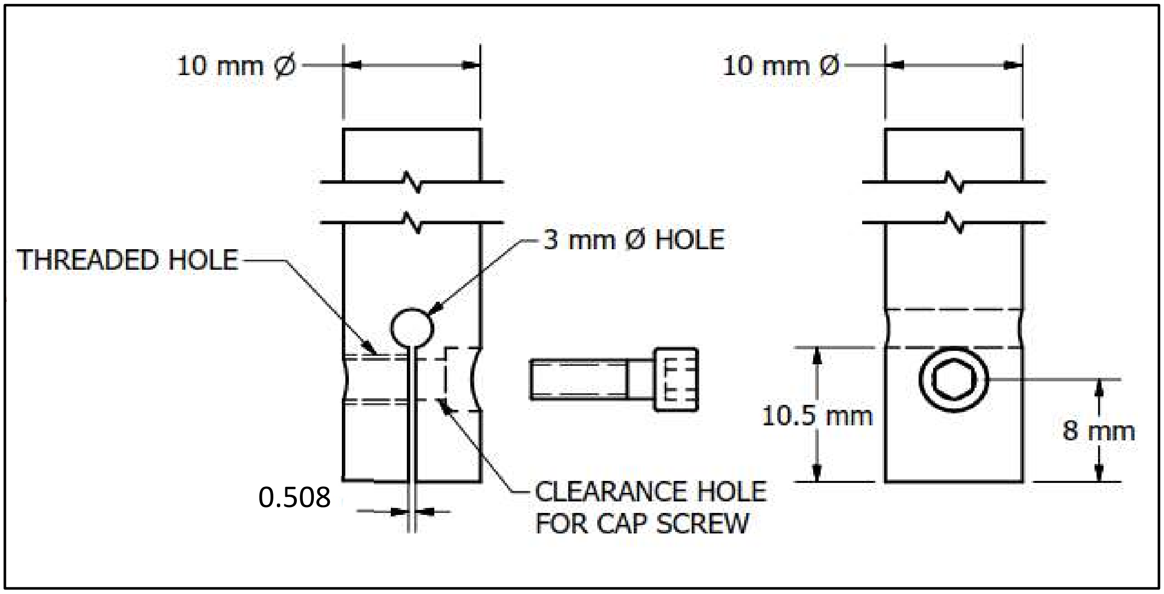

Figure B-2. Fibre grip design

The load cell was fabricated using a section of aluminium which was cut using an end mill. The output of the load cell is a strain reading from the strain gauge on the top of the load cell which was placed near the rigid clamped connection to an aluminium rod. Ten known weights were placed on the fixture to calibrate the load cell. The data calibration was completed in the scientific python package, Anaconda, as was the post-processing of the data. The masses of these know weights and the corresponding strain readings from the load cell are provided in Table B-1. Based on the values presented in Table B-1, the data was calibrated using a linear fit, as shown in Figure B-3.

Table B-1. Load cell calibration masses

Calibration Mass (g)	Cumulative Mass (g)	Load (N)	Load Cell Output (με)
0	0	0	-545
4.40	4.40	0.04316	-534
4.88	9.28	0.09104	-519
4.88	14.16	0.13891	-506
4.85	19.01	0.18649	-492
4.92	23.93	0.23475	-477
4.91	28.84	0.28292	-465
4.82	33.66	0.33020	-451
4.96	38.62	0.37886	-437
4.30	42.92	0.42105	-425
4.86	47.78	0.46872	-411

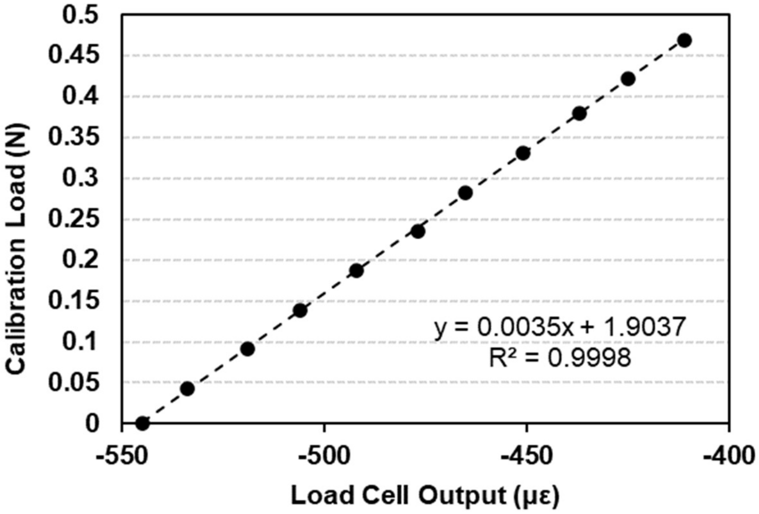

Figure B-3. Load cell calibration

The post-processing of the data was performed by a program written in the Python programming language. The program takes the test data, the specimen diameter, the gauge length and the displacement rate as preliminary inputs. It plots the raw data and prompts the user to define the range of the valid test data (i.e. eliminate the data recorded before the testing began and remove the data recorded after the specimen was broken) by providing start and end indices of the valid section of data. The program then implements a moving average filter with an N-value of 100 which improves the resolution of the data from approximately 0.02 N to approximately 0.002 N, which is an improvement by a factor of 10.

Once the data has been averaged, the program converts load to stress using the fibre diameter and time to strain using the gauge length and displacement rate. Figure B-4 shows an example of the raw data plotted by the program and the final stress-strain diagram plotted by the program.

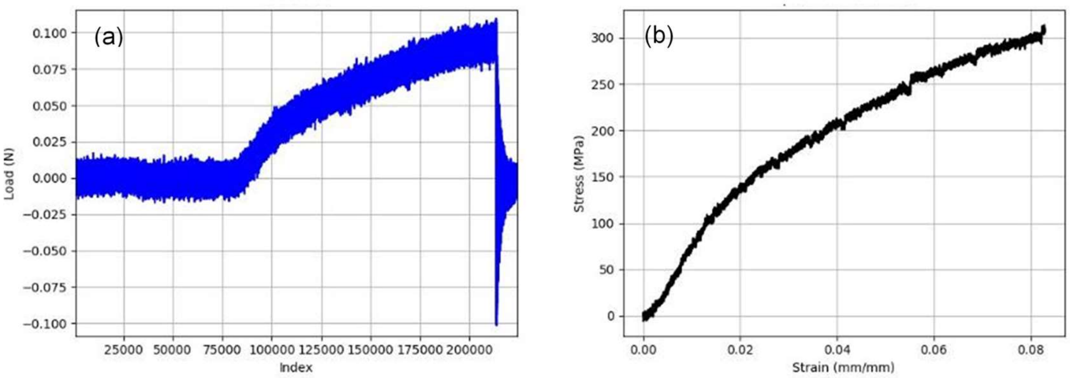

Figure B-4. Post-processing program outputs for specimen FF-5 (a) raw load data (b) stress-strain diagram

B.3. FIBRE TESTS

Thus far, eleven flax fibres have been tested in uniaxial tension as a part of this study. Each specimen had a gauge length of 10 mm and was tested at a rate of 0.01 mm/s using an Instron test frame and the load cell as described in the previous section. Nineteen more fibres will be tested as a part of this study; the full test matrix is presented in Table B-2.

Table B-2. Test matrix for tensile tests of single flax fibres

Specimen Group	Source Location	Source Details	Number of Specimens	Number of Specimens Tested
FF-NS	Nova Scotia	Farmed fibre	10	N/A
FF-BD	United Kingdom	Extracted from 2x2 twill flax fabric	10	5
FF-UD	United Kingdom	Extracted from unidirectional flax fabric	10	6

Figure B-5 shows a picture of the tensile test set-up used for the tests of the first eleven specimens. The specimens were carefully extracted from a 2x2 twill flax fabric using tweezers and glued to paper specimen tabs which were cut to the gauge length of 10 mm. The specimen was then placed in the fibre grips and fixed in place by tightening the cap screws. Once the fibre and paper tab were in place the paper tab was cut (as seen in Figure B-5c) and the test was ready to start.

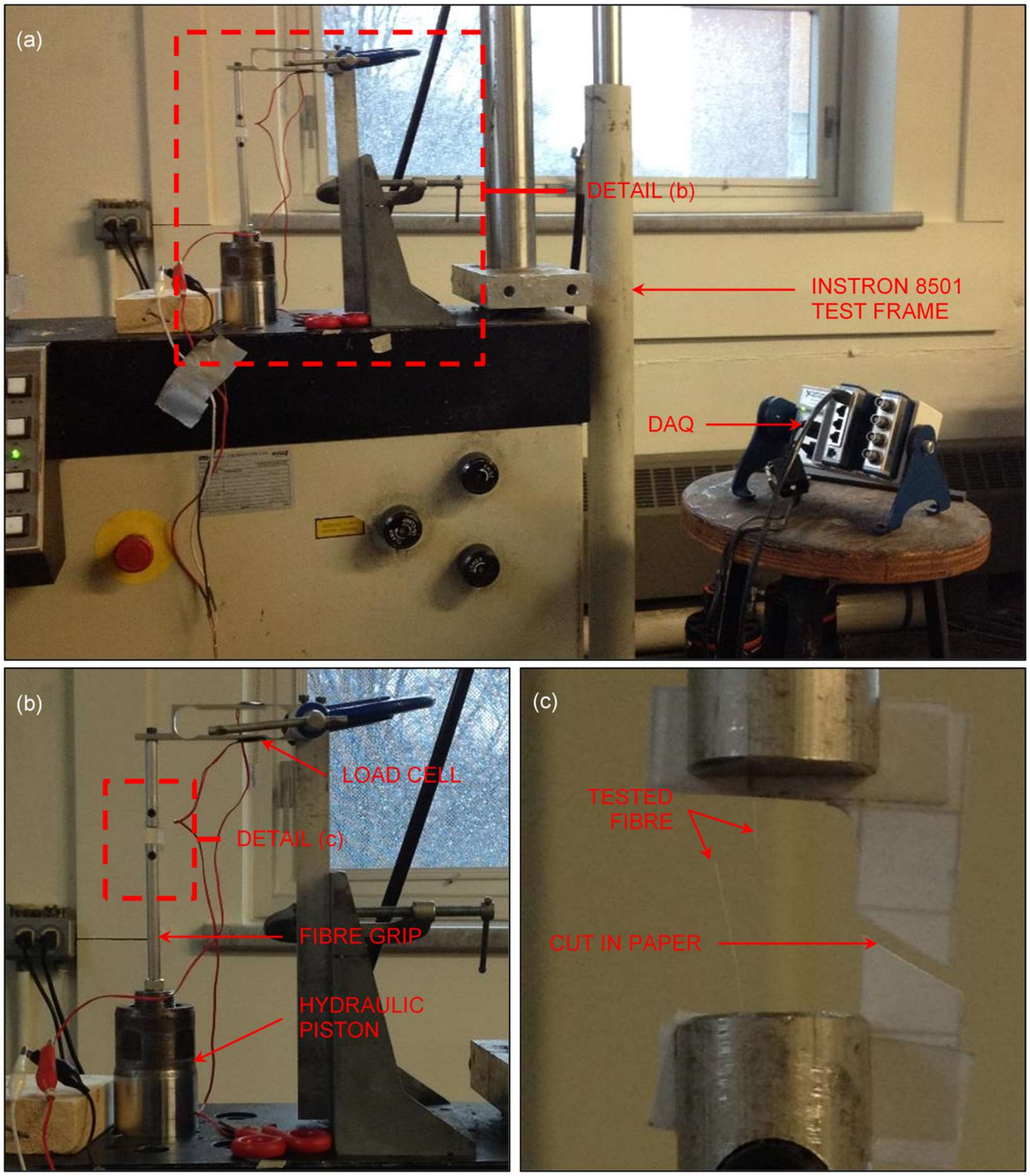

Figure B-5. Test set-up (a) general test set-up; (b) close-up; and (c) detail of a tested fibre

B.4. RESULTS AND DISCUSSIONS

The results of the tested specimens are presented in Table B-3. Figure B-6 shows the stress-strain plots of the tested specimens. The tested fibres were not observed under a microscope to obtain an accurate measurement of diameter and therefore the stress calculations were based on a nominal fibre diameter of 19.93 µm. This value was determined by taking the average of the fibre diameters from a previous set of preliminary tests. In these previous tests, three photos along the length of each fibre were captured using a microscope. Then the diameter of each fibre was measured at six points along the fibre length using an image processing software. Based on scanning electron microscope (SEM) imagery as shown in Figure B-7, it is known that the fibres have a hollow cross section. However, for the calculation of stress in this study, this was neglected; that is, the gross cross-sectional area was used for the stress calculations. Upon examination of the data, it was determined that specimen FF-BD-3 experienced pre-mature failure and therefore, it was not used when calculating the average values shown in Table B-3 and Figure B-6. This per-mature failure could have been caused from specimen handling or been due to a defect in the fibre prior to extraction from the flax fabric.

Table B-3. Fibre test results

Specimen	Primary Modulus (GPa)	Secondary Modulus (GPa)	Secondary to Primary Modulus (%)	Tensile Strength (MPa)	Ultimate Strain (mm/mm)
FF-BD-1	7.67	4.43	58	352	0.0622
FF-BD-2	8.16	2.15	26	265	0.0939
FF-BD-3 *	4.69	N/A	N/A	182	0.0389
FF-BD-4	6.67	1.93	29	295	0.0868
FF-BD-5	8.69	2.45	28	314	0.0829
Average	7.80	2.74	35	307	0.0815
St. Dev.	0.86	1.15	15	36	0.0136
FF-UD-1	6.82	2.76	40	316	0.0736
FF-UD-2	10.95	2.47	23	286	0.0646
FF-UD-3	7.71	3.54	46	379	0.0714
FF-UD-4	11.88	2.91	24	333	0.0691
FF-UD-5	8.33	2.99	36	313	0.0607
FF-UD-6	9.70	3.46	36	385	0.0837
Average	9.23	3.02	34	335	0.0705
St. Dev.	1.96	0.41	9	39	0.0080

** Presumed premature failure; not included in the average and standard deviation (St. Dev.) calculations*

Table B-3 shows that the mechanical properties of the FF-UD and FF-BD fibres are similar and both show that the secondary modulus is approximately one third of the primary fibre modulus. Interestingly, the paper by Betts et al. (2017c) showed that the secondary modulus of FFRPs is approximately two thirds of the primary modulus. Upon examination of Table B-3, it seems that the primary modulus, secondary modulus, and ultimate strength of the unidirectional fibres are higher than the bidirectional fibres; however, an analysis of variance (ANOVA) with a confidence level of 95% shows that the difference between the groups is statistically negligible.

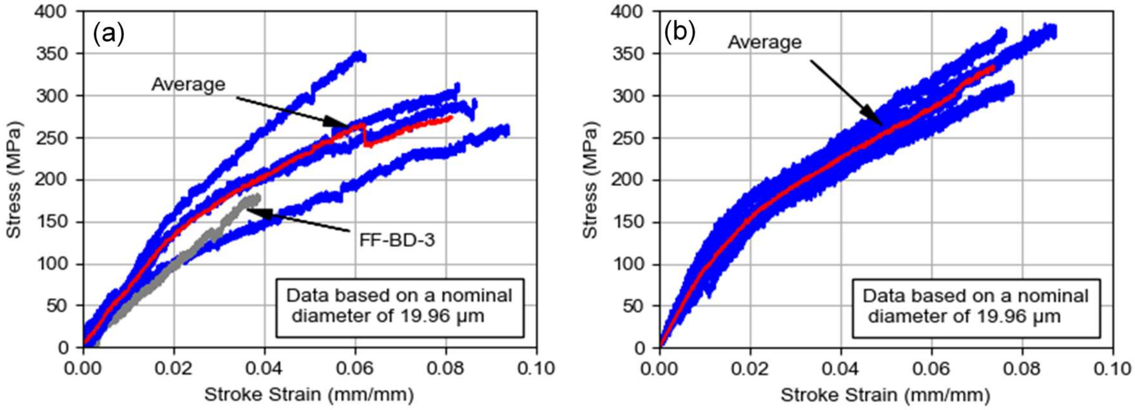

Figure B-6. Stress-strain plots of tested flax fibres (a) FF-BD specimens (FF-BD-3 not included in the average); and (b) FF-UD specimens

B.4.1. Nonlinear Behaviour of Flax Fibres

As shown in Figure B-6, the tested specimens (excluding FF-BD-3) all showed a nonlinear mechanical response to the tensile loading. This result is evidence that the nonlinear behaviour of their composites is potentially caused by the nonlinear nature of the individual fibres. Future studies will include an in-depth analysis of the effect of the fibre nonlinearity on FFRP nonlinearity as well as determining the cause of the fibre nonlinearity.

Per Sparnins (2006), elementary flax fibres are made up of smaller meso fibrils and micro fibrils. This was also observed by the authors as shown in SEM photograph of a flax fibre shown in Figure B-7. The current hypothesis of fibre nonlinearity is that until the transition point, the meso and micro fibrils work together and provide the primary fibre stiffness. At that point, the micro fibrils fail and the overall stiffness of the fibre is reduced until ultimate failure of the meso fibrils.

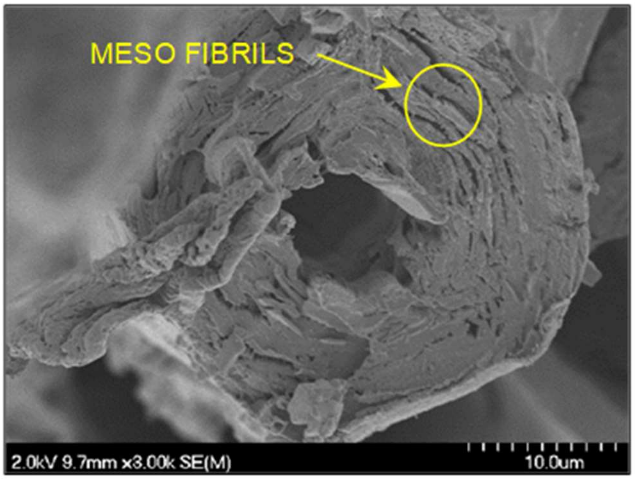

Figure B-7. SEM photograph of elementary flax fibre

B.4.2. Effect of Flax Fibre Behaviour on Composite Behaviour

The unidirectional fibres (ie. FF-UD specimens) were extracted from the same fabric used in the previous study by (Betts et al. 2017c). Figure B-8 presents a plot comparing the results of the fibres, the matrix, and the composite. As discussed later, the strain data provided by the tests is erroneously high. Therefore, to better compare the fibres with the matrix and composite, the fibre strain data was calibrated using data from the study by Betts et al. (2017c). Figure B-8a shows the fibre data calibrated using Rule of Mixtures using the simplifying assumption that the composite had no voids. Figure B-8b shows the fibre data calibrated such that the rupture strain of the fibre matches the composite rupture strain. To accurately compare the fibre, matrix and composite, a more accurate measurement of strain data is required.

Additionally, based on the data by Betts et al. (2017c), the maximum stress estimation of the fibres according to rule of mixtures would be 273 MPa. As shown in Table 3, the unidirectional fibre tests showed a maximum stress of 335 MPa. Because the FFRPs exhibited a nonlinear mechanical behaviour, the rule of mixtures may not accurately predict the behaviour of the fibres which could be the cause of this discrepancy.

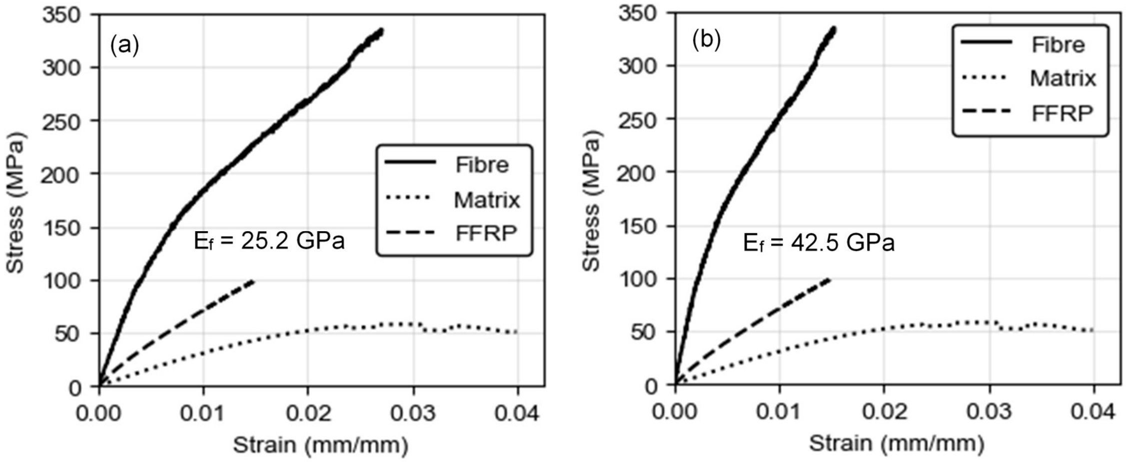

Figure B-8. Effect of flax fibres on composite behaviour (a) strain data adjusted to Rule of Mixtures (b) strain data adjusted to composite rupture

B.4.2. Sources of Error

The young's modulus of flax fibres is typically between 50 GPa and 70 GPa (Sparnins 2006), therefore upon examination the data presented in Table B-3, it is apparent that the modulus values determined through testing are low. This is most likely due to erroneously high strain readings, which could be explained by several sources of error, including:

- load cell deflection
- incorrect gauge length estimation, which is affected by:
    - fibre twist (or "waviness")
    - fibre placement on the paper tabs
- fibre slippage
- the use of a nominal fibre diameter
- neglecting the deduction of cross-sectional area due to the fibre hollowness.
- fibre fragility (potential to damage fibre before testing)

Some of these sources of error can be mitigated by implementing additional protocols into the test procedure. These protocols include: using an LVDT to measure the deflection of the load cell, using a laser extensometer to measure displacement between fibre grips and measuring the individual fibre diameters before testing.

B.5. CONCLUSIONS

As a part of this study thirty fibre specimens will be tested in uniaxial tension using a load cell that was designed and fabricated by the authors. Thus far, eleven of the flax fibre specimens have been tested. The results of the tests show that the fibres extracted from the bidirectional fabric have an ultimate tensile strength of 307 MPa and the fibres extracted from the unidirectional fabric have an ultimate tensile strength of 335 MPa. The rule of mixtures predicts an ultimate strength of 273 MPa, however, this discrepancy could be caused by the nonlinear nature of flax fibres and FFRPs. Fibres extracted from both sources exhibit a nonlinear mechanical response, specifically a bilinear response where the secondary modulus is approximately one third of the primary modulus. This supports the hypothesis that the nonlinear behaviour of flax fibre-reinforced polymers is caused by the behaviour of the individual fibres. Currently, the strain estimation is erroneously high which affects the calculation of the young's modulus. The implementation of additional protocols in the test procedure will help mitigate the sources of error. This study is a part of ongoing research and future studies include: testing of more fibres from different sources, determining cause of fibres' nonlinear behaviour and studying the effect of growth location.

B.6. ACKNOWLEDGEMENTS

The authors would like to thank Brian Kennedy and Jesse Keane for their assistance in the lab and acknowledge the use of the fibre grip design by John Noddin and Kevin Borgel. The authors would also like to thank Bioindustrial Innovation Canada (BIC), Queen's University and Dalhousie University for their in-kind financial support.

B.7. REFERENCES

Betts, D., Sadeghian, P., and Fam, A. (2017a). “Cumulative impact energy absorption of sandwich panels with foam cores and flax FRP facues.” 17th International Conference on Non-Conventional Materials and Technologies, 1–10.

Betts, D., Sadeghian, P., and Fam, A. (2017b). “Structural Behaviour of Sandwich Panels Constructed of Foam Cores and Flax FRP Facings.” CSCE Annual Conference, Vancouver, BC, Canada, 1–10.

Betts, D., Sadeghian, P., and Fam, A. (2017c). “Tensile properties of flax frp composites.” Asia Pacific Conference on FRP in Structures, International Institute for FRP in Construction, Singapore.

Christian, S. J., and Billington, S. L. (2011). “Mechanical response of PHB- and cellulose acetate natural fiber-reinforced composites for construction applications.” Composites Part B, Elsevier Ltd, 42(7), 1920–1928.

Codyre, L., Mak, K., and Fam, A. (2016). “Flexural and axial behaviour of sandwich panels with bio-based flax fibre-reinforced polymer skins and various foam core densities.” Journal of Sandwich Structures and Materials, 1–22.

Mak, K., Fam, A., and Macdougall, C. (2015). “Flexural Behavior of Sandwich Panels with Bio-FRP Skins Made of Flax Fibers and Epoxidized Pine-Oil Resin.” Journal of Composites for Construction, 19(2003), 1–13.

Mathura, N., and Cree, D. (2016). “Characterization and mechanical property of Trinidad coir fibers.” Journal of Applied Polymer Science, 133(29), 1–9.

Sparnins, E. (2006). “Mechanical properties of flax fibers and their composites.” Lulea University of Technology.

Yan, L., Kasal, B., and Huang, L. (2016). “A review of recent research on the use of cellulosic fibres, their fibre fabric reinforced cementitious, geo-polymer and polymer composites in civil engineering.” Composites Part B: Engineering, Elsevier Ltd, 92(April), 94–132.

APPENDIX C: PYTHON SCRIPT FOR THE NONLINEAR INCREMENTAL ITERATIVE MODEL PRESENTED IN CHAPTER 3

```
# -*- coding: utf-8 -*-
"""
                     Results of Ramped Impact Tests

                                 and

             Modeling of Impact using Energy Balance Method

"""



""" ===================== START-UP ======================= """

from pandas import read_csv
from pylab import (linspace,zeros,plot,xlabel,ylabel,xlim,ylim,grid,
legend,figure,scatter,savefig,minorticks_on,column_stack,ceil,bar,xticks,mean,
roots,isreal,axhline)
import mypy
from sympy.solvers import solve
from sympy import Symbol

mypy.dillplotparamspres()
color1 = [0.95,0.95,0.95]
color2 = [0.15,0.15,0.15]

""" ====================== INPUTS ======================== """

P1FLC32 = read_csv("Results - P-1FL-C32-1.txt",sep="\t",header=0)
P1FLC64 = read_csv("Results - P-1FL-C64-1.txt",sep="\t",header=0)
P1FLC96 = read_csv("Results - P-1FL-C96-1.txt",sep="\t",header=0)

P2FLC32 = read_csv("Results - P-2FL-C32-1.txt",sep="\t",header=0)
P2FLC64 = read_csv("Results - P-2FL-C64-1.txt",sep="\t",header=0)
P2FLC96 = read_csv("Results - P-2FL-C96-1.txt",sep="\t",header=0)

P3FLC32 = read_csv("Results - P-3FL-C32-1.txt",sep="\t",header=0)
P3FLC64 = read_csv("Results - P-3FL-C64-1.txt",sep="\t",header=0)
P3FLC96 = read_csv("Results - P-3FL-C96-1.txt",sep="\t",header=0)


#============================================================#
#                                                            #
# Files are formatted such that the columns are:             #
#                                                            #
#   0:    Drop Height (mm)                                   #
#   1:    Calculated Velocity (m/s)                          #
#   2:    Test Velocity (m/s)                                #
#   3:    Potential Energy (Nm)                              #
#   4:    Stiffness (N/mm)                                   #
#   5:    Damped Period (s)                                  #
#   6:    Damping Coefficient (%)                            #
#   7:    Displacement (mm)                                  #
#   8:    Acceleration of Drop Weight (m/s**2)               #
#   9:    Maximum Strain in Bottom Face (mm/mm)              #
#  10:    Minimum Strain in Top Face (mm/mm)                 #
#  11:    Shear Modulus of Core (MPa)                        #
#  12:    Measured Specimen Widths (mm)                      #
#  13:    Measured Specimen Thicknesses (mm)                 #
```

```
#                                                            #
#============================================================#

c = 75        # core thickness in millimeters
Efu = 5500    # Ultimate Secant modulus in MPa of face material
m = 10.413    # drop weight mass in kg
L = 1117      # test span in mm

Efo = 7510    # Initial Modulus in MPa of Face Material
su = 45.4     # Ultimate Strength of Face Material
eu = 0.0083   # Ultimate Strain of Face Material

""" ================== USER FUNCTIONS ================== """

def axmax(max_data):

    if max_data <= 50:
        max_data = ceil(max_data/10)*10.0
    elif max_data <= 100:
        max_data = ceil(max_data/20)*20.0
    elif max_data <= 150:
        max_data = ceil(max_data/25)*25.0
    elif max_data <= 200:
        max_data = ceil(max_data/50)*50.0
    else:
        max_data = ceil(max_data/100)*100.0

    return max_data


def plotmodel(A,Efu,Efo,su,eu,m,L,c,f1,f2,nom,p_triant):

    # INPUTS
    b = A['width (mm)'].mean()
    h_s = A['thk (mm)'].mean()
    t = (h_s-c)/2
    d = c + t

    # CORE MATERIAL PROPERTIES
    if A['Core'].sum() == 32:
        Ec = (2.301+3.19)/2
        Gco = 2.067
        tcu = 0.172
        ycu = 0.25
        #k = 98
    elif A['Core'].sum() == 64:
        Ec = (9.646+10.748)/2
        Gco = 5.856
        tcu = 0.379
        ycu = 0.25
        #k = 252
    elif A['Core'].sum() == 96:
        Ec = (20.29+15.709)/2
        Gco = 7.234
        tcu = 0.585
        ycu = 0.25
        #k = 702

    #k = k*(b/1000)
    #If = (b*(t**3))/12

    # GET SANDWICH PANEL PROPERTIES
    AA = (b*d**2)/c
    G1 = Gco
    D1 = mypy.flexrigid(Efu,Ec,b,c,d,t)
    #beta = mypy.beta(k,Ef,If)


    # LOOP SET-UP
    h = linspace(0,A['Drop Height'].max(),int(A['Drop Height'].max()/10))
    load_model1=zeros(len(h))
```

```
    ep_model1=zeros(len(h))
    en_model1=zeros(len(h))
    ta=zeros(len(h))

    # DEVELOP MODEL STARTING DATA
    for i in range(0,len(h)):

        AG1 = AA*G1

        load_model1[i] = mypy.ultload(D1,AG1,m,h[i],L)
        ep_model1[i],en_model1[i] = mypy.ultstrains(load_model1[i],L,t,d,b,Efu)

        ta[i] = load_model1[i]/(2*AA)

    # LOOP SET-UP
    delta_model=zeros(len(h))
    load_model=zeros(len(h))
    energy_model=zeros(len(h))
    ep_model=zeros(len(h))
    en_model=zeros(len(h))
    s_perc=zeros(len(h))
    b_perc=zeros(len(h))
    tau_model=zeros(len(h))
    count = 0
    # DEVELOP MODEL DATA
    for i in range(1,len(h)):

        e = ep_model1[i]
        tc = ta[i]
        loop_chk = False

        while loop_chk == False:


            x = Symbol('x')
            s = float(max(solve((x**2)*(eu-su/Efo)/(su**2) + (x/Efo) - e, x)))

            print(s)

            Ef = s/e
            D = mypy.flexrigid(Ef,Ec,b,c,d,t)

            C1 = (2/(ycu**3))*(0.55*Gco*ycu-tcu)
            C2 = (1/(ycu**2))*(3*tcu-2.1*Gco*ycu)
            C3 = Gco
            C4 = -tc

            ycroots = roots([C1,C2,C3,C4])

            for k in range(0,len(ycroots)):

                if isreal(ycroots[k]) and ycroots[k] >= 0 and ycroots[k] <= ycu:
                    yc = ycroots[k].real

            G = tc/yc
            AG = AA*G

            load_model[i] = mypy.ultload(D,AG,m,h[i],L)
            ep_model[i],en_model[i] = mypy.ultstrains(load_model[i],L,t,d,b,Ef)
            tau_model[i] = load_model[i]/(2*AA)


            if e / ep_model[i] < 1.001 and e / ep_model[i] > 0.999 and tc / tau_model[i]
< 1.001 and t / tau_model[i] > 0.999:
                loop_chk = True

            e = ep_model[i]
            tc = tau_model[i]

        count = count + 1
```

```
        figure(40)
        plot([0,e],[0,s])
        figure(41)
        plot([0,yc],[0,tc])
        energy_model[i] = m*9.81*h[i]/1000
        delta_model[i],s_perc[i],b_perc[i] = mypy.ultdeflect(D,AG,m,h[i],L)
        load_model[i] = mypy.ultload(D,AG,m,h[i],L)
        ep_model[i],en_model[i] = mypy.ultstrains(load_model[i],L,t,d,b,Ef)

    # GET ACTUAL MAX POINTS
    max_y = max(max(delta_model[:]),max(A['delta (mm)']))
    max_x = max(energy_model[:])

    # SET MAXIMUM LIMITS FOR PLOTS
    max_y = axmax(max_y)
    max_x = axmax(max_x)

    if check == 'y':
        # PLOT DISPLACEMENT VS. ENERGY MODEL AND TEST RESULTS
        figure(f1,[2.25,2],dpi=300)
        scatter(A['PE (N-m)'],A['delta (mm)'],color=color1,marker='o',facecolors='none')
        plot(energy_model,delta_model,color=color1)
        xlim(0,max_x)
        ylim(0,max_y+5)
        grid(False)
        xlabel("Impact Energy, J")
        minorticks_on()
        ylabel("Displacement, mm")
        #legend(["Model",nom],edgecolor='k',facecolor='white',fancybox=False)

        savefig("Displ-Energy - %s.tiff"%nom,bbox_inches='tight',facecolor=color2)


        # PLOT STRAIN VS. ENERGY MODEL
        figure(f2,[2.25,2],dpi=300)
        scatter(A['PE (N-m)'],A['strainmax
(mm/mm)'],color=color1,marker='o',facecolors='none')
        scatter(A['PE (N-m)'],A['strainmin
(mm/mm)'],color=color1,marker='o',facecolors='none')
        plot(energy_model,ep_model,color=color1)
        plot(energy_model,en_model,color=color1)
        grid(False)
        xlabel("Impact Energy, J")
        ylabel("Strain, mm/mm")
        xlim(0)
        minorticks_on()

        savefig("Strains-Energy - %s.tiff"%nom,bbox_inches='tight',facecolor=color2)


    # SAVE RESULTS OF DEFLECTION MODEL
    deltamodel = column_stack((energy_model,delta_model))
    strainmodel = column_stack((energy_model,ep_model,en_model))

    # MODEL PREDICTION OF MAXIMUM IMPACT ENERGY
    en_max_test = max(A['PE (N-m)'])
    en_max_model = ((p_triant**2)/2)*(((L**3)/(48*D))+(L/(4*AG)))/1000

    energies = [en_max_test,en_max_model]

    return deltamodel,energies,b_perc,s_perc,strainmodel


def comparemodels(fnum,A,B,C,a,b,c,nom,fc):

    figure(fnum,[2.75,2.25],dpi=300)
    scatter(A['PE (N-m)'],A['delta (mm)'],color='k',marker='^',s=7.5,facecolors='none')
    scatter(B['PE (N-m)'],B['delta (mm)'],color='C0',marker='s',s=7.5,facecolors='none')
    scatter(C['PE (N-m)'],C['delta (mm)'],color='C3',marker='o',s=7.5,facecolors='none')
    plot(a[:,0],a[:,1],'k',linestyle='dashed',alpha=0.75)
    plot(b[:,0],b[:,1],'C0',linestyle='dashed',alpha=0.75)
```

```
    plot(c[:,0],c[:,1],'C3',linestyle='dashed',alpha=0.75)
    xlim(0)
    ylim(0)
    minorticks_on()
    xlabel("Energy, J")
    ylabel("Displacement, mm")


    if fc == 'f':
        savefig("Effect of Facing Thickness - %s.tiff"%nom,bbox_inches='tight')
    elif fc =='c':
        savefig("Effect of Core Denisity - %s.tiff"%nom,bbox_inches='tight')


    return



""" ================== MAIN FUNCTION =================== """

# CHECK IF USER WANTS TO SEE ALL PLOTS
check = raw_input("Do you want to plot each model separately? (y/n): ")

m132,e132,b132,s132,epn132 = plotmodel(P1FLC32,Efu,Efo,su,eu,m,L,c,0,1,'1FL-C32',1310)
m164,e164,b164,s164,epn164 = plotmodel(P1FLC64,Efu,Efo,su,eu,m,L,c,2,3,'1FL-C64',2420)
m196,e196,b196,s196,epn196 = plotmodel(P1FLC96,Efu,Efo,su,eu,m,L,c,4,5,'1FL-C96',2420)

m232,e232,b232,s232,epn232 = plotmodel(P2FLC32,Efu,Efo,su,eu,m,L,c,6,7,'2FL-C32',2620)
m264,e264,b264,s264,epn264 = plotmodel(P2FLC64,Efu,Efo,su,eu,m,L,c,8,9,'2FL-C64',4830)
m296,e296,b296,s296,epn296 = plotmodel(P2FLC96,Efu,Efo,su,eu,m,L,c,10,11,'2FL-C96',4830)

m332,e332,b332,s332,epn332 = plotmodel(P3FLC32,Efu,Efo,su,eu,m,L,c,12,13,'3FL-C32',3270)
m364,e364,b364,s364,epn364 = plotmodel(P3FLC64,Efu,Efo,su,eu,m,L,c,14,15,'3FL-C64',7250)
m396,e396,b396,s396,epn396 = plotmodel(P3FLC96,Efu,Efo,su,eu,m,L,c,16,17,'3FL-C96',7250)


# CHECK IF USER WANTS TO COMPARE DATA
compare = raw_input("Do you want to see the effect of facing/core? (y/n): ")
if compare != 'y' and compare != 'n':
    compare = raw_input("Please choose 'y' or 'n': ")

# COMPARE DATA
if compare == 'y':

    # CHECK IF USER WANTS TO SEE EFFECT OF FACING OR CORE
    which = raw_input("Do you want to see effect of facing (f) or core (c)? (f/c): ")
    if which != 'f' and which != 'c':
        which = raw_input("Please choose 'f' or 'c': ")

    if which == 'f':

        comparemodels(18,P1FLC32,P2FLC32,P3FLC32,m132,m232,m332,'C32',which)
        comparemodels(19,P1FLC64,P2FLC64,P3FLC64,m164,m264,m364,'C64',which)
        comparemodels(20,P1FLC96,P2FLC96,P3FLC96,m196,m296,m396,'C96',which)

    elif which == 'c':

        comparemodels(18,P1FLC32,P1FLC64,P1FLC96,m132,m164,m196,'1FL',which)
        comparemodels(19,P2FLC32,P2FLC64,P2FLC96,m232,m264,m296,'2FL',which)
        comparemodels(20,P3FLC32,P3FLC64,P3FLC96,m332,m364,m396,'3FL',which)


# PLOT ENERGIES TEST AND MODEL

tests_E = [e132[0],e164[0],e196[0],e232[0],e264[0],e296[0],e332[0],e364[0],e396[0]]
models_E = [e132[1],e164[1],e196[1],e232[1],e264[1],e296[1],e332[1],e364[1],e396[1]]

xvals1 = [1,3,5,7,9,11,13,15,17]
width = 0.8

xvals2 = zeros(len(xvals1))
```

```
for i in range(0,len(xvals1)):
    xvals2[i] = xvals1[i] + width

figure(21,[7,4],dpi=300)
bar(xvals1,tests_E,align='edge',width=width,tick_label=['1FL-C32','1FL-C64','1FL-
C96','2FL-C32','2FL-C64','2FL-C96','3FL-C32','3FL-C64','3FL-C96'],color='k')
bar(xvals2,models_E,align='edge',width=width,tick_label=['1FL-C32','1FL-C64','1FL-
C96','2FL-C32','2FL-C64','2FL-C96','3FL-C32','3FL-C64','3FL-
C96'],color='grey',hatch='///')
ylabel("Energy, J")
ylim(0,300)
legend(['Test','Model'],facecolor='white',edgecolor='k',fancybox=False)
savefig("Energy - Model vs Tests.tiff",bbox_inches='tight')



# PLOT PERCENT OF DEFLECTION MODEL

xvals3 = [1,2,3,4,5,6,7,8,9]
width1 = 0.9
b_perc =
[mean(b132[1:]),mean(b164[1:]),mean(b196[1:]),mean(b232[1:]),mean(b264[1:]),mean(b296[1:]
),mean(b332[1:]),mean(b364[1:]),mean(b396[1:])]
s_perc =
[mean(s132[1:]),mean(s164[1:]),mean(s196[1:]),mean(s232[1:]),mean(s264[1:]),mean(s296[1:]
),mean(s332[1:]),mean(s364[1:]),mean(s396[1:])]
bars = [100,100,100,100,100,100,100,100,100]

figure(22,[3.5,2])
bar(xvals3,bars,width=width1,tick_label=['1FL-C32','1FL-C64','1FL-C96','2FL-C32','2FL-
C64','2FL-C96','3FL-C32','3FL-C64','3FL-C96'],color='k',alpha = 1,edgecolor='k')
bar(xvals3,s_perc,width=width1,tick_label=['1FL-C32','1FL-C64','1FL-C96','2FL-C32','2FL-
C64','2FL-C96','3FL-C32','3FL-C64','3FL-C96'],color='white',alpha =
1,edgecolor='k',hatch='///')
grid(False)
ylabel("Deflection Contribution, %")
legend(["Bending         ","Shear"],facecolor="white",edgecolor="k",bbox_to_anchor=(0.86,
-0.35),ncol=2)
ylim(0,110)
xlim(0)
xticks(rotation=90)

savefig("Deflection Contribution-Energy.tiff",bbox_inches='tight',dpi=450)





# ========================= DATA PLOTS ========================= #


# DEFLECTION DATA #

# PLOT DEFLECTIONS OF C32

figure(23,[2.45,2.15],dpi=600)
plot(P3FLC32['PE (N-m)'],P3FLC32['delta (mm)'],color='k',marker='s',ms=3)
plot(P2FLC32['PE (N-m)'],P2FLC32['delta (mm)'],color='C0',marker='o',ms=3)
plot(P1FLC32['PE (N-m)'],P1FLC32['delta (mm)'],color='C3',marker='^',ms=3)
xlim(0)
ylim(0,100)
minorticks_on()
xlabel("Energy, J")
ylabel("Deflection, mm")

savefig("C32 - Deflection.tiff",bbox_inches='tight')

# PLOT DEFLECTIONS OF C64

figure(24,[2.45,2.15],dpi=600)
plot(P3FLC64['PE (N-m)'],P3FLC64['delta (mm)'],color='k',marker='s',ms=3)
```

```
plot(P2FLC64['PE (N-m)'],P2FLC64['delta (mm)'],color='C0',marker='o',ms=3)
plot(P1FLC64['PE (N-m)'],P1FLC64['delta (mm)'],color='C3',marker='^',ms=3)
xlim(0)
ylim(0,100)
minorticks_on()
xlabel("Energy, J")
ylabel("Deflection, mm")

savefig("C64 - Deflection.tiff",bbox_inches='tight')


# PLOT DEFLECTIONS OF C96

figure(25,[2.45,2.15],dpi=600)
plot(P3FLC96['PE (N-m)'],P3FLC96['delta (mm)'],color='k',marker='s',ms=3)
plot(P2FLC96['PE (N-m)'],P2FLC96['delta (mm)'],color='C0',marker='o',ms=3)
plot(P1FLC96['PE (N-m)'],P1FLC96['delta (mm)'],color='C3',marker='^',ms=3)
xlim(0)
ylim(0,100)
minorticks_on()
xlabel("Energy, J")
ylabel("Deflection, mm")

savefig("C96 - Deflection.tiff",bbox_inches='tight')



# STIFFNESS #

def pltaves(ins,fnum,colour):

    ave = mean(ins['K (N/mm)'])
    aves = [ave,ave]
    en = [min(ins['PE (N-m)']),max(ins['PE (N-m)'])]

    figure(fnum)
    plot(en,aves,colour)

    return aves

# PLOT STIFFNESS OF C32
figure(26,[2.45,2.15],dpi=600)
scatter(P3FLC32['PE (N-m)'],P3FLC32['K (N/mm)'],color='k',marker='s',s=10)
scatter(P2FLC32['PE (N-m)'],P2FLC32['K (N/mm)'],color='C0',marker='o',s=10)
scatter(P1FLC32['PE (N-m)'],P1FLC32['K (N/mm)'],color='C3',marker='^',s=10)
xlim(0)
ylim(0,300)
minorticks_on()
xlabel("Energy, J")
ylabel("Stiffness, N/mm")

pltaves(P3FLC32,26,'k')
pltaves(P2FLC32,26,'C0')
pltaves(P1FLC32,26,'C3')

savefig("C32 - Stiffness.tiff",bbox_inches='tight')


# PLOT Stiffness OF C64

figure(27,[2.45,2.15],dpi=600)
scatter(P3FLC64['PE (N-m)'],P3FLC64['K (N/mm)'],color='k',marker='s',s=10)
scatter(P2FLC64['PE (N-m)'],P2FLC64['K (N/mm)'],color='C0',marker='o',s=10)
scatter(P1FLC64['PE (N-m)'],P1FLC64['K (N/mm)'],color='C3',marker='^',s=10)
xlim(0)
ylim(0,300)
minorticks_on()
xlabel("Energy, J")
ylabel("Stiffness, N/mm")

pltaves(P3FLC64,27,'k')
```

```
pltaves(P2FLC64,27,'C0')
pltaves(P1FLC64.head(3),27,'C3')

savefig("C64 - Stiffness.tiff",bbox_inches='tight')


# PLOT Stiffness OF C96

figure(28,[2.45,2.15],dpi=600)
scatter(P3FLC96['PE (N-m)'],P3FLC96['K (N/mm)'],color='k',marker='s',s=10)
scatter(P2FLC96['PE (N-m)'],P2FLC96['K (N/mm)'],color='C0',marker='o',s=10)
scatter(P1FLC96['PE (N-m)'],P1FLC96['K (N/mm)'],color='C3',marker='^',s=10)
xlim(0)
ylim(0,300)
minorticks_on()
xlabel("Energy, J")
ylabel("Stiffness, N/mm")

pltaves(P3FLC96,28,'k')
pltaves(P2FLC96,28,'C0')
pltaves(P1FLC96,28,'C3')

savefig("C96 - Stiffness.tiff",bbox_inches='tight')





# DAMPING COEFFICIENT #

# PLOT DAMPING COEFFICIENT OF C32

figure(29,[2.45,2.15],dpi=600)
scatter(P3FLC32['PE (N-m)'],P3FLC32['xi (%)'],color='k',marker='s',s=10)
scatter(P2FLC32['PE (N-m)'],P2FLC32['xi (%)'],color='C0',marker='o',s=10)
scatter(P1FLC32['PE (N-m)'],P1FLC32['xi (%)'],color='C3',marker='^',s=10)
xlim(0)
ylim(0)
minorticks_on()
xlabel("Energy, J")
ylabel("Damping Coefficient, %")

savefig("C32 - Damping Coefficient.tiff",bbox_inches='tight')


# PLOT DAMPING COEFFICIENT OF C64

figure(30,[2.45,2.15],dpi=600)
scatter(P3FLC64['PE (N-m)'],P3FLC64['xi (%)'],color='k',marker='s',s=10)
scatter(P2FLC64['PE (N-m)'],P2FLC64['xi (%)'],color='C0',marker='o',s=10)
scatter(P1FLC64['PE (N-m)'],P1FLC64['xi (%)'],color='C3',marker='^',s=10)
xlim(0)
ylim(0)
minorticks_on()
xlabel("Energy, J")
ylabel("Damping Coefficient, %")

savefig("C64 - Damping Coefficient.tiff",bbox_inches='tight')


# PLOT DAMPING COEFFICIENT OF C96

figure(31,[2.45,2.15],dpi=600)
scatter(P3FLC96['PE (N-m)'],P3FLC96['xi (%)'],color='k',marker='s',s=10)
scatter(P2FLC96['PE (N-m)'],P2FLC96['xi (%)'],color='C0',marker='o',s=10)
scatter(P1FLC96['PE (N-m)'],P1FLC96['xi (%)'],color='C3',marker='^',s=10)
xlim(0)
ylim(0)
minorticks_on()
xlabel("Energy, J")
ylabel("Damping Coefficient, %")
```

```
savefig("C96 - Damping Coefficient.tiff",bbox_inches='tight')



# STRAINS #

# PLOT STRAINS OF C32

figure(32,[2.45,2.15],dpi=600)
plot(P3FLC32['PE (N-m)'],P3FLC32['strainmax (mm/mm)'],color='k',marker='s',ms=3)
plot(P2FLC32['PE (N-m)'],P2FLC32['strainmax (mm/mm)'],color='C0',marker='o',ms=3)
plot(P1FLC32['PE (N-m)'],P1FLC32['strainmax (mm/mm)'],color='C3',marker='^',ms=3)
plot(P3FLC32['PE (N-m)'],P3FLC32['strainmin (mm/mm)'],color='k',marker='s',ms=3)
plot(P2FLC32['PE (N-m)'],P2FLC32['strainmin (mm/mm)'],color='C0',marker='o',ms=3)
plot(P1FLC32['PE (N-m)'],P1FLC32['strainmin (mm/mm)'],color='C3',marker='^',ms=3)
xlim(0)
ylim(-0.01,0.015)
minorticks_on()
axhline(0,color='k',linewidth=1.0)
xlabel("Energy, J")
ylabel("Strain, mm/mm")

savefig("C32 - Strains.tiff",bbox_inches='tight')


# PLOT STRAINS OF C64

figure(33,[2.45,2.15],dpi=600)
plot(P3FLC64['PE (N-m)'],P3FLC64['strainmax (mm/mm)'],color='k',marker='s',ms=3)
plot(P2FLC64['PE (N-m)'],P2FLC64['strainmax (mm/mm)'],color='C0',marker='o',ms=3)
plot(P1FLC64['PE (N-m)'],P1FLC64['strainmax (mm/mm)'],color='C3',marker='^',ms=3)
plot(P3FLC64['PE (N-m)'],P3FLC64['strainmin (mm/mm)'],color='k',marker='s',ms=3)
plot(P2FLC64['PE (N-m)'],P2FLC64['strainmin (mm/mm)'],color='C0',marker='o',ms=3)
plot(P1FLC64['PE (N-m)'],P1FLC64['strainmin (mm/mm)'],color='C3',marker='^',ms=3)
xlim(0)
ylim(-0.01,0.015)
minorticks_on()
axhline(0,color='k',linewidth=1.0)
xlabel("Energy, J")
ylabel("Strain, mm/mm")
savefig("C64 - Strains.tiff",bbox_inches='tight')


# PLOT STRAINS OF C96

figure(34,[2.45,2.15],dpi=600)
plot(P3FLC96['PE (N-m)'],P3FLC96['strainmax (mm/mm)'],color='k',marker='s',ms=3)
plot(P2FLC96['PE (N-m)'],P2FLC96['strainmax (mm/mm)'],color='C0',marker='o',ms=3)
plot(P1FLC96['PE (N-m)'],P1FLC96['strainmax (mm/mm)'],color='C3',marker='^',ms=3)
plot(P3FLC96['PE (N-m)'],P3FLC96['strainmin (mm/mm)'],color='k',marker='s',ms=3)
plot(P2FLC96['PE (N-m)'],P2FLC96['strainmin (mm/mm)'],color='C0',marker='o',ms=3)
plot(P1FLC96['PE (N-m)'],P1FLC96['strainmin (mm/mm)'],color='C3',marker='^',ms=3)
xlim(0)
ylim(-0.01,0.015)
minorticks_on()
axhline(0,color='k',linewidth=1.0)
xlabel("Energy, J")
ylabel("Strain, mm/mm")

savefig("C96 - Strains.tiff",bbox_inches='tight')
```

APPENDIX D: PYTHON SCRIPT FOR TWO-WAY ANALYTICAL PROCEDURE PRESENTED IN CHAPTER 7

```
""" N O N L I N E A R    M I N D L I N    P L A T E    M O D E L L I N G """

"""         P r o g r a m    b y    D i l l o n    B e t t s          """


""" =========================== PROGRAM NOTES ============================= """

"""
This program performs a model to predict the load-deflection and load-strain
behaviour of two-way sandwich plates constructed with nonlinear faces and core
materials. The model accounts for the nonlinearity of the constituents through
the use of a secant modulus at each model step.


Notes on Data Inputs

      1.  Models are currently using ONE-ONS properties
          a.  WRP, WFT 2FL coupon test data was adjusted for 2.5 mm thickness
              i.    AVE STRESS * AVE THICKNESS / 2.5
          b.  Then for 1FL, thk was assumed to be 1.25 mm and for 3FL, 3.75 mm

      2.  Models are currently using C96 shear test data
"""



""" ============================== START-UP =============================== """

from pylab import (pi,plot,xlabel,ylabel,xlim,ylim,figure,savefig,linspace,
                   zeros,loadtxt,sin,cos,column_stack,polyfit,savetxt,axvline)

import sympy as sp

from mypy import dillplotparams,find_nearest

dillplotparams()



""" =============================== INPUTS ================================ """

# ----------------------------- USER INPUTS -------------------------------- #

M = '1'     # '1','2','3'... - Flax layers
C = '96'       # 32, 64, 96 - Core Density

Ks = 5./6

if M == '1':
    c_plot = 'k'
elif M == '2':
    c_plot = 'k'
elif M == '3':
    c_plot = 'k'


# --------------------------- COMPUTER INPUTS ------------------------------ #

#for M in ('1','2','3','4','5','6','7'):

if C == '32' or C == '64' or (C == '96' and M != '1' and M != '2' and M != '3'):
```

```
    ins = loadtxt('C:\Users\Dillon\Documents\Research\Phase 2\Specimen\Modelling\inputs-
%sfl-C%s-ONS.txt'%(M,C),
                  skiprows=1)
elif C == '96' and (M == '1' or M == '2' or M == '3'):
    ins = loadtxt('C:\Users\Dillon\Documents\Research\Phase
2\Specimen\Static\Modelling\inputs-%sfl-C%s-ONS.txt'%(M,C),
                  skiprows=1)
    LD = loadtxt('C:\Users\Dillon\Documents\Research\Phase 2\Specimen\Static\\%sFL-C%s-
1\\%sFL-C%s-1 - LD.txt'%(M,C,M,C),
                     skiprows=1)
    LSbwrp = loadtxt('C:\Users\Dillon\Documents\Research\Phase 2\Specimen\Static\\%sFL-
C%s-1\\%sFL-C%s-1 - LS_b_wrp.txt'%(M,C,M,C),
                         skiprows=1)
    LSbwft = loadtxt('C:\Users\Dillon\Documents\Research\Phase 2\Specimen\Static\\%sFL-
C%s-1\\%sFL-C%s-1 - LS_b_wft.txt'%(M,C,M,C),
                         skiprows=1)
    LStwrp = loadtxt('C:\Users\Dillon\Documents\Research\Phase 2\Specimen\Static\\%sFL-
C%s-1\\%sFL-C%s-1 - LS_t_wrp.txt'%(M,C,M,C),
                         skiprows=1)
    LStwft = loadtxt('C:\Users\Dillon\Documents\Research\Phase 2\Specimen\Static\\%sFL-
C%s-1\\%sFL-C%s-1 - LS_t_wft.txt'%(M,C,M,C),
                         skiprows=1)
    LQPD = loadtxt('C:\Users\Dillon\Documents\Research\Phase 2\Specimen\Static\\%sFL-C%s-
1\\%sFL-C%s-1 - LQPD-AVE.txt'%(M,C,M,C),
                       skiprows=1)

L = ins[0]
u = ins[1]
t = ins[2]
c = ins[3]
sfu = ins[4]
efu = ins[5]
Efo = ins[6]
v = ins[7]
Gco = ins[8]
ycu = ins[9]
taucu = ins[10]
P_max = ins[11]
sfu_wft = ins[12]
d = c + t

""" ============================= MODELLING =============================== """

# ----------------------- KIRCHOFF-MINDLIN MODELLING ------------------------ #

# PRELIMNARY CALCULATIONS --------------------------------------------------- #
F11 = 1/(sfu**2.)
F22 = 1/(sfu_wft**2.)
#F1 = (1/sfu)-(1/sfu)
#F2 = (1/sfu_wft)-(1/sfu_wft)
F12star = -0.5
F12=F12star*(F11*F22)**(0.5)


# VARIABLE INITIALIZATION FOR LOOP ------------------------------------------ #
P = linspace(0,P_max,int(P_max/250))
sf = zeros(len(P))
efx = zeros(len(P))
Ef = zeros(len(P))
yc = zeros(len(P))
tau = zeros(len(P))
D = zeros(len(P))
Gc = zeros(len(P))
sfx = zeros(len(P))
w_kirch = zeros(len(P))
w_mind = zeros(len(P))
w_mindquart = zeros(len(P))
y_mind = zeros(len(P))
tau_mind = zeros(len(P))
Pu = 0
ult_ind = 0
```

```
ult_chk = False


# MODELLING IN LOOP ---------------------------------------------------------- #

for i in range(len(w_mind)):

    if i == 0 or i == 1:
        Gc[i] = Gco
        Ef[i] = Efo
    else:
        yc[i] = 2*(w_mind[i-1]-w_kirch[i-1])/L
        tau[i] = (2/ycu**3.)*(0.55*Gco*ycu-taucu)*yc[i]**3. + (1/ycu**2.*(3*taucu-
2.1*Gco*ycu))*yc[i]**2. + Gco*yc[i]
        Gc[i] = tau[i]/yc[i]
        Ef[i] = sf[i-1]/efx[i-1]

    D[i] = Ef[i]*t*(d)**2/(2*(1-v**2))

    S_kirch = 0
    S_mind = 0
    S_strain = 0
    S_shear = 0
    S_mindquart = 0
    xi = L/2
    eta = L/2
    x = L/4
    y = L/4
    for n in range(1,31,1):
        for m in range(1,31,1):
            S_strain = S_strain +
m/(n*(m**2.+n**2.)**2.)*sin(m*pi*u/(2*L))*sin(n*pi*u/(2*L))*sin(m*pi/2)**2*sin(n*pi/2)**2
            S_kirch = S_kirch +
(1/(m*n))*(1/(m**2.+n**2.)**2.)*sin(m*pi*u/(2*L))*sin(n*pi*u/(2*L))*sin(m*pi/2)**2*sin(n*
pi/2)**2
            S_mind = S_mind +
(1/(m*n))*((1/(Ks*Gc[i]*c*(m**2.+n**2.)))+(L**2./(D[i]*pi**2.*(m**2.+n**2.)**2.)))*sin(m*
pi*u/(2*L))*sin(n*pi*u/(2*L))*sin(m*pi/2)**2*sin(n*pi/2)**2
            S_mindquart = S_mindquart +
(1/(m*n))*((1/(Ks*Gc[i]*c*(m**2.+n**2.)))+(L**2./(D[i]*pi**2.*(m**2.+n**2.)**2.)))*sin(m*
pi*u/(2*L))*sin(n*pi*u/(2*L))*sin(m*pi*xi/(L))*sin(n*pi*eta/(L))*sin(m*pi*x/(L))*sin(n*pi
*y/(L))

    efx[i] = 8*P[i]*L**2.*d/(D[i]*pi**4.*u**2.)*S_strain

    xs = sp.Symbol('xs')
    sf[i] = float(max(sp.solve((xs**2)*(efu-sfu/Efo)/(sfu**2) + (xs/Efo) - efx[i], xs)))
    sfx[i] = efx[i]*Ef[i]/(1-v)

    w_mind[i] = 16*P[i]*L**2./(pi**4.*u**2.)*S_mind
    w_mindquart[i] = 16*P[i]*L**2./(pi**4.*u**2.)*S_mindquart
    w_kirch[i] = (16*P[i]*L**4./(u**2.*pi**6.*D[i]))*S_kirch


    if ((F11 + F22 + 2*F12)*sfx[i]**2. >= 1 and ult_chk == False):
        ult_ind = i
        ult_chk = True
        fail = 'face'
        print fail
        break
    elif (tau[i] >= taucu and ult_chk == False):
        ult_ind = i
        ult_chk = True
        fail = 'core'
        print fail
        break


# DATA OUTPUTS --------------------------------------------------------------- #
```

```
# Ultimate Deflection - Mindlin --------------------------------------------- #
w_mu = w_mind[ult_ind]

# Percentage of bending deflection
w_bu = w_kirch[ult_ind]/w_mu*100

# Percentage of shear deflection
w_su = 100-w_bu

# Ultimate Deflection - Mindlin - Quarter Point ----------------------------- #
w_muq = w_mindquart[ult_ind]

# Ultimate Load - Mindlin --------------------------------------------------- #
P_mu = P[ult_ind]

# Flexural Plate Stiffness - Mindlin ---------------------------------------- #
LD_mind = column_stack((w_mind[0:ult_ind],P[0:ult_ind]))

# to match the bounds used in the test data, x1 = 0.5 mm and x2 = 2 mm
start = list(w_mind).index(find_nearest(w_mind,0.5))
stop =  list(w_mind).index(find_nearest(w_mind,2.0))
mb = polyfit(LD_mind[start:stop,0],LD_mind[start:stop,1],1)
K_m = mb[0]

# Flexural Plate Stiffness - Mindlin - Quarter Point ------------------------ #
LD_mindquart = column_stack((w_mindquart[0:ult_ind],P[0:ult_ind]))

# to match the bounds used in the test data, x1_qp = 1.5 mm and x2_qp = 3 mm
start_qp = list(w_mindquart).index(find_nearest(w_mindquart,1.5))
stop_qp =  list(w_mindquart).index(find_nearest(w_mindquart,3.0))
mb_qp = polyfit(LD_mindquart[start_qp:stop_qp,0],LD_mindquart[start_qp:stop_qp,1],1)
K_mq = mb_qp[0]

# Store Mindlin Model Results ----------------------------------------------- #
results = column_stack((P_mu/1000,w_mu,w_muq,K_m,K_mq,w_su))
savetxt("C:\Users\Dillon\Documents\Research\Phase 2\Specimen\Static\Modelling\\Results -
%sFL-C%s.txt"%(M,C),
        results,
        header="Ultimate Load, kN\tUltimate Deflection, mm\tUltimate Quarter Point
Deflection, mm\tStiffness, N/mm\tQuarter Point Stiffness, N/mm\tContribution of Shear
Deflection, %",
        delimiter="\t")



# PLOTTING ------------------------------------------------------------------ #

# Load-Deflection Plot ------------------------------------------------------ #

figure(0, [3.5,3])
plot(LD[:,0],LD[:,1],color=c_plot,linewidth=1.0)
#plot(w_kirch[0:ult_ind],P[0:ult_ind]/1000,'purple',linestyle='--')
plot(w_mind[0:ult_ind],P[0:ult_ind]/1000,color=c_plot,linestyle='--',linewidth=1.0)

xlim(0,30)
ylim(0,30)
xlabel('Center Deflection, mm')
ylabel('Load, kN')
savefig('Load-Deflection-%sFL-C%s.tiff'%(M,C),bbox_inches='tight',dpi=600)


# Load-Strain Plot ---------------------------------------------------------- #

figure(1, [3.5,3])

plot(LSbwrp[:,0],LSbwrp[:,1],color=c_plot,linewidth=1.0)
plot(LSbwft[:,0],LSbwft[:,1],color=c_plot,linewidth=1.0)
plot(LStwrp[:,0],LStwrp[:,1],color=c_plot,linewidth=1.0)
plot(LStwft[:,0],LStwft[:,1],color=c_plot,linewidth=1.0)

plot(efx[0:ult_ind],P[0:ult_ind]/1000,color=c_plot,linestyle='--',linewidth=1.0)
```

```
plot(-efx[0:ult_ind],P[0:ult_ind]/1000,color=c_plot,linestyle='--',linewidth=1.0)

ylim(0,30)

xlabel('Face Strain, mm/mm')
ylabel('Load, kN')
axvline(x=0, color='k', linewidth = 1.0)


savefig('Load-Strain-%sFL-C%s.tiff'%(M,C),bbox_inches='tight',dpi=600)


# Load-Quarter Point Deflection Plot ---------------------------------------- #

figure(2, [3.5,3])

plot(LQPD[:,0],LQPD[:,1],color=c_plot,linewidth=1.0)
plot(w_mindquart[0:ult_ind],P[0:ult_ind]/1000,color=c_plot,linestyle='--',linewidth=1.0)

xlabel('Quarter Point Deflection, mm/mm')
ylabel('Load, kN')
xlim(0,20)
ylim(0,30)

savefig('Load-Quarter Point Deflection-%sFL-C%s.tiff'%(M,C),bbox_inches='tight',dpi=600)
```

APPENDIX E: SAMPLE LS DYNA CODE FOR PANEL 3FL-C96 UNDER QUASI-STATIC LOADING

```
$# LS-DYNA Keyword file created by LS-PrePost(R) V4.3.20 - 09Jan2018
$# Created on Jan-04-2021 (12:01:48)
*KEYWORD MEMORY=500M NCPU=8
*TITLE
$#                                                                         title
Quarter Model of Two-Way Sandwich Plates
*CONTROL_IMPLICIT_AUTO
$#   iauto    iteopt    itewin     dtmin     dtmax     dtexp     kfail    kcycle
         1       100        20       0.0     0.001       0.0         0         0
*CONTROL_IMPLICIT_DYNAMICS
$#   imass     gamma      beta    tdybir    tdydth    tdybur     irate
         0       0.5      0.25       0.01.00000E281.00000E28         0
*CONTROL_IMPLICIT_GENERAL
$#  imflag       dt0    imform      nsbs       igs     cnstn      form    zero_v
         1       0.0         2         1         2         0         0         0
*CONTROL_IMPLICIT_SOLUTION
$#  nsolvr    ilimit    maxref     dctol     ectol     rctol     lstol    abstol
        12        11        15       0.1       0.11.00000E10       0.91.0000E-10
$#   dnorm    diverg     istif   nlprint    nlnorm   d3itctl     cpchk
         2         1         1         0         2         0         0
$#  arcctl    arcdir    arclen    arcmth    arcdmp    arcpsi    arcalf    arctim
         0         0       0.0         2         2         0         0         0
$#   lsmtd     lsdir      irad      srad      awgt      sred
         4         2       0.0       0.0       0.0       0.0
*CONTROL_IMPLICIT_SOLVER
$#  lsolvr    lprint     negev     order      drcm    drcprm   autospc   autotol
         4         2         2         0         4       0.0         1       0.0
$#  lcpack    mtxdmp
         2         0
*CONTROL_TERMINATION
$#  endtim    endcyc     dtmin    endeng    endmas
       1.0         0       0.0       0.01.000000E8
*DATABASE_SPCFORC
$#      dt    binary      lcur     ioopt
     0.001         0         0         1
*DATABASE_BINARY_D3PLOT
$#      dt      lcdt      beam     npltc    psetid
     0.001         0         0         0         0
$#   ioopt
         0
*DATABASE_EXTENT_BINARY
$#   neiph     neips    maxint    strflg    sigflg    epsflg    rltflg    engflg
         0         0         3         1         1         1         1         1
$#  cmpflg    ieverp    beamip     dcomp      shge     stssz    n3thdt   ialemat
         0         0         0         1         1         1         2         1
$# nintsld   pkp_sen      sclp     hydro     msscl     therm    intout    nodout
         0         0       1.0         0         0         0
$#    dtdt    resplt     neipb
         0         0         0
*BOUNDARY_PRESCRIBED_MOTION_RIGID_ID
$#      id                                                               heading
         1Loading
$#     pid       dof       vad      lcid        sf       vid     death     birth
         1         3         2         1     -75.0         01.00000E28       0.0
*BOUNDARY_SPC_SET
$#    nsid       cid      dofx      dofy      dofz     dofrx     dofry     dofrz
         1         0         0         1         0         0         0         0
*SET_NODE_LIST
$#     sid       da1       da2       da3       da4    solver
         1       0.0       0.0       0.0       0.0MECH
```

[LIST OF NODES NOT SHOWN]

```
*BOUNDARY_SPC_SET
$#    nsid       cid      dofx      dofy      dofz     dofrx     dofry     dofrz
```

```
         2         0         1         0         0         0         0         0
*SET_NODE_LIST
$#     sid       da1       da2       da3       da4    solver
         2       0.0       0.0       0.0       0.0MECH
[LIST OF NODES NOT SHOWN]

*BOUNDARY_SPC_SET
$#    nsid       cid      dofx      dofy      dofz     dofrx     dofry     dofrz
         3         0         1         1         1         1         0         1
*SET_NODE_LIST_TITLE
NODESET(SPC) 3
$#     sid       da1       da2       da3       da4    solver
         3       0.0       0.0       0.0       0.0MECH
[LIST OF NODES NOT SHOWN]


*BOUNDARY_SPC_SET
$#    nsid       cid      dofx      dofy      dofz     dofrx     dofry     dofrz
         4         0         1         1         1         0         1         1
*SET_NODE_LIST_TITLE
NODESET(SPC) 4
$#     sid       da1       da2       da3       da4    solver
         4       0.0       0.0       0.0       0.0MECH
[LIST OF NODES NOT SHOWN]

*CONTACT_AUTOMATIC_SURFACE_TO_SURFACE_MORTAR_ID
$#     cid                                                                 title
         1Loading Disc to Rubber Pad
$#    ssid      msid     sstyp     mstyp    sboxid    mboxid       spr       mpr
         7         1         3         3         0         0         0         0
$#      fs        fd        dc        vc       vdc    penchk        bt        dt
       0.8       0.8       0.0       0.0       0.0         0       0.01.00000E20
$#     sfs       sfm       sst       mst      sfst      sfmt       fsf       vsf
       5.0       1.0       0.0       0.0       1.0       1.0       1.0       1.0
$#    soft    sofscl    lcidab    maxpar     sbopt     depth     bsort    frcfrq
         0       0.1         0     1.025       2.0         2         0         1
$#  penmax    thkopt    shlthk     snlog      isym     i2d3d    sldthk    sldstf
       0.0         0         0         0         0         0       0.0       0.0
$#    igap    ignodprfac/mpadtstif/mpar2   unused     unused    flangl   cid_rcf
         5         0       0.0       0.0                           0.0         0
*CONTACT_AUTOMATIC_SURFACE_TO_SURFACE_MORTAR_ID
$#     cid                                                                 title
         2Panel to Supports
$#    ssid      msid     sstyp     mstyp    sboxid    mboxid       spr       mpr
         4         1         3         2         0         0         0         0
$#      fs        fd        dc        vc       vdc    penchk        bt        dt
1.00000E-41.00000E-4       0.0       0.0       0.0         0       0.01.00000E20
$#     sfs       sfm       sst       mst      sfst      sfmt       fsf       vsf
       5.0       1.0       0.0       0.0       1.0       1.0       1.0       1.0
$#    soft    sofscl    lcidab    maxpar     sbopt     depth     bsort    frcfrq
         0       0.1         0     1.025       2.0         2         0         1
$#  penmax    thkopt    shlthk     snlog      isym     i2d3d    sldthk    sldstf
       0.0         0         0         0         0         0       0.0       0.0
$#    igap    ignodprfac/mpadtstif/mpar2   unused     unused    flangl   cid_rcf
         5         0       0.0       0.0                           0.0         0
*SET_PART_LIST_TITLE
Supports
$#     sid       da1       da2       da3       da4    solver
         1       0.0       0.0       0.0       0.0MECH
$#    pid1      pid2      pid3      pid4      pid5      pid6      pid7      pid8
         5         6         0         0         0         0         0         0
*CONTACT_AUTOMATIC_SURFACE_TO_SURFACE_MORTAR_TIED_ID
$#     cid                                                                 title
         3Top Face to Core
$#    ssid      msid     sstyp     mstyp    sboxid    mboxid       spr       mpr
         3         2         3         3         0         0         0         0
$#      fs        fd        dc        vc       vdc    penchk        bt        dt
      10.0      10.0       0.0       0.0       0.0         0       0.01.00000E20
$#     sfs       sfm       sst       mst      sfst      sfmt       fsf       vsf
       5.0       1.0       0.0       0.0       1.0       1.0       1.0       1.0
$#    soft    sofscl    lcidab    maxpar     sbopt     depth     bsort    frcfrq
```

```
         0       0.1         0     1.025       2.0         2         0         1
$#  penmax    thkopt    shlthk     snlog      isym     i2d3d    sldthk    sldstf
       0.0         0         0         0         0         0       0.0       0.0
$#    igap    ignodprfac/mpadtstif/mpar2    unused    unused    flangl   cid_rcf
         5         0       0.0       0.0                           0.0         0
*CONTACT_AUTOMATIC_SURFACE_TO_SURFACE_MORTAR_TIED_ID
$#     cid                                                                 title
         4Bottom Face to Core
$#    ssid      msid     sstyp     mstyp    sboxid    mboxid       spr       mpr
         3         4         3         3         0         0         0         0
$#      fs        fd        dc        vc       vdc    penchk        bt        dt
      10.0      10.0       0.0       0.0       0.0         0       0.01.00000E20
$#     sfs       sfm       sst       mst      sfst      sfmt       fsf       vsf
       5.0       1.0       0.0       0.0       1.0       1.0       1.0       1.0
$#    soft    sofscl    lcidab    maxpar     sbopt     depth     bsort    frcfrq
         0       0.1         0     1.025       2.0         2         0         1
$#  penmax    thkopt    shlthk     snlog      isym     i2d3d    sldthk    sldstf
       0.0         0         0         0         0         0       0.0       0.0
$#    igap    ignodprfac/mpadtstif/mpar2    unused    unused    flangl   cid_rcf
         5         0       0.0       0.0                           0.0         0
*CONTACT_AUTOMATIC_SURFACE_TO_SURFACE_MORTAR_ID
$#     cid                                                                 title
         5Rubber Pad to Panel
$#    ssid      msid     sstyp     mstyp    sboxid    mboxid       spr       mpr
         7         2         3         3         0         0         0         0
$#      fs        fd        dc        vc       vdc    penchk        bt        dt
       0.8       0.8       0.0       0.0       0.0         0       0.01.00000E20
$#     sfs       sfm       sst       mst      sfst      sfmt       fsf       vsf
       1.0       1.0       0.0       0.0       1.0       1.0       1.0       1.0
*PART
$#                                                                         title
Loading Disc
$#     pid     secid       mid     eosid      hgid      grav    adpopt      tmid
         1         1         4         0         0         0         0         0
*SECTION_SOLID_TITLE
Solid
$#   secid    elform       aet
         1        -2         0
*MAT_RIGID_TITLE
Steel Loading Disc
$#     mid        ro         e        pr         n    couple         m     alias
         47.85000E-9  200000.0       0.3       0.0       0.0       0.0
$#     cmo      con1      con2
       0.0         0         0
$#lco or a1        a2        a3        v1        v2        v3
       0.0       0.0       0.0       0.0       0.0       0.0
*PART
$#                                                                         title
Top Face
$#     pid     secid       mid     eosid      hgid      grav    adpopt      tmid
         2         1         2         0         0         0         0         0
*MAT_NONLINEAR_ORTHOTROPIC_TITLE
FFRP in Compression
$#     mid        ro        ea        eb        ec      prba      prca      prcb
         21.21300E-9    6730.0    2588.0    2588.0       0.3       0.3       0.3
$#     gab       gbc       gca        dt     tramp     alpha
    1262.0    1262.0    1262.0       0.0       0.0       0.0
$#   lcida     lcidb     efail    dtfail     cdamp      aopt      macf
         4         4       0.0       0.0       0.0        -1         1
$#      xp        yp        zp        a1        a2        a3
       0.0       0.0       0.0       0.0       0.0       0.0
$#      v1        v2        v3        d1        d2        d3      beta
       0.0       0.0       0.0       0.0       0.0       0.0       0.0
$#   lcidc    lcidab    lcidbc    lcidca
         0         6         0         0
*PART
$#                                                                         title
Core
$#     pid     secid       mid     eosid      hgid      grav    adpopt      tmid
         3         1         3         0         0         0         0         0
*MAT_LOW_DENSITY_FOAM_TITLE
```

```
Foam Core
$#     mid        ro         e      lcid        tc        hu      beta      damp
         39.6000E-11      35.1         51.00000E20       1.0       0.0       0.0
$#   shape      fail    bvflag        ed     beta1      kcon       ref
       1.0       0.0       0.0       0.0       0.0       0.0       0.0
*PART
$#                                                                         title
Bottom Face
$#     pid     secid       mid     eosid      hgid      grav    adpopt      tmid
         4         1         1         0         0         0         0         0
*MAT_NONLINEAR_ORTHOTROPIC_TITLE
FFRP in Tension (Bottom)
$#     mid        ro        ea        eb        ec      prba      prca      prcb
         11.21300E-9    6352.0    5636.0    2840.0      0.23      0.23      0.23
$#     gab       gbc       gca        dt     tramp     alpha
    1262.0    1262.0    1262.0       0.0       0.0       0.0
$#   lcida     lcidb     efail    dtfail     cdamp      aopt      macf
         2         3       0.0       0.0       0.0        -1         1
$#      xp        yp        zp        a1        a2        a3
       0.0       0.0       0.0       0.0       0.0       0.0
$#      v1        v2        v3        d1        d2        d3      beta
       0.0       0.0       0.0       0.0       0.0       0.0       0.0
$#   lcidc    lcidab    lcidbc    lcidca
         0         6         0         0
*PART
$#                                                                         title
Support1
$#     pid     secid       mid     eosid      hgid      grav    adpopt      tmid
         5         1         5         0         0         0         0         0
*MAT_ELASTIC_TITLE
Steel Support
$#     mid        ro         e        pr        da        db  not used
         57.85000E-9  200000.0       0.3       0.0       0.0         0
*PART
$#                                                                         title
Support2
$#     pid     secid       mid     eosid      hgid      grav    adpopt      tmid
         6         1         5         0         0         0         0         0
*PART
$#                                                                         title
Rubber Pad
$#     pid     secid       mid     eosid      hgid      grav    adpopt      tmid
         7         1         6         0         0         0         0         0
*MAT_BLATZ-KO_RUBBER_TITLE
Rubber Pad
$#     mid        ro         g       ref
         61.55200E-9      15.0       0.0
*SECTION_SOLID_TITLE
Core Solid
$#   secid    elform       aet
         2         1         0
*DEFINE_COORDINATE_NODES_TITLE
Warp/Weft Direction
$#     cid        n1        n2        n3      flag       dir
         1      5078      5100      5199         0X
*DEFINE_CURVE_TITLE
Loading Movement
$#    lcid      sidr       sfa       sfo      offa      offo    dattyp     lcint
         1         0       1.0       1.0       0.0       0.0         0         0
$#                a1                  o1
                 0.0                 0.0
                 1.0                 1.0
*DEFINE_CURVE_TITLE
FFRP Warp Tension
$#    lcid      sidr       sfa       sfo      offa      offo    dattyp     lcint
         2         0       1.0       1.0       0.0       0.0         0         0
[CURVE DATA NOT SHOWN]

*DEFINE_CURVE_TITLE
FFRP Weft Tension
$#    lcid      sidr       sfa       sfo      offa      offo    dattyp     lcint
```

```
         3         0       1.0       1.0       0.0       0.0         0         0
[CURVE DATA NOT SHOWN]

*DEFINE_CURVE_TITLE
FFRP Compression
$#    lcid      sidr       sfa       sfo      offa      offo    dattyp     lcint
         4         0       1.0       1.0       0.0       0.0         0         0
[CURVE DATA NOT SHOWN]

*DEFINE_CURVE_TITLE
Foam Compression - 96
$#    lcid      sidr       sfa       sfo      offa      offo    dattyp     lcint
         5         0       1.0       1.0       0.0       0.0         0         0
[CURVE DATA NOT SHOWN]

*DEFINE_CURVE_TITLE
FFRP Shear
$#    lcid      sidr       sfa       sfo      offa      offo    dattyp     lcint
         6         0       1.0       1.0       0.0       0.0         0         0
[CURVE DATA NOT SHOWN]

*SET_NODE_LIST_TITLE
Node set 5
$#     sid       da1       da2       da3       da4    solver
         5       0.0       0.0       0.0       0.0MECH
[CURVE DATA NOT SHOWN]

*SET_NODE_LIST_TITLE
Node set 5
$#     sid       da1       da2       da3       da4    solver
         5       0.0       0.0       0.0       0.0MECH
[LIST OF NODES NOT SHOWN]

*ELEMENT_SOLID
$#   eid     pid      n1      n2      n3      n4      n5      n6      n7      n8
       1       1     647     594     981    1331     590     590    1061    1061
[LIST OF ELEMENTS/NODES NOT SHOWN]

*NODE
$#   nid               x               y               z      tc      rc
       1            75.0             0.0            31.4       0       0
[LIST OF NODES NOT SHOWN]

*END
```

APPENDIX F: PYTHON POST-PROCESSING SCRIPT FOR QUASI-STATIC TWO-WAY FINITE ELEMENT ANALYSIS

```
# -*- coding: utf-8 -*-
"""
Created on Fri Apr 10 12:41:56 2020

@author: Dillon
"""


""" ============================= START-UP ================================ """

from pylab import (plot,xlabel,ylabel,xlim,ylim,figure,savefig,
                   axvline,genfromtxt,loadtxt,interp,text,annotate)

from mypy import dillplotparams, stiffx

import pandas as pd

dillplotparams()



""" ============================== INPUTS ================================= """

# PLOT TEST DATA?

PlotTestData = False


# MODEL NAME

nom = "no fail - moderate - refined mesh"


# CORE DENSITY

C = 96


# FLAX LAYERS

FL = 3

Ef_wrp = 3480 # initial = 6352, ultimate = 3480
Ef_wft = 2540 # initial = 6352, ultimate = 2540

if C == 96:
    c1='k'
    t_core_fail = 0.476 # Test = 0.476; ELFOAM AVE = 0.537
    t_core_fail_low = 0.374 # Test - 1 SD = 0.374; ELFOAM PERP = 0.489
    t_core_fail_high = 0.578 # Test + 1 SD = 0.578; ELFOAM PARA = 0.585
    E_c = 35.1
    v_c = 0.3
elif C == 64:
    c1='b'
    t_core_fail = (0.344  + 0.379)/2
    t_core_fail_low = 0.344
    t_core_fail_high = 0.379
    E_c = 12.6
    v_c = 0.3
elif C ==32:
    c1='r'
    t_core_fail = (0.124 + 0.172)/2
    t_core_fail_low = 0.124
```

```
    t_core_fail_high = 0.172
    E_c = 4.9
    v_c = 0.3

B1 = 3*(12*(3-v_c)**2.*(1+v_c)**2.)**(-1./3)
s_crit_wrp = B1*Ef_wrp**(1./3)*(E_c)**(2./3)
s_crit_wft = B1*Ef_wft**(1./3)*(E_c)**(2./3)


# FAILURE CRITERIA

s_wft_fail = 51.3
s_wrp_fail = 69.
s_shear_fail = 10.

t_core_fail = 0.476 # Test = 0.476; ELFOAM AVE = 0.537
t_core_fail_low = 0.374 # Test - 1 SD = 0.374; ELFOAM PERP = 0.489
t_core_fail_high = 0.578 # Test + 1 SD = 0.578; ELFOAM PARA = 0.585


# DYNA MODELS
displ_dyna = genfromtxt("C:\Users\Dillon\Documents\Research\FEM
Modelling\#_Current\Static\Two Way\\%dfl-c%d-quarter - %s\displ"%(FL,C,nom),
                       skip_header=8,skip_footer=1,usecols=1)
time_dyna_hist = genfromtxt("C:\Users\Dillon\Documents\Research\FEM
Modelling\#_Current\Static\Two Way\\%dfl-c%d-quarter - %s\displ"%(FL,C,nom),
                       skip_header=8,skip_footer=1,usecols=0)

load_dyna_raw = genfromtxt("C:\Users\Dillon\Documents\Research\FEM
Modelling\#_Current\Static\Two Way\\%dfl-c%d-quarter - %s\load"%(FL,C,nom),
                       skip_header=8,skip_footer=1,usecols=1)
time_dyna_load = genfromtxt("C:\Users\Dillon\Documents\Research\FEM
Modelling\#_Current\Static\Two Way\\%dfl-c%d-quarter - %s\load"%(FL,C,nom),
                       skip_header=8,skip_footer=1,usecols=0)

e_t_wrp_dyna = genfromtxt("C:\Users\Dillon\Documents\Research\FEM
Modelling\#_Current\Static\Two Way\\%dfl-c%d-quarter - %s\e_t_wrp"%(FL,C,nom),
                       skip_header=8,skip_footer=1,usecols=1)
e_t_wft_dyna = genfromtxt("C:\Users\Dillon\Documents\Research\FEM
Modelling\#_Current\Static\Two Way\\%dfl-c%d-quarter - %s\e_t_wft"%(FL,C,nom),
                       skip_header=8,skip_footer=1,usecols=1)
e_b_wrp_dyna = genfromtxt("C:\Users\Dillon\Documents\Research\FEM
Modelling\#_Current\Static\Two Way\\%dfl-c%d-quarter - %s\e_b_wrp"%(FL,C,nom),
                       skip_header=8,skip_footer=1,usecols=1)
e_b_wft_dyna = genfromtxt("C:\Users\Dillon\Documents\Research\FEM
Modelling\#_Current\Static\Two Way\\%dfl-c%d-quarter - %s\e_b_wft"%(FL,C,nom),
                       skip_header=8,skip_footer=1,usecols=1)

s_t_wrp_dyna = genfromtxt("C:\Users\Dillon\Documents\Research\FEM
Modelling\#_Current\Static\Two Way\\%dfl-c%d-quarter - %s\s_t_wrp"%(FL,C,nom),
                       skip_header=8,skip_footer=1,usecols=1)
s_t_wft_dyna = genfromtxt("C:\Users\Dillon\Documents\Research\FEM
Modelling\#_Current\Static\Two Way\\%dfl-c%d-quarter - %s\s_t_wft"%(FL,C,nom),
                       skip_header=8,skip_footer=1,usecols=1)

s_comp_wrp_dyna = genfromtxt("C:\Users\Dillon\Documents\Research\FEM
Modelling\#_Current\Static\Two Way\\%dfl-c%d-quarter - %s\s_comp_wrp"%(FL,C,nom),
                       skip_header=8,skip_footer=1,usecols=1)
s_comp_wft_dyna = genfromtxt("C:\Users\Dillon\Documents\Research\FEM
Modelling\#_Current\Static\Two Way\\%dfl-c%d-quarter - %s\s_comp_wft"%(FL,C,nom),
                       skip_header=8,skip_footer=1,usecols=1)

s_b_wrp_dyna = genfromtxt("C:\Users\Dillon\Documents\Research\FEM
Modelling\#_Current\Static\Two Way\\%dfl-c%d-quarter - %s\s_b_wrp"%(FL,C,nom),
                       skip_header=8,skip_footer=1,usecols=1)
s_b_wft_dyna = genfromtxt("C:\Users\Dillon\Documents\Research\FEM
Modelling\#_Current\Static\Two Way\\%dfl-c%d-quarter - %s\s_b_wft"%(FL,C,nom),
                       skip_header=8,skip_footer=1,usecols=1)

tresca_core_dyna = genfromtxt("C:\Users\Dillon\Documents\Research\FEM
Modelling\#_Current\Static\Two Way\\%dfl-c%d-quarter - %s\\tresca_mid_core"%(FL,C,nom),
```

```
                       skip_header=8,skip_footer=1,usecols=1)

buckle_time = genfromtxt("C:\Users\Dillon\Documents\Research\FEM
Modelling\#_Current\Static\Two Way\\%dfl-c%d-quarter - %s\\buckle_time.txt"%(FL,C,nom))

# Load is calculated at different time steps than the other data. Therefore,
# we have to interpolate the load onto the same x scale as the other data.
load_dyna = interp(time_dyna_hist,time_dyna_load,load_dyna_raw)


# LOAD TEST DATA

if C == 96 and PlotTestData == True:
    LDdata = loadtxt("C:\Users\Dillon\Documents\Research\Phase 2\Specimen\Static\\%dFL-
C96-1\\%dFL-C96-1 - LD.txt"%(FL,FL))
    LS_t_wrp_data = loadtxt("C:\Users\Dillon\Documents\Research\Phase
2\Specimen\Static\\%dFL-C96-1\\%dFL-C96-1 - LS_t_wrp.txt"%(FL,FL))
    LS_t_wft_data = loadtxt("C:\Users\Dillon\Documents\Research\Phase
2\Specimen\Static\\%dFL-C96-1\\%dFL-C96-1 - LS_t_wft.txt"%(FL,FL))
    LS_b_wrp_data = loadtxt("C:\Users\Dillon\Documents\Research\Phase
2\Specimen\Static\\%dFL-C96-1\\%dFL-C96-1 - LS_b_wrp.txt"%(FL,FL))
    LS_b_wft_data = loadtxt("C:\Users\Dillon\Documents\Research\Phase
2\Specimen\Static\\%dFL-C96-1\\%dFL-C96-1 - LS_b_wft.txt"%(FL,FL))



""" ============================ POST-PROCESSING ============================ """

# CHECK EACH ITEM FOR FAILURE

fail_int = 1000
fail = "Failure Not Found"
fail_i = "No Core Shear Failure Detected"
core_fail = False
core_fail_low = False
core_fail_high = False
core_fail_int = 0
core_fail_low_int = 0
core_fail_high_int = 0

for i in range(0,len(displ_dyna)):

    # FFRP Compression Failure
    if s_t_wrp_dyna[i] <= -s_wrp_fail:
        fail_int = i
        fail = "Top Face Warp Compression Failure"
        break
    if s_t_wft_dyna[i] <= -s_wft_fail:
        fail_int = i
        fail = "Top Face Weft Compression Failure"
        break
    if s_b_wrp_dyna[i] <= -s_wrp_fail:
        fail_int = i
        fail = "Bottom Face Warp Compression Failure"
        break
    if s_b_wft_dyna[i] <= -s_wft_fail:
        fail_int = i
        fail = "Bottom Face Weft Compression Failure"
        break

    # FFRP Tension Failure
    if s_t_wrp_dyna[i] >= s_wrp_fail:
        fail_int = i
        fail = "Top Face Warp Tension Failure"
        break
    if s_t_wft_dyna[i] >= s_wft_fail:
        fail_int = i
        fail = "Top Face Weft Tension Failure"
        break
    if s_b_wrp_dyna[i] >= s_wrp_fail:
        fail_int = i
```

```
            fail = "Bottom Face Warp Tension Failure"
            break
        if s_b_wft_dyna[i] >= s_wft_fail:
            fail_int = i
            fail = "Bottom Face Weft Tension Failure"
            break

        # Core Shear Failure
        if tresca_core_dyna[i] >= t_core_fail and core_fail == False:
            core_fail_int = i
            core_fail = True
        if tresca_core_dyna[i] >= t_core_fail_low and core_fail_low == False:
            core_fail_low_int = i
            core_fail_low = True
        if tresca_core_dyna[i] >= t_core_fail_high and core_fail_high == False:
            core_fail_high_int = i-1
            core_fail_high = True
            fail_int = i
            fail = "Core Shear Failure"
            break

        # Top Face Wrinkling
        if s_comp_wft_dyna[i] <= -s_crit_wft:
            fail_int = i
            fail = "Compression Wrinkling in the Weft Direction"
            break
        if s_comp_wrp_dyna[i] <= -s_crit_wrp:
            fail_int = i
            fail = "Compression Wrinkling in the Warp Direction"
            break

        # Stability Failure
        if buckle_time != 0 and buckle_time >= time_dyna_hist[i]:
            fail_int = i
            fail = "Stability Failure"


# TRUNCATE DATA BASED ON FAILURE

displ_dyna = -displ_dyna[0:fail_int]
load_dyna = 4*load_dyna[0:fail_int]/1000
e_t_wrp_dyna = e_t_wrp_dyna[0:fail_int]
e_t_wft_dyna = e_t_wft_dyna[0:fail_int]
e_b_wrp_dyna = e_b_wrp_dyna[0:fail_int]
e_b_wft_dyna = e_b_wft_dyna[0:fail_int]

# SAVE LS DYNA DATA

Results = {"Displacement":displ_dyna,"Load":load_dyna,
           "Top Warp Strain":e_t_wrp_dyna,"Top Weft Strain":e_t_wft_dyna,
           "Bottom Warp Strain":e_b_wrp_dyna,"Bottom Weft Strain":e_b_wft_dyna}

outputs_df = pd.DataFrame(Results)

outputs_df.to_csv("FE Results - %dFL-C%d - %s.txt"%(FL,C,nom),sep="\t",index=False)

""" ============================== PLOTS ================================== """

print "Average Core Shear Failure Load:\t%.2f kN"%load_dyna[core_fail_int]
print "Lower Bound Core Shear Failure Load:\t%.2f kN"%load_dyna[core_fail_low_int]
print "Upper Bound Core Shear Failure Load:\t%.2f kN"%load_dyna[core_fail_high_int]
print "Ultimate Failure Load:\t\t\t%.2f kN"%load_dyna[fail_int-1]
print "Ultimate Failure Type:\t\t\t",fail


# ========================== LOAD-DISPLACEMENT ============================== #

figure(0,[3.5,3])
plot(displ_dyna,load_dyna,color=c1,linestyle="--")

# Plot Shear Failure Loads
```

```
if core_fail_int != 0:

plot(displ_dyna[core_fail_int],load_dyna[core_fail_int],color=c1,marker='o',markerfacecol
or=c1)
if core_fail_low_int != 0:

plot(displ_dyna[core_fail_low_int],load_dyna[core_fail_low_int],color=c1,marker='s',marke
rfacecolor='none')
if core_fail_high_int != 0:

plot(displ_dyna[core_fail_high_int],load_dyna[core_fail_high_int],color=c1,marker='^',mar
kerfacecolor='none')

# Plot Test Data for C96 Specmiens
if C == 96 and PlotTestData == True:
    plot(LDdata[:,0],LDdata[:,1],color=c1,linestyle="-")

xlim(0)
ylim(0)
xlabel("Center Deflection, mm")
ylabel("Load, kN")
savefig("Load-Deflection - Dyna vs. Test - %dFL-C%d.tiff"%(FL,C),
        bbox_to_inches = 'tight',
        dpi = 1200)



# ============================= LOAD-STRAIN ================================= #

figure(2,[3.5,3])
plot(e_t_wrp_dyna,load_dyna,color=c1,linestyle="--")
plot(e_t_wft_dyna,load_dyna,color=c1,alpha=0.25,linestyle="--")

# Plot Shear Failure Loads (Top)
if core_fail_int != 0:

plot(e_t_wrp_dyna[core_fail_int],load_dyna[core_fail_int],color=c1,marker='o',markerfacec
olor=c1)

plot(e_t_wft_dyna[core_fail_int],load_dyna[core_fail_int],color=c1,alpha=0.25,marker='o',
markerfacecolor=c1)
if core_fail_low_int != 0:

plot(e_t_wrp_dyna[core_fail_low_int],load_dyna[core_fail_low_int],color=c1,marker='s',mar
kerfacecolor='none')

plot(e_t_wft_dyna[core_fail_low_int],load_dyna[core_fail_low_int],color=c1,alpha=0.25,mar
ker='s',markerfacecolor='none')
if core_fail_high_int != 0:

plot(e_t_wrp_dyna[core_fail_high_int],load_dyna[core_fail_high_int],color=c1,marker='^',m
arkerfacecolor='none')

plot(e_t_wft_dyna[core_fail_high_int],load_dyna[core_fail_high_int],color=c1,alpha=0.25,m
arker='^',markerfacecolor='none')

plot(e_b_wrp_dyna,load_dyna,color=c1,linestyle="--")
plot(e_b_wft_dyna,load_dyna,color=c1,alpha=0.25,linestyle="--")

# Plot Shear Failure Loads (Bottom)
if core_fail_int != 0:

plot(e_b_wrp_dyna[core_fail_int],load_dyna[core_fail_int],color=c1,marker='o',markerfacec
olor=c1)

plot(e_b_wft_dyna[core_fail_int],load_dyna[core_fail_int],color=c1,alpha=0.25,marker='o',
markerfacecolor=c1)
if core_fail_low_int != 0:

plot(e_b_wrp_dyna[core_fail_low_int],load_dyna[core_fail_low_int],color=c1,marker='s',mar
kerfacecolor='none')
```

```
plot(e_b_wft_dyna[core_fail_low_int],load_dyna[core_fail_low_int],color=c1,alpha=0.25,mar
ker='s',markerfacecolor='none')
if core_fail_high_int != 0:

plot(e_b_wrp_dyna[core_fail_high_int],load_dyna[core_fail_high_int],color=c1,marker='^',m
arkerfacecolor='none')

plot(e_b_wft_dyna[core_fail_high_int],load_dyna[core_fail_high_int],color=c1,alpha=0.25,m
arker='^',markerfacecolor='none')

# Plot Test Data for C96 Specmiens
if C == 96  and PlotTestData == True:
    plot(LS_t_wrp_data[:,0],LS_t_wrp_data[:,1],color=c1,linestyle="-")
    plot(LS_t_wft_data[:,0],LS_t_wft_data[:,1],color=c1,alpha=0.25,linestyle="-")
    plot(LS_b_wrp_data[:,0],LS_b_wrp_data[:,1],color=c1,linestyle="-")
    plot(LS_b_wft_data[:,0],LS_b_wft_data[:,1],color=c1,alpha=0.25,linestyle="-")

#xlim(-0.005,0.02)
ylim(0)
axvline(0,linewidth=0.75,color='k')
xlabel("Face Strain, mm/mm")
ylabel("Load, kN")
savefig("Load-Strain - Dyna vs. Test - %dFL-C%d.tiff"%(FL,C),
        bbox_to_inches = 'tight',
        dpi = 1200)



""" ============================= OUTPUTS ================================= """

# ============================= STIFFNESSES ================================= #

# For the tests, 3 mm to 6 mm deflection is good first
# linear portion

x1 = 3.
x2 = 6.

Kdyn = stiffx(displ_dyna,load_dyna*1000,x1,x2)
if PlotTestData == True:
    Kdat = stiffx(LDdata[:,0],LDdata[:,1]*1000,x1,x2)
    K = [Kdat,Kdyn,Kdat/Kdyn]

print "Initial Stiffness:\t\t\t%0.0f N/mm"%Kdyn

# ============================ MAX DEFLECTION ================================ #

ddyn = max(displ_dyna)
if PlotTestData == True:
    ddat = max(LDdata[:,0])
    d = [ddat,ddyn,ddat/ddyn]

print "Ultimate Deflection:\t\t\t%0.1f mm"%ddyn

# ============================== MAX LOAD =================================== #

Pdyn = max(load_dyna)
if PlotTestData == True:
    Pdat = max(LDdata[:,1])
    P = [Pdat,Pdyn,Pdat/Pdyn]


# ============================ SAVE TO FILE ================================= #

if C == 96 and PlotTestData == True:

    names = ["Test","Dyna","Test/Model Ratio"]

    Outputs = {"Names":names,"Stiffnesses N/mm":K,"Ultimate Load, kN":P,
               "Ultimate Deflection, mm":d}
```

```
    outputs_df = pd.DataFrame(Outputs)

    outputs_df.to_csv("Dyna vs Test - %dFL-C%d.txt"%(FL,C),sep="\t",index=False)

Outputs2 = {"ID":"%dFL-C%d"%(FL,C),"Stiffness N/mm":Kdyn,"Ultimate Load kN":Pdyn,
            "Ultimate Deflection mm":ddyn,"Failure Mode":fail}

outputs2_df = pd.DataFrame(Outputs2,index=[0])

outputs2_df.to_csv("FE ultimate conditions - %dFL-C%d - %s.txt"%(FL,C,nom),sep="\t")
```

APPENDIX G: SAMPLE LS DYNA CODE FOR PANEL 3FL-C96 UNDER AN 80 JOULE IMPACT

```
$# LS-DYNA Keyword file created by LS-PrePost(R) V4.3.20 - 09Jan2018
$# Created on Feb-08-2021 (16:12:31)
*KEYWORD MEMORY=500M NCPU=8
*TITLE
$#                                                                         title
Quarter Model of Two-Way Sandwich Plates
*CONTROL_TERMINATION
$#  endtim    endcyc     dtmin    endeng    endmas
      0.02         0       0.0       0.01.000000E8
*DATABASE_SPCFORC
$#      dt    binary      lcur     ioopt
5.00000E-5         0         0         1
*DATABASE_BINARY_D3PLOT
$#      dt      lcdt      beam     npltc    psetid
5.00000E-5         0         0         0         0
$#   ioopt
         0
*DATABASE_EXTENT_BINARY
$#   neiph     neips    maxint    strflg    sigflg    epsflg    rltflg    engflg
         0         0         3         1         1         1         1         1
$#  cmpflg    ieverp    beamip     dcomp      shge     stssz    n3thdt   ialemat
         0         0         0         1         1         1         2         1
$# nintsld   pkp_sen      sclp     hydro     msscl     therm    intout    nodout
         0         0       1.0         0         0         0
$#    dtdt    resplt     neipb
         0         0         0
*BOUNDARY_SPC_SET
$#    nsid       cid      dofx      dofy      dofz     dofrx     dofry     dofrz
         1         0         0         1         0         0         0         0
*SET_NODE_LIST
$#     sid       da1       da2       da3       da4    solver
         1       0.0       0.0       0.0       0.0MECH
[LIST OF NODES NOT SHOWN]

*BOUNDARY_SPC_SET
$#    nsid       cid      dofx      dofy      dofz     dofrx     dofry     dofrz
         2         0         1         0         0         0         0         0
*SET_NODE_LIST
$#     sid       da1       da2       da3       da4    solver
         2       0.0       0.0       0.0       0.0MECH
[LIST OF NODES NOT SHOWN]

*BOUNDARY_SPC_SET
$#    nsid       cid      dofx      dofy      dofz     dofrx     dofry     dofrz
         3         0         1         1         1         1         0         1
*SET_NODE_LIST
$#     sid       da1       da2       da3       da4    solver
         3       0.0       0.0       0.0       0.0MECH
[LIST OF NODES NOT SHOWN]

*BOUNDARY_SPC_SET
$#    nsid       cid      dofx      dofy      dofz     dofrx     dofry     dofrz
         4         0         1         1         1         0         1         1
*SET_NODE_LIST
$#     sid       da1       da2       da3       da4    solver
         4       0.0       0.0       0.0       0.0MECH
[LIST OF NODES NOT SHOWN]

*CONTACT_AUTOMATIC_SURFACE_TO_SURFACE_ID
$#     cid                                                                 title
         1Loading Disc to Rubber
$#    ssid      msid     sstyp     mstyp    sboxid    mboxid       spr       mpr
         7         1         3         3         0         0         0         0
$#      fs        fd        dc        vc       vdc    penchk        bt        dt
```

```
       0.8       0.8       0.0       0.0       0.0         0       0.01.00000E20
$#     sfs       sfm       sst       mst      sfst      sfmt       fsf       vsf
       5.0       1.0       0.0       0.0       1.0       1.0       1.0       1.0
$#    soft    sofscl    lcidab    maxpar     sbopt     depth     bsort    frcfrq
         0       0.1         0     1.025       2.0         2         0         1
$#  penmax    thkopt    shlthk     snlog      isym     i2d3d    sldthk    sldstf
       0.0         0         0         0         0         0       0.0       0.0
$#    igap    ignodprfac/mpadtstif/mpar2   unused     unused    flangl   cid_rcf
         5         0       0.0       0.0                                 0.0         0
*CONTACT_AUTOMATIC_SURFACE_TO_SURFACE_ID
$#     cid                                                                 title
         2Rubber to Panel
$#    ssid      msid     sstyp     mstyp    sboxid    mboxid       spr       mpr
         7         2         3         3         0         0         0         0
$#      fs        fd        dc        vc       vdc    penchk        bt        dt
       0.8       0.8       0.0       0.0       0.0         0       0.01.00000E20
$#     sfs       sfm       sst       mst      sfst      sfmt       fsf       vsf
       5.0       1.0       0.0       0.0       1.0       1.0       1.0       1.0
$#    soft    sofscl    lcidab    maxpar     sbopt     depth     bsort    frcfrq
         0       0.1         0     1.025       2.0         2         0         1
$#  penmax    thkopt    shlthk     snlog      isym     i2d3d    sldthk    sldstf
       0.0         0         0         0         0         0       0.0       0.0
$#    igap    ignodprfac/mpadtstif/mpar2   unused     unused    flangl   cid_rcf
         5         0       0.0       0.0                                 0.0         0
*CONTACT_TIED_SURFACE_TO_SURFACE_ID
$#     cid                                                                 title
         3Top Face to Core
$#    ssid      msid     sstyp     mstyp    sboxid    mboxid       spr       mpr
         3         2         3         3         0         0         0         0
$#      fs        fd        dc        vc       vdc    penchk        bt        dt
      10.0      10.0       0.0       0.0       0.0         0       0.01.00000E20
$#     sfs       sfm       sst       mst      sfst      sfmt       fsf       vsf
       5.0       1.0       0.0       0.0       1.0       1.0       1.0       1.0
$#    soft    sofscl    lcidab    maxpar     sbopt     depth     bsort    frcfrq
         0       0.1         0     1.025       2.0         2         0         1
$#  penmax    thkopt    shlthk     snlog      isym     i2d3d    sldthk    sldstf
       0.0         0         0         0         0         0       0.0       0.0
$#    igap    ignodprfac/mpadtstif/mpar2   unused     unused    flangl   cid_rcf
         5         0       0.0       0.0                                 0.0         0
*CONTACT_TIED_SURFACE_TO_SURFACE_ID
$#     cid                                                                 title
         4Bottom Face to Core
$#    ssid      msid     sstyp     mstyp    sboxid    mboxid       spr       mpr
         3         4         3         3         0         0         0         0
$#      fs        fd        dc        vc       vdc    penchk        bt        dt
      10.0      10.0       0.0       0.0       0.0         0       0.01.00000E20
$#     sfs       sfm       sst       mst      sfst      sfmt       fsf       vsf
       5.0       1.0       0.0       0.0       1.0       1.0       1.0       1.0
$#    soft    sofscl    lcidab    maxpar     sbopt     depth     bsort    frcfrq
         0       0.1         0     1.025       2.0         2         0         1
$#  penmax    thkopt    shlthk     snlog      isym     i2d3d    sldthk    sldstf
       0.0         0         0         0         0         0       0.0       0.0
$#    igap    ignodprfac/mpadtstif/mpar2   unused     unused    flangl   cid_rcf
         5         0       0.0       0.0                                 0.0         0
*CONTACT_AUTOMATIC_SURFACE_TO_SURFACE_ID
$#     cid                                                                 title
         5Panel to Bottom Supports
$#    ssid      msid     sstyp     mstyp    sboxid    mboxid       spr       mpr
         4         1         3         2         0         0         0         0
$#      fs        fd        dc        vc       vdc    penchk        bt        dt
1.00000E-41.00000E-4       0.0       0.0       0.0         0       0.01.00000E20
$#     sfs       sfm       sst       mst      sfst      sfmt       fsf       vsf
       5.0       1.0       0.0       0.0       1.0       1.0       1.0       1.0
$#    soft    sofscl    lcidab    maxpar     sbopt     depth     bsort    frcfrq
         0       0.1         0     1.025       2.0         2         0         1
$#  penmax    thkopt    shlthk     snlog      isym     i2d3d    sldthk    sldstf
       0.0         0         0         0         0         0       0.0       0.0
$#    igap    ignodprfac/mpadtstif/mpar2   unused     unused    flangl   cid_rcf
         5         0       0.0       0.0                                 0.0         0
*SET_PART_LIST_TITLE
Supports
```

```
$#     sid       da1       da2       da3       da4    solver
         1       0.0       0.0       0.0       0.0MECH
$#    pid1      pid2      pid3      pid4      pid5      pid6      pid7      pid8
         5         6         0         0         0         0         0         0
*CONTACT_AUTOMATIC_SURFACE_TO_SURFACE_ID
$#     cid                                                                 title
         6Panel to Top Supports
$#    ssid      msid     sstyp     mstyp    sboxid    mboxid       spr       mpr
         2         2         3         2         0         0         0         0
$#      fs        fd        dc        vc       vdc    penchk        bt        dt
     0.001     0.001       0.0       0.0       0.0         0       0.01.00000E20
$#     sfs       sfm       sst       mst      sfst      sfmt       fsf       vsf
       5.0       1.0       0.0       0.0       1.0       1.0       1.0       1.0
$#    soft    sofscl    lcidab    maxpar     sbopt     depth     bsort    frcfrq
         0       0.1         0     1.025       2.0         2         0         1
$#  penmax    thkopt    shlthk     snlog      isym     i2d3d    sldthk    sldstf
       0.0         0         0         0         0         0       0.0       0.0
$#    igap    ignodprfac/mpadtstif/mpar2   unused     unused    flangl   cid_rcf
         5         0       0.0       0.0                           0.0         0
*SET_PART_LIST_TITLE
Top Supports
$#     sid       da1       da2       da3       da4    solver
         2       0.0       0.0       0.0       0.0MECH
$#    pid1      pid2      pid3      pid4      pid5      pid6      pid7      pid8
         8         9         0         0         0         0         0         0
*PART
$#                                                                         title
Loading Disc
$#     pid     secid       mid     eosid      hgid      grav    adpopt      tmid
         1         1         4         0         0         0         0         0
*SECTION_SOLID_TITLE
Solid
$#   secid    elform       aet
         1        -2         0
*MAT_ELASTIC_TITLE
Impactor
$#     mid        ro         e        pr        da        db  not used
         45.68230E-9  200000.0       0.3       0.0       0.0         0
*PART
$#                                                                         title
Top Face
$#     pid     secid       mid     eosid      hgid      grav    adpopt      tmid
         2         1         2         0         0         0         0         0
*MAT_NONLINEAR_ORTHOTROPIC_TITLE
FFRP in Compression
$#     mid        ro        ea        eb        ec      prba      prca      prcb
         21.21300E-9    6730.0    2588.0    2588.0       0.3       0.3       0.3
$#     gab       gbc       gca        dt     tramp     alpha
    1262.0    1262.0    1262.0       0.0       0.0       0.0
$#   lcida     lcidb     efail    dtfail     cdamp      aopt      macf
         4         4       0.0       0.0       0.0        -1         1
$#      xp        yp        zp        a1        a2        a3
       0.0       0.0       0.0       0.0       0.0       0.0
$#      v1        v2        v3        d1        d2        d3      beta
       0.0       0.0       0.0       0.0       0.0       0.0       0.0
$#   lcidc    lcidab    lcidbc    lcidca
         0         6         0         0
*PART
$#                                                                         title
Core
$#     pid     secid       mid     eosid      hgid      grav    adpopt      tmid
         3         1         3         0         0         0         0         0
*MAT_LOW_DENSITY_FOAM_TITLE
Foam Core
$#     mid        ro         e      lcid        tc        hu      beta      damp
         39.6000E-11      35.1         51.00000E20       1.0       0.0       0.0
$#   shape      fail    bvflag        ed     beta1      kcon       ref
       1.0       0.0       0.0       0.0       0.0       0.0       0.0
*PART
$#                                                                         title
Bottom Face
```

```
$#     pid     secid       mid     eosid      hgid      grav    adpopt      tmid
         4         1         1         0         0         0         0         0
*MAT_NONLINEAR_ORTHOTROPIC_TITLE
FFRP in Tension (Bottom)
$#     mid        ro        ea        eb        ec      prba      prca      prcb
         11.21300E-9    6352.0    5636.0    2840.0      0.23      0.23      0.23
$#     gab       gbc       gca        dt     tramp     alpha
    1262.0    1262.0    1262.0       0.0       0.0       0.0
$#   lcida     lcidb     efail    dtfail     cdamp      aopt      macf
         2         3       0.0       0.0       0.0        -1         1
$#      xp        yp        zp        a1        a2        a3
       0.0       0.0       0.0       0.0       0.0       0.0
$#      v1        v2        v3        d1        d2        d3      beta
       0.0       0.0       0.0       0.0       0.0       0.0       0.0
$#   lcidc    lcidab    lcidbc    lcidca
         0         6         0         0
*PART
$#                                                                         title
Support1
$#     pid     secid       mid     eosid      hgid      grav    adpopt      tmid
         5         1         5         0         0         0         0         0
*MAT_ELASTIC_TITLE
Steel Support
$#     mid        ro         e        pr        da        db  not used
         57.85000E-9  200000.0       0.3       0.0       0.0         0
*PART
$#                                                                         title
Support2
$#     pid     secid       mid     eosid      hgid      grav    adpopt      tmid
         6         1         5         0         0         0         0         0
*PART
$#                                                                         title
Rubber Pad
$#     pid     secid       mid     eosid      hgid      grav    adpopt      tmid
         7         1         6         0         0         0         0         0
*MAT_BLATZ-KO_RUBBER_TITLE
Rubber Pad
$#     mid        ro         g       ref
         61.55200E-9      15.0       0.0
*PART
$#                                                                         title
Support1 Top
$#     pid     secid       mid     eosid      hgid      grav    adpopt      tmid
         8         1         5         0         0         0         0         0
*PART
$#                                                                         title
Support2 Top
$#     pid     secid       mid     eosid      hgid      grav    adpopt      tmid
         9         1         5         0         0         0         0         0
*SECTION_SOLID_TITLE
Core Solid
$#   secid    elform       aet
         2         1         0
*INITIAL_VELOCITY_GENERATION
$#nsid/pid      styp     omega        vx        vy        vz     ivatn      icid
         1         2       0.0       0.0       0.0   -7961.0         0         0
$#      xc        yc        zc        nx        ny        nz     phase    irigid
       0.0       0.0       0.0       0.0       0.0       0.0         0         0
*DEFINE_COORDINATE_NODES_TITLE
Warp/Weft Direction
$#     cid        n1        n2        n3      flag       dir
         1      5078      5100      5199         0X
*DEFINE_CURVE_TITLE
Loading Movement
$#    lcid      sidr       sfa       sfo      offa      offo    dattyp     lcint
         1         0       1.0       1.0       0.0       0.0         0         0
$#                a1                  o1
                 0.0                 0.0
                 1.0                 1.0
*DEFINE_CURVE_TITLE
FFRP Warp Tension
```

```
$#    lcid      sidr       sfa       sfo      offa      offo    dattyp     lcint
         2         0       1.0       1.0       0.0       0.0         0         0
[CURVE DATA NOT SHOWN]

*DEFINE_CURVE_TITLE
FFRP Weft Tension
$#    lcid      sidr       sfa       sfo      offa      offo    dattyp     lcint
         3         0       1.0       1.0       0.0       0.0         0         0
[CURVE DATA NOT SHOWN]

*DEFINE_CURVE_TITLE
FFRP Compression
$#    lcid      sidr       sfa       sfo      offa      offo    dattyp     lcint
         4         0       1.0       1.0       0.0       0.0         0         0
[CURVE DATA NOT SHOWN]

*DEFINE_CURVE_TITLE
FFRP Shear
$#    lcid      sidr       sfa       sfo      offa      offo    dattyp     lcint
         6         0       1.0       1.0       0.0       0.0         0         0
[CURVE DATA NOT SHOWN]

*SET_NODE_LIST_TITLE
Node set 5
$#     sid       da1       da2       da3       da4    solver
         5       0.0       0.0       0.0       0.0MECH
[LIST OF NODES NOT SHOWN]

*ELEMENT_SOLID
$#   eid     pid      n1      n2      n3      n4      n5      n6      n7      n8
       1       1     647     594     981    1331     590     590    1061    1061
[FULL LIST OF ELEMENTS NOT SHOWN]
```